Doctoral Dissertation
Doctoral Program in Electrical, Electronics and Communications Engineering (36th cycle)

The radiosonde cluster network: A novel approach to track Lagrangian fluctuations inside atmospheric clouds

Shahbozbek Abdunabiev
* * * * * *

Supervisors
Prof. Daniela Tordella, Supervisor
Prof. Eros Gian Alessandro Pasero, Co-supervisor

Doctoral Examination Committee:
Prof. Robert Breidenthal, Referee, University of Washington
Prof. Szymon Malinowski, Referee, University of Warsaw
Prof. Enrico Ferrero, Universita' degli Studi del Piemonte Orientale
Prof. Marco Vanni, Politecnico di Torino
Prof. Carlo Novara, Politecnico di Torino

Politecnico di Torino
October 18, 2024

I hereby declare that, the contents and organisation of this dissertation constitute my own original work and does not compromise in any way the rights of third parties, including those relating to the security of personal data.

. . . . . .

Shahbozbek Abdunabiev

Turin, October 18, 2024

Summary

Understanding cloud dynamics and turbulence within clouds is critical for climate modeling and weather prediction. However, directly measuring cloud fluctuations remains challenging, especially for small-scale phenomena. Traditional radiosonde deployments lack the ability to track fluctuations over extended distances and the entire range of turbulence spatial scales. This work proposes two novel approaches for studying cloud processes: in-field observations using a radiosonde cluster network and numerical simulations of turbulent cloud-clear-air interactions in the presence of water droplets.

The radiosonde cluster network comprises miniaturized radiosondes equipped with sensors for pressure, humidity, temperature, velocity, acceleration, magnetic field strength and position information. The system offers advantages over traditional radiosonde deployments. It tracks fluctuations of physical quantities within clouds and provides simultaneous measurements across the cloud volume. Furthermore, it enables the direct quantification of Lagrangian turbulent dispersion. In-field experiments validated the system's accuracy and demonstrated its ability to perform spectral analysis of fluctuations and distance neighbor graph statistics of Lagrangian dispersion.

The numerical simulations employ three-dimensional direct numerical simulations (DNS) to investigate the interactions between turbulence and cloud droplets in the highly anisotropic interfacial layer, the region where the cloud interacts and entrains to clear air or vice-versa. The simulations closely resemble actual warm clouds, incorporating the same level of supersaturation, liquid water content, number of droplets, density stratification perturbation, and kinetic energy ratio between cloud and clear air regions. The simulations shed light on the intermittency acceleration within the interfacial layer, droplet population dynamics, collision kernel and its relation with turbulent fluctuations, supersaturation balance and microphysical time scales.

These studies provide valuable insights into cloud dynamics and turbulence evolution, contributing to a deeper understanding of cloud formation, growth, and dissipation. The combined use of in-field observations and numerical simulations offers a powerful approach for advancing cloud research and improving climate modeling.

Acknowledgements

My PhD journey was far from a solitary endeavor; it was made possible through the unwavering support and guidance of many individuals. I would like to express my deepest gratitude to my supervisors, Prof. Daniela Tordella and Prof. Eros Pasero. In particular, I am profoundly thankful to Prof. Tordella, whose constant mentorship, invaluable advice, and steadfast support were instrumental in the realization of this PhD. Her guidance shaped my research and provided direction throughout every phase of my work.

I am also deeply grateful to my parents for their unwavering prayers and continuous encouragement, and to my wonderful wife for her patience and support. Their belief in me was invaluable throughout this journey, even when it might not have been evident in my accomplishments.

Throughout my doctoral studies, I had the privilege of collaborating with many colleagues, fellow researchers, and students. I extend my heartfelt thanks to all of them for their support during my time at Politecnico di Torino. Early on, I was fortunate to meet Dr. Federico Fraternale, Dr. Mina Golshan, and Anja Visočnik, who helped me integrate into the group. Federico, in particular, was my initial mentor in numerical simulations and scientific programming. With Mina, I not only conducted numerical studies but also shared valuable experiences during our radiosonde experiments. I also appreciated collaborating with Ludovico Fossa during his master's thesis and later research. During the experimental phase, I worked closely with Dr. Miryam Paredes, who designed the first version of the radiosonde, and we conducted many experiments together. I also collaborated with several master's students under Prof. Tordella's supervision. I would especially like to thank Niccolò Gallino and Andrea Caporali for their significant contributions to the development of the radiosonde cluster system. With Niccolò, we conducted cluster experiments in Chilbolton, UK, as well as in Udine and the Aosta Valley. I am also grateful to the staff at ARPA-Piemonte, ARPA-FVG, INRIM, and the Chilbolton Observatory for their support during these experiments.

Lastly, I would like to thank all my friends who supported me outside the academic environment and anyone whose name I may have unintentionally left out.

Thank you all for being an essential part of this journey.

Shahboz

...

Contents

List of Tables

List of Figures

Chapter 1

Introduction to atmospheric observations

The atmosphere, a dynamic and ever-changing veil surrounding our planet. It has driven humanity to explore its complexities since ancient times. The early motivations for observing the atmosphere were rooted in understanding its fundamental nature and describing its complexities. Today, the focus has shifted towards weather forecasting, climate projections, and environmental protection. This is leading the need for comprehensive atmospheric studies and the development of novel techniques to enhance observational capabilities.

This evolution aims to improve existing observation systems, from the macroscale, encompassing large-scale atmospheric dynamics, to the mesoscale, where smaller-scale weather phenomena emerge, and down to the microscale, where turbulent eddies and cloud formation play a significant role.

To enhance climate change projections, a deep understanding of how climate change may influence various processes, such as the microphysics of clouds, cloud-radiation interactions, and the dynamics of atmospheric and marine boundary layers, is crucial. These processes operate across a wide range of spatial and temporal scales, and their intricate interactions not only affect the hydrological cycle but also influence the general atmospheric circulation. The enhancement of atmospheric observations has profound implications for situational awareness, providing real-time knowledge of potential adverse weather conditions, including storms, lightning, fog, and heavy rain. Understanding weather and climate variability is essential for optimizing activities in various sectors, such as transportation, healthcare, civil protection, agriculture, food production, and renewable energy generation [1].

To achieve this comprehensive understanding of the atmosphere, Earth is constantly under observation by a vast network of meteorological satellites, thousands of ground-based observation stations (including radars, lidars), weather aircraft, ships, and balloon-borne instrumentation (including radiosondes, rawinsondes, and dropsondes). These

platforms collectively measure a wide range of weather parameters, such as temperature, cloudiness, and wind profile, as well as atmospheric constituents like ozone, carbon monoxide, and aerosols. Figure 1.1 highlights the diverse range of instrumentation currently available for atmospheric observations. The Global Observing System (GOS) framework of the World Meteorological Organization (WMO) categorizes observation platforms into several groups [2]:

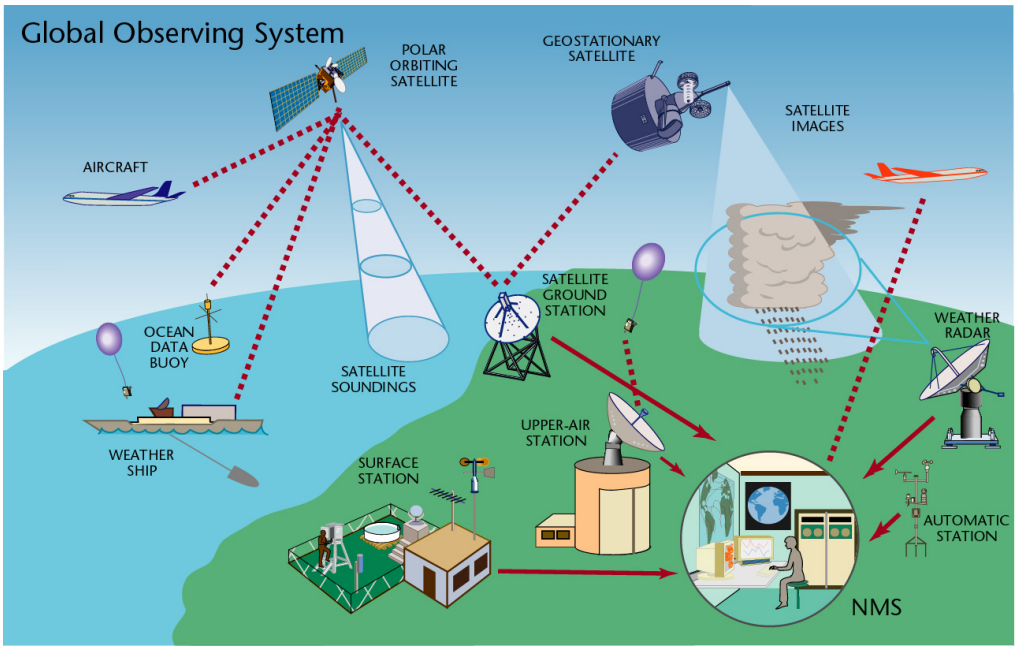

Figure 1.1: Global atmospheric observing platforms. Here, NMS stands for National Meteorological or Hydrological Services. Source: WMO, 2016 [2].

- *Surface observations*: Made at meteorological stations worldwide, measuring air temperature, pressure, humidity, wind speed and direction, and cloud cover.
- *Upper-air observations*: Conducted using radiosondes or rawinsondes launched into the atmosphere, providing temperature, pressure, humidity, and wind speed data from near the surface to altitudes of up to 30 kilometers.
- *Marine observations*: Collected at weather stations on ships and buoys, providing information on air temperature, pressure, humidity, wind speed and direction, and sea surface temperature.
- *Aircraft-based observations*: Obtained from specially equipped weather aircraft, spanning altitudes up to 12 kilometers and measuring a wide range of meteorological parameters, including cloud cover, temperature, pressure, humidity, and wind speed.

- *Satellite observations*: Provided by satellites orbiting Earth, equipped with instruments that measure various meteorological parameters, such as temperature, pressure, humidity, cloud cover, and sea surface temperature, enabling global maps of weather conditions and tracking of weather systems.
- *Weather radar observations*: Utilizing radar waves, these instruments detect the intensity of precipitation and other atmospheric phenomena, particularly useful for identifying thunderstorms, hurricanes, and severe weather events.
- *Other platforms*: Including lidar, which employs laser light to measure atmospheric structure; infrared sounders, which determine atmospheric temperature by measuring infrared radiation; and meteorological balloons, which carry instruments into the atmosphere.

These diverse observation platforms provide the foundation for understanding global-scale processes, such as the radiative energy budget, the hydrological cycle, weather patterns and prediction, and chemical composition of atmosphere.

Atmospheric clouds are complex phenomena, which play crucial role for all global scale atmospheric processes and were center of exploration [3]. Cloud-related properties are subject to constant observation by different instrumentation for different purposes. Most of the currently available instrumentation measures cloud-related quantities to some extent. Following subsections highlight the importance of cloud observations and research. Furthermore, the most important sources of cloud observational dataset are pointed out, which are the large subset of the current global observing system.

1.1 Hydrological cycle

The hydrological cycle is essential to global atmospheric cycle and is described as the circulation of water throughout the Earth-Atmosphere system. At its core, the hydrological cycle is the motion of water from the ground to the atmosphere and back again as a result of chain of processes, such as evaporation, transpiration, condensation and precipitation. A major source of atmospheric water vapor is evaporation from the oceans, together with contribution of evapo-transpiration from the ground surface and plants. Water vapor comprises only 1%–4% (by volume) of the atmosphere, yet it plays a critical role in weather and in Earth's energy balance. Water vapor absorbs and radiates electromagnetic radiation in a broad range of spectral bands that provide the basis for remote sensing of tropospheric and stratospheric water in all its phases [4].

Atmospheric clouds are integral part of global water cycle and atmospheric circulation. They involve mechanisms to form/grow due to *condensation* by capturing evaporated water vapor; *transport liquid water and vapor content* to larger distances; provide internal conditions for tiny condensation particles, through collision and coalescence, grow too large for the rising air to support, and thus fall to the Earth.

1.2 Radiative energy budget

Clouds play a vital role in our climate by regulating the amount of solar energy that reaches the surface and the amount of the Earth's energy that is radiated back into space. The more energy that is trapped by the planet, the warmer our climate will grow. If less energy is collected, the climate will become cooler. Understanding this energy balance is fundamental to answering any of the questions posed by climate change.

Depending on their altitude, structure and composition (ice or water) clouds will regulate energy differently. One cloud may trap heat by reflecting energy back to the surface. Another may reflect sunlight and cause the surface to cool. You may have noticed that a cloudless night can be much colder than a cloudy night. Without the heating of the sun and a layer of clouds to insulate us, the surface radiates more heat into space on cloudless nights, making them colder. To study these characteristics, researchers combine data from a variety of instruments to form a complete understanding of cloud radiative properties.

Clouds are critical not only in cycling water through the atmosphere and transporting it throughout the globe, but also in modulating the radiative energy budget of the planet through interactions with solar and infrared (IR) radiation. As a key source of freshwater, precipitation and knowing when, where, and how much it rains or snows around the world is important for science and society. Precipitation also represents an important energy (latent heat) and hydrologic exchange between Earth's atmosphere and its surface [4].

Clouds cool the Earth surface by reflecting sunlight back to the space by around 12 ˚C, an effect that is basically caused by *strato-cumulus (warm)* clouds. However, at the same time, the cooling effect of clouds is partially compensated by a 'blanketing' effect: cooler clouds reduce the amount of heat radiating into space by absorbing the heat coming from the Earth's surface and re-radiating some of it back downward. The blanketing effect warms Earth's surface of approximately 7˚C. These processes averages out to a net loss of 5 ˚C[5].

1.3 Complex dynamics of atmospheric clouds

Clouds are ubiquitous in the Earth's atmosphere, ranging from the surface as fog to the mesosphere as noctilucent clouds. They form when air is cooled to the point where it becomes *saturated with water vapor*. This can happen in a variety of ways, such as when air is lifted up or when it loses energy by radiating heat. Clouds can form at temperatures above or below freezing, and they can exist as liquid water droplets, ice crystals, or a mixture of both. The wide range of altitudes and meteorological conditions that can lead to cloud formation results in a tremendous variety of cloud forms, from towering cumulus clouds to wispy cirrus clouds that may be invisible to the naked eye [3].

Despite their ubiquity and significance in weather and climate, clouds remain a major source of uncertainty in weather forecasting and climate models. This uncertainty stems from the complex interplay of physical and chemical processes that govern cloud formation and evolution, spanning a wide range of scales from microns to kilometers [6, 7].

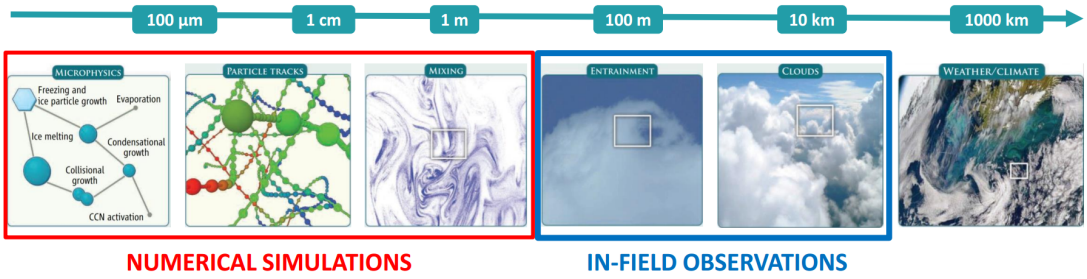

Figure 1.2: A matter of scale. Cloud formation involves a wide range of physical and chemical processes spanning various scales, from micron-sized droplet collisions to airflow dynamics covering thousands of meters [6].

Within clouds, small droplets and ice particles are embedded in a turbulent flow, which is characterized by strong fluctuations in temperature, humidity, aerosol concentration, and cloud particle dynamics. Turbulence plays a crucial role in driving entrainment, stirring, and mixing within clouds, influencing the growth and decay of cloud particles, as well as phase transitions such as nucleation, condensation, and freezing. These processes, in turn, feed back on the turbulent flow through buoyancy and drag forces [6, 8].

One of the key challenges in cloud research is understanding how small-scale processes, such as cloud droplet activation and the growth and evolution of cloud particle size distributions, influence the macroscopic properties of clouds. These seemingly unrelated processes have a profound impact on cloud lifetime, extent, precipitation efficiency, and radiative properties. To fully comprehend the role of clouds in the Earth's climate system, it is essential to unravel the intricate connections between these scales [9].

Researchers are developing laboratory facilities to simulate droplet activation, ice nucleation, and condensational growth under realistic turbulence and thermodynamics conditions. Lagrangian particle tracking techniques are being used to elucidate cloud particle dynamics in both laboratory settings and real clouds. Scale-resolving numerical simulations are capturing the interplay of turbulent mixing and nonlinear phase transitions, providing valuable insights into cloud dynamics [6, 9].

Given the uncertainties surrounding cloud representation in climate models, more observations are needed to improve our understanding of cloud processes. The challenge lies in bridging the gap between the micro-scale processes of aerosol and particle

microphysics and the macro-scale turbulent dynamics of clouds, while also integrating knowledge from diverse scientific and engineering disciplines. The Cloud - MicroPhysics - Turbulence - Telemetry (COMPLETE) project within the Horizon 2020 framework has provided an inter-disciplinary research training environment for enhancing the understanding and modeling of atmospheric clouds [10].

In conclusion, clouds are complex and dynamic systems that play a critical role in weather and climate. To better understand and model clouds, we need to address the challenges of bridging scales and integrating knowledge from multiple disciplines. By combining laboratory and field observations, numerical simulations, and theoretical insights, we can gain a deeper understanding of cloud processes and their implications for weather and climate.

1.3.1 Horizon 2020 COMPLETE project

The accurate representation of clouds in climate models remains a significant challenge, owing to the intricate interplay of physical and chemical processes that occur across a vast range of scales, from microscopic interactions of droplets and ice particles to the turbulent flow dynamics of the entire cloud system. These processes are highly non-stationary, inhomogeneous, and intermittent, making them challenging to study and model [11, 12].

Recognizing the need for a comprehensive approach to cloud research, the Cloud - MicroPhysics - Turbulence - Telemetry (COMPLETE) project was launched under the Horizon 2020 framework. The project aimed to foster an inter-disciplinary research training network, preparing high-potential early-stage researchers (ESRs) with expertise in both scientific and industrially-oriented skills. This training program was designed to advance our understanding of cloud physics and related turbulent dynamics, addressing the limitations of cloud parameterization in climate models.

One of the key objectives of COMPLETE was to bridge the gap between laboratory and field observations, numerical simulations, and theoretical insights. This involved developing advanced instrumentation and sensors for measuring aerosol and dust particles, water droplets, humidity, turbulent velocity, and acceleration in atmospheric and laboratory conditions [10, 13].

The project also focused on theoretical and numerical studies of turbulence-interfacial phenomena in warm clouds. Researchers analyzed information on turbulent velocity fluctuations and the structure of thermodynamic fields (temperature, humidity, and liquid water content) to understand the role of turbulence in cloud processes. Specific research areas included the dynamics of turbulent entrainment of dry environmental air into the cloud and the microphysical and dynamical effects of turbulent mixing following the entrainment.

In addition, the project investigated the microphysics of clouds, examining the main phenomena that govern cloud formation and evolution, such as humidity, droplet growth, size distributions, collision kernels, and droplet coalescence. Researchers also explored

aerosol-cloud interactions, focusing on the dynamics of aerosols and particles in clouds, particularly the differences in dynamics of inertial and non-inertial particles in shear- and buoyancy-driven flows.

The COMPLETE project's findings are expected to significantly improve our understanding of cloud processes and their impact on weather and climate. By bridging scales and integrating knowledge from multiple disciplines, the project has provided valuable insights into the intricacies of cloud dynamics, paving the way for more accurate cloud parameterization in climate models.

1.4 Instrumentation and observation techniques of atmospheric clouds

The complex nature of clouds and general atmospheric boundary layer (ABL) necessitates the use of a variety of instrumentation systems to effectively study their behavior and impact on weather and climate. Each instrument contributes distinct information, and the overlapping of data sets collected by different instruments is crucial for cross-validation and comprehensive understanding. Table 1.1 summarizes a list of currently available instrumentation, indicating the physical phenomena observed, the type of technology employed, and the observation scale. Even though we can not cover the all available instrumentation and techniques for cloud observation, we delve into the details of each listed instrument in the following subsections.

Table 1.1: Comparison of available instrumentation for atmospheric cloud observations.

Instrument	Observed physical phenomena	Technology type	Observation scale
Radar	Wind profile, precipitation, cloud structure, cloud fraction, cloud top-height	*Ground-based*, radiometry at 3-GHz, 35-GHz, 94-GHz bands	**Local**, tens of km, continuous measurements
Lidar	Cloud base, classification of clouds, aerosol content, temperature	*Ground-based/airborne*, laser lights at near-infrared band	**Local/regional**, tens of km, continuous measurements
Meteorological satellites	Cloud cover, type, top-height and cloud phase; Wind speed based on the cloud movement; LWC estimation, precipitation, temperature and pressure	Satellite radiometry, spectroscopy, sounding	**Global**, up to full coverage of Earth surface, continuous measurements
Aircraft	Microphysics, turbulence, radiation, temperature, pressure, humidity	*Airborne*, a set of portable sensor systems	**Regional**, for a few hours
Radiosonde (dropsonde, rawindsonde, etc.)	Vertical profiles of ambient temperature, pressure, humidity, wind speed, and wind direction	Upward (downward) moving balloon	**Regional**, possibly traversing the clouds for a few time and length scale

1.4.1 Radars and lidars

Radars and lidars are currently the most important source of observational information about clouds in forecast models [14]. They provide crucial information about cloud morphology, humidity and precipitation levels, liquid and ice water content (LWC and IWC) and cloud dynamics. Additionally, dual-Doppler radar observations can reveal the three-dimensional mean velocity and vorticity fields within clouds [15].

Basic Radar Principles for Cloud Observations. Radars measure the range-normalized intensity of the backscattered signal, known as radar reflectivity. This parameter reflects the concentration and size of hydrometeors (water droplets and ice particles) within the cloud. Radar reflectivity is typically expressed in decibels (dB), with a value of 0 dB indicating no precipitation and higher values indicating stronger precipitation.

Prior to the 1990s, most operational radars could only measure reflectivity, while modern radars can also quantify other parameters, such as Doppler velocity, which enables the estimation of wind speed within the cloud. This information is essential for understanding cloud dynamics and their influence on atmospheric circulation.

Most radars currently operate at S-band (10 cm wavelength), C-band (5 cm wavelength), and X-band (3 cm wavelength). S-band radars are most commonly used for surveillance, since they suffer from attenuation the least. C-band radars are employed for precipitation estimation and Doppler wind measurements, while X-band radars are employed for high-resolution precipitation estimation and research [1, 16].

LIDARs (LIght Detection And Ranging). Lidars operate at wavelengths closer to that of light. They detect backscattering from aerosols rather than from larger scatterers such as hydrometeors. This allows them to penetrate deeper into clouds and provide information on their vertical structure and composition. Radiation is transmitted as a collimated beam by a telescope. LIDAR beams are highly collimated, enabling the detection of fine-scale features within clouds. They have been deployed on ground-based towers, airborne platforms, and satellites, providing versatile cloud observations. Some LIDARs also have Doppler capability, enabling wind measurements in the boundary layer, particularly in areas with abundant aerosols.

Raman lidars offer a unique capability to remotely measure temperature and water vapor mixing ratio by comparing the backscattered signals at different frequencies. In the case of water vapor measurements, different gases can also be distinguished [1]. Raman lidars are relatively expensive due to the high power of their transmitters and large receiver apertures. However, they provide invaluable insights into cloud microphysics and thermodynamic structure.

By combining data from radars, lidars, and microwave radiometers, scientists can gain a more comprehensive understanding of cloud structure and composition [14]. This data synergy provides insights into cloud vertical extent, cloud boundaries, cloud cover fraction, cloud macrophysical properties, and cloud thermodynamic phase.

1.4.2 Meteorological satellites

Satellites provide a valuable means for observing clouds and their properties on global scales. They offer a unique perspective, as they can image clouds from above, providing a synoptic overview of cloud distribution and evolution. Satellite-based cloud observations are crucial for understanding cloud-climate interactions and for improving weather and climate forecasting[4].

The introduction of meteorological satellites can be traced back to the launch of the TIROS (Television and Infra-Red Observation Satellite) system, the first satellite dedicated to atmospheric observations, on April 1, 1960 [17]. Since then, satellites have played a pivotal role in advancing our understanding of clouds and their role in Earth's energy budget.

Meteorological satellites operate in two main orbits: Low Earth Orbit (LEO) and Geostationary Earth Orbit (GEO). LEO satellites orbit the Earth at altitudes of around 500-1000 kilometers, providing frequent observations of rapidly evolving phenomena such as storms, hurricanes and fog radiation. GEO satellites orbit the Earth at altitudes of around 35,786 kilometers, providing continuous coverage of specific regions. They can provide temperature, and moisture profiles for numerical weather prediction codes [1].

Satellite-based cloud observations are available in a variety of data products, tailored to specific applications. These data products include cloud type information, cloud water content, cloud top height, and cloud cover fraction. Furthermore, they can detect rainfall and snowfall, providing information about the distribution and intensity of precipitation. In addition, satellites can also measure the amount of solar radiation that enters the Earth's atmosphere and the amount of infrared radiation that is emitted back to space.

Several satellite missions have been instrumental in improving our understanding of clouds. CERES (Clouds and the Earth's Radiant Energy System), for instance, has produced a unique suite of data products for studying Earth's energy budget [18]. CloudSat's Cloud Profiling Radar (CPR) has provided detailed measurements of cloud top height and cloud water content [19]. Similarly, CALIPSO (Cloud–Aerosol Lidar and Infrared Pathfinder Satellite Observations) has collected high-resolution data on cloud properties, including cloud type, particle size, and optical thickness [20]. The Pathfinder Atmospheres Extended (PATMOS-x) project, launched in 2004, has expanded the coverage and accuracy of cloud data products, contributing significantly to our understanding of the Earth's atmosphere and its interactions with clouds [21]. It included all AVHRR sensors, including those launched into morning and midmorning orbits by the European Organisation for the Exploitation of Meteorological Satellites (EUMETSAT) and National Oceanic and Atmospheric Administration (NOAA).

Early satellites, however, lacked coverage in the polar regions, limiting their ability to fully characterize cloud properties. Modern satellites, equipped with advanced sensors and orbiting global coverage, have furnished new estimates of clouds, aerosols,

ocean surface temperature, snowpack and sea ice, vegetation, surface winds, and trace gases. As satellite technology continues to advance, we can expect even more sophisticated cloud observations, leading to further advancements in weather forecasting, climate modeling, and environmental monitoring.

1.4.3 Airborne measurements

Aircraft equipped with sophisticated instrumentation can conduct comprehensive measurements of aerosol properties, chemical composition, cloud physics, and fundamental meteorological parameters. Commercial aircraft even routinely measure temperature and moisture parameters. Over 700,000 automated observations per day (before the 2020-21 pandemic) are obtained from the globally deployed Aircraft Meteorological Data Relay (AMDAR) system, which utilizes existing aircraft sensors, computers, and communication systems to transmit meteorological data to ground stations via satellite or radio links [22].

Long-range research aircraft can effectively sample variables crucial for understanding radiative forcing and climate change, including atmospheric gas concentrations, aerosols, and upwelling and downwelling solar and terrestrial radiation. Smaller aircraft can be deployed to probe mesoscale and cloudscale systems, measuring properties such as liquid water, cloud droplets, and other hydrometeors. In addition to the radars mentioned above, research aircraft can also employ lidars and millimeter (cloud) radars [1]. One notable example is the Facility for Airborne Atmospheric Measurements (FAAM) aircraft, jointly organized and managed by UK MET OFFICE and Natural Environment Research Council (NERC) [23].

FAAM offers a diverse suite of instrumentation to conduct measurements of aerosol properties, chemical composition, droplet size distribution, droplet shapes, and turbulence intensity within clouds [24, 25]. FAAM utilizes a Particle Soot Absorption Photometer (PSAP) to measure aerosol absorption, employing a simple filter technique to achieve accurate readings [26]. It also employs a dual-column Cloud Condensation Nuclei (CCN) Counter to determine the proportion of aerosol capable of forming cloud droplets.

In situ airborne measurements of cloud particles provide valuable insights into cloud processes such as formation, growth, and dissipation. Imaging probes provide detailed information on particle shape and size, enabling researchers to better understand cloud microphysical properties. These probes capture two-dimensional representations of individual particles, allowing researchers to quantify particle shape for sizes ranging from 15 micrometers to 6 millimeters. Additonally, turbulent wind measurements are essential for understanding the interactions between the atmosphere and the land or sea surface, particularly in the lower atmosphere. Airborne platforms can provide valuable data on turbulent wind profiles, which are crucial for improving weather forecasting and climate models.

1.4.4 Balloon-borne measurements

The balloon-borne instrumentation and observations techniques provided the very initial toolset for studying the atmosphere. The history of the balloon-borne experiments goes back to as early as 18th century. The hot-air balloon that the Montgolfier brothers successfully tested in public in Annonay in the south of France on 5 June 1783 is regarded as humankind's first balloon (Fig. 1.3). One of the first scientific use case of the balloons was reported on August 24, 1804 by French scientist, J. L. Gay-Lussa [27]c. He was able to ascend up to 8000 m of altitude and brought barometer, a thermometer and a hygrometer during the flight.

Figure 1.3: First public demonstration of hot-air balloon in Annonay, France on 4 June 1783. Source: Wikimedia Commons [28], available for public domain.

Balloon-borne techniques have been widely utilized for various applications, including scientific in-situ experiments, engineering applications, and routine meteorological observations. Over the past 160 years, advancements in this field have led to the development of a diverse range of balloon-borne measurement systems tailored for atmospheric studies. These systems encompass large hot-air balloons, superpressure balloons equipped with extensive instrumentation for upper-air observations, smaller

balloons carrying radiosondes for vertical profiling, and even miniaturized dropsondes for localized measurements.

Complementing conventional pilot and radiosonde balloons, constant-level balloons, constructed from inextensible materials, rise to a predefined altitude and maintain their position. These balloons come in two forms: large constant-level balloons and superpressure constant-level balloons. Tetroons, tetrahedral-shaped superpressure constant-level balloons, are particularly useful for trajectory studies [29].

The appeal of balloon-borne techniques for atmospheric observations lies in their inherent advantages, such as affordability, streamlined preparation procedures, and the ease of launching [27].

Radiosondes

Radiosondes, which typically utilize spherical balloons to carry a payload of instrumentation including sensors, data acquisition and transmission devices during in-field observations [29]. These lightweight instruments ascend into the atmosphere, measuring key meteorological parameters like temperature, pressure, humidity, and wind speed at various altitudes. Periodic radiosonde measurements provide feedback information on fundamental meteorological quantities for weather forecasting and monitoring applications. Additionally, they serve as initial conditions for numerical weather simulations, enabling the prediction of future weather patterns.

Radiosonde networks, established across the globe, ensure continuous monitoring of atmospheric conditions. Each launching site conducts automatic, semi-automatic or manual radiosonde soundings one or two times per day at fixed time of the day. GRUAN (Global Climate Observing System Reference Upper-Air Network) is one such international network, which aims to provide high quality meteorological information on surface, stratosphere and troposhere measurements[30]. In Italy, seven dedicated radiosonde launching sites operate under the supervision of regional environmental protection agencies, such as ARPA-Piemonte (Arpa Piemonte - Agenzia Regionale per la Protezione Ambientale). These sites conduct daily automatic radiosoundings, contributing to the country's meteorological network.

For detailed investigations of the boundary layer and lower troposphere, specialized radiosondes have been developed. These instruments offer enhanced measurement sensitivity, spatial resolution, and temporal resolution, enabling a more comprehensive understanding of atmospheric processes within these layers. These radiosondes measure temperature, pressure, humidity, and wind speed from the ground to altitudes of 3 to 5 kilometers. In certain cases, pressure measurements may be omitted for measurements up to 2000 meters to reduce data size and system cost. Additionally, simpler radiosondes that only measure temperature are available [29].

Despite their capabilities, current atmospheric profiling radiosondes and dropsondes have limitations in their ability to provide long-term cloud datasets. Their rapid

ascent rates, typically ranging from 150 to 200 meters per minute, restrict their duration within clouds or cloudy boundary layers. This brevity hinders the acquisition of comprehensive data sets necessary for in-depth investigations of cloud structure, flow dynamics, and thermodynamics.

Tethered balloon-borne systems

Tethered balloon-borne systems offer an alternative approach for conducting high-resolution measurements of turbulent fluctuations within the atmosphere, starting from the ground level to the altitudes of 1500 m. These systems, which typically employ larger balloons, can lift heavier payloads, including multiple sensor packages. Sensor data can be transmitted via radio or stored directly in a processing unit within the payload. Tethered balloon-borne systems provide invaluable insights into the turbulent characteristics of clouds and the boundary layer [8, 31, 32, 33].

One notable example is the Airborne Cloud Turbulence Observation System (ACTOS), a tethered balloon-borne instrumental payload capable of conducting measurements with a resolution of 10 centimeters within a cloudy boundary layer (Siebert, Lehmann, and Wendisch [8]). ACTOS incorporates hot-wire anemometers, fine-wire resistance ultrafast thermometers (UFT), Forward Scattering Spectrometer Probe (FSSP), and a particle volume monitor (PVM-100A) for measuring liquid water content. The system's large balloon, with a volume of 400 cubic meters, supports a 200-kilogram payload, enabling measurements at high sampling rates (up to 100 Hz) for velocity and temperature while maintaining a nearly constant altitude and low horizontal speed. This capability is particularly useful for studying local turbulent characteristics, such as isotropy, turbulent kinetic energy (TKE) dissipation levels, and spectral profiles of velocity structures.

Tethered balloon-borne systems, while categorized as balloon-borne instrumentation, resemble airborne measurements in their ability to conduct high-resolution observations. However, they introduce significantly less disturbance to the surrounding flow dynamics compared to aircraft-based measurements.

1.4.5 Numerical studies of clouds and ABL

Direct numerical simulations (DNS) can provide valuable insights into the intricate dynamics and intermittency of cloud formations. However, due to computational limitations, DNS simulations can only resolve a very small portion of clouds, typically on the scale of a few meters [34, 35, 36]. This restricts their ability to provide a comprehensive understanding of cloud behavior on a larger scale, such as at the tens-of-kilometer level.

Deterministic climate models, on the other hand, typically have grid sizes of 10 kilometers, although state-of-the-art models can achieve finer resolutions of up to 2.2 kilometers [37, 38]. These models offer a more global perspective on cloud systems but often employ simplified representations of cloud processes.

Climate simulation models employ two primary approaches to represent clouds and cloudiness: *convection-parameterizing* and *convection-resolving*. Convection-parameterizing models, which are widely used, employ statistical relationships to estimate cloud properties, but they tend to overestimate humidity (cloudiness) in the lower troposphere (850 hPa) and underestimate it in the mid-troposphere (700 hPa, 500 hPa). In the upper troposphere (200 hPa), both convection-parameterizing and convection-resolving models generally produce similar results [37].

Mid-level clouds are particularly challenging to simulate due to the frequent occurrence of strong updrafts, strong vertical mixing, and favorable dynamical and microphysical conditions that lead to the formation of mixed-phase clouds [37]. Convection-parameterizing schemes may underestimate the amount of mid-level clouds in climate simulations [39], while convection-resolving simulations require immense computational resources (e.g., 90 million core hours [38]).

Data assimilation techniques and new generation unified models are being developed to improve the accuracy of numerical simulations and reduce uncertainties [11]. These efforts aim to address the limitations of convection-parameterizing models while minimizing the computational cost of convection-resolving simulations.

1.4.6 Summary and outlook

Assessing the impact of climate change on cloud dynamics necessitates comprehensive micro- and mesoscale observational studies to isolate the effects of large-scale meteorological variability from those induced by changes in aerosol-droplet properties. Cloud and precipitation formation is influenced by both large-scale forcings and microphysical processes. Consequently, it is crucial to not only examine instantaneous relationships between microphysical and macrophysical variables but also track their temporal evolution. This requires a holistic perspective that integrates microphysical observations with large-scale meteorological variability [11].

Initiatives like Cloudnet [14], COMPLETE [10], and CloudSat [19] have made significant contributions to our understanding of clouds and improved cloud representation in weather and climate models. However, direct measurements of internal cloud fluctuations are essential to fully comprehend their spatiotemporal evolution. Measuring quantities such as temperature, pressure, humidity, velocity, acceleration, and the magnetic field within clouds would provide valuable insights into cloud dynamics and the forces that drive them. Unfortunately, current instrumentation and measurement techniques limit our ability to obtain such direct observations.

Lagrangian tracking of flow parcels within clouds can potentially capture these internal fluctuations, allowing for simultaneous multi-point measurements across the cloud volume. However, this approach remains challenging due to technical limitations. Understanding the relative motion and fluctuations of physical quantities is crucial for unlocking the intricacies of turbulent dispersion and diffusion within clouds [7].

To address this challenge, innovative measurement systems and novel approaches

are needed to directly capture the internal dynamics of clouds. By bridging the gap between microscale processes and large-scale atmospheric conditions, we can gain a deeper understanding of cloud response to a changing climate, leading to more accurate weather and climate predictions.

1.5 A novel approach to cloud observations and modeling

Despite significant advancements in cloud modeling and observation techniques, direct measurements of the internal fluctuations and forces that drive cloud dynamics remain elusive. These fluctuations influence cloud formation, growth, and dissipation, which in turn impact the Earth's energy balance and weather patterns. To address this gap, the present work introduces two novel approaches: in-field observations using a radiosonde cluster network and numerical simulations of cloud-turbulence interactions [7, 40, 34, 35, 36]. The combination of in-field measurements and numerical simulations offers a powerful strategy for advancing our understanding of cloud processes and their impact on the Earth's climate.

1.5.1 Using the POLITO-COMPLETE radiosonde cluster network

Lagrangian observations have been pioneered by Richardson (1926) [41], who investigated the relative motion of a set of flow particles to elucidate the underlying reasons for relative turbulent dispersion and diffusion. Beyond particle motion, physical quantities can also be measured along each fluid particle's trajectory as time progresses.

Conventional cloud observations, such as lidars and radars, provide limited information about the internal dynamics of clouds. The proposed radiosonde cluster network aims to overcome this limitation by tracking the motion and properties of multiple flow parcels within clouds. This approach enables direct quantification of Lagrangian turbulent dispersion and diffusion, providing insights into the transport and mixing processes within clouds [7, 40].

The radiosonde cluster network consists of miniaturized radiosondes equipped with sensors for pressure, humidity, temperature, and inertial measurement unit (IMU) data. These radiosondes are released from a ground station and drift with the ambient air flow, sampling the surrounding environment along their trajectories. By analyzing the trajectories of multiple radiosondes, it is possible to reconstruct the spatial and temporal evolution of turbulent dispersion within clouds.

Conventional meteorological balloons typically rely on materials like rubber or polyethylene, which pose environmental concerns. In contrast, the radiosonde cluster network employs biodegradable balloons [42]. This innovative approach not only reduces the environmental impact of balloon-based observations but also offers advantages in terms of stability and flight duration. The biodegradable balloons provide a

fixed volume for the radiosondes, ensuring a consistent environment for measurements within the isopycnic layers of clouds and the ABL.

To validate the feasibility of the radiosonde cluster approach, a series of field tests was conducted between September 2021 and July 2023. These experiments involved releasing a cluster of tens of radiosondes, providing simultaneous measurements over a 10-kilometer region. In some cases, the measurements extended up to 50 kilometers. The results of these field tests were promising, demonstrating the ability of the radiosonde cluster network to track turbulent fluctuations and obtain the Lagrangian statistical properties of cloud dynamics [7].

The detailed results of these in-field experiments are presented in our paper Abdunabiev et al. [7]. In Chapter 4, we describe the radiosonde network and its capabilities. Chapter 5 highlight the key findings from the validation tests, demonstrating the accuracy and effectiveness of the radiosonde cluster network in capturing the intricacies of cloud dynamics.

1.5.2 Numerical simulations of turbulent cloud-particle interactions

Three-dimensional direct numerical simulations (DNS) are used to investigate the interactions between turbulence and cloud droplets in the interfacial layer, the region where the cloud transitions to clear air [43, 36]. The Eulerian description of turbulent velocity, temperature, and vapor fields is coupled with the Lagrangian tracking of two different kinds of droplet populations: monodisperse and polydisperse. A shear-free turbulent mixing layer mimics the background air flow at the cloud top, simulating the cloud's interaction with the surrounding environment.

Our simulations closely resemble actual warm clouds, incorporating the same level of supersaturation, liquid water content, number of droplets, density stratification perturbation, and kinetic energy ratio between cloud and clear air regions. The observation duration is limited to a few seconds, corresponding to approximately ten initial eddy turnover times. During this period, kinetic energy throughout the system decays by 95%. The interfacial layer (the shear-free turbulent mixing layer at the cloud-clear-air interface) also experiences a significant decrease in kinetic energy, reaching 85% depletion[34].

The simulations show that the interfacial layer experiences a rapid acceleration of droplet dynamics compared to the cloud region. This acceleration is attributed to the intermittency of the turbulence, which creates strong local fluctuations in the flow and supersaturation. The simulations also reveal that the collision kernel, a key parameter in droplet growth models, needs to be adapted to account for the unstable and inhomogeneous conditions of the interfacial layer [34].

Our recent numerical studies analyzed the supersaturation balance in highly intermittent shearless turbulent mixing layers under conditions with no mean updraft. We investigated the evolution of the cloud-clear air interface and the droplets therein

using direct numerical simulations [35]. Comparing horizontal averages of the phase relaxation, evaporation, reaction, and condensation times within the cloud-clear air interface for the initial monodispersed and polydisperse droplet populations revealed a clustering of values. For the monodisperse population, this clustering occurred around 20-30 seconds in the central area of the mixing layer, just before the location of the maximum supersaturation turbulent flux. The polydisperse population exhibited a similar clustering pattern, but condensation time was also included.

The mismatch between the time derivative of supersaturation and the condensation term in the interfacial mixing layer was found to be correlated with the planar covariance of the horizontal longitudinal velocity derivatives of the carrier air flow and the supersaturation field. This suggests a potential quasi-linear relationship between these quantities [35].

1.6 Thesis organization

Chapter 2 provides an extensive overview of Lagrangian investigations of atmospheric clouds, encompassing numerical, in-field, and laboratory-based approaches.

Chapter 3 delves into our numerical methodology for examining droplet-turbulence interactions, the dynamics of the interfacial region between a cloud and clear air, and the analysis of microphysical timescales such as reaction, phase, and evaporation times for both monodisperse and polydisperse populations.

Chapter 4 introduces our proposed in-field observation system, built upon the radiosonde cluster system. Furthermore, the Chapter discusses the traceability of the system, the quality of the acquired dataset, and validation with reference systems. Chapter 5 presents the results from preliminary in-field experiment campaigns.

We draw our conclusions from the numerical and experimental investigations of atmospheric clouds and the atmospheric boundary layer (ABL) in Chapter 6.

Chapter 2

Lagrangian observations

Atmospheric observations can be mapped within either the Eulerian or Lagrangian reference frame. The Lagrangian approach tracks air parcels as they move through the atmosphere, offering unique advantages for studying mixing and dispersion processes (Yeung [44]). However, traditional atmospheric observations primarily utilize the Eulerian framework, relying on large-scale, high-precision, and often expensive instrumentation like radars, lidars, fixed weather stations, and aircraft.

In contrast, Lagrangian observations aim to capture atmospheric processes within a reference frame that moves with the air itself. This approach is particularly well-suited for studying time-evolving phenomena. Pioneering Lagrangian measurements involved balloons equipped with tracers, allowing researchers to track the position or trajectory of the balloon during its flight (Richardson [41], Businger et al. [45], and Businger, Johnson, and Talbot [46]). Modern Lagrangian sensors, including radiosondes, drifters, and rawinsondes, can follow quasi-Lagrangian trajectories under certain conditions (Abdunabiev et al. [7] and Markowski et al. [47]).

The Lagrangian approach is often overlooked in fluid mechanics textbooks beyond the concept of the material derivative[44]. Traditional turbulence measurements are primarily conducted in the Eulerian frame, exemplified by anemometers placed at fixed ground locations or on airplanes. Measurements from airplanes or large balloons require corrections to account for the platform's motion, as neither truly moves with the air mass they are measuring. While some balloon-borne instrument studies are now conducted by satellites, balloons remain a valuable tool for high and low-altitude research [45].

For Lagrangian observations, ideally, particles or tracers should be small relative to the phenomena being observed and neutrally buoyant to minimize their impact on the flow. The motion of such passive trackers can be described with the following simple equations, in derivative and integral forms:

$$\frac{d\mathrm{r}}{dt} = \mathrm{w}(t), \quad \mathrm{r}(t) = \mathrm{r}_0 + \int_0^t \mathrm{w}(t')dt', \tag{2.1}$$

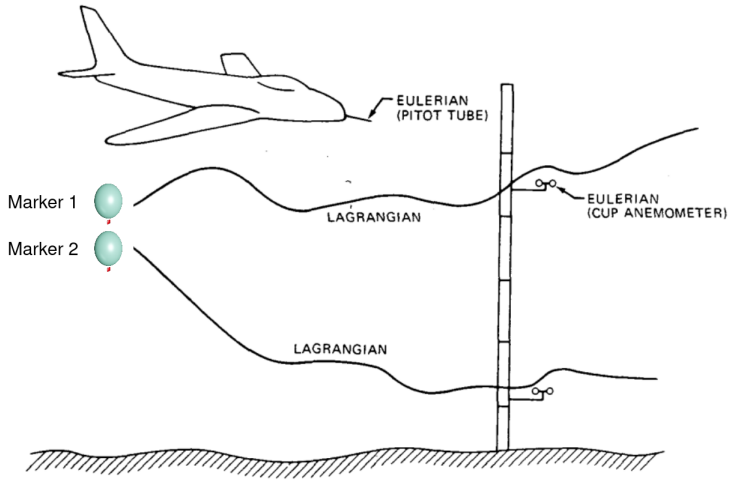

Figure 2.1: Eulerian and Lagrangian wind measuring systems. True Lagrangian wind measurements are given by tagged air markers 1 and 2. Adopted from Hanna, Briggs, and Hosker [48].

where $w(t)$ is Lagrangian velocity, $r(t)$ is the separation vector and r_0 is the initial separation vector.

As depicted in Figure 2.1, Lagrangian measurements involve tracking air parcel markers (e.g., markers 1 and 2) as they move with the airflow without disturbing it. Turbulent diffusion is inherently a Lagrangian process, and ideally measurements should be made in this reference frame. However, most turbulence measurements are taken in the Eulerian frame and then converted to the Lagrangian frame. Since Eulerian measurements are more common, relationships have been established to connect quantities measured in the two reference frames [44].

Lagrangian observations offer distinct advantages over Eulerian measurements, particularly for studying cloud behavior in the context of a changing climate. Here are some key benefits:

- **Following the flow:** A well-designed Lagrangian system can mimic the motion of a small air parcel, allowing us to directly track its properties as it travels within the evolving airflow. In the Lagrangian frame of reference, the mean wind appears to be zero [45, 46].
- **Wider spatial and temporal coverage**: Compared to traditional fixed-point observations, Lagrangian experiments can encompass a broader range of spatial and temporal scales. This is particularly advantageous for long-range studies, eliminating the need for dense networks of fixed stations across vast observation domains [45].
- **Enhancing numerical simulations:** Lagrangian experiments play a crucial role in advancing numerical Lagrangian simulations. They provide valuable insights

into atmospheric processes, improving model parameterizations. Additionally, Lagrangian datasets serve as vital benchmarks for existing models and simulations. Capturing the time evolution of the air parcel is particularly important for validating numerical schemes [11].

While various approaches exist for studying atmospheric flows (numerical simulations, laboratory experiments, remote sensing, in-field measurement), Lagrangian experiments offer a unique strength - directly tracking and measuring cloud properties within their dynamic environment. Lagrangian observations have significantly contributed to our understanding of air mass transformations and associated physical and chemical processes. However, their full potential for studying atmospheric boundary layer dynamics, particularly cloud behavior in a changing climate, remains largely untapped (Brenguier and Wood [11]).

To fully realize the potential of Lagrangian experiments for cloud research, several key areas require focused development:

- **Multi-parameter observations** encompassing various sampling directions and data relevant to multiple scientific disciplines.
- **Fine sampling resolutions** to capture finer-scale atmospheric processes crucial for accurately representing cloud dynamics in models.
- **Data-model synergy** to achieve a more comprehensive understanding of cloud evolution through integration of observational data with atmospheric simulations.
- **Cross-validation** with complementary techniques like remote sensing or Eulerian measurements to ensure the accuracy and reliability of Lagrangian datasets.

The Lagrangian approach offers a powerful tool for studying a wide range of phenomena, extending far beyond the scope of this Chapter. Applications can be found in diverse fields such as aerosol science, multiphase flows, and even medical tracer imaging [44]. While this text has emphasized the importance of Lagrangian observations for studying cloud behavior, it's important to recognize their broader applicability in atmospheric research. These observations are valuable for investigating various atmospheric phenomena, including:

- *Dispersion of pollutants*: Tracking the movement of air parcels can help us understand how pollutants disperse and impact air quality over different spatial scales.
- *Volcanic ash plumes*: Lagrangian observations can be used to predict the trajectory of volcanic ash plumes, aiding in the development of effective mitigation strategies.
- *Long-range atmospheric transport*: Studying the long-range movement of air masses using Lagrangian techniques provides valuable insights into global atmospheric circulation patterns. Furthermore, the velocity gradients and multipoint structure of the velocity field within these air masses offer unique information on the flow's kinematics and topological properties [44].

- *Biological Oceanography*: There is growing recognition of the impact of turbulence on the dynamics and life cycle of small organisms like plankton and fish larvae. A better understanding of these interactions, through Lagrangian observations, can lead to substantial economic benefits, such as improved fishery management techniques. [44].

Lagrangian observations offer a powerful approach for studying cloud dynamics within the atmospheric boundary layer. By focusing on advancements in multi-parameter observations, high-resolution sampling, data-model synergy, and cross-validation techniques, Lagrangian experiments can unlock their full potential for improving our understanding of cloud processes in a changing climate. Furthermore, their applicability extends beyond clouds, making them valuable tools for investigating a broader range of atmospheric phenomena.

2.1 In-field Lagrangian experiments: enhancing their capability towards small spatial length ranges

In-field Lagrangian observations play a vital role in refining the parameterization of physical quantities and processes within global climate and weather prediction models. Dedicated closure experiments bridge the gap between observed and predicted datasets, facilitating model validation through simulations with different control parameters. These periodic Lagrangian measurements provide valuable data for verifying predicted atmospheric properties like temperature, humidity, pressure, wind speed, and direction. Compared to fixed-point observations, in-field measurements capture a broader range of spatial and temporal variability, leading to improved constraints on model parameters. Additionally, redundant measurements and analyses enhance cross-validation, bolstering the robustness of both measurement systems and simulation models (Brenguier and Wood [11]).

During the travel of a Lagrangian tracer (e.g., balloon), each measurement requires precise time and position tags. The position tag can be interpreted in various ways, such as displacement vector, separation vector, and so on. Here's an illustrative example:

- $T(t, x)$: Temperature at a given time t and position x. However, position itself is also a function of time, denoted as $x(t)$.
- $T(t, r(t))$: Temperature at time t and the trajectory point $r(t)$.

The autocorrelation of $r(t)$ provides insights into when the trajectory deviates from local flow dynamics and becomes increasingly deviated from initial conditions.

Dynamic, thermodynamic, and microphysical properties exhibit significant variations and co-variability at the kilometer scale (smaller than typical climate model grid boxes). This variability, which affects aerosol-cloud interactions and large-scale cloud properties, is crucial for accurate climate modeling. Therefore, designing a sampling

strategy that effectively captures these statistical connections between variables at subgrid scales is essential [11].

Lagrangian instruments, such as radiosondes, drifters, and buoys, have been used to explore vast regions of both the atmosphere and ocean. Free-drifting instruments enable extensive coverage at a lower cost compared to direct, point-to-point sampling [49]. However, creating a perfect Lagrangian drifter with zero mass is impossible. Therefore, these instruments are often referred to as "pseudo-Lagrangian drifters" [47].

The most crucial information obtained is the position or trajectory of the probe during its flight. Physical quantities are then associated with this trajectory. Spatio-temporal resolution is critical for obtaining high-quality Lagrangian statistics. Traditionally, Lagrangian tracers relied on satellite-based position tracking and data transmission systems like Argos. However, recent applications are increasingly adopting GNSS (Global Navigation Satellite System) sensors for more precise trajectory tracking [7, 40, 47, 49, 50].

Pioneering Lagrangian Observations: Balloon-borne Experiments

Balloon-borne experiments have played a significant historical role in furthering Lagrangian atmospheric observations [45, 46]. A notable example is the EOLE experiment conducted in the early 1970s [51]. This large-scale experiment released 483 balloons into the southern hemisphere stratosphere and tracked them using the EOLE satellite. The satellite could track up to 512 balloons with an accuracy of 1-2 km, providing valuable insights into regional synoptic wind patterns (see Fig. 6 in Morel and Bandeen [51]).

One key objective of EOLE was to study the dispersion of balloon pairs at the 200 hPa pressure level. This data allowed researchers to estimate the energy spectrum over spatial scales of 100 to 1000 km. Analysis of the EOLE dataset by Morel and Larceveque [52] yielded estimates of mean square relative velocity and diffusivity. The study concluded that two-dimensional eddy dispersion in this region exhibited homogeneity, isotropy, and stationarity up to 1000 km scales. Additionally, the observed spectrum agreed with a k^{-3} power law for two-dimensional turbulence. Lacorata et al. [53] revisited the EOLE dataset to investigate the energy spectrum behavior in the inertial subrange using a finite-scale Lyapunov exponent (FSLE) approach. Their findings suggested agreement with a $k^{-5/3}$ spectrum within the observed range (100-1000 km), while exhibiting exponential separation scaling at sub-100 km scales.

Another large-scale experiment, the Tropical Wind, Energy Conversion, and Reference Level Experiment (TWERLE), was conducted between 1975 and 1976 [54]. This experiment involved releasing 393 constant-level balloons tracked by satellites. The TWERLE dataset was analyzed by Er-El and Peskin [55] to study two-particle relative dispersion as a function of time within the 150 hPa level of the Southern Hemisphere. The root mean square (RMS) errors in position and velocity during these observations

were estimated to be 5 km and 1.5 m/s, respectively. These errors were primarily attributed to limitations in satellite tracking and instrument accuracy. However, analysis of relative balloon displacements allowed the researchers to evaluate the Richardson-Obukhov power law ($l^2\ t^3$) [41, 56]. The study identified two distinct dispersion regimes: exponential growth for shorter time scales and t^3 scaling for longer time scales.

The ASTEX campaign (Albrecht et al. [57]) employed Lagrangian experiments to investigate cloud properties, particularly stratocumulus and cumulus clouds within the marine boundary layer. Tetroon-shaped balloons were deployed to reach medium boundary layer heights (500-750 m). This experiment marked the **introduction of GNSS** sensors into the Lagrangian experimental context, significantly improving position accuracy to up to 50 m (compared to previous experiments). The text rightly points out that GNSS technology has advanced considerably since then, with current capabilities reaching meter-level accuracy. Additionally, the ASTEX campaign proposed a mechanism to control balloon altitude using a combination of constant-volume and zero-pressure balloons. However, as Businger et al. [45] noted, maintaining constant altitude is not always desirable, as it can limit the ability to capture vertical flow dynamics.

The aforementioned experiments, along with others, clearly demonstrate the importance of Lagrangian in-field measurements. In most cases, Lagrangian datasets were collected within the context of broader experimental campaigns, enabling valuable cross-validation opportunities. However, there is still a need to optimize Lagrangian tracking systems to achieve even higher position accuracy (better than ± 1 meter) and improved temporal resolution (less than or equal to 1 second). These advancements necessitate the design, development, and refinement of in-field Lagrangian observation tools and techniques to capture atmospheric dynamics at the finest spatial scales.

2.2 Laboratory techniques: particle tracking experiments

While in-field (in-situ) observations offer valuable insights into atmospheric phenomena, laboratory experiments provide a complementary approach with several advantages. Salazar and Collins [58] summarized various laboratory techniques used to study pair dispersion in isotropic turbulent flows. Toschi and Bodenschatz [59] further highlighted the statistical properties of Lagrangian particles within fully developed turbulent flows using a combination of experimental and numerical techniques.

Laboratory experiments can be conducted under controlled conditions, allowing for repeated trials under nearly identical circumstances. This facilitates detailed analysis by performing ensemble averaging and reduces variability in the data. Recent advancements in three-dimensional stereoscopic particle imaging and high-speed detection have enabled the simultaneous measurement of multiple particle trajectories within a turbulent flow field [60, 59, 58].

Experimental data can be susceptible to *measurement noise*, which requires careful filtering and correction techniques to avoid biasing the results. Another limitation of laboratory experiments is the difficulty in achieving high Reynolds numbers comparable to those found in natural atmospheric flows. *Lower Reynolds* numbers in laboratory settings can lead to discrepancies when scaling results to natural phenomena. Furthermore, selecting appropriate tracer particles is crucial. Ideally, the particles should be small enough to follow the flow faithfully without introducing significant diffusion or buoyancy effects. Additionally, they need to be identifiable within the measurement volume for extended periods.

At the moment, the most successful technique for Lagrangian turbulence studies involves the optical tracking of tracer particles. This method, known as particle-tracking velocimetry (PTV) or Lagrangian particle tracking, allows for measurement of particle positions, velocities, and accelerations[59]. PTV method introduced by Virant and Dracos [61] significantly enhanced laboratory data quality. They used multiple multiple cameras for stereoscopic reconstruction of three-dimensional particle trajectories. Another advanced silicon-detector method was presented by La Porta et al. [62], based on technology from high-energy physics. The new method offers data acquisition rates exceeding 70,000 measurements per second. This high rate is particularly valuable for studying flows with high Reynolds numbers, where the Kolmogorov frequency (characteristic frequency of small-scale eddies) is large. These advancements have enabled reliable measurements of fluid-particle acceleration in laboratory settings [44].

2.3 Numerical Simulations of Lagrangian particles: techniques and limitations

Numerical simulations offer a powerful and cost-effective alternative to in-situ observations and laboratory experiments for studying Lagrangian particles (droplets, aerosols, etc.) within a fluid flow. These simulations employ various techniques, such as Direct Numerical Simulations (DNS), Large Eddy Simulations (LES), and Kinematic Simulations (KS), to track the motion of these particles [63].

DNS provides the most accurate representation of the fluid motion by solving the Navier-Stokes equations at high resolutions to capture all turbulent scales. However, DNS simulations treat Lagrangian particles as point-particles with no influence on the flow itself. This approach is computationally expensive, limiting the achievable Reynolds numbers [44]. LES offers a balance between computational cost and accuracy. It directly simulates the large-scale turbulent motions, while modeling the smaller scales using subgrid-scale models. This allows for simulations with higher Reynolds numbers compared to DNS. KS utilizes a pre-computed flow field, often obtained from a DNS simulation, to study Lagrangian particle motion. This approach can account for two-way coupling between the particles and the flow, but the accuracy depends on the quality of the pre-computed flow field [44, 63].

Compared to studying just the Eulerian velocity field, Lagrangian simulations are computationally expensive [59]. This is because they involve tracking the motion of numerous particles throughout the flow. Extracting reliable statistical data requires tracking a large number of statistically independent particles. This becomes even more demanding for complex flows or higher-order statistical moments [44]. Managing and analyzing the resulting large datasets can be time-consuming. For particles with finite size or inertia, additional modeling is often needed in DNS and LES simulations. Although this poses no problems for passive tracers, some level of modeling is necessary for particles; consequently, a validation of the models against experiments is mandatory [34, 59, 58].

Computational limitations make it challenging to achieve long simulations, restricting the study of long-term particle behavior. Section A.2 will highlight the introduction of point-particles into the DNS domain, where communication overhead increased significantly computer cores due to turbulent clustering. This unpredictable clustering leads to uneven workload distribution across cores, hindering performance and limiting parallelization effectiveness. Moreover, a significant portion of research has focused on isotropic turbulence, which may not directly translate to real-world scenarios with anisotropic turbulence [64, 58, 65, 66].

Lagrangian numerical simulations necessitate specific conditions to ensure reliable statistical analysis, as emphasized by Yeung [44]. These conditions address the initial flow data, particle tracking accuracy, and statistical sampling:

The core requirement is a *well-resolved*, instantaneous (not time-averaged) *velocity field* derived from the Navier-Stokes equations. This detailed velocity data is crucial for accurately simulating particle motion within the flow.

Second, *the choice of interpolation scheme* significantly impacts the accuracy of particle tracking, especially when dealing with a large number of particles. The ideal scheme should be both efficient and minimize numerical noise generation. Cubic splines offer a good balance between these factors, providing high accuracy (fourth-order) and smooth transitions (twice-continuously differentiable) during particle movement across grid points. This smoothness helps to minimize numerical artifacts that can arise when differentiating Lagrangian time series (e.g., calculating acceleration from velocity data) [44, 59].

Finally, to obtain reliable ensemble averages, a *sufficient number of statistically independent particles* must be tracked. This is particularly important for capturing higher-order statistical moments, which are sensitive to rare but impactful events, and for studying inhomogeneous turbulence. Ensuring statistical independence often necessitates tracking a larger number of particles compared to simpler scenarios.

2.4 Lagrangian analysis of turbulent dispersion

Turbulent dispersion plays a crucial role in various natural phenomena and technological processes, influencing heat and mass transfer. Examples include water droplet growth and collisions in clouds, rain formation, plankton accumulation in the oceans, transport and sedimentation of sand particles in the environment, fuel mixing in combustion engines, etc. [67, 68]. Studying this phenomenon from a Lagrangian perspective, focusing on the motion of individual particles, provides valuable insights.

The concept of relative turbulent dispersion was introduced by Lewis Fry Richardson in 1926 [41]. He sought to explain the observed increase in turbulent diffusivity within the atmosphere, where the rate of particle separation grows significantly as we move from small (molecular) scales to larger (atmospheric circulation) scales (Sawford [64] and Salazar and Collins [58]). Richardson's approach, though initially considered unconventional, involved studying the separation statistics of a cluster of "marked molecules" within a turbulent flow. He defined the "*distance-neighbor graph*," which is essentially the probability density function (pdf) for the separation distance between a pair of particles within the cluster. This concept is now known as the *distance-neighbor function* [64].

Several techniques have been developed to study turbulent dispersion focusing on the different parameters: (i) Analyzing **mean separation distance** between pairs of particles; (ii) Multi-particle dispersion analysis using four-particle tetrahedron [69, 70, 70]; (iii) Original distance-neighbor graph analysis [41, 67]; (iv) Analyzing the convex hull, the smallest convex shape enclosing all the particles [71, 72].

While much of the existing research focuses on statistically stationary, homogeneous, and isotropic turbulence [58], this present work explores the more realistic scenario of non-stationary, time-decaying, and non-homogeneous turbulence. Our previous work under these conditions investigated particle growth rate, collision-coalescence, intermittency acceleration, and the interplay between micropyhysical timescales and supersaturation balance [34, 35].

Atmospheric diffusion analysis via distance-neighbor graph (DNG)

State-of-the-art Lagrangian dispersion studies suggest that under stationary and homogeneous conditions, the squared separation distance between fluid particles grows proportionally to time cubed ($l^2 \sim t^3$) [58, 67, 64]. Richardson's work on diffusion, based on the distance-neighbor graph function, concluded that diffusion increases with separation distance ($F(l) \sim l^{4/3}$) [41]. Later, Batchelor [73] generalized this function to three dimensions. Obukhov (1941) independently derived a similar relationship linking separation distance directly with time, leading to the combined Richardson-Obukhov t^3 theory [56]. Here we briefly highlight atmospheric dispersion (diffusion) analysis via distance neighbor graphs.

The DNG, denoted by Q, provides a statistical representation of particle neighbor

distribution within a turbulent flow. Each element $Q_{n,n+1}$ represents the average number of neighboring droplets per unit length within the distance interval between n*h and (n+1)*h. Here, h is a user-defined bin size. The calculation of Q is based on the following equation:

$$Q_{n,n+1} = \frac{1}{N}(D^1_{n,n+1} + D^2_{n,n+1} + D^3_{n,n+1} + ... + D^N_{n,n+1}), \tag{2.2}$$

where D^k represents a number of neighbors in the given distance interval $(n, n+1)$ for the k-th water droplet.

DNG is computed from the time series of particle positions. Figure 2.2 (not shown here) illustrates water droplets extracted from a anisotropic turbulent mixing region within a DNS simulation (details provided in Chapter 3, Figure 3.2). Around 430 water droplets are scattered across the xz plane (z-axis representing buoyancy and the direction affected by gravity). The initial panel (t/τ_0 = 0.454) shows the droplets concentrated within a small neighborhood (2cm x 2cm x 2cm cubic domain) located at (24.4, 24.4, 24.4) cm relative to the simulation domain's origin (bottom edge of the parallelepiped in Figure 3.2).

Figure 2.3 (not shown here) depicts DNG plots for these droplets at different time instances. The histogram format emphasizes the DNG's symmetry property (as highlighted by Richardson [41]).

Richardson (1926) aimed to develop a diffusion equation for the concentration field relative to a moving cloud's center of mass [41]. While his primary focus was on this practical problem, the DNG served as a "mathematical specification" [64].

A key property of the DNG is that the total area under the Q curve remains constant over time as diffusion progresses. This suggests that Q satisfies a specific type of differential equation:

$$\frac{\partial Q}{\partial t} = \frac{\partial}{\partial l} \left\{ \begin{array}{l} \text{some function of } l \text{ which attains a limit as} \\ l \to \infty \text{ equal to that attained as } l \to -\infty \end{array} \right\} \tag{2.3}$$

This equation ensures that the sum of changes in Q across all length intervals distances remains zero (considering total number of tracked particles remains the same):

$$\int_{-\infty}^{\infty} \frac{\partial Q}{\partial t}\, dl = 0, \tag{2.4}$$

Or in discrete form, we can write it as following, which is more suitable for working with numerical and experimental dataset:

$$\sum_{k=l_{min}}^{l_{max}} \frac{\partial Q_k}{\partial t} = 0. \tag{2.5}$$

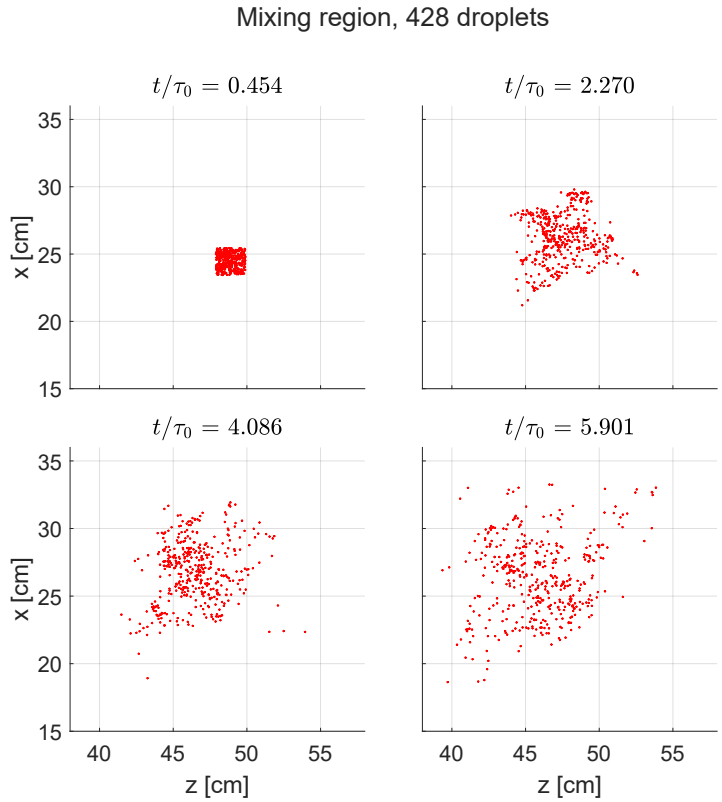

Figure 2.2: Droplet positions in simulation domain represented in xz plane. Figures are generated for 4 different time instances. **428** droplets are selected within the same cell (neighborhood) initially and they are located in 2cm x 2cm x 2cm domain at initial position of (24.4,24.4,48.9) cm. Reference system is parallelliped described in Figure 3.2 with origin at the bottom edge.

The diffusion rate is known to increase with the separation distance (l) between neighboring particles. This can be expressed by Equation 2.6, where $F(l)$ represents the diffusion function (also referred to as K or $K(l)$ in literature):

$$\frac{\partial Q}{\partial t} = \frac{\partial}{\partial l}\left(F(l)\frac{\partial Q}{\partial l}\right), \tag{2.6}$$

According to Richardson [41], $F(l)$ can be approximated by a power-law scaling ($F(l) \sim l^{4/3}$).

This power-law relationship aligns with Obukhov's equation (Equation 2.7), which relates the squared separation distance (l^2) to time cubed (t^3) through parameters like initial separation distance (l_0^2) and the rate of kinetic energy dissipation (ε). This combined theory is known as the Richardson-Obukhov (R-O) t^3-theory[56, 67]:

$$l^2 = {l_0}^2 + g_l \varepsilon t^3, \tag{2.7}$$

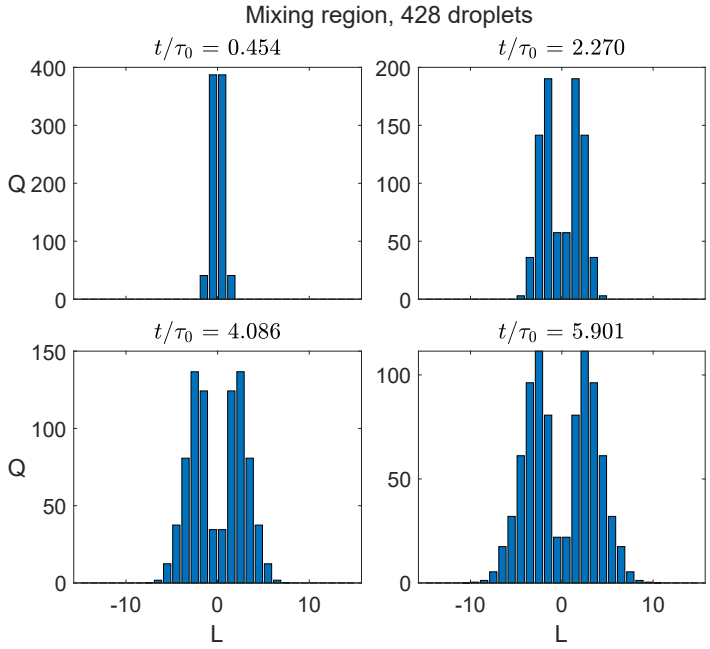

Figure 2.3: Mean number of neighbors, Q with the respect to distance L between droplets (the distance is computed in **3D** space for droplets in Figure 2.2). Computation has been done from h to 15h, where h = 2 cm. Each bin represents mean number of neighbors within each length interval.

where g_l is referred as "R-O constant" [67, 58].

While the Richardson-Obukhov t^3 theory applies to stationary and homogeneous conditions, our research focuses on more realistic scenarios involving time-decaying (non-stationary) and non-homogeneous turbulence [34, 35]. This necessitates the use of time-dependent diffusion functions.

We can incorporate this temporal dependence into the diffusion function, $F(l,t)$, as follows:

- *cloud* - homogeneous time-decaying turbulent region: $F(l,t) \sim \varepsilon(t)^{1/3}\ l^{4/3}$ (matches the Richardson-Obukhov scaling) or more generally as $F(l,t) \sim \varepsilon(t)^{\beta}\ l^{\alpha}$
- *mixing* - anisotropic time-decaying turbulent region: $F(l,t) \sim \varepsilon(t)^{\beta}\ S(t)\ l^{\alpha}$

Here, $\varepsilon(t)$ represents the time-dependent kinetic energy dissipation rate. The term $S(t)$ in the mixing region function captures the effects of anisotropy, potentially linked to small-scale measures like longitudinal velocity derivative fluctuations or supersaturation and their higher-order moments (skewness and kurtosis). This generalized form allows for a more flexible characterization of diffusion behavior under various non-stationary and non-homogeneous turbulence conditions.

Chapter 3

Numerical investigations of top cloud boundary: mixing, droplet dynamics and microphysics

Warm atmospheric clouds exhibit a complex interplay between small-scale and large-scale phenomena. While some key processes are well understood, others remain debated in the cloud physics and turbulence communities. Lukewarm clouds, typically found at altitudes of 1-2 km and lasting for hours or even days, are in a constant state of evolution. These clouds typically have dimensions of hundreds of meters and a characteristic timescale of approximately 100 seconds [9, 74]. Droplets, which nucleate through water vapor condensation, generally have diameters under 30 microns and primarily follow air currents with minimal interaction. However, fully resolving all scales involved in cloud dynamics with numerical simulations remains a significant computational challenge [75].

Our recent numerical studies focus on the impact of turbulent mixing at cloud boundaries and its influence on droplet growth, collision, and precipitation [34, 35]. The cloud boundary, where cloud - saturated water vapor interact with drier "clear air", presents a particularly intricate scenario due to highly intermittent and anisotropic turbulent conditions. We aim to simulate more realistic, dynamic regimes using DNS. The importance of mixing is especially evident at growing cloud tops, where the distinction between homogeneous and inhomogeneous mixing becomes crucial, as microphysical timescales can differ significantly from turbulent timescales [76, 77, 78]. DNS provides insights into this complexity by resolving turbulence down to the finest scales.

The shear-free mixing layer, considered an effective numerical model for cloud edges, involves the interaction of two turbulent regions with different kinetic energies. Notably, in our recent studies, we observed significant acceleration in droplet dynamics within a horizontal interfacial mixing layer under unstable stratification. This acceleration was attributed to the intermittency of small-scale turbulence driven by the flow's anisotropy [34].

Previous studies have investigated this mixing layer through laboratory experiments [79, 80] and DNS; however, most simulations of lukewarm clouds have traditionally assumed static and homogeneous conditions [81, 82, 83, 84]. These investigations have explored various aspects, including the impact of energy cascades on droplet dispersion, two-way interphase coupling in droplet-laden shear layers, the influence of gravity on collision and coalescence, and the effects of both large and small-scale eddies on condensation and evaporation [81, 82, 83, 84, 34, 35].

Philofluid Research Group has a longstanding tradition of conducting numerical investigations into turbulent flows. This work spans from the earliest versions of the group's code, which simulated Homogeneous Isotropic Turbulent (HIT) on a cubic domain (Iovieno, Cavazzoni, and Tordella [43]), to the latest iterations that incorporate water droplets (Golshan et al. [34], Fossà et al. [35], and Gallana et al. [36]). For further details on different versions of the DNS software, see Section A.2.1 in the Appendixs. As part of my PhD research and due to my strong interest in High Performance Computing (HPC) and programming, I became actively involved in numerical studies of warm clouds. I joined the Philofluid code development at version 1.4p, which solves the Navier-Stokes equations for velocity fluctuations along with scalars such as water vapor and temperature. My contributions include testing, bug fixing, and, most importantly, post-processing analysis of simulation datasets.

Most of the obtained results were already published in recent publications with our colleagues in Philofluid research group: (i) Golshan et al. [34] and Gallana et al. [36] describe the adopted physical model and initial results droplet population dynamics, collision kernels; (ii) Fossà et al. [35] on the supersaturation balance and microphysical response of droplets. This chapter revisits and reorganizes these findings, with a specific focus on Lagrangian droplet dynamics, which is where my particular interest within the group lies. The following aspects are explored in greater detail:

- The evolution of droplet distribution due to condensation, evaporation, and collisions.
- The acceleration of intermittency within the turbulent mixing region and its influence on droplet dynamics.
- The evolution of the collision kernel.
- The microphysical timescales of water droplets.

Furtermore, the current focus of our post-processing analysis concerns *Lagrangian dispersion and correlations.*

3.1 Physical model

Our model simulates cloud boundaries through shear-less mixing between a small cloud-top region and an adjacent clear air region with equivalent volume but differing turbulent intensities. Figure 3.1 illustrates the complex dynamics of the cloud-clear-air interaction, where clouds can host as high as 10 to 20 times more TKE than the surrounding clear air. Initial conditions replicate local mild unstable stratification in density and temperature. Our simulations employ an Eulerian representation for turbulent velocity, temperature, and vapor fields, coupled with a Lagrangian description for two droplet populations. The droplet model incorporates evaporation, condensation, collision, and coalescence. We focus on the effects of transient anisotropic turbulence emulates the top cloud boundary (red rectangle, see Figure 3.1) on two initially randomly positioned droplet populations: monodisperse and polydisperse. Unlike the phantom collision model used by Franklin [85], we utilize a geometrical collision model combined with condensational growth.

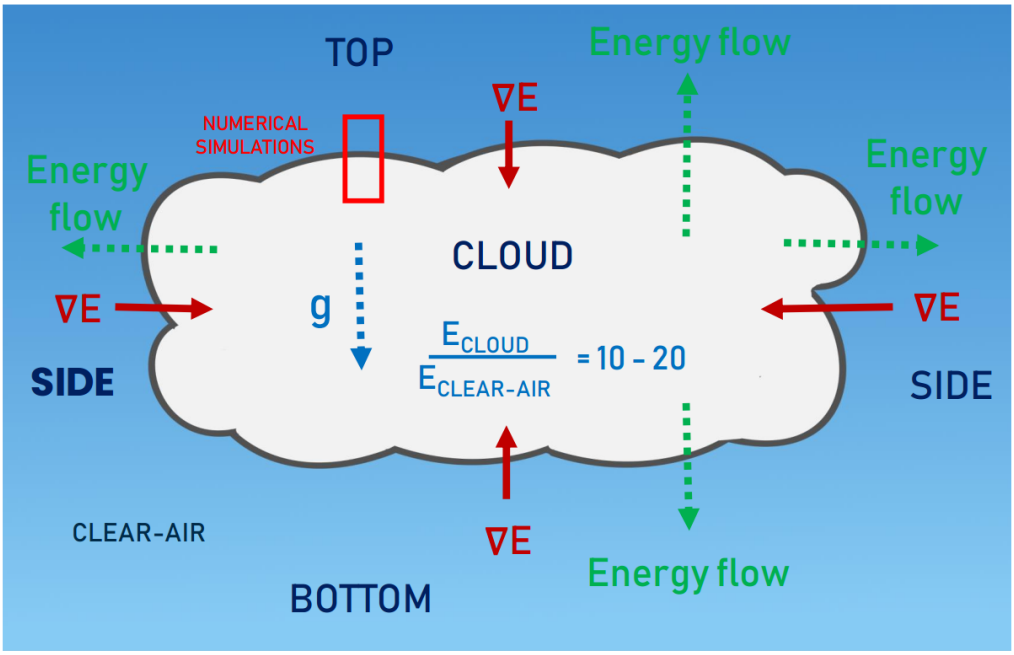

Figure 3.1: Cloud interface model. Cloud region is highly intermittent and embodies high turbulent kinetic energy with respect to the surrounding clear-air region. Red rectangle on the top part highlights the part of cloud chosen for numerical studies.

Figure 3.2 depicts this dynamic boundary modeled as a shear-less turbulent mixing layer, an idealized interface separating two distinct regions [34, 35, 36]. The bottom half of the domain represents a warmer, droplet-laden cloud region rich in water vapor and kinetic energy, while the top half represents a less energetic clear air region. The computational domain is a parallelepiped composed of two adjacent cubes. This flow

model is advantageous for several reasons:

- **Naturally unsteady**: Like real clouds, the mixing layer is constantly changing and evolving.
- **Realistic Scale Gradients**: It allows for a gradient in the integral scale (size of the largest turbulent eddies), similar to what's observed in clouds, aligning with the changes in kinetic energy and enstrophy.
- **Captures Anisotropy**: The mixing layer inherently captures the small-scale turbulence and directional dependence present at cloud boundaries, as indicated by different values on the diagonals of velocity fluctuation derivative moment tensors [84].
- **Simplicity and relevance**: The decaying shear-less mixing layer is a fundamental model that lacks the complexity of turbulence production from mean shear, a common feature in atmospheric flows that often leads to cloud dissolution. This simplification allows us to focus on the key dynamics at cloud boundaries.

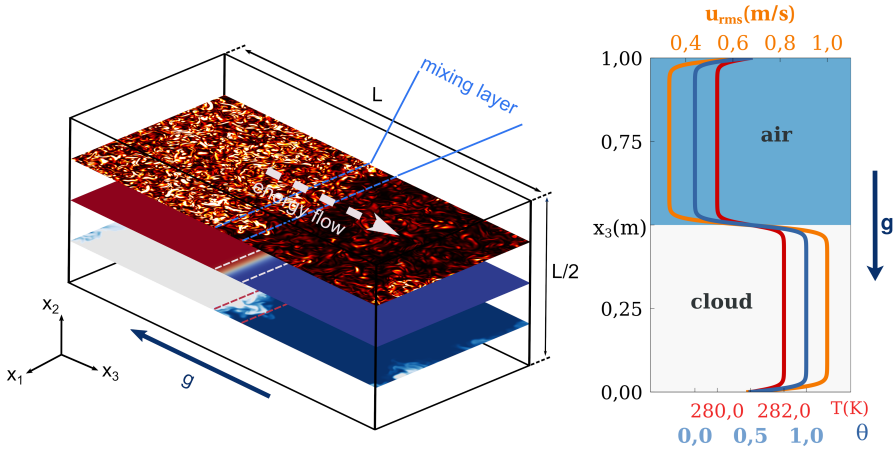

Figure 3.2: Overview of the physical system, cloud - clear air transient interaction and profiles of averaged physical quantities. Schematics of the simulation domain (left panel) and of the initial profiles of the *rms* velocity (orange), temperature (red) and vapor content (blue) (right panel). The turbulent kinetic energy flow is from bottom to top along x_3 direction, $E_1/E_2 \approx 7$.

Our simulations closely mirror conditions found in cloud border regions, as detailed in Tables A.1 and A.2 of Appendix A. The high-frequency wave numbers of the inertial range and the dissipative range observed in *field* atmospheric measurements are effectively captured by our numerical setup, as demonstrated in Figure 3.3. We use the

incompressible Navier-Stokes equations with the Boussinesq approximation for temperature and vapor density to efficiently model buoyancy effects within the cloud. Additionally, scalar transport equations are included to accurately track water vapor and thermal energy balance. Details of the governing equations are provided in Section A.1, Appendix.

Individual water droplets are modeled using a Lagrangian approach that accounts for both Stokes drag and gravitational settling. This model interacts with the vapor and temperature fields through shared evaporation-condensation terms. While the position, velocity, and radius of each droplet are tracked, the interaction remains one-way, meaning the droplets do not influence the overall fluid flow.

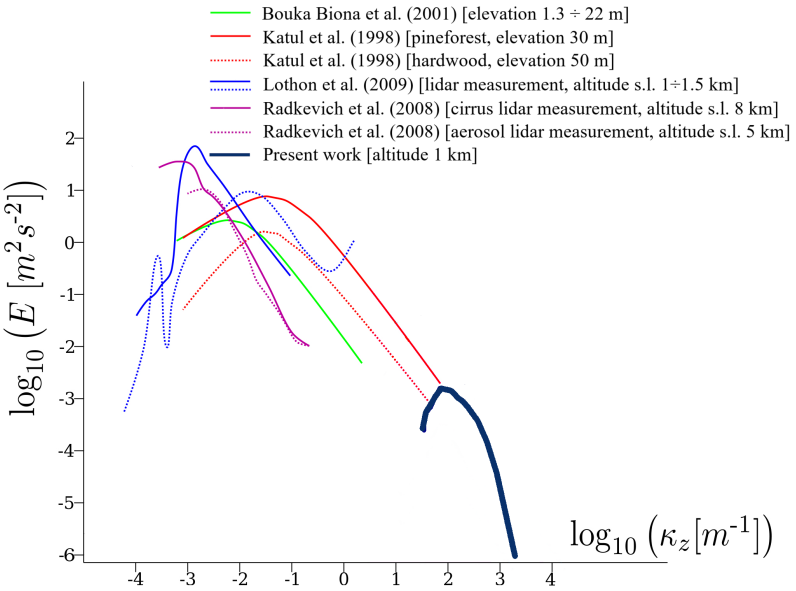

Figure 3.3: TKE Spectrum. The dark blue spectrum on the right represents the small-scale inertial and dissipative ranges studied in this work, contextualized alongside in situ atmospheric measurements (colored spectra showing energy injection and low wave number inertial scales). The goal of these simulations is to capture the small-scale range of the spectrum that in situ measurements have been unable to detect.

3.1.1 Modeling the motion of Lagrangian droplets

In the simulation, cloud droplets are treated as point-like particles, always smaller than the grid size. The liquid water content is then represented by an ensemble of N droplets

within each grid cell. Each droplet follows a **Lagrangian path**, governed by the following equations:

$$\frac{dX_i}{dt} = v_{p_i} \tag{3.1}$$

$$\frac{dv_{p_i}}{dt} = \frac{u_i(X_i,t) - v_{p_i}}{\tau_i} + \left(1 - \frac{\rho_a}{\rho_w}\right) g \tag{3.2}$$

Here, $u(X_i,t)$ and v_{p_i} denote the velocity of the fluid and the droplet, respectively, in the i-th direction. ρ_w, ρ_a, are the densities of water and air, respectively. The droplet acceleration considers Stokes' drag and gravity, with negligible effects from Faxen and Basset history forces [86, 87, 9, 87, 34, 35]. The droplet response time τ_d for the k-th droplet with radius R_k is given by [88]:

$$\tau_i = \frac{2}{9}\frac{\rho_w}{\rho_a}\frac{\mathrm{R_i}^2}{\nu} \tag{3.3}$$

where ν is the air kinematic viscosity.If the droplet radius falls below a critical value where the response time is smaller than the numerical integration time step, the droplet is removed. However, this situation is negligible for the polydisperse population, affecting less than 1 in 1000 droplets (see Table A.1, LWC = $0.79 g/m^3$).

In the simulation, the flow field at each droplet's location is crucial for the Lagrangian equations. However, the direct effect of droplet drag on the flow is simplified and neglected in the buoyancy term of the momentum equation. The droplets influence the flow indirectly through their impact on the temperature field and vapor mixing ratio via condensation and evaporation rates.

This simplification is justified by two factors: (i) the droplets have very low Stokes' numbers (Reynolds numbers much less than 1), signifying minimal interaction with the flow; (ii)the liquid water mass loading is low relative to the air volume. In fact, for radii in the range $[1-30]\mu$m, the initial transient values of Stokes' numbers are in $[0.02-0.7]$, while the end of transient values are in $[0.002-0.066]$, which means Reynolds numbers of the drops much lower than 1. This approach balances computational efficiency with reasonable accuracy for the simulation goals [89, 90].

Droplet growth in the simulation is governed by condensation, evaporation, and collision-coalescence processes. The model tracks each droplet's interaction with the surrounding air, coupling these growth processes with droplet motion to accurately simulate their behavior.

Droplet growth by condensation-evaporation

The growth of cloud droplets through condensation and evaporation processes is modeled based on Köhler theory, which describes the spontaneous growth of cloud condensation nuclei (CCN) into cloud droplets in response to ambient supersaturation [91, 92, 93, 94]. This model has been simplified for particles larger than CCN [95, 96, 97, 87, 98].

In addition to water droplets, the atmosphere contains various particles, including solid, soft, and liquid ones, some of which are hydrophilic and water-soluble. When these water-soluble particles, known as soluble CCN, mix with cloud droplets, they can affect the rate of droplet evaporation, a phenomenon known as the **Raoult effect**. Additionally, the curvature of droplets influences evaporation; smaller droplets with higher curvature are more prone to losing water vapor, which is described by the **Kelvin effect**.

Both the Kelvin and Raoult effects are incorporated into the model for droplet growth. The growth rate of the k-th spherical droplet is given by Hudson and Da [99], Ghan et al. [100], and Saito and Gotoh [101]:

$$\frac{dR_k}{dt} = \frac{K_s}{R_k}\left(S - \frac{A}{R_k} + \frac{Br_d^3}{R_k^3}\right) \tag{3.4}$$

Here, K_s is the diffusion coefficient related to the condensation rate field C_d (see equation A.8 for details), S represents supersaturation, A is the Kelvin coefficient, B is the hygroscopicity parameter, R_k is the radius of the k-th droplet, and r_d is the accumulation radius. The second and the third terms on the right-hand side represent Kelvin and Raoult terms, respectively.

Since the coefficients A, B, and r_d are hypothesized to be constant, the droplet growth rate primarily depends on the local value of S and the droplet radius R. Figure 3.4 shows the growth (shrinkage) rate for three constant values of supersaturation S. The orange curve, representing a saturated environment, illustrates the competing effects of the Kelvin and Raoult terms. In these conditions, the Kelvin effect becomes significant for $R < 1\,\mu\text{m}$, but is soon outweighed by the Raoult effect as the droplet (aerosol) radius drops below $\cong 23\,\text{nm}$, where the Raoult term dominates.

The diffusion coefficient K_s is slightly affected by local equilibrium thermodynamics [102, 93, 100]. It includes self-limiting effects due to latent heat release but is generally treated as a constant under typical warm cloud conditions. This constant varies weakly with temperature (ranges from $5.07 \cdot 10^{-11}\ \text{m}^2\ \text{s}^{-1}$ at $T = 270\,\text{K}$ to $1.17 \cdot 10^{-10}\ \text{m}^2\ \text{s}^{-1}$ at $T = 293\,\text{K}$[96, 103]). For our simulations, with an initial volume-averaged temperature of 281 K, we use the value $8.6 \cdot 10^{-11}\ \text{m}^2\ \text{s}^{-1}$.

Droplet-size distributions

This research explores two types of cloud droplet distributions in simulations: **monodisperse** (all droplets same size) and **polydisperse** (droplets of various sizes). In both cases, the droplets are initially randomly distributed within the cloud region. The total number of droplets is determined by typical liquid water content found in warm clouds and the chosen initial droplet size. For instance, for the monodisperse population, the total number of droplets, $N_{tot-mono} = 8 \cdot 10^6$, is derived from the typical liquid water

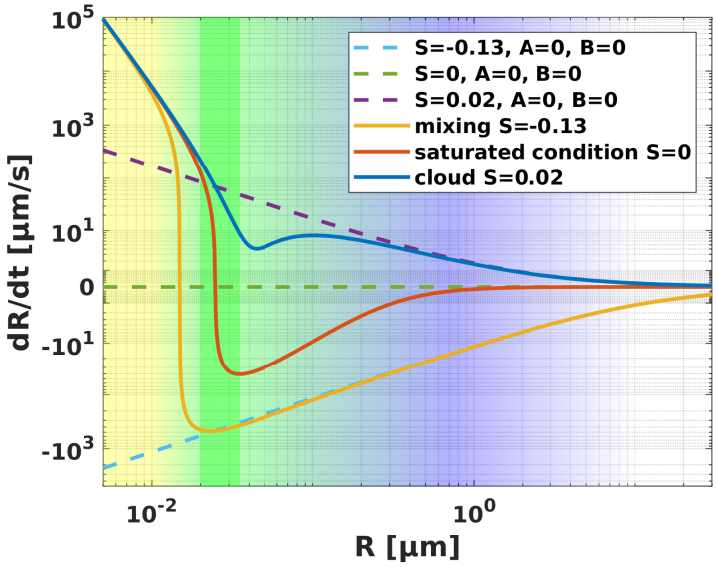

Figure 3.4: The graph shows the growth rate (Equation 3.4) of a water droplet (with radius R) under different flow conditions. The three lines represent different levels of water vapor in the air: (i) supersaturated ($S = 0.02$, as in the cloud region of the present work), saturated ($S = 0$) and subsaturated ($S = -0.3$) conditions. The dashed lines show how much growth is due to water vapor alone, ignoring other factors. The green bar highlights the size range where two additional factors, curvature (Kelvin term) and dissolved particles (Raoult term), become important for growth. For larger droplets (above $1\mu m$ in this case), these factors have little impact, but they become more significant for smaller ones.

content $LWC_0 \sim 0.8 g/m^3$ and the selected initial radius, $R_{0,mono} = 15\mu$m:

$$N_{tot-mono} = LWC_0 \frac{4}{3}\pi\rho_w R_{0,mono}^3. \tag{3.5}$$

Two contrasting initial populations were selected for analysis, as depicted in Figure 3.5. This choice was made due to the lack of a universally accepted form for the size distribution of warm natural clouds in existing literature. Several factors contribute to this difficulty. Firstly, diverse mechanisms for droplet nucleation, growth, and removal occur throughout a cloud's lifecycle and across different regions within it, as highlighted in Chandrakar et al. [104]. Additionally, our aim to model the dynamic evolution of a cloud-clear air boundary pushes us beyond simplified assumptions of static and spatially uniform conditions. These limitations inherent to theoretical approaches have prompted researchers to explore more advanced methods, such as the maximum entropy principle [105, 106] and stochastic condensation-evaporation models based on Langevin equations [107, 108, 109, 110].

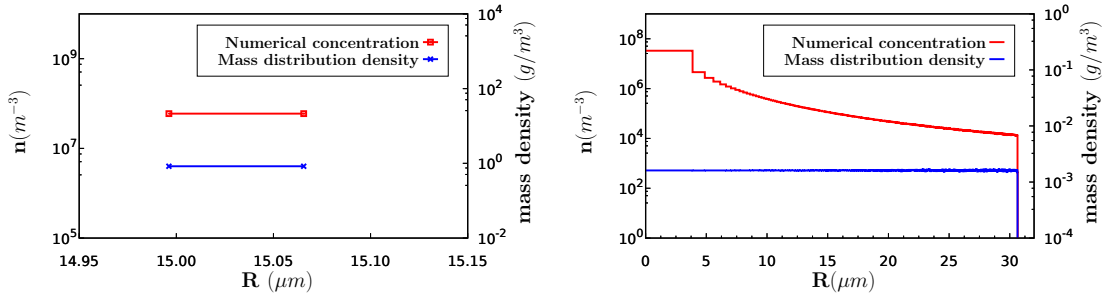

Figure 3.5: Monodisperse (left panel, $8 \cdot 10^6$ particles) and Polydisperse (right6rt panel, 10^7 particles) drop size distributions; for both distributions the initial value of total liquid content is $LWC_0 = 0.8\text{g/cm}^3$

Collision-coalescence events

Collisions between spherical droplets l and k occur when the distance between their centers is less than the sum of their radii:

$$\left[\sum_{i=1}^{3}\left(X_{li} - X_{ki}\right)^2\right]^{1/2} \leq R_l + R_k$$

The resulting droplet inherits the combined mass and momentum of the two original droplets. The present work focuses on the effects associated with anisotropy and intermittency of the interfacial layer separating the cloud region from the clear-air ambient. A common assumption is that collisions happen very efficiently, almost always leading to a combined droplet [111, 112] (see for instance Wang, Wexler, and Zhou [112], Tables 2,3 and 4). This simplification excludes factors that might reduce collision efficiency, allowing for a more focused initial analysis.

The system's non-equilibrium state quickly drives smaller turbulence scales towards anisotropy, inducing significant pressure transport compared to turbulent velocity transport, as observed in Tordella, Iovieno, and Bailey [113] and Tordella and Iovieno [84, 114]. These factors, along with the cloud-clear air interaction, uniquely affect droplet collision rates, an area previously unexplored. The enhanced airflow penetration into the low-turbulence region reveals new insights into droplet collisions and their behavior across the interface layer and into the clear air.

Additionally, droplet size distribution significantly influences the frequency of collisions. In monodisperse populations (all droplets of the same size), collisions are infrequent, as turbulence is required to push droplets at different velocities to induce collisions. In contrast, polydisperse clouds (with droplets of various sizes) experience more frequent collisions due to differences in inertia and gravity [115, 111]. The evolution of the collision kernel for two different initial populations in the turbulent simulation domain is discussed in Section 3.2.2.

3.2 Results: simulation data analysis and outcomes

This section examines the mixing of the background flow and scalars, along with droplet dynamics, over time (up to 10 eddy turnover times) and along the non-homogeneous direction, x_3. To focus on cloud-clear air interface dynamics, droplet and flow statistics are extracted from horizontal x_1-x_2 planes at a fixed x3, and plotted versus normalized height $(x_3 - x_c)/L_3$, where x_c is the interface position and $L_3 = 2L1{,}2$ (twice the cube edge length, see Table A.2). Mean, standard deviation, and higher-order moments are computed for cells at each x_3 plane. Details of the numerical experiment setup, DNS computational aspects, and data generation can be found in Appendix Section A.2. They are not repeated here for clarity.

We compare droplet growth and interaction processes (condensation-evaporation and collision-coalescence) between monodisperse and polydisperse populations. The average kinetic energy (E) decreases quickly during the transient (highlighted in Figure A.1), but the normalized energy highlights unstable stratification, amplifying convection near the interface and enhancing vertical mixing of droplets, vapor, and internal energy towards the subsaturated region. Figure 3.6 shows the domain's inner slice, highlighting the temporal evolution of the mixing layer through water vapor concentration (q_v), velocity enstrophy decay ($\mathscr{E}(\boldsymbol{\omega}) \equiv \int_\Omega |\boldsymbol{\omega}|^2 \, dx$) and the spatial distribution of droplets.

Figure 3.7 visualizes scalar mixing via temperature fluctuations (T′T′) across the xz plane at three times, revealing a central fully mixed region and partially mixed top and bottom regions, which evolve as turbulence subsides. Figure 3.8 further illustrates the high intermittency of supersaturation near the cloud-clear air interface, where skewness and kurtosis values are pronounced on both sides of the mixing layer, reflecting varying vapor fluxes at the cloudy region and subsaturated border [34, 35, 36].

3.2.1 Lagrangian droplet dynamics

Figure 3.9 presents the evolution of monodisperse and polydisperse droplet distributions across the mixing layer, depicting both droplet radius and concentration along x_3. Initially, droplets occupy the lower domain region, randomly distributed within the cloud. Due to cloud supersaturation (Figure 3.8(a)), uniform condensation growth occurs within the cloud. As mixing progresses, some droplets are advected into the upper, subsaturated clear-air region. Here, smaller droplets rapidly evaporate and are removed by the algorithm. Decreasing dissipation rate (ε) during the transient increases the likelihood of heavier droplet settling, as the small-scale Froude number (Fr_η) scales sublinearly with ε ($\mathrm{Fr}_\eta \sim \varepsilon^{3/4}$) [88].

In the monodisperse case (Figure 3.9(a)), the mean radius plot shows a nearly flat plateau within the cloud core. This plateau shrinks as the shearless mixing progresses (blue-shaded area). Concentration plots (Figure 3.9(b)) follow the same trend.

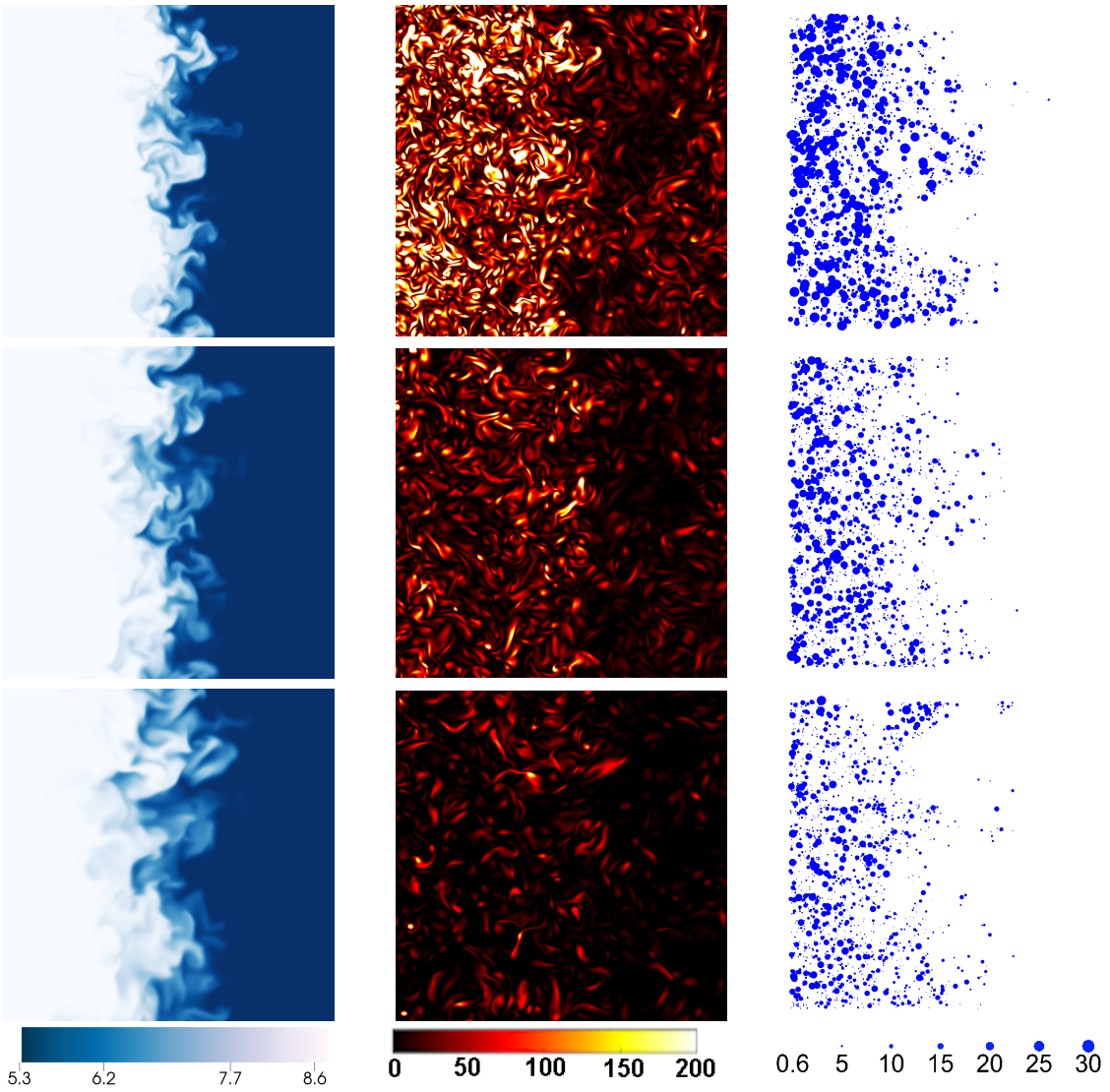

Figure 3.6: Inside a turbulent mixing layer between cloud and clear-air: water vapor (kg/m^3), enstrophy (s^{-2}) and droplets (diameter in arbitrary units, polydisperse). Top to bottom: 3, 6, and 9 eddy turnover times.

For the polydisperse case (Figures 3.9(c) and (d)), the constant-radius region is narrower and peaks near the top of the mixing layer due to increased collision frequency. The large size disparity ($1.25 \cdot 10^5$ volume ratio between largest and smallest droplets) further amplifies collisions, leading to approximately $5 \cdot 10^4$ collisions out of 10^7 droplets within 8 physical time scales. See Figures 3.17 and 3.18 (Section 3.2.2) for collision kernel details within the cloud and mixing layer regions.

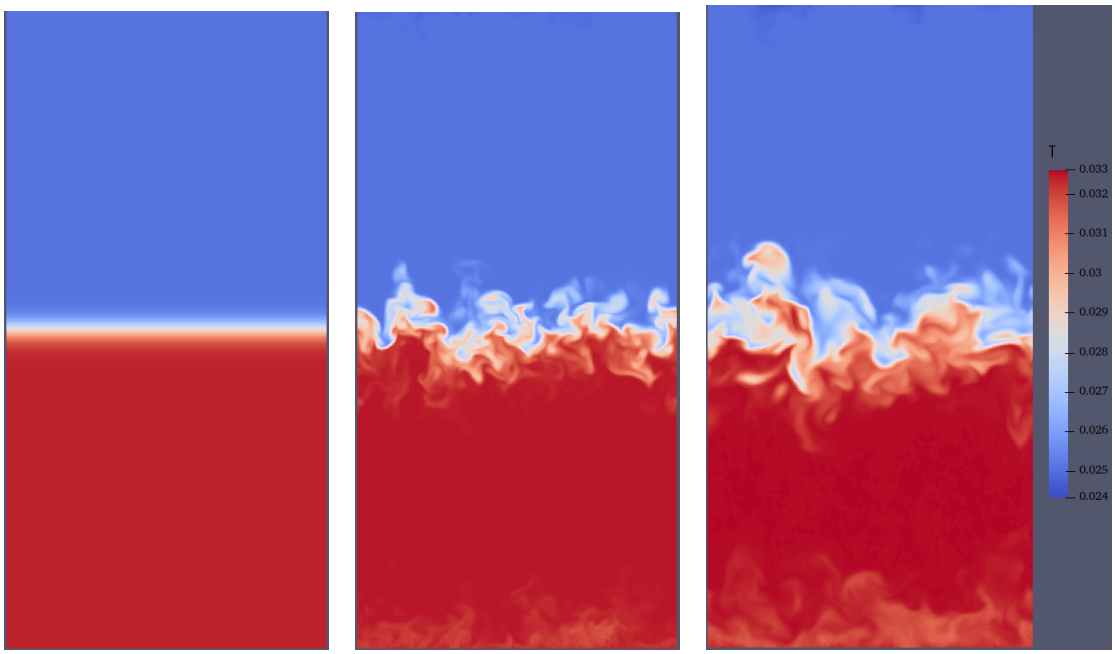

(a) $t/\tau_0 = 0$ (b) $t/\tau_0 = 5$ (c) $t/\tau_0 = 10$

Figure 3.7: The mixing of a scalar field (temperature fluctuations, T') by showing its distribution over the x_1 - x_3 (xz) plane. The bottom portion represents the cloud region, while the top portion represents the clear-air region. Three time instances are highlighted: (a) initial condition, (b) middle of the transient decay phase and (c) near the end of the simulation. Color legend is provided qualitatively, in non-dimensional units.

A. Temporal variations of droplet distributions: cloud and mixing regions

Figures 3.10 and 3.11 illustrate the evolution of numerical and mass concentrations for both mono-disperse and poly-disperse droplet populations at different time instances during the transient. Complementary to Figure 3.9, these figures depict size-resolved distributions (per radius class) instead of planar averages across the non-homogeneous (x_3) direction. Notably, both figures reveal a distinct enhancement in the distribution shape within the mixing layer, suggesting a more intense process compared to the cloud region.

Monodisperse distribution. Figure 3.10 shows a progressive expansion of the distribution towards smaller sizes compared to the initial 15 μm radius. At around 8.54 τ within the interfacial mixing zone, the numerical concentration of 13μm drops is 100 times higher than inside the cloud, with a minimum radius slightly below 11 μm compared to the cloud's minimum of nearly 13 μm. The width of the distribution part related to coalesced droplets is significantly broader within the mixing layer. Notably,

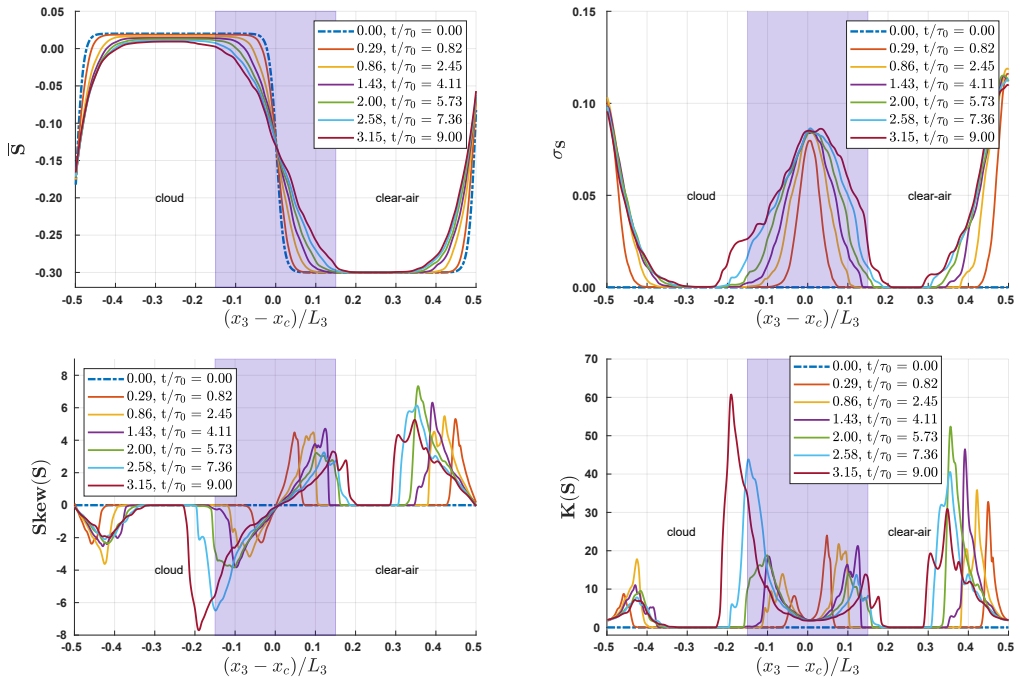

Figure 3.8: Monodisperse droplet population. Planar averages and statistical moments of supersaturation across the cloudy - under-saturated ambient air interface layer. (a) Supersaturation (or saturation deficit) across the layer. (b) Standard deviation. (c) Skewness. (d) Kurtosis. The initial distributions are plotted with black dash-dotted lines. The approximate extension of the interface mixing layer is indicated as the blue-shaded area between the cloudy and clear air regions.

collisions occur between droplets with radii deviating from the initial 15 µm, unlike the cloud where collisions primarily involve near-identical 15 µm droplets. This indicates much stronger evaporation within the anisotropic mixing region, a fact further supported by Figure 3.12 (c, d), which depicts the concurrent processes of condensation and evaporation. We will delve deeper into these aspects later.

Polydisperse distribution. Figure 3.11 initially presents a polydisperse distribution with uniform mass across size classes from 0.6 to 30 µm within the cloud region. Similar to the monodisperse case, the dynamics within the mixing region are more intense compared to the cloud. The concentration at larger radii (around 30 µm) exhibits a three-order-of-magnitude decrease within the interface, as shown in Figure 3.11(b). Both panels (a) and (b) demonstrate a distribution expansion up to radii of around 38 µm, achievable by the coalescence of two 30 µm droplets. However, in the cloud region, coalescence growth is accompanied by significant condensation, which is marginally present in the interface region beyond 30 µm radii.

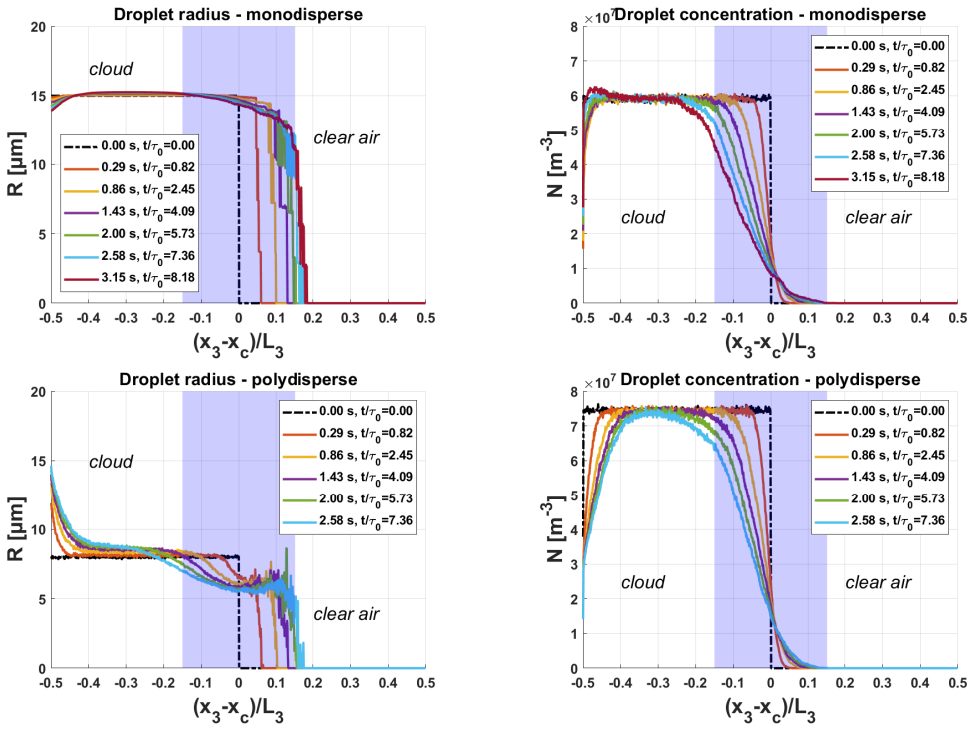

Figure 3.9: (a, c) Average mean droplet radius and (b, d) concentration (N) across horizontal planes. Shearless mixing occurs within the shaded area. The dash-dotted line represents initial conditions.

B. Effects of condensation and evaporation on the distribution shape

Figures 3.12, 3.13 shed light on the contrasting roles of condensation and evaporation in the structural evolution of droplet distributions. These figures, arranged top to bottom, present data on positive growth (condensation, expansion to the right hand side), negative growth (evaporation, expansion to the left hand side), and their combined effects at a time near the transient's end (around 7 eddy turnover times).

Monodisperse Case (Figure 3.12):

- Cloud Region (panels a, c and e): Here, condensation is present but milder than evaporation (around 10 times less). Interestingly, condensation is more intense on coalesced drops (top right of panel a). A narrow radius range (15.125-15.25 μm) exhibits perfect balance between condensation and evaporation (panels c, e).
- Mixing Region (panels b, d and f): Highest condensation occurs for droplets near 15 μm and coalesced droplets near 18.9 μm. However, evaporation balances condensation at these radii. Importantly, evaporation becomes significant, generating droplets as small as 11.8 μm after 8.5 τ_0, despite falling kinetic energy intensity (by 6 times in the clear-air region and 18 times in the cloud region). Notably,

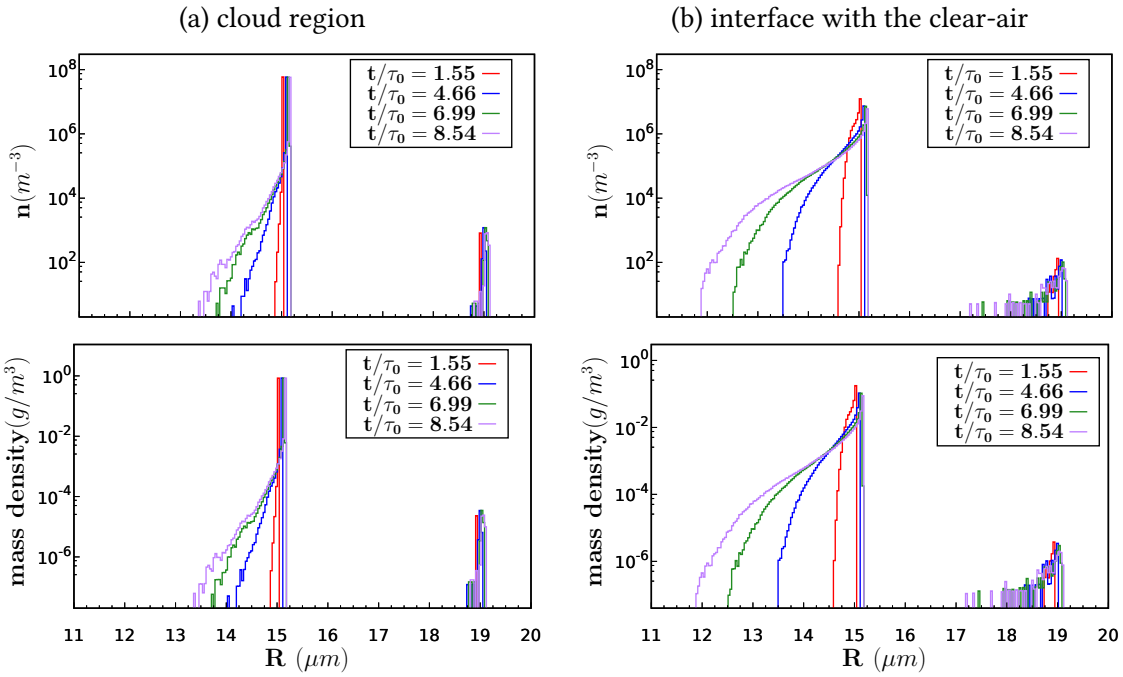

Figure 3.10: **Monodisperse** droplet distributions at different time instances. (a) Droplet size and mass distribution in the cloud region for an initial radius of 15 m and 8 million droplets. (b) Droplet size and mass distribution in the interface region between cloud and clear-air.

evaporation immediately affects collided particles here, unlike in the cloud region. Overall, evaporation and collision dominate over condensation in the interface.

Polydisperse Case (Figure 3.13):

- Cloud Region (panels a, c and e): Unlike the monodisperse case, condensation dominates evaporation only for droplets within a specific size range (2-6 µm) throughout the simulation. Within the interface, evaporation dominates throughout transient decay.
- Mixing region (panels b, d and f): Evaporation always prevails over condensation, though a near balance is reached for 3 µm droplets. Smaller drops experience more intense evaporation due to the curvature effect (negative *Kelvin term*, Eq. 3.4), leading to an evaporation rate three times higher than condensation. Both condensation and evaporation rates in the interface exhibit non-linear behavior, peaking around five eddy turnover times.

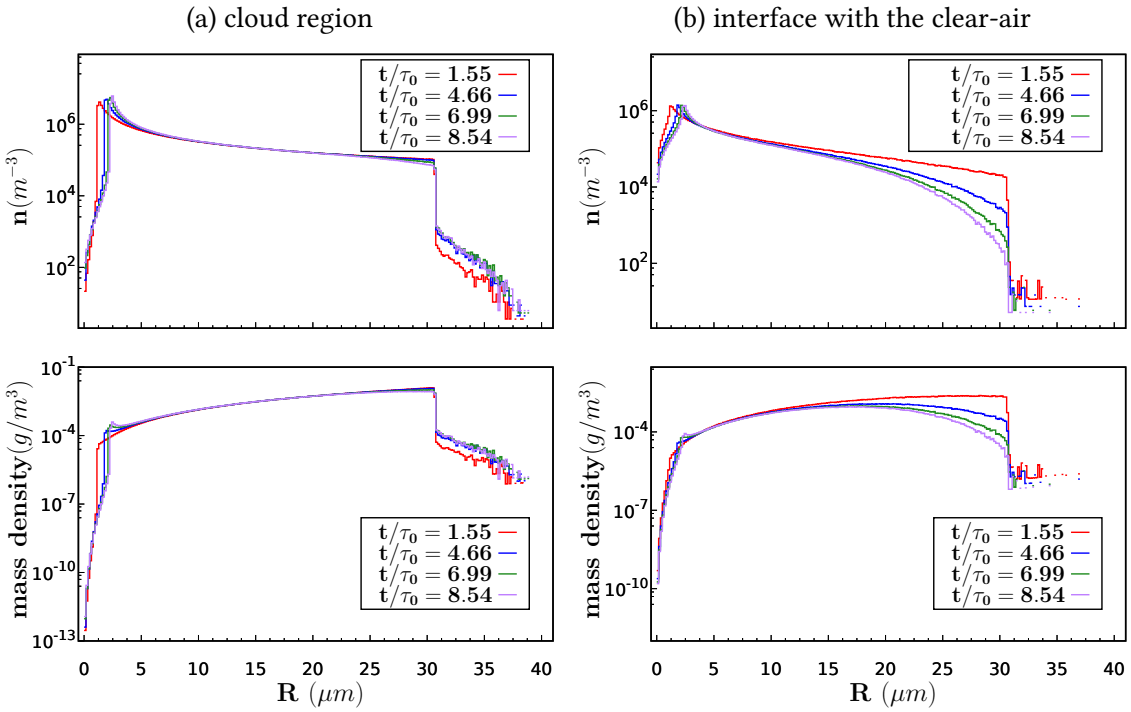

Figure 3.11: **Polydisperse** droplet distributions at different time instances for 10 million initial droplets with radii from 0.6 to 30 m. (a) Droplet size and mass distribution in the cloud region. (b) Droplet size and mass distribution in the interface region between cloud and clear-air.

C. Long-term behavior of size distributions

While the system eventually reaches a state of non-uniform residual turbulence with decreasing collision rates, analyzing drop size distributions (Figures 3.10, 3.11) alone is insufficient to quantify condensation-evaporation details as seen in Figures 3.12, 3.13.

Figures 3.14 and 3.15 focus on shape, width, position, and peak values of size distributions in ranges where condensation-evaporation processes are dominant. Here, coalescence events of larger particles are excluded (>18 μm for monodisperse, >31 μm for polydisperse).

Figure 3.14 highlights properties of the monodisprese distribution. Top two panels highlight that both distributions (within cloud and interface regions) are highly skewed towards the left direction, indicating the general negative growth rate among population (evaporation effect). Long-term behavior of the distribution broadening was assessed in panels c and d by observing temporal evolution of its standard deviation (σ) and width (w_{fixed}) at chosen levels (as a function of the peak of the distribution, 0.03% of n_{peak}). Temporal evolution of these characteristic values are fitted with linear interpolation functions, highlighted with thin dark gray lines and summarized in Table 3.1. In general σ values are higher inside the mixing region than the cloud and has ∼

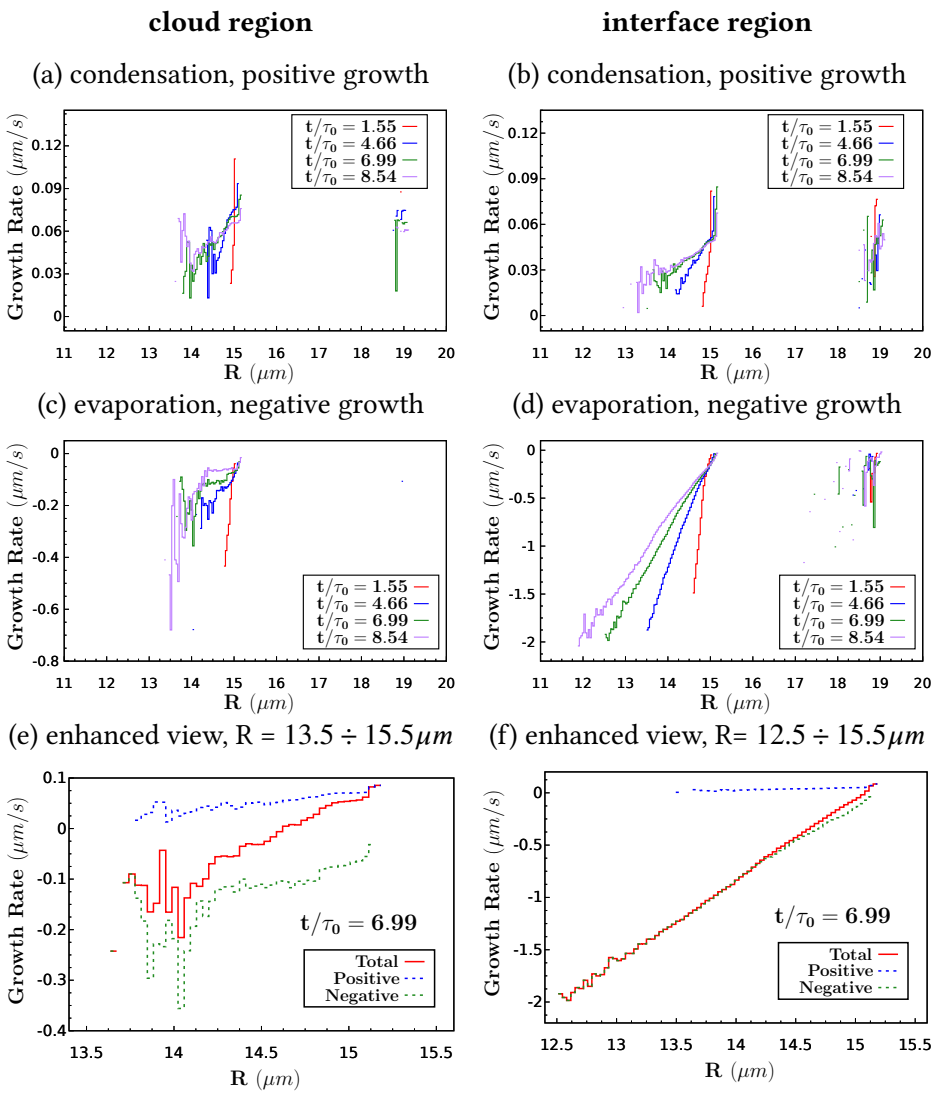

Figure 3.12: The mean droplet radius **growth rate** for different radius classes in a **monodisperse** droplet distribution, calculated across both the cloud and interfacial mixing regions. The top panels display positive growth due to condensation, the middle panels show negative growth due to evaporation, and the bottom panels depict the resulting mean growth rate at a specific time instance, near transient end ($t/\tau_0 \simeq 7$).

15 times faster growth rate. The similar behavior was observed for the w_{fixed} values, where the difference reached $\sim$ 6 times. Panels e and f shows that peak radius grows slightly more in the interface, while peak concentration value decays faster.

Unlike the monodisperse case, trends are reversed for the polydisperse distribution as depicted in Figure 3.15. The distribution skews right (panels a, b) and shrinks over time (panels c, d). The peak also moves rightward. Notably, width is measured at 3% of

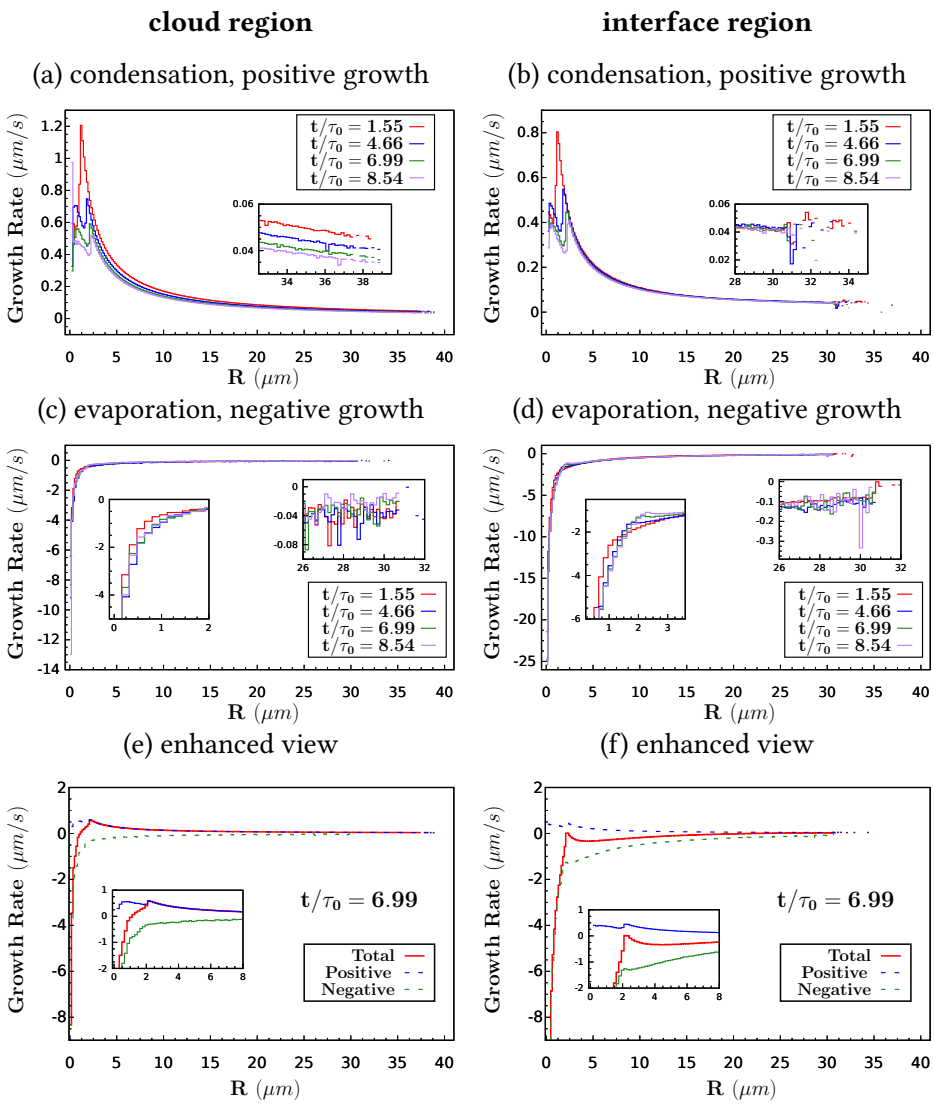

Figure 3.13: The mean droplet radius **growth rate** for different radius classes in a **polydisperse** droplet distribution, calculated across both the cloud and interfacial mixing regions. The top panels display positive growth due to condensation, the middle panels show negative growth due to evaporation, and the bottom panels depict the resulting mean growth rate at a specific time instance, near transient end ($t/\tau_0 \simeq 7$).

the peak (unlike the monodisperse case) and fitted exponentially (except for the standard deviation, which remains linear). The shrinking is faster (4 times) in the interface region (Table 3.1). Exponential fitting shows a 6x faster scaling (negative exponent), suggesting a slowdown towards saturation levels due to overall flow decay. Peak radius grows similarly in both regions (panels e, f), while peak concentration grows only in the cloud (becoming more prominent), similar to the monodisperse case. However, it

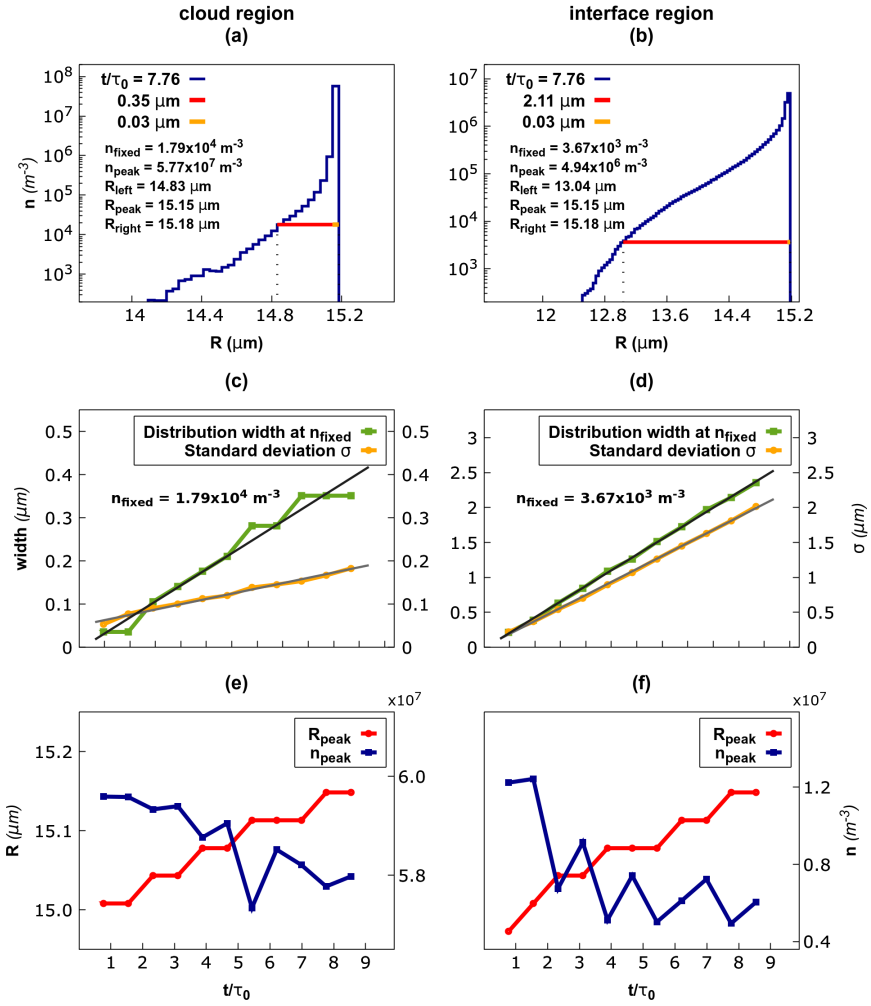

Figure 3.14: **Monodisperse droplet distribution characteristics.** (a, b) The distribution, its left and right half width relative to the peak value at selected time instance. (c, d) Distribution width (green) and its linear fit (black line, cloud: 0.047 $(t/\tau_0) - 0.006$, mixing: 0.28 $(t/\tau_0) - 0.02$). Additionally, standard deviation (orange) and its linear fit (gray line, cloud: 0.015 $(t/\tau_0) + 0.05$, mixing: 0.23 $(t/\tau_0) + 0.003$). (e, f) Peak distribution value (blue) and corresponding droplet radius class (red) over time.

remains constant in the mixing region, reflecting the slower shrinking process observed in panel d.

As seen in Figures 3.14 and 3.15 (panels c, d), the monodisperse distribution expands, while the polydisperse one shrinks over time (equations in figure captions and Table

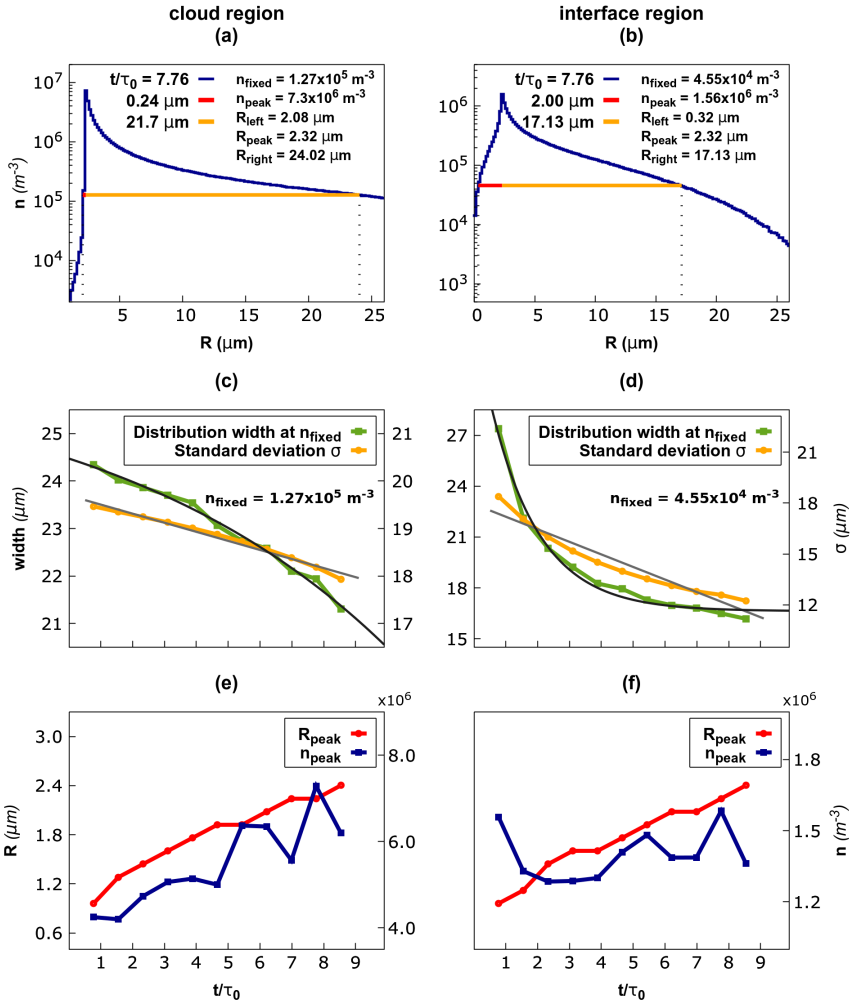

Figure 3.15: **Polydisperse droplet distribution characteristics.** (a, b) The distribution, its left and right half width relative to the peak value at selected time instance. (c, d) Distribution width (green) and its exponential fit (black line, cloud: $26.47 - 2\exp(0.11\ (t/\tau_0))$, mixing: $16.62 - 17.23\ \exp(-0.67\ (t/\tau_0))$). Additionally, standard deviation (orange) and its linear fit (gray line, cloud: $-0.19\ (t/\tau_0) + 19.69$, mixing: $-0.74\ (t/\tau_0) + 17.94$). (e, f) Peak distribution value (blue) and corresponding droplet radius class (red) over time.

3.1). Comparing these equations for each region allows us to estimate the characteristic time for both distributions to reach the same width under the same evaporation-condensation conditions.

In the cloud, this time is $100\tau_0$, while in the interface region, it's $18.5\tau_0$, indicating a remarkable acceleration (~5 times) within the shear-free mixing layer separating the

cloud from the sub-saturated air. Note that at this time, the turbulence intensity will be reduced to about 1/100th of its initial value.

Table 3.1: Droplet size distribution trends within the cloud and interfacial layer during the transient decay. Fitting laws are presented for both monodisperse and polydisperse populations in each region separately.

Property	**Fitting law (region-distribution)**	
	CLOUD	INTERFACIAL MIXING
Monodisperse population		
Standard deviation	$\sigma_{CM}(t) = 0.015\, t/\tau_0 + 0.05$	$\sigma_{IM}(t) = 0.23\, t/\tau_0 + 0.003$
Width w at the 0.03% of the probability density peak	$w_{CM}(t) = 0.047\, t/\tau_0 - 0.006$	$w_{IM}(t) = 0.28\, t/\tau_0 - 0.02$
Polydisperse population		
Standard deviation	$\sigma_{CP}(t) = -0.19\, t/\tau_0 + 19.69$	$\sigma_{IP}(t) = -0.74\, t/\tau_0 + 17.94$
Width at the 3% of the probability density peak	$w_{CP}(t) = 26.47 - 2\ \exp(0.11 t/\tau_0)$	$w_{IP}(t) = 16.62 - 17.23\ \exp(-0.67 t/\tau_0)$

Suffices: CM - cloud mono, CP - cloud poly, IM - interface mono and IP - interface poly

Even though turbulence and kinetic energy decrease overall within the interface, process acceleration is surprisingly faster there. This can be explained by the unique small-scale turbulence properties in the interface, characterized by *anisotropy* and *intermittency*.

Figure 3.16 shows thatlongitudinal velocity derivative moments across and parallel to the layer depart significantly from isotropic values [34]. The non-homogeneous direction (x_3) exhibits more intermittency than orthogonal directions [84]. This anisotropy reduces the squeezing of fluid filaments parallel to the interface but enhances it orthogonally. This likely leads to:

- **Higher collision rates and local supersaturation across the interface**: This could explain increased condensation for coalesced droplets in the x_3 direction.
- **Enhanced evaporation through parallel filament expansion**: This balances the increased condensation.

Importantly, the large-scale turbulence has minimal influence within the mixing layer due to the fixed domain and slow variation of large scales and kinetic energy ratios outside the region [83].

Exploring more the underlying reasons for this acceleration presents a promising direction for future particle-laden numerical simulations.

3.2.2 Collision kernel evolution within time decaying turbulence

This analysis explores the challenges of collision-coalescence processes and collision kernels in turbulent flows with rapid decay. The collision kernel, a factor within the

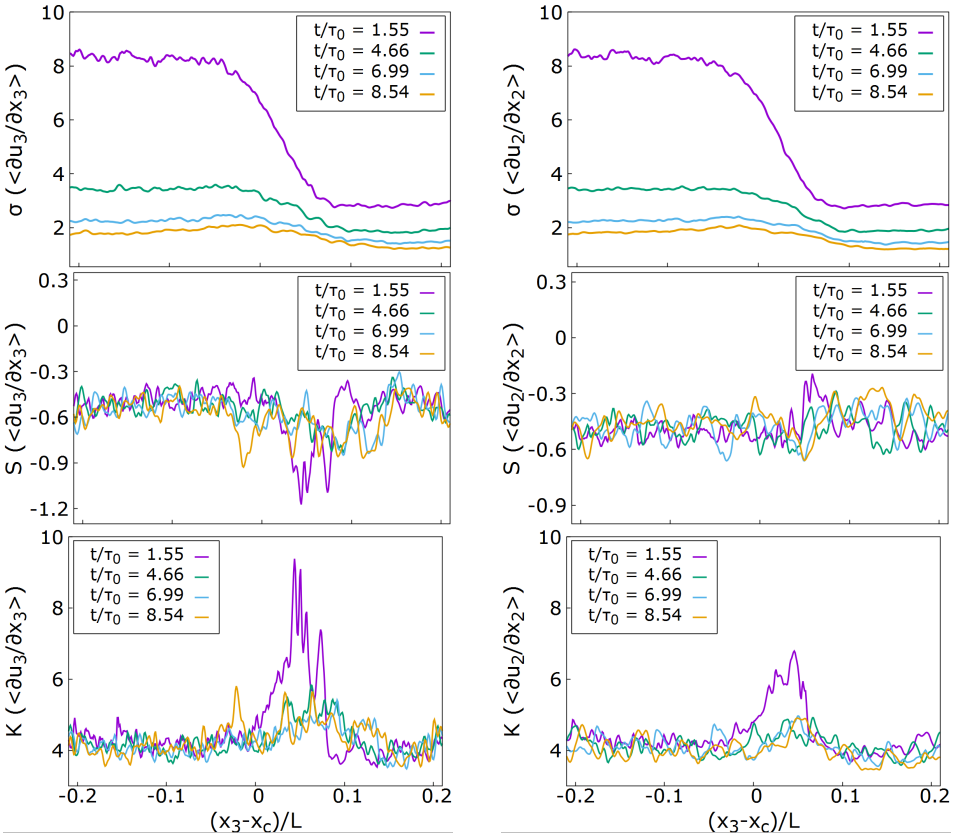

Figure 3.16: The statistical moments of the longitudinal velocity derivative fluctuation. The left panel shows the derivative across the interface (x_3 direction), while the right panel shows it along the interface (x_2 direction). The contrasting behaviors in these two directions highlight the inherent anisotropy of the small-scale turbulence within this shear-free layer.

Population Balance Equation (PBE) for droplet dynamics, is typically assumed independent of time and space [116, 117, 118]. However, this work highlights the limitations of this assumption in realistic scenarios involving inhomogeneous turbulence with rapid decay.

When turbulence intensity decays over 90% within 10 eddy turnover times (a significant transient), the kernel becomes dependent on the initial droplet size distribution. This arises from the conflicting timescales: (i) Turbulence-driven collision rates decrease rapidly; (ii) The droplet population lacks sufficient time to reach the asymptotic state dictated by the system's physical parameters (supersaturation, temperature, etc.). This asymptotic state is reached in $18.5\tau_0$ (interface) and $100\tau_0$ (cloud) (Section above). Additionally, lukewarm cloud turbulence has a global timescale of only 100 seconds, rendering "asymptotic" conditions questionable. The dynamics here are more accurately described as a series of distinct transients.

Given this context, it is proposed to extend the collision kernel concept to explicitly account for its temporal and spatial dependence. Notably, within the cloud-air interface, even while decaying, turbulence significantly accelerates evaporation and collisions compared to the homogeneous cloud region.

Traditional studies of turbulent flows laden with particles often assume steady-state, homogeneous, isotropic turbulence. In this scenario, the kernel is time-independent due to both steady turbulence and sufficient time for droplets to reach the asymptotic state. Such studies are numerous and historically important Wang et al. [119], Grabowski and Wang [120], and Devenish et al. [88]. The observed particle concentration variations significantly exceed predictions from statistical models [121], raising concerns about their applicability to represent particle-laden turbulent flows.

A. Kernel values computation

The collision kernel measurement simulates a small, initial perturbation of the cloud-clear air interface with mild unstable stratification. Collisions are considered geometric due to Stokes' drag inclusion in the particle momentum equation, but droplet-droplet aerodynamic interactions are neglected. The collision and coalescence efficiencies are assumed to be unity [122, 123]. The initial LWC is 0.8 g m^{-3}, typical of cumulus clouds.

The collision kernel is computed as:

$$\Gamma_{\mathrm{FS,SPP}}(\mathrm{R}_1, \mathrm{R}_2; \mathrm{t}, \mathscr{V}_\mathrm{r}) = \frac{\mathrm{N}_\mathrm{coll}}{\mathrm{n}_1 \mathrm{n}_2} \frac{\mathscr{V}_\mathrm{r}}{(\mathrm{t}_2 - \mathrm{t}_1)}, \tag{3.6}$$

where,

- FS means flow structure
- SPP: Set of relevant physical parameters
- $N_{\mathrm{coll}}(\mathrm{R}_1, \mathrm{R}_2, \mathrm{t} \in [\mathrm{t}_1, \mathrm{t}_2])$ is the number of collisions between droplets of radii R_1 and R_2 within time window $[t_1, t_2]$ and volume $\mathscr{V}_r = L_1 \times L_2 \times \Delta x_3$.
- n_1, n_2: Number of droplets in size classes R_1, R_2 within the same time and volume.

For any given time range ($[t_1, t_2]$), the computed $\Gamma_{\mathrm{FS,SPP}}(\mathrm{R}_1, \mathrm{R}_2)$ values are symmetric. This means it holds the same value for both pairs of (R_1, R_2) and (R_2, R_1). This is evident in the illustrations of kernel values in Figures 3.17 and 3.18.

Polydisperse Drop Population

Figure 3.17 panels show collision kernel values of polydisperse population for one-third of the transient, separately for each region. Due to the large size disparity (largest/smallest volume ratio ≈1.25 x 10^5), numerous collisions (≈5 x 10^4) occur among 10^7 droplets over 10 physical timescales.

Values inside interface region (left column) are generally *higher* than cloud values (right column). The kernel exhibits discrete jumps, with values differing by one or more orders of magnitude within the same region. The number of collisions inside the mixing

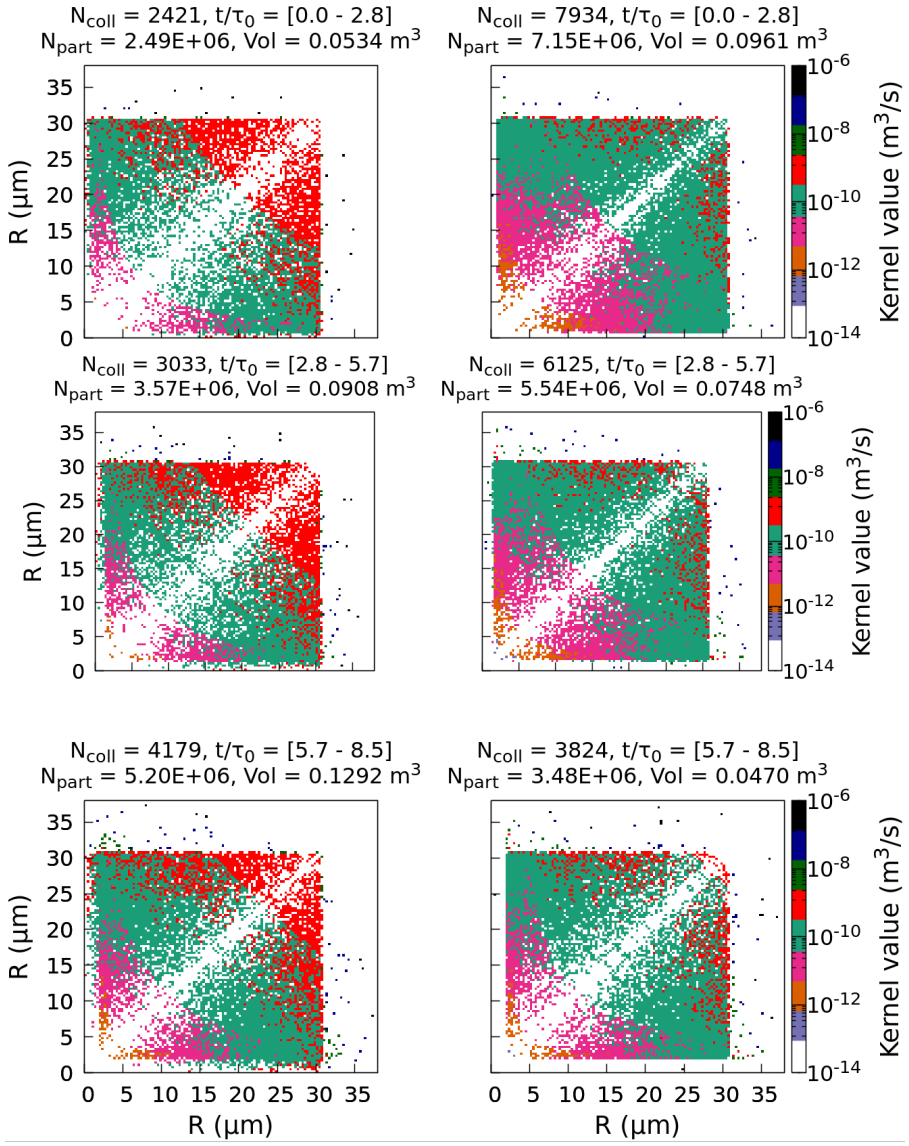

Figure 3.17: **Polydisperse collision kernel evolution** within the cloud-air interface (left) and the homogeneous cloud region (right) for a polydisperse droplet size distribution in an unstable, time-decaying cloud-air interaction. Ensemble average over three simulations. Each panel reports mean values over 256 discrete radii classes during one-third of the transient decay.

increases throughout the transient, while cloud collisions decrease. By the end, interface collisions exceed cloud collisions (4179 vs. 3824). However, the total number of collisions are decreasing over time. Points outside the [0-30] μm x [0-30] μm region represent droplets from potential double or triple collisions (seen in Figures 3.11 and 3.13), with maximum values of 1 x 10^6.

Despite energy decay (Figure A.1), the absolute number of interface collisions increases, while the collision density slightly decreases by 30%. We will revisit this in the context of collision correlation with velocity and passive scalar fluctuation intermittency.

Monodisperse Drop Population

Collision analysis for monodisperse population (Figure 3.18) shows significant change in number of collisions. Compared to the polydisperse case, the monodisperse population exhibits dramatically fewer collisions (around 400 out of 7 million drops) due to the initial identical size (particles with the same inertia are less likely to collide [111]). Inside the cloud region (right panels), collision density decays 76% alongside a 92% kinetic energy drop throughout the transient. On the other hand, in the mixing region (left panels), kernel values hold the similar levels despite 86% kinetic energy decay and a 50% decrease of numerical concentration. This also coincides with rapid droplet evaporation within the expanding interface.

Preliminary analysis from three ensemble-averaged simulations suggests that the diagonal spreading of the kernel is about 18% per eddy turnover time and lateral spreading is 25%. Moreover, the spreading factor is more evident for the mixing region than the cloud region due to wider range of droplet radii sizes and collisions. It is overseen that to achieve an ensemble average with a few thousand collisions, we estimate needing 100-200 realizations in the future simulations.

Numerical convergence of kernel values

The presented kernel calculations utilize a uniform radius discretization, approximating the true particle counts (n_1 and n_2) by assuming infinitesimal radius bins ($\delta R \to 0$). To assess convergence, we performed computations with varying radius classes (16 - 512 classes with $\delta R \in [0.8 - 2.5]$ μm) for the polydisperse population (radius range: 0.6-30 μm). However the most of the final results for polydisperse population are presented with 128 or 256 radii classes (Figures 3.17, 3.21 and 3.22).

Ensemble averages over three simulations (see Figures 3.19, and 3.20) were used for this analysis. Using 512 classes (bin size, $\delta R = 0.78$ μm) achieved good convergence for the collision count, but introduced rounding errors in the kernel values below 10^{-11} (as shown in Figure 3.20). This limitation arises due to double-precision calculations. Extrapolation suggests requiring 10^6 classes for full convergence, exceeding current capabilities (210-220 classes) even with quad-precision. Furthermore, current dataset can not provide sufficient numerical concentration of collisions and water droplets per radius class.

Alternative methods can be investigated like the Direct Simulation Monte Carlo (DSMC) method, commonly used in molecular gas dynamics. DSMC has become more

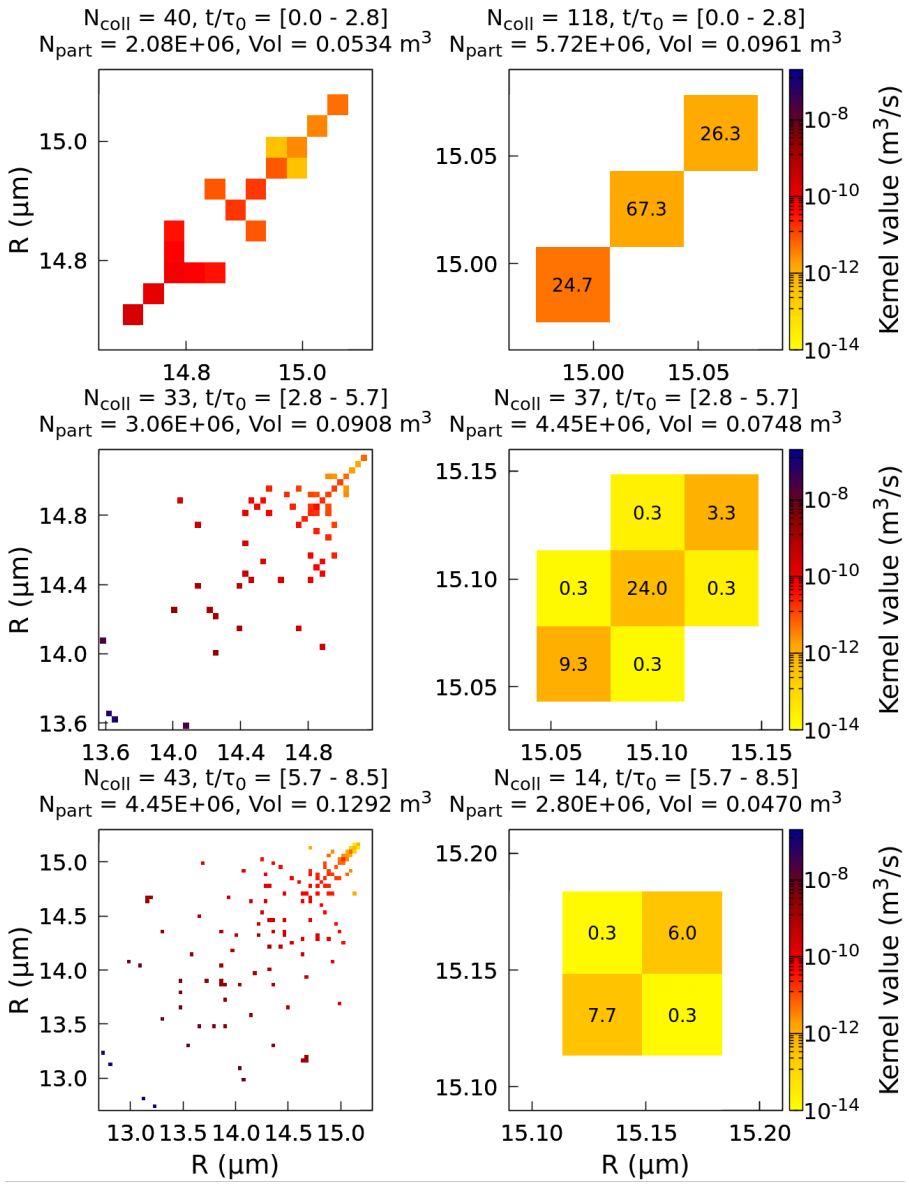

Figure 3.18: **Monodisperse collision kernel evolution** within the cloud-air interface (left) and the homogeneous cloud region (right) for a polydisperse droplet size distribution in an unstable, time-decaying cloud-air interaction. Ensemble average over three simulations. Each panel shows means during one-third of the transient decay. Number of radius classes varies (3-32).

accessible and holds promise for simulating low-density or small-scale gas flows, potentially offering advantages over our current approach.

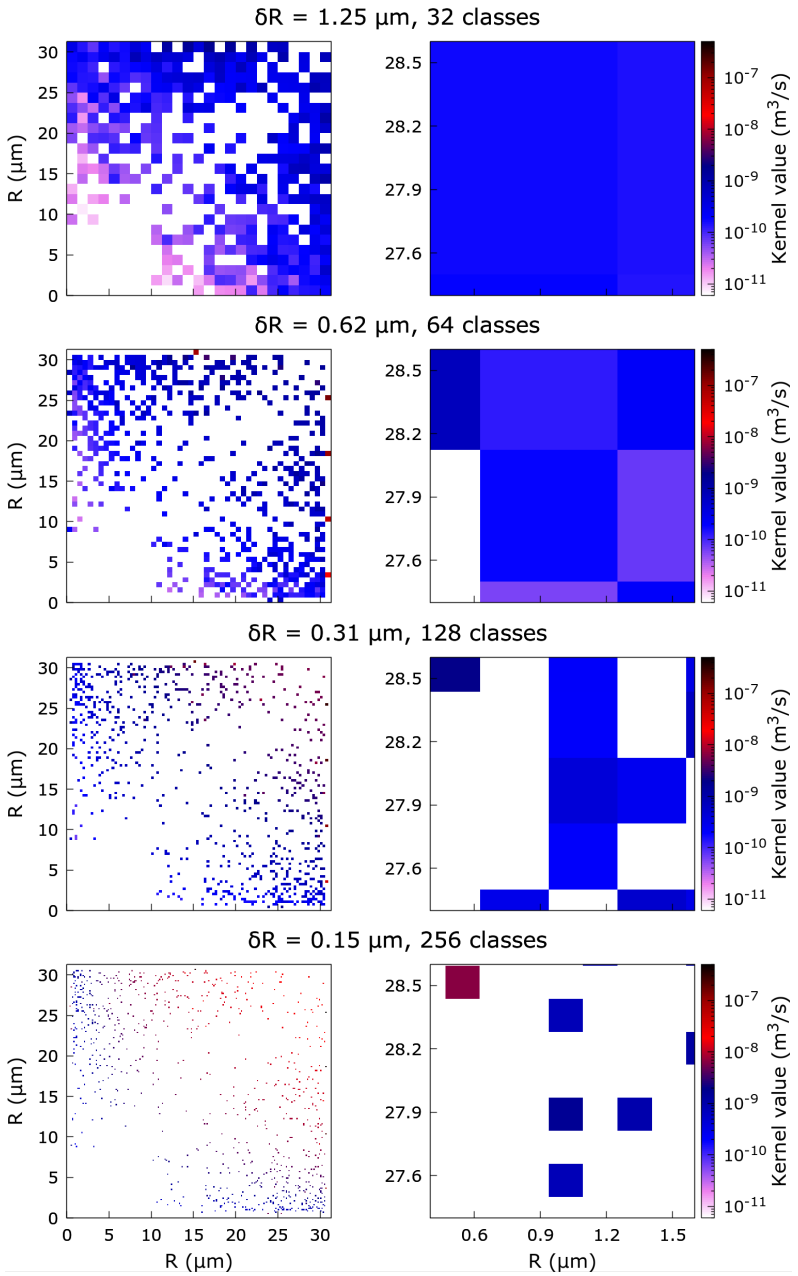

Figure 3.19: **Polydisperse Drop Kernel Convergence.** Convergence analysis of the collision kernel within the cloud-clear air interface (t/τ_0 = [0.0 - 0.8]) for different numbers of radius classes (32 to 256). The four right panels ($R_1 \in [0.4, 1.6]$ μm, $R_2 \in [27.4, 28.6]$ μm) zoom in on the corresponding regions in the left four panels ($R_1, R_2 \in [0, 31.5]$ μm).

B. Collision Kernel Morphology

Analyzing the polydisperse population across shorter time intervals reveals a layered structure in the collision kernel (128 radius classes, see Figures figures 3.21 and 3.22).

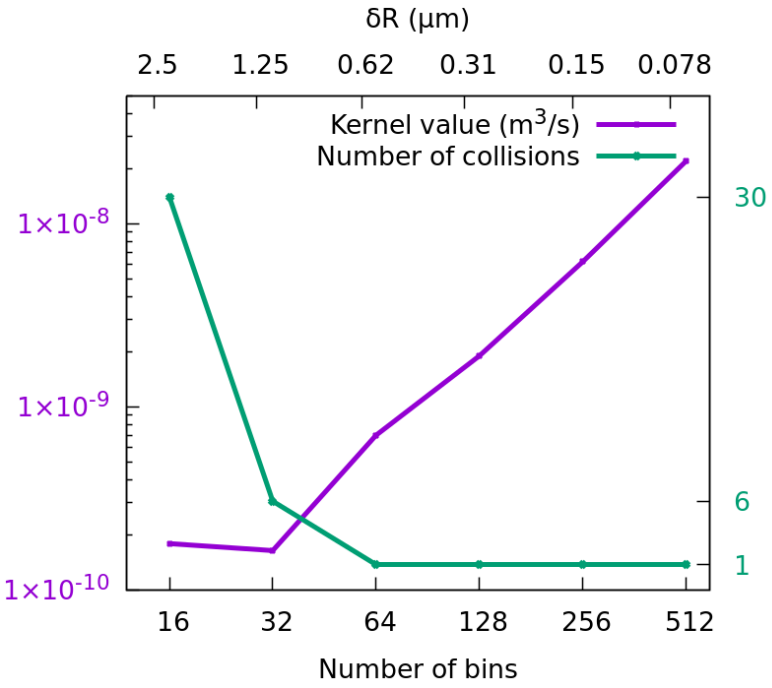

Figure 3.20: **Collision Count and Kernel Convergence.** Convergence of collision count and kernel values within the mixing region (t/τ_0 = [0.0 - 0.8] R_1 = 28.59 $\pm$ δR/2 and R_2 = 0.47 $\pm$ δR/2). While significant for the entire system, convergence is not uniform across the field.

Peak values concentrate in the corners, representing collisions between smallest and largest droplets. Intermediate values correspond to large drop collisions, while minimal values reflect small drop collisions. Collisions between same-radius drops have zero probability. This trend holds for both interface and cloud regions, with lower values in the cloud (less than one order of magnitude difference).

To achieve statistically significant results with a few thousand collision events, we estimate needing 10-20 realizations for the polydisperse case and 100 realizations for the monodisperse case.

The present results are compared to the Saffman-Turner (ST) model[111], widely used in multi-phase turbulent flows. However, the ST model assumes steady-state, homogeneous, isotropic turbulence, unlike the current system with transient decay, inhomogeneous turbulence, and unstable density stratification. Despite these differences, the ST model provides a valuable comparison to highlight differences between near-ergodic and fully non-ergodic systems.

Figure 3.23 shows the three contributions in the ST kernel model: collisions due to particle inertial effects (term A), gravity effect on particle motion (term B), and passive turbulent transport (term C). Notably, the ST model does not consider Reynolds number, assumed to be very large. Interestingly, term C plays a minor role with respect to

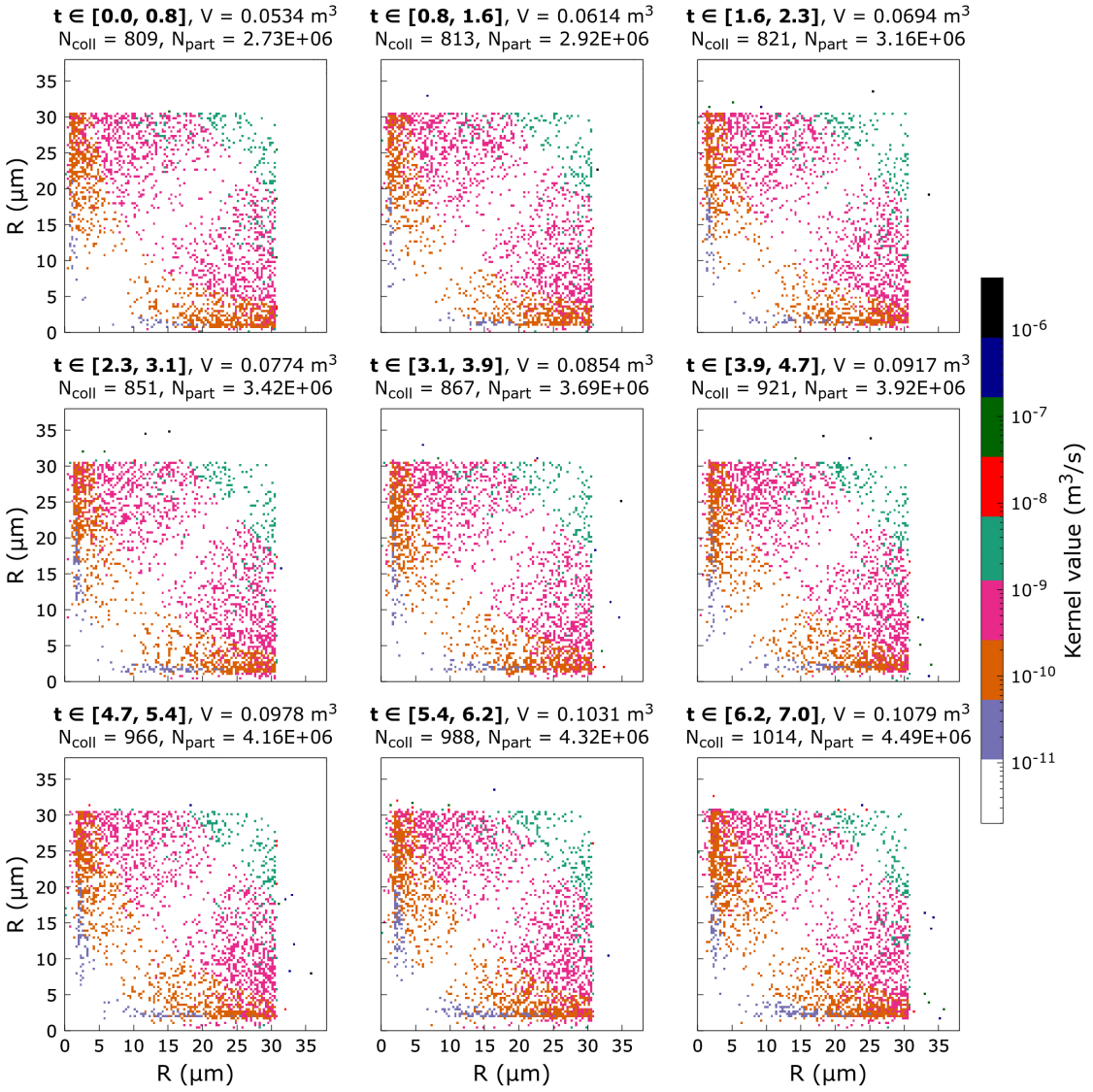

Figure 3.21: **Kernel value evolution for polydisperse population within the interface region.** Ensemble average over three realization simulation data. Values computed over 128 radii classes.

terms A and B in this model for the specified conditions ($\epsilon = 10$ cm^2/m^3 and an air temperature of 280 K).
The bottom panels compare the ST model with the current polydisperse kernel during a similar dissipation period. Simulated kernel values are generally lower (from a few percent to 90-100%) and have a different shape (band-like rather than butterfly).

It can be optimal to conduct a dedicated simulation campaign to obtain quantitatively accurate collision kernel values and morphology under non-homogeneous, time-decaying conditions. This will require ensemble averages on a large number of samples:

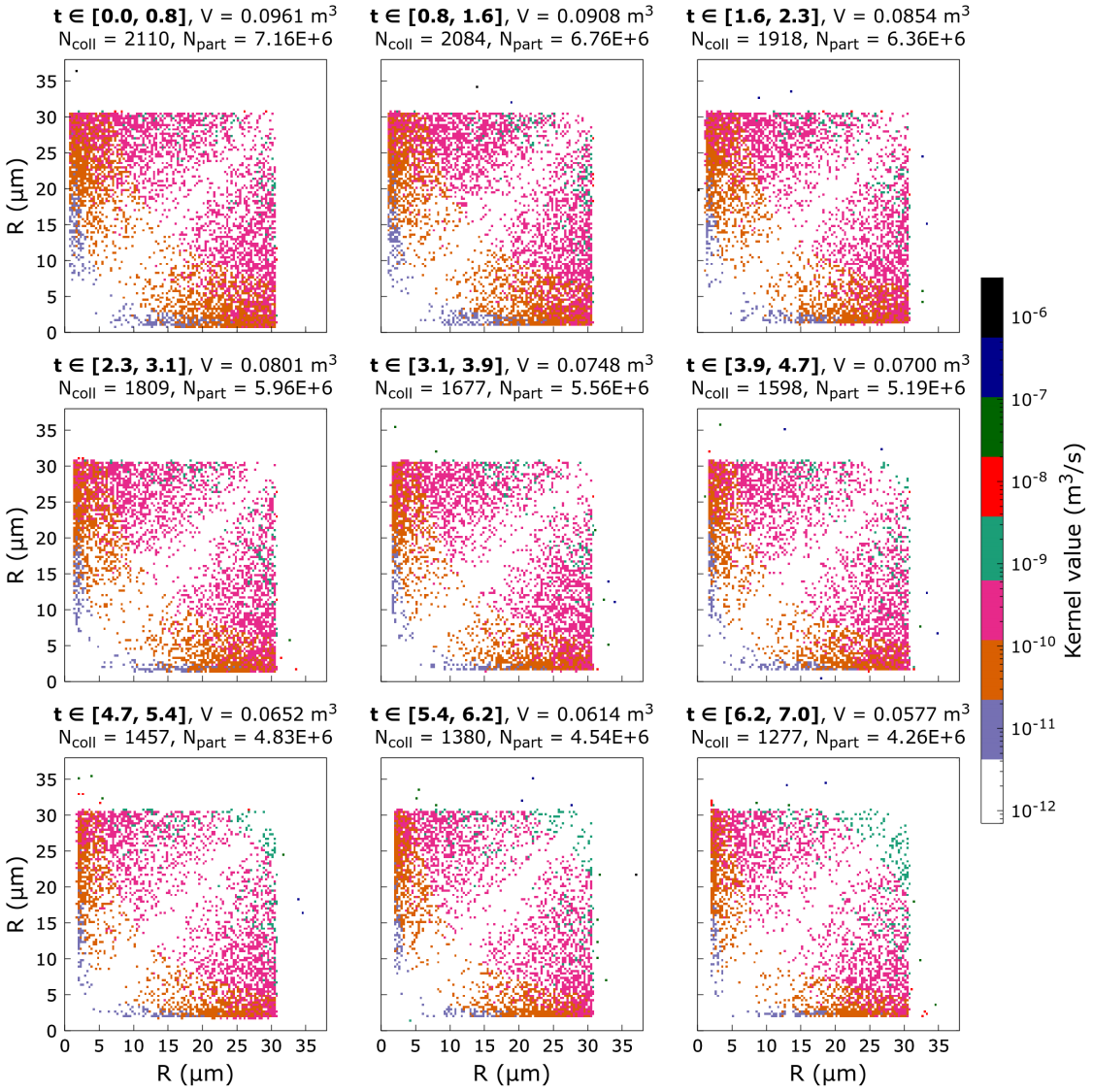

Figure 3.22: **Kernel value evolution for polydisperse population within the cloud region.** Ensemble average over three realization simulation data. Values computed over 128 radii classes.

10-20 for the polydisperse case (targeting 10^4+ collisions) and 100 for the monodisperse case (targeting 10^3+ collisions).

C. Small scale turbulent velocity fluctuation and collision count correlation.

The last part of the section analyzes the correlation between collisions and small-scale anisotropy. The collision rate observed in the simulation of the polydisperse droplet population at the cloud-air interface is naturally correlated with the fine-scale (inertial

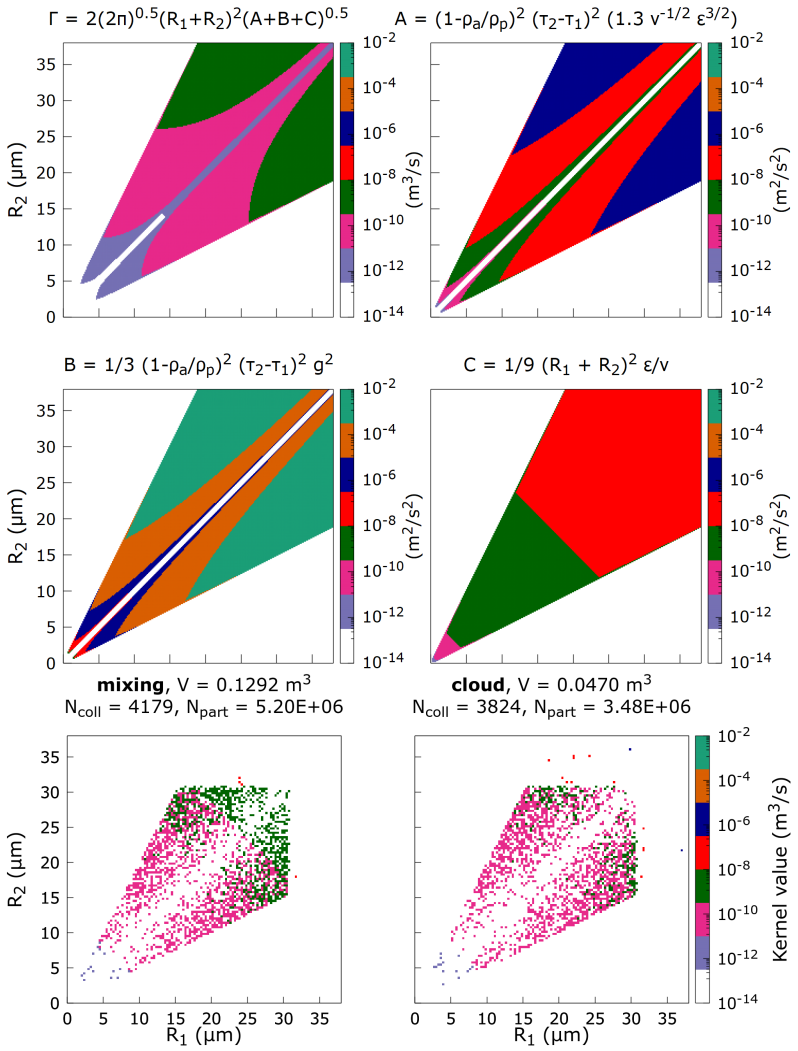

Figure 3.23: **Comparison of Collision Kernels.** Saffman-Turner Model (top left): Valid for steady-state, HIT, $\epsilon = 10\ cm^2/s^3$, $R_1, R_2 \in [0, 38]\ \mu m$, $R_1/R_2 <= 2$ and $R_2/R_1 <= 2$. Top right and middle panels, the three ST terms: droplet motion relative to the air, droplet relative motion due to gravity, droplet motion with the air, respectively. Simulation (bottom panels): Unsteady, inhomogeneous, with anisotropic small scale. Dissipation has a comparable value for the time range $t/\tau_0 \in [5.7, 8.5]$. Kernel values for the polydisperse population. Left: mixing interface, right: cloud region. The portion of the R_1, R_2 graph where the model is valid is only considered.

and viscous) behavior of the turbulence. This is evident from the computed correlation index between the statistical moments of the velocity derivative (Figure 3.16) and collision counts. Figure 3.24 reveals an extremely high correlation (0.9 - 0.94) within the cloud region.

(a) Standard deviation of velocity longitudinal derivative and collision count

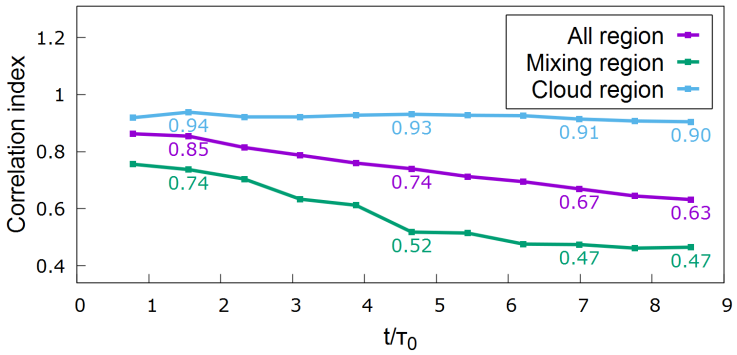

(b) Skewness of velocity longitudinal derivative and collision count

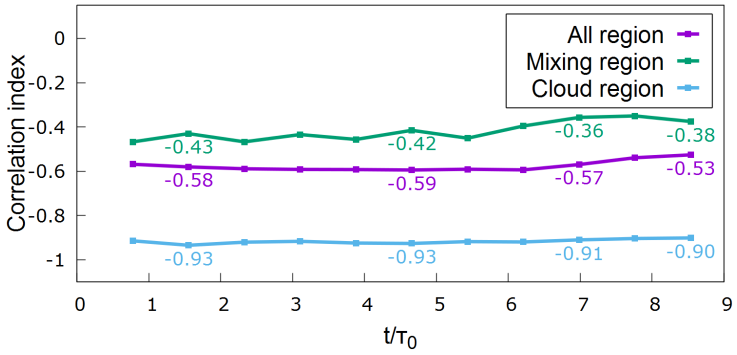

(c) Kurtosis of velocity longitudinal derivative and collision count

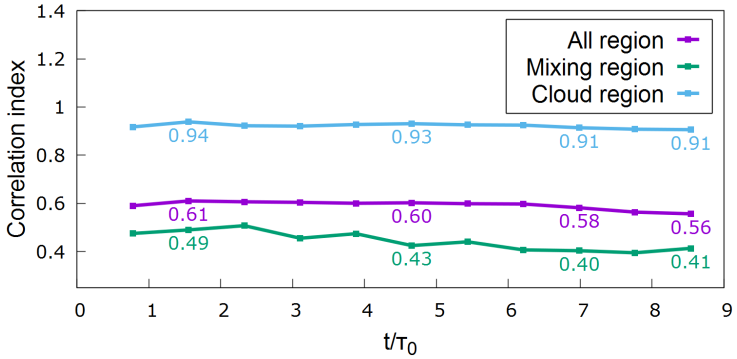

Figure 3.24: **Correlation between small-scale turbulence and collision count.** Intermittency of small-scale fluctuations represented by anisotropy-related quantities, such as skewness, and kurtosis of the longitudinal derivative fluctuation $(\partial u_3/\partial x_3)$[84]. Collision count is a number of collisions within the given region.

Interestingly, even at the interface, the correlation remains relatively high (around 0.5) throughout the simulated decay. This is despite the highly anisotropic and rapidly decaying nature of the small-scale velocity field at the interface (lacking a mean shear flow). This finding highlights the continued potential for water droplet growth through collision-induced coalescence at the cloud border.

3.2.3 Microphysical time responses of water droplets

The importance of mixing at growing cloud tops in unstable environments was highlighted by Warner [76]. Latham and Reed [77], Baker, Corbin, and Latham [78] distinguished between homogeneous and inhomogeneous mixing, where the microphysical time scale can differ significantly from the turbulent mixing time scale. This difference is captured by the Damköhler number, Da, which represents the ratio between these two time scales. The same turbulent flow can encompass a wide range of Da values due to the energy cascade [124].

Several time scales, including evaporation, phase relaxation, and reaction time scales, have been used to define Da and parameterize the impact of entrainment and mixing of clear air at cloud boundaries [125]. These time scales influence the microphysical processes within the cloud.

The key driver of droplet condensation and evaporation is supersaturation ($S = RH - 1$), where RH is the relative humidity [126]. S varies spatially and temporally, determined by the local, instantaneous water vapor concentration (ρ_v) and temperature (T) through the Clausius-Clapeyron equation. To account for this variability, most presented time scale results are accompanied by the mean profile of supersaturation.

A. Phase relaxation

Supersaturation is commonly modeled using an evolution equation to represent the water vapor budget within a developing cloud [88]. This equation balances a production term ($\mathscr{P}$) representing vapor influx and a depletion term ($\mathscr{C}$) due to condensation on droplet surfaces [126, 127]:

$$\frac{dS}{dt} = \mathscr{P} + \mathscr{C} \tag{3.7}$$

The condensation term depends on the local supersaturation as following:

$$\mathscr{C} = -\frac{S}{\tau_{phase}} = 4\pi\kappa_v N\overline{R}S. \tag{3.8}$$

The production term ($\mathscr{P}$) varies depending on the chosen model. It is often modeled as a linear function of the vertical updraft velocity [128, 129]. $\mathscr{P}$ can also represent the net flux of supersaturated water vapor through the parcel boundaries. In this analysis, $\mathscr{P}$ is set to zero due to the *absence of updraft*. Additionally, Equation (3.7) neglects:

- **Advection and diffusion**: Processes influencing the surrounding environment ($\mathrm{Re}_{drop} \ll 1$) are not considered.
- **Spatial variability**: Supersaturation (S) is treated as a global property of the cloud parcel [102].

However, studies suggest that under specific conditions, diffusive transport can become significant [130].

In a homogeneous, statistically balanced cloud layer with zero mean vertical velocity, no net vertical transport of cooling vapor parcels occurs. Additionally, equation (1.21) simplifies to an exponential solution (details omitted) when neglecting updraft, allowing supersaturation to relax towards zero [131]:

$$\frac{dS}{dt} \cong -4\pi\kappa_v N\overline{R}S = -\frac{S}{\tau_{phase}} \tag{3.9}$$

The time constant of this relaxation, the phase relaxation time (τ_{phase}), depends on the assumption of a constant integral droplet radius ($N\overline{R}$) and captures both supersaturation and liquid water content variations in a homogeneous context [132, 125]:

$$\tau_{phase} = \left(4\pi\kappa_v N\overline{R}\right)^{-1} \tag{3.10}$$

The choice of τ_{phase} in this study aligns with microphysical time scales used in prior DNS studies of entrainment and mixing [124, 96, 133, 87, 134]. This time scale, along with the turbulent mixing time scale (τ_{turb}), defines the Damköhler number (Da). Da characterizes the relative importance of microphysical processes compared to turbulent mixing [124]:

$$\mathrm{Da} = \frac{\tau_{turb}}{\tau_{microphysics}}$$

Large Da values indicate a rapid microphysical response to mixing, often associated with inhomogeneous mixing [135]. Conversely, small Da values suggest a slower response and often indicate homogeneous mixing [77, 78].

B. Evaporation-condensation and reaction time scales

While constant supersaturation and integral radius are convenient assumptions for defining time scales, they may not be suitable for highly anisotropic and inhomogeneous environments like the mixing layer separating the cloud from the dry air. Here, momentum, energy, and water vapor fluxes are non-zero and peak near the layer's center [80, 113, 36]. This mismatch between assumptions and realities necessitates different time scales:

- **Evaporation time scale** (τ_{evap}): Estimates the time for a single droplet to evaporate completely in a uniform, subsaturated environment, assuming constant supersaturation:

$$\tau_{evap} = -\frac{R_0^2}{2K_s S_0} \tag{3.11}$$

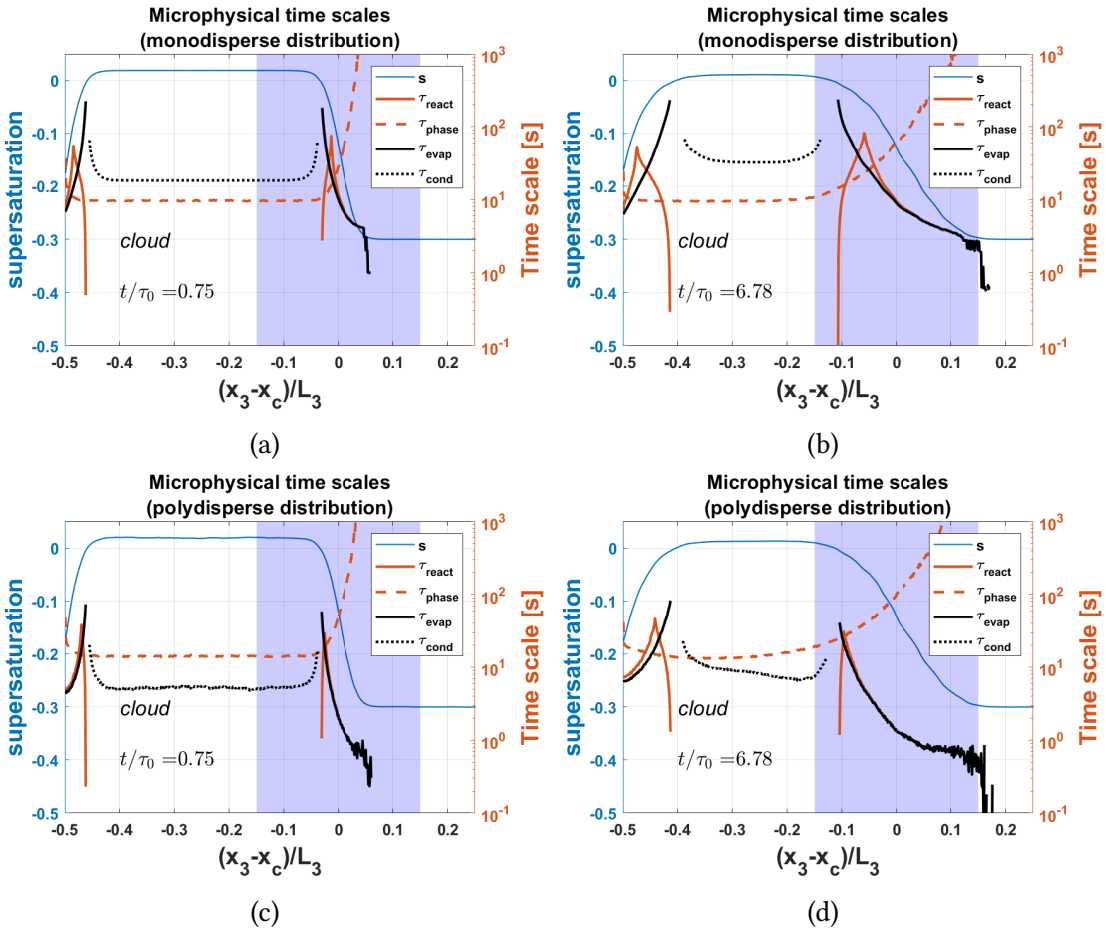

Figure 3.25: **Distribution of time scales and supersaturation across the non-homogeneous vertical direction.** Planar average values are presented for both monodisperse (a, b) and polydisperse (c, d) cases. Data are displayed at two different time steps: the beginning (a, c) and the end (b, d) of the transient period. Supersaturation $\overline{S}$ (Figure 3.8a) is also plotted for reference.

- **Condensation time scale** (τ_{cond}): Arbitrarily defined as the time for a droplet to double its radius under constant local supersaturation:

$$\tau_{cond} = \frac{3}{2}\frac{R_0^2}{K_s S_0}. \tag{3.12}$$

  This is relevant only in supersaturated regions.
- **Reaction time scale** (τ_{react}) is defined as the shortest time that has elapsed since either the droplet has evaporated completely or the parcel has become saturated [132]. It considers variations in both supersaturation (S) and integral radius ($\overline{NR}$) by solving the coupled system of governing equations (Equations 3.4 and 3.9).

It should be noted that τ_{evap} and τ_{react} are only defined for the subsaturated regions, whereas τ_{phase} is defined for non-zero values of the integral radius, and can also be used in supersaturated regions.

Microphysical Time Scales in the Mixing Layer

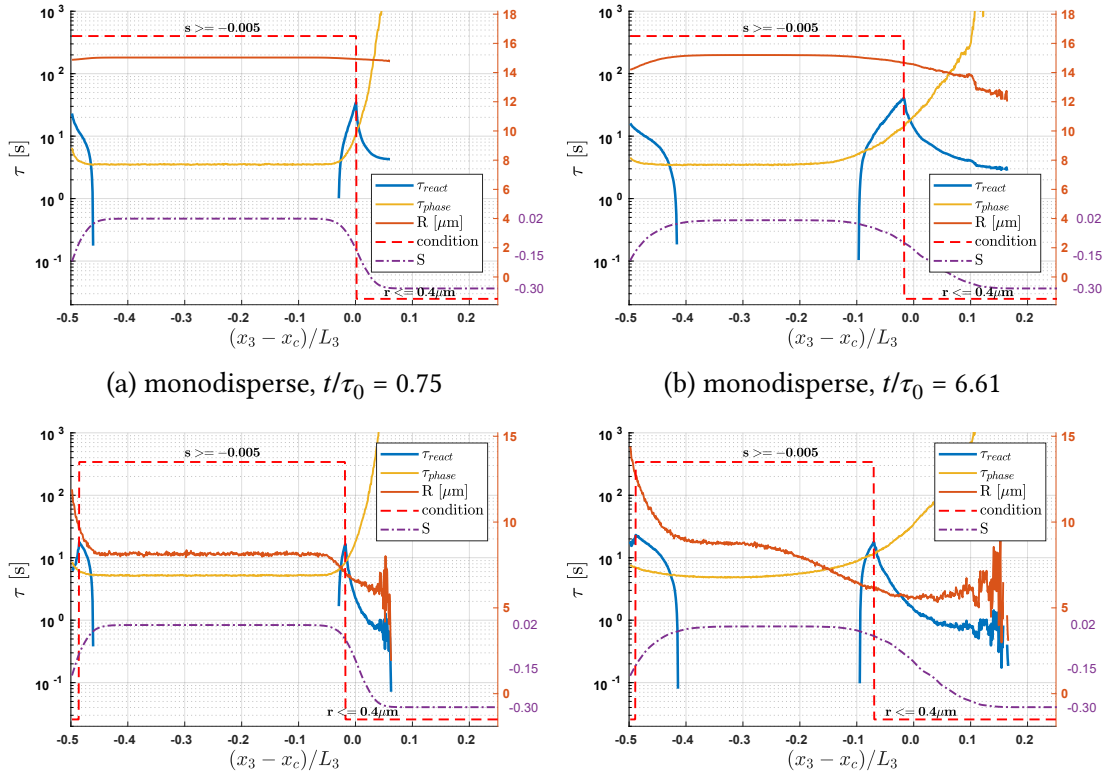

(a) monodisperse, t/τ_0 = 0.75

(b) monodisperse, t/τ_0 = 6.61

(c) polydisperse, t/τ_0 = 0.75

(d) polydisperse, t/τ_0 = 6.61

Figure 3.26: **Planar averages of reaction time and phase relaxation time scales.** This figure expands on Figure 3.25, providing a more detailed view of the reaction time (τ_{react}) distribution. Dashed red lines indicate the first condition (supersaturation or evaporation) reached at each vertical location while solving the coupled system of Equations 3.4 and 3.9. (a, b) Monodisperse case. (c, d) Polydisperse case. Planar averaged supersaturation (S) and radius (R) are included for reference.

Figure 3.25 shows the horizontal averages of these time scales across the domain for different time steps and initial droplet size distributions. Note that different averaging methods (individual cell vs. averaged quantities) can lead to slightly different results, as seen in Figure 3.26 for the monodisperse case at a specific time.

Condensation and evaporation times diverge near saturation ($S = 0$), where they are undefined (Figure 3.8a). Phase relaxation time (τ_{phase}) increases across the mixing

layer due to decreasing mean radius and droplet concentration. This growth eventually slows as the layer widens towards the clear-air side. This indefinite growth of τ_{phase} in the inerface region is consistent with observations by Siebert and Shaw (2017) [129].

Condensation time is generally higher than the phase relaxation time in the monodisperse case but becomes comparable in the polydisperse case within the mixing region. It increases in the bottom region due to sedimentation. The evaporation time oscillates significantly on the right side of Figure 3.25 due to the higher collision rate in that region, as seen in Figures 3.10 and 3.11.

Figure 3.26 provides a more detailed view of the reaction time (τ_{react}) computation. The dashed red lines within each panel highlight two distinct regions of τ_{react}, linked to supersaturation values (S) and the dry radius threshold (minimum radius for considering a droplet fully evaporated). In the monodisperse case, the reaction time converges to the saturation time (ratio $\rho_v/\rho_{vs} = 0.995$), where the skewness of S is negative, while it is converging to the evaporation time ($r \leq 0.4\ \mu m$) when S is positively skewed [35].

Interestingly, a clustering of τ_{phase}, τ_{react}, and τ_{evap} is observed within the mixing layer in Figure 3.25, *preceding the peak turbulent flux location* (Figure 3.27). This suggests a potential connection between microphysical processes and the strongest turbulent mixing zone. Before this location, τ_{react} is much shorter than the other times. After this location: (i) τ_{react} collapses to τ_{evap}, which becomes significantly shorter than τ_{phase}; (ii) In the polydisperse case, τ_{cond} also joins the cluster, reflecting rapid condensation for small droplets.

Overall, the analysis of microphysical time scales reveals their complex behavior within the mixing layer and highlights their potential connection to the turbulent mixing process.

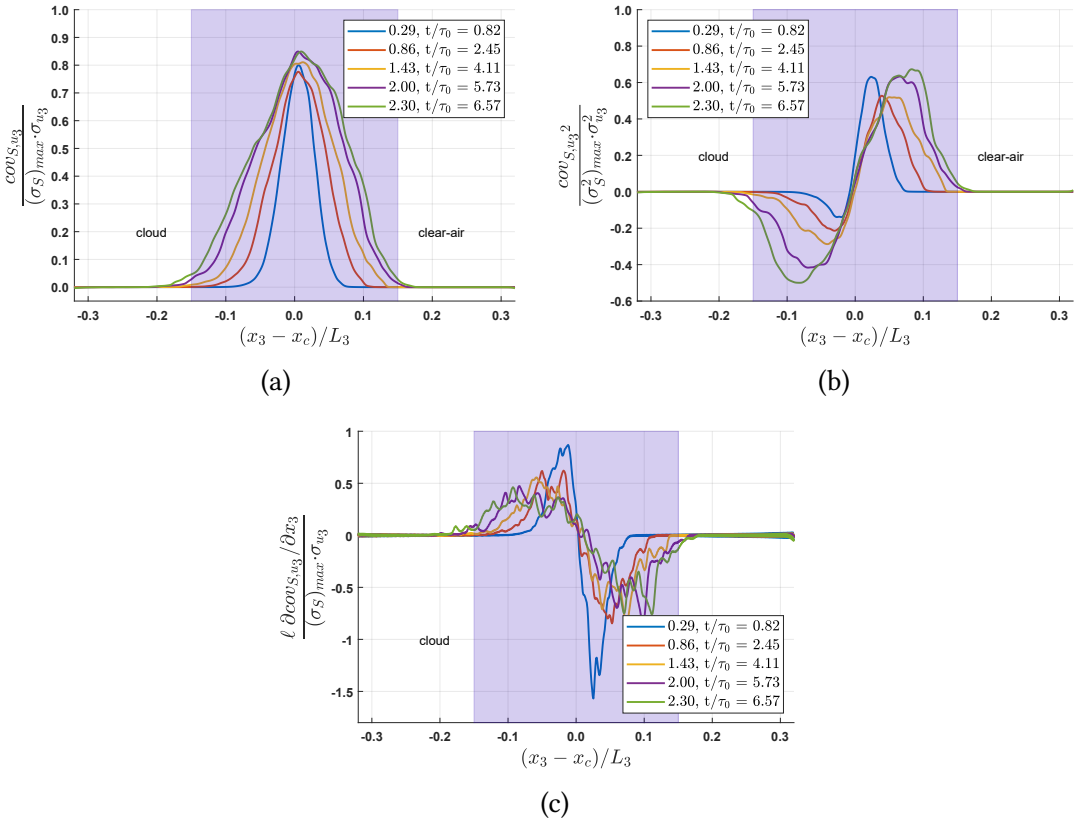

Figure 3.27: **Supersaturation flux statistics from the monodisperse simulation dataset.** The panels show: (a) Normalized covariance (flux) between supersaturation and the vertical velocity component. (b) Normalized covariance between supersaturation and the square of the vertical velocity component. (c) Normalized derivative of the covariance (flux) between supersaturation and the vertical velocity component. The difference between the monodisperse and polydisperse population distributions for these statistics is negligible.

Chapter 4

The radiosonde cluster network: design and validation

This study introduces a novel measurement system utilizing a cluster of miniaturized radiosondes to track atmospheric fluctuations over a 10 km range. Beyond cloud observations, this system is applicable for environmental monitoring in urban or industrial areas [7]. Balloon-borne radiosondes, traditionally used as Lagrangian markers for long-term field observations, such as lower stratosphere circumnavigations [45, 55, 136], have been employed in studies of tornadogenesis [137, 47], ocean observations [49, 138], and large-scale atmospheric phenomena at high altitudes [52]. This new approach draws inspiration from L.F. Richardson's 1926 experimental method [41].

The present in-field measurement system consists of a network of ground stations and a cluster of miniaturized radiosondes, developed during the H2020-COMPLETE project [10]. It has been demonstrated among various research communities including atmospheric physics [139, 140, 141], meteorology [142], and metrology/remote sensing networks [143, 144]. Key design aspects has been outlined in recent publications by Paredes Quintanilla et al. [40] and Abdunabiev et al. [7].
The system offers three main advantages:

1. **Direct quantification of Lagrangian dispersion**: Allows to obtain direct measurements of Lagrangian turbulent dispersion and diffusion within the field.
2. **Tracking fluctuations in warm clouds (ABL)**: Enables tracking fluctuations of various physical quantities inside warm clouds.
3. **Insights into small-to-medium scale cloud dynamics**: Provides simultaneous measurements from different cloud locations for a broader understanding of cloud behavior.

Between June 2021 and June 2024, we have conducted in-field experiments using both single and multiple radiosondes under varying environmental conditions. Sensor accuracy was rigorously verified by comparing them with reference values from traceable instruments at meteorological stations provided by INRIM, ARPA-Piemonte, MET

OFFICE, OAVdA, and Chilbolton Observatories.

Validation tests, including single-sonde setups, dual-sounding, and multiple tethered sondes, are discussed in Section 4.3. These validations paved the way for in-field free-flying cluster experiments in both Alpine environments (Valle d'Aosta, Italy) and near-coastal (Chilbolton, UK) ABLs, assessing the feasibility of analyzing measured fluctuations and applying Richardson's distance neighbor graph statistics for atmospheric turbulent dispersion [41]. The results of cluster experiments are discussed in Chapter 5.

4.1 System design

Instrumenting probes to observe different cloud sections at varying scales throughout a cloud's lifetime is a challenging task. To address this, the measurement system was proposed as depicted in Figure 4.1. The system consists of three main core components:

- A cluster of radiosondes;
- A set of receiver stations;
- A post-processing machine.

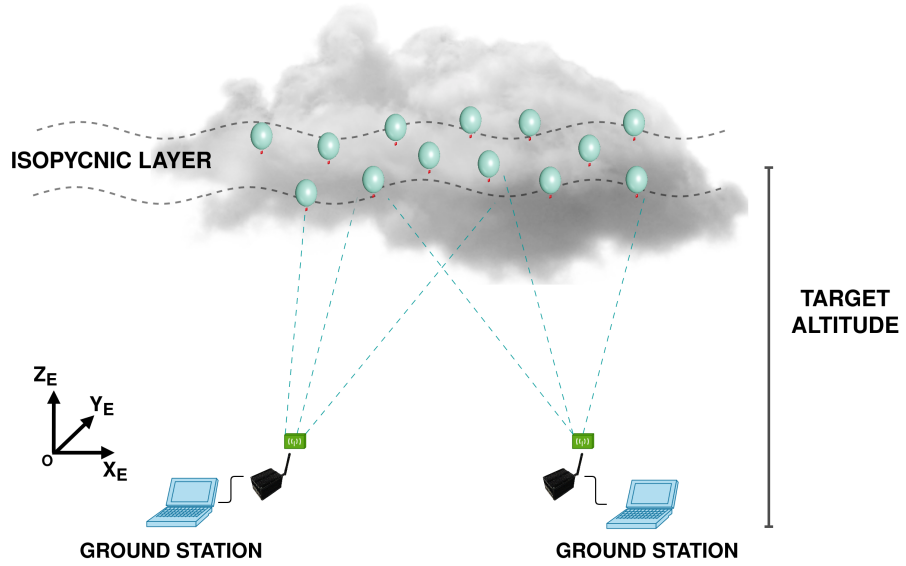

Figure 4.1: Illustration of the in-field experiment featuring a cluster of radiosondes and a set of receiver stations. The radiosondes are depicted floating within an isopycnic layer at the pre-determined target altitude (1-2 km). The launch point of the cluster serves as the origin (X_E,Y_E,Z_E) of the experimental observation frame.

The objective is to deploy the radiosondes within warm clouds (or other atmospheric environments) where they passively follow the fluid flow across isopycnic layers at the target altitude. This allows us to gain insights into the real dynamics of the

surrounding fluid, whether it's a cloud (when the balloon is inside) or clear air (when outside).

Each radiosonde transmits sensor data to ground stations using the LoRa radio transmission protocol. LoRa is a low-power, long-distance communication technology that utilizes license-free ISM bands for low data rate exchange. Ground stations receive data and relay it to the post-processing machine for storage. Redundant reception by multiple stations can help to minimize data losses. The design of the radiosonde electronics, environmental chamber testing, and initial field performance are detailed in a previous our recent work by Paredes Quintanilla et al. [40].

4.1.1 The radiosonde network architecture

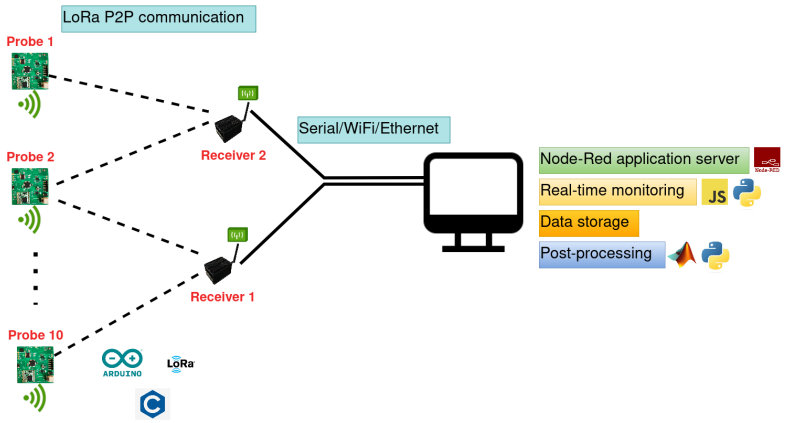

Figure 4.2: Radiosonde network architecture. For clarity, this diagram depicts only the transmitter components of the radiosondes. In actual operation, each radiosonde comprises a biodegradable balloon carrying an electronic board (radioprobe).

The radiosonde network leverages a LoRa-based wireless sensor network (WSN) architecture, specifically employing a star network topology (see Figure 4.2). In this configuration, each radiosonde acts as a leaf node, communicating directly with a central ground receiver station, forming a point-to-point link. This contrasts with other WSN architectures, such as:

- *Mesh networks*: Nodes can relay data for other nodes, creating a multi-hop communication path. This can be advantageous for wider coverage areas but may increase complexity and latency.
- *Clustered networks*: Nodes are grouped into clusters, each with a designated cluster head that relays data to a central node. This offers scalability but introduces additional management overhead and power consumption of the cluster head.

The selection of the star network topology is justified by several factors. The star network's simplicity makes it straightforward to implement and maintain, well-suited

for this research project. Additionally, point-to-point links ensure reliable data transmission with low latency, crucial for capturing real-time atmospheric fluctuations. Finally, direct communication with the nearby ground station allows radiosondes to operate in low-power mode, extending operational lifetime.

However, the star network also has limitations. The ground station is a single point of failure, disrupting communication if it malfunctions. Furthermore, the maximum communication distance is primarily determined by the ground station's transmission power and the surrounding environment.

Previous research has explored the applicability of this star network architecture in diverse scenarios, demonstrating its feasibility for various WSN applications [145, 146, 143]. Initial field tests conducted within the current context were also presented by Paredes Quintanilla et al. [40].

Unlike typical LoRa-based WSNs that rely on the LoRaWAN infrastructure, this application establishes an ad-hoc private network to fulfill its specific requirements. This is achieved using the RFM95 transceiver module from HopeRF [147]. Based on the Semtech SX1276 chip, the RFM95 module enables reliable data transmission over long distances with high immunity to interference. Additionally, its optimized power usage is crucial for maximizing the operational life of the battery-powered radiosondes.

The RFM95 module supports power transmission ranges from 5 dBm (3.16 mW) to 20 dBm (100 mW). However, European regulations set by the European Telecommunications Standards Institute (ETSI) limit the maximum power to 14 dBm (25.12 mW) [148]. Both ground stations and radiosondes are equipped with the RFM95 module, facilitating seamless communication within the star network architecture [40].

4.1.2 Radioprobes

During the system's development, I was involved from the prototyping phase, which was initially based on the Arduino Pro Mini board. Before designing the Printed Circuit Board (PCB), a conceptual prototype of the radioprobe was created and tested using the Arduino framework. This involved using an Arduino Pro Mini board featuring the **ATmega328** microcontroller chip by Microchip [149], along with individual sensor evaluation boards. After validating the prototype, the ATmega328 microcontroller was integrated into the first version of the radioprobe's PCB. The PCB hardware design, which included two complex chip antennas for the GNSS sensor and LoRa transmitter, was completed by my colleague Miryam Paredes [150]. I was responsible for firmware development and data post-processing during design and testing. Later, I also contributed to developing a new ground station.

The assembled radiosonde (Figure 4.3(a)) consists of a biodegradable balloon carrying a radioprobe electronic board (Figure 4.3(b)). Filled with helium, the balloon allows the radiosonde to remain airborne for several hours while the battery-powered radioprobe transmits sensor measurements.

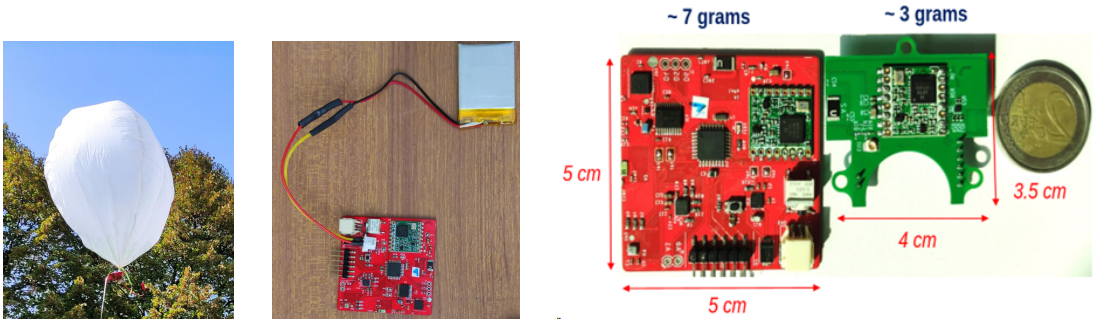

(a) (b) (c)

Figure 4.3: (a) Radiosonde attached to the ground with a thread during an in-field test. (b) The current version of the radioprobe electronic board with a battery. (c) The current prototype (red) is presented together with a prospective smaller two-layer design (green) and a two-euro coin for size comparison.

The radioprobe's embedded electronics measure various environmental factors, including velocity, acceleration, pressure, temperature, and humidity fluctuations. Figure 4.3(c) depicts both the current prototype (red) and a smaller, two-layer prospective design (green). This work focuses on the current prototype. Its electronic board integrates essential components: (Figure 4.4):

- *Microcontroller*: Processes and controls other components, acquires sensor readings, and automates device functions.
- *Radio Transmission Module (LoRa)*: Enables one-way wireless communication with ground stations using radio signals.
- *PHT (Pressure, Humidity, and Temperature) Module*: Measures these essential atmospheric parameters.
- *Positioning unit* comprising GNSS and IMU sensors: Provides position, velocity, and time (PVT) data. Moreover, it measures 3 components of acceleration, angular velocity and magnetic field readings in inertial reference frame.
- *Power Module*: Manages power distribution to the board's components.
- *Ceramic chip antennas*: Facilitate communication for the GNSS sensor and radio transmission module.

Sensor selection

Sensors were selected for their compact size and low power consumption, and they are configured to operate in energy-efficient modes whenever possible. For instance, the U-blox GNSS sensor employs a "Super-E mode" to minimize power usage [152]. While other studies may use higher-precision GNSS sensors [137], these options typically consume more power, which is critical in our application. Additionally, the current GNSS

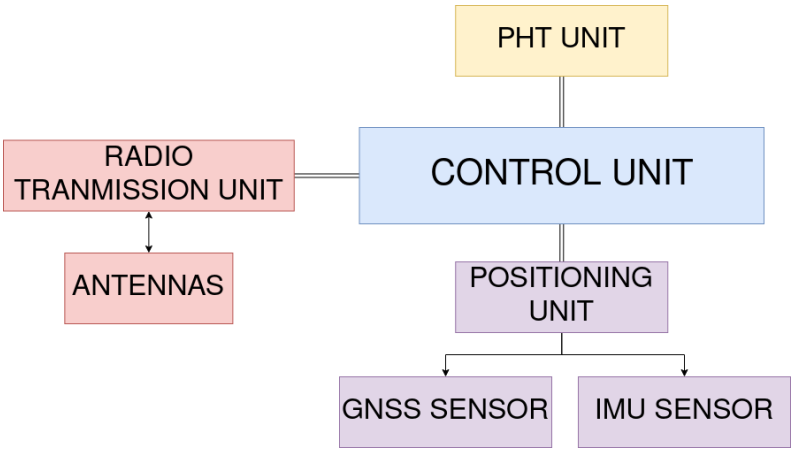

Figure 4.4: Radioprobe building blocks.

Table 4.1: Sensor specifications. This table lists the physical quantities measured during the experiments. It includes the measurement ranges, accuracies as specified in the sensor datasheets, and the corresponding sensor component names. Note that in the "Acceleration" row, "g" represents the standard gravity acceleration of 9.81 m/s^2.

Physical quantity	Range	Declared accuracies	Device Name
Pressure	[300, 1100] mbar	± 1 hPa	Bosch BME280 [151]
Humidity	[0, 100] %	± 3 %	
Temperature	[-40, 85] ˚C	± 1-1.5 ˚C	
Longitude	[-180, 180] degrees	Horizontal accuracy = ±3.5m	UBLOX ZOE-M8B [152]
Latitude	[-90, 90] degrees		
Altitude	< 50000 m	± 7.0 m	
Speed	< 500 m/s	± 0.4 m/s	
Acceleration	[-16, 16] g	± 90 mg	STM LSM9DS1 [153]
Magnetic field	[-16, 16] gauss	± 1 gauss	

sensor uses the proprietary UBX-PVT protocol [154], which provides compact PVT information in a single reading, eliminating the need for multiple NMEA (National Marine Electronics Association) packets [155]. Sensor devices, their operating ranges and measured physical quantities are reported in Table 4.1

The current radioprobe electronic board costs around 90 USD per unit for an order of 20 pieces. This cost decreases to 57 USD and 54 USD per unit for orders of 1,000 and 10,000 pieces, respectively. The unit cost encompasses sensors, PCB substrate, assembly, battery, and other components. Compared to commercially available radiosondes for sounding experiments, this design offers lower cost together with compact and

lightweight design. Estimated at 90 USD per unit (order of 20), compared to 155 USD (low altitude radiosonde) and 200 USD (high altitude radiosonde) [156, 157].

The green design in Figure 4.3(c) represents a potential future direction, aiming for further miniaturization and potentially lower costs.

4.1.3 Isopycnic floating and biodegradable balloon

During experiments, the radiosonde system needed to maintain a nearly constant altitude. To achieve this, non-elastic, biodegradable balloons made from Mater-Bi were designed and used. This material retains its quasi-spherical shape without expanding, ensuring consistent float altitude [42, 27].

Traditional meteorological balloons often use materials like rubber and polyethylene. However, this project prioritizes biodegradable options and utilizes **Mater-Bi** to provide a fixed volume for flight within isopycnic layers (constant density layer) inside clouds and the ABL.

Furthermore, the use of biodegradable materials for both balloons and potentially the electronic boards minimizes the environmental impact of the radiosonde system. Basso et al. [42] compared Mater-Bi and other green polymers like PLA with conventional balloon materials such as latex and mylar as part of the COMPLETE project. The study, conducted in collaboration with IIT (Italian Institute of Technology) Genoa, evaluated properties such as tensile strength, hydrophobicity, helium permeability, and resistance to environmental factors like temperature and humidity. Mater-Bi, when coated with a mixture of carnauba wax, pine resin, and acetone, or hydrophobic nano-silica and dimethyl silicone oil, was found to be the most suitable material, meeting all required specifications.

In recent field experiments, we utilized spherical balloons (20 cm radius, R_b) made from commercially available 20 μm thick Mater-Bi bags, with a density of 1.24 g/cm^3. This material is thinner than the 30 μm used in Basso et al. [42], resulting in a 1.5 times lighter balloon and a reduced overall payload (see Eq. 4.1). Balloon dimensions were chosen considering the weight of the radiosonde electronics, battery, and standard atmospheric parameters at the target floating altitude (Table 4.2). The volume required for stable floating at a fixed altitude is given by:

$$V_b = \frac{m_r + m_b}{\rho_a - \rho_g} = \frac{m_r + m_b}{\rho_a(1 - M_g/M_a)}, \tag{4.1}$$

where:

- Subscripts b, r, a, and g refer to balloon, radioprobe, air, and gas (helium), respectively.
- m_r denotes the mass of the radioprobe with battery and connections.
- m_b is the mass of the balloon.
- ρ_a and ρ_g are air and gas densities at a given altitude.

- M_a and M_g represent the molar masses of air and gas inside the balloon.
- $V_b = 4/3\pi R_b^3$ is the volume of the balloon, and
- $m_b = S\Delta\rho_m = 4\pi R_b^2\ \Delta\ \rho_m$, where S is the surface area of the balloon with radius R_b, while Δ and ρ_m refer to the sheet thickness and density of the Mater-Bi material.

Table 4.2: Standard atmospheric parameters for the potential operating altitude range of the radiosonde [158]. The table presents altitude (height above sea level), temperature (T), pressure (P), and air density (ρ_a).

Altitude [m]	T [K]	P [hPa]	ρ_a [kg/m^3]
0	288	1013	1.22
500	285	950	1.17
1000	282	900	1.11
1500	278	850	1.06
2000	275	795	1.01
2500	272	748	0.95
3000	269	701	0.90

Figure 4.5 illustrates the relationship between attainable altitude and balloon radius. With the current radioprobe weight of 17.5 g (Table 4.3), a 20 cm radius balloon can reach approximately 1700 m above sea level, while a 21 cm radius balloon can reach around 2600 m.

Table 4.3: Radiosonde Payload Distribution. The weight of the balloon, calculated for a spherical balloon with the specified radius (in brackets), is included.

Part	Mass [grams]
Radioprobe	7
Battery	8
Connections	2.5
Balloon	12.5 (R=20 cm)
Total	30

While the balloon reaches an equilibrium level, factors like neutral buoyancy oscillation, gravity waves, and turbulence can cause instability. The Brunt-Vaisala period provides an estimate of the natural oscillation period of the balloon system [45]. These considerations will be revisited during the analysis of fluctuations discussed in Chapter 5.

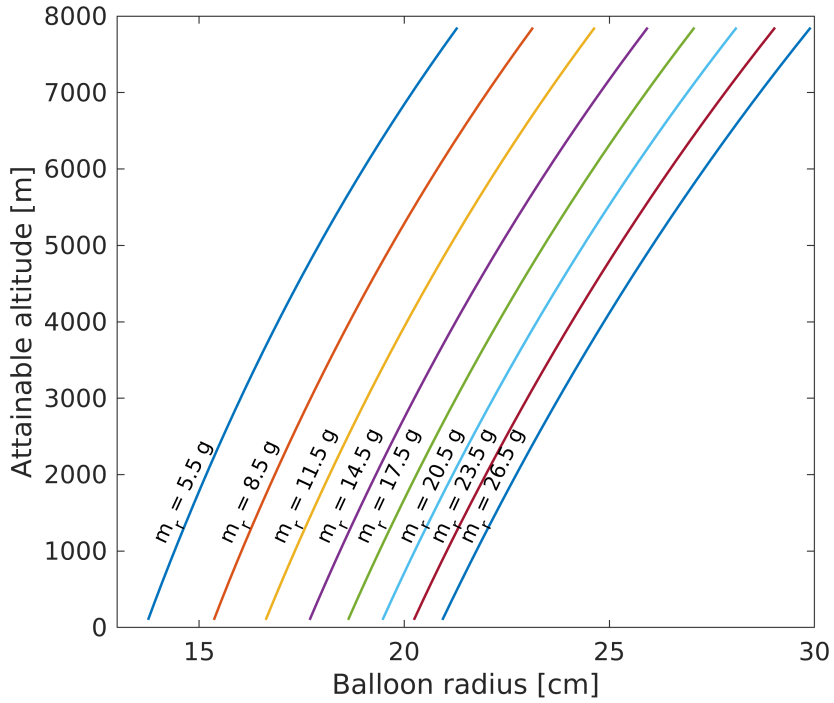

Figure 4.5: the relationship between attainable altitude and balloon radius, considering the selected material properties and helium gas. The current design utilizes biodegradable Mater-Bi (Novamont) with a density of 1.24 g/cm^3 and a thickness of 20 μm. The solid lines represent different possible radiosonde weights (radioprobe, battery, and connections) ranging from 5.5 g to 26.5 g. The green line corresponds to the current prototype weight of 17.5 g, with a detailed breakdown provided in Table 4.3.

4.1.4 Ground station

Figure 4.6 illustrates the main components of the ground station used for data reception from the radiosondes. During the experiments, we utilized various ground stations, primarily employing point-to-point LoRa receivers. Two commonly used models were the **Adafruit Feather 32u4**[159] and the **Dragino LG01v2**[160].

The Adafruit Feather 32u4 LoRa Radio (RFM9x), nicknamed "RadioFruit," is a microcontroller board with a built-in LoRa transceiver for long-range, low-data-rate communication. It features an 868/915 MHz radio module and supports USB and battery charging. The Dragino LG01v2 is an open-source, single-channel LoRa gateway. It bridges a LoRa wireless network to an IP network via Wi-Fi, Ethernet, or an optional 4G cellular module. This design allows users to send data over long distances at low data rates using the LoRa protocol. In contrast to LoRaWAN, the LG01v2 is specifically designed for peer-to-peer (P2P) LoRa communication, minimizing deployment costs for private P2P networks by utilizing a single-channel LoRa module.

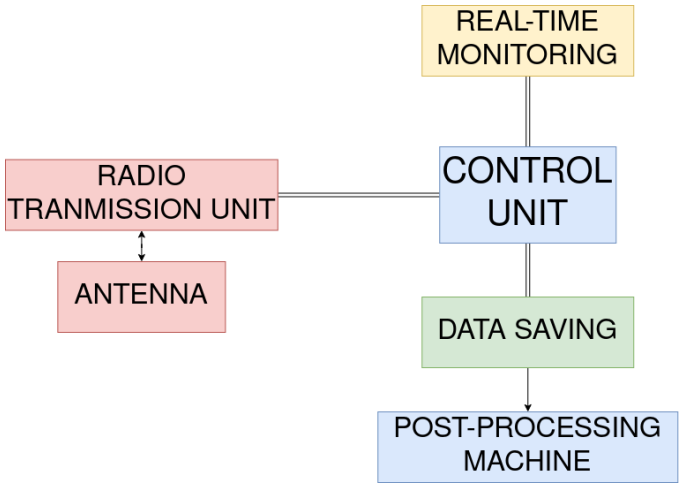

Figure 4.6: Logical building blocks of the ground station.

4.1.5 Data processing

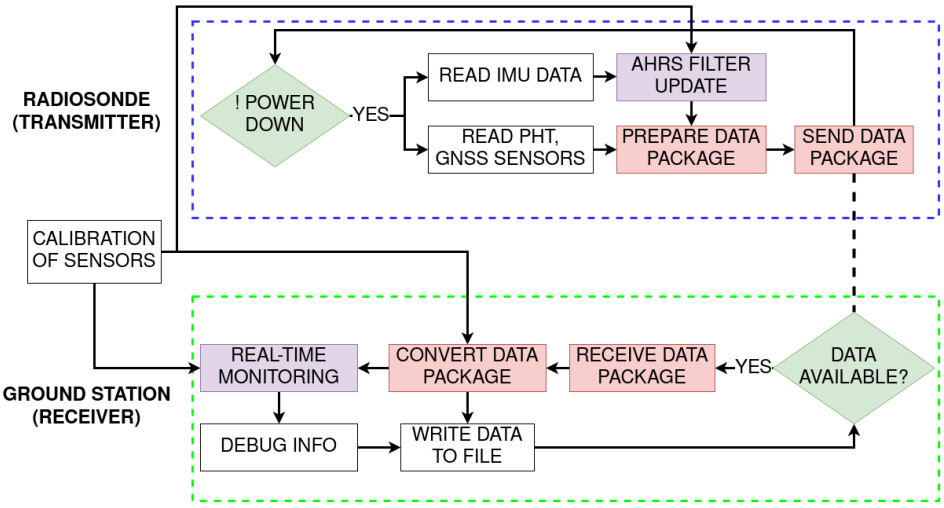

Figure 4.7: The data processing flow of the radiosonde network is shown as the communication between a single radiosonde (dashed blue rectangle) and a ground station (dashed green rectangle). Calibration values of the sensors were used for both the radiosonde and the ground station. Specific pre-launch calibrations were carried out to identify the possible bias offset values of the accelerometer, the magnetometer and the pressure humidity and temperature MEMS (Micro-electromechanical systems) sensors.

Figure 4.7 outlines the data processing flow of the radiosonde system, encompassing both onboard (transmitter) and ground station (receiver) functions. To optimize efficiency, processing is divided strategically. The radioprobe performs preliminary

processing, while computationally intensive tasks are handled by the ground station with the aid of a post-processing machine.

As illustrated in Figure 4.7, the radioprobe's Attitude and Heading Reference System (AHRS) filter processes sensor data before transmission. The AHRS filter utilizes data from a 9-DOF IMU sensor (accelerometers, gyroscopes, and magnetometers) to determine the radioprobe's orientation (course). It also incorporates sensor calibration data [161] to minimize potential sensor reading errors.

IMU sensor readings, initially provided in the sensor's body frame (xyz), are transformed into the local experiment frame (X_e, Y_e, Z_e) using the AHRS filter's orientation data. This allows for consistent interpretation and analysis of the data. Furthermore, the local frame acceleration data can be used for positioning during GNSS outages. This is achieved by integrating the acceleration data with GNSS data using a Kalman filter, which operates in "predict" and "update" modes [162]. During prediction, IMU data provides relative position information based on the previous reference position. When GNSS data becomes available, the reference position is updated. This approach enables position estimation even when GNSS is unavailable, potentially reducing overall power consumption as the GNSS sensor draws significantly more power than other sensors.

Real-time monitoring and data saving are crucial aspects of the data processing flow. The Linux-powered Dragino LG01v2 offers local storage capabilities, while the Adafruit Feather 32u4 requires a separate post-processing machine (e.g., laptop or PC) to operate.

4.2 Metrological traceability

The validation process for the mini-radiosondes prioritizes a robust metrological foundation. This foundation ensures that readings from the radiosondes are comparable and establishes a link to absolute values of measured quantities, such as temperature and humidity. INRIM was involved in this validation process because of its well-established expertise in the metrology of meteorology and the climate [163, 164] and because of its previous experiments on radiosondes [165, 166]. The preliminary calibration and characterization of the sensors were performed through climate chamber experiments in INRIM's Applied Thermodynamics Laboratory. During the tests, selected low-cost MEMS sensor, BME280 [151] was evaluated with respect to reference sensors by INRIM, such as platinum resistance thermometers (PT100), and a Delta Ohm humidity probe.

Well-defined in-field test procedures were established before launching balloons equipped with the radiosondes. These procedures could involve *tethered* balloons for controlled testing or *free-flying* balloons for in-situ data collection. The first stage of experiments took place at the INRIM campus. Radiosonde sensor readings were compared with reference sensors (Vaisala WXT510) previously calibrated at the INRIM laboratory. These procedures also helped identify the most suitable radiosonde layout configuration (refer to Figure 4.9) by quantifying sensor accuracy against the reference sensors.

A portable system was assembled to act as an on-site calibration device for pre-launch checks during the in-field experiment with a cluster of free-floating radiosondes (OAVdA, St. Barthelemy, Italy, November 3, 2022). This system included a PT100 CalPower platinum resistance thermometer (calibrated at INRIM) as a reference sensor housed within a Barani helical passive solar shield. An additional unshielded PRT sensor was used to replicate real-world solar radiation conditions and estimate its influence. A Fluke DAQ 1586A multimeter acquired resistance data and calculated corrected temperature values using a calibration curve. An appropriate launch zone location, free from obstacles, was chosen for pre-launch radiosonde checks.

Mini-radiosondes were compared against INRIM facility measurements during the in-field experiment. This involved coupling them to the system in an open area for 10 minutes before launch. Sensor readings were collected to assess comparability (ΔT_{rel}, difference between the mean temperature and individual radiosonde readings) and accuracy (ΔT_{abs}, difference between mini-radiosonde readings and reference sensor readings). This procedure allowed for evaluating both the spread in readings between radiosondes and calculating the pre-launch correction (ΔT).

In addition to calibration and pre-launch tests, dual-sounding experiments were conducted to quantify uncertainties in radiosonde sensor measurements. Temperature, humidity, pressure, and positioning data were compared with reference radiosondes during three experiments between October 2020 and July 2023 (see Section 4.3.3 for results and discussion). Mean differences ($< T - T_{ref} >$) and normalized mean differences relative to the reference sensor readings ($< (T - T_{ref})/T_{ref} >$) were examined for temperature measurements across various altitudes and experiment sites.

The sensor accuracy values initially reported in Table 4.1 were based on manufacturer datasheets and considered preliminary. These values were revisited based on the observed accuracies obtained from the comparison tests. The actual performance of the radiosonde sensors is presented in Sections 4.3.1, 4.3.3 and 5.1.

4.3 Validation of the measurement system

Validation tests carried out starting from the initial conceptual prototype development. The preliminary results were presented in the works of Basso et al. [42] and Paredes Quintanilla et al. [40], together with the electronic design of the first prototype. However, not all the components of the measurement system were fully field-tested or confirmed in the earlier works. Furthermore, some post-processing techniques can only be used after appropriate in-field tests have been conducted. In the recent publication by our group, we highlighted the main results from validation tests starting from the experiments fixed point measurements to field experiments with multiple tethered balloons (see Abdunabiev et al. [7]). In this section, validation test results are revisited, where the proposed measuring system is compared and validated relative to established measurement methods and instrumentation during climate chamber tests, fixed point

measurements at the ground level and vertical profiling observations of the atmosphere. Table 4.4 gives a list of field experiments carried out during the development of the radiosonde cluster system.

Table 4.4: In-field measurement campaigns during the development of the radiosonde cluster and measurement system.

Date	Description	Place	Coverage
Oct 28, 2020 June 9, 2021	Two dual launch experiments with Vaisala RS-41 SG probe in collaboration with ARPA-Piemonte	Levaldigi Airport, Cuneo, Italy	Vertical atmospheric profiling, up to 14 km in distance and 9 km in altitude.
July 20, 2021	Radiosonde configuration testing; 2 configurations	INRIM, Turin, Italy	short-range, controlled setup, up to 100 m.
Sep 29, 2021	Testing the cluster of tethered radiosondes (5 sondes)		
Feb 10, 2022	-Testing the cluster of tethered radiosondes (5 sondes) in approximately operational environment; -Radiosonde balloon tracking with stereo vision analysis.	OAVdA, St. Barthelemy, Aosta, Italy	short-range, controlled setup, up to 100 - 150 m.
July 6, 2023	Dual launch experiment with Vaisala RS-41 SGP probe in collaboration with MET OFFICE (UK)	Chilbolton Observatory, Chilbolton, UK	long-range, vertical profiling, up to 34 km horizontally within 100 – 12000m altitude range during the ascent

4.3.1 Climate chamber tests

Temperature and humidity sensor calibration and validation were conducted at the Applied Thermodynamics Laboratory of the INRiM using a climatic chamber specifically designed for meteorological and climate metrology (Kambic KK190 CHLT) [163]. The chamber allows for precise temperature control (-40 ^{o}C to 180 ^{o}C) and relative humidity control (10% to 98% RH). Reference temperature values were obtained from four platinum resistance thermometers (Pt100) calibrated by INRiM and placed within the chamber. These Pt100 readings were acquired using a high-precision Fluke 1594a Super-Thermometer.

Similarly, reference humidity values were obtained using a Delta Ohm humidity and temperature probe calibrated at INRiM, connected to an HD27.17TS datalogger. The Pt100 uncertainty ranges from 0.011 ^oC (positive temperatures) to 0.020 ^oC (negative temperatures), and the total uncertainty of the Delta Ohm probe is ±3% RH.

To assess both sensor accuracy and potential variations in sensor behavior, three radioprobe electronic boards were tested inside the chamber alongside the reference sensors. Temperature and relative humidity measurements from the BME280 sensor were extracted through microcontroller commands using the I2C communication interface at a 1 Hz sampling frequency.

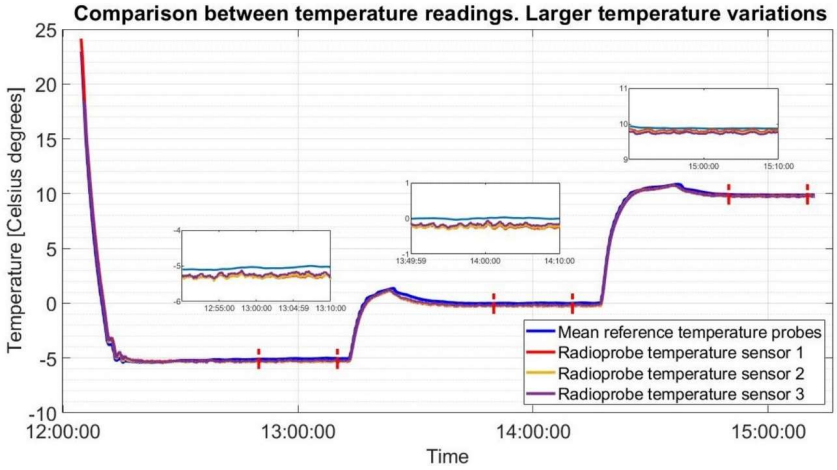

Figure 4.8: **Comparison of temperature measurements in climate chamber.** Readings are given for the three radioprobe sensors and reference sensor. The chamber temperature was varied from an initial state of T = +24 ^oC, RH = 30% to reach set points of T = −5 ^oC, T = 0 ^oC, and T = 10 ^oC. See Table 4.5 for details. Adopted from Figure 7 of Paredes Quintanilla et al. [40].

The initial climate chamber configuration was set to 20 ^oC temperature and 30% RH. Subsequently, controlled variations were introduced in temperature and humidity. The first test involved small, incremental temperature increases of 2 ^oC (maintaining 30% RH) until reaching 24 ^oC, with each step lasting approximately 30 minutes. Following this, the chamber was configured for larger temperature variations (starting from 24 ^oC and 30% RH) to reach -5 ^oC, 0 ^oC, and 10 ^oC. Each temperature step required about 1 hour to ensure system temperature stability, simulating the conditions radioprobes might encounter on-site (warm clouds typically have temperatures above 0 ^oC, but negative values were included to test sensor performance in extreme situations). The results of this second test are presented in Figure 4.8.

Analysis of the results revealed better temperature sensor response for positive values, with increased deviation and mean bias at sub-zero temperatures. However, this is considered acceptable within the context of the current radioprobe's application (warm clouds within the ABL).

Table 4.5: Statistical comparison of temperature measurements between radioprobe and INRiM reference sensors inside climate chamber. Values for mean temperature ($\overline{T}$), mean bias ($\overline{\Delta T}$) and standard deviation (σ_T) of readings are provided across three test configurations.

Config.	**Setup 1 −5.00 ^oC**			**Setup 2 0.00 ^oC**			**Setup 3 10.00 ^oC**		
Sensor	$\overline{T}[^oC]$	$\overline{\Delta T}[^oC]$	$\sigma_T\,[^oC]$	$\overline{T}[^oC]$	$\overline{\Delta T}[^oC]$	$\sigma_T\,[^oC]$	$\overline{T}[^oC]$	$\overline{\Delta T}[^oC]$	$\sigma_T\,[^oC]$
Probe 1	-5.31	0.25	0.04	-0.25	0.25	0.03	9.82	0.06	0.02
Probe 2	-5.30	0.24	0.04	-0.23	0.23	0.03	9.75	0.13	0.03
Probe 3	−5.25	0.18	0.04	-0.17	0.18	0.03	9.74	0.13	0.02
Reference probe	−5.063	-	-	0.002	-	-	9.878	-	-

Table 4.6: Statistical comparison of humidity measurements between radioprobe and INRiM reference sensors inside climate chamber. Values for mean humidity ($\overline{RH}$), mean bias ($\overline{\Delta RH}$) and standard deviation ($\sigma_R H$) of readings are provided across three test configurations.

Config.	**Setup 1 10 %**			**Setup 2 40 %**			**Setup 3 60 %**		
Sensor	$\overline{RH}[\%]$	$\overline{\Delta RH}[\%]$	$\sigma_{RH}[\%]$	$\overline{RH}[\%]$	$\overline{\Delta RH}[\%]$	$\sigma_{RH}[\%]$	$\overline{RH}[\%]$	$\overline{\Delta RH}[\%]$	$\sigma_{RH}[\%]$
Probe 1	13.12	2.62	0.01	35.31	2.37	0.10	56.13	3.57	0.07
Probe 2	14.74	4.24	0.02	35.64	2.04	0.12	54.53	5.17	0.05
Probe 3	14.16	3.66	0.02	36.06	1.62	0.12	55.69	4.01	0.04
Reference probe	10.50	-	-	37.68	-	-	59.70	-	-

The third test involved changing the relative humidity at a constant temperature of 30 ^oC, with steps from 10% RH to 40%, and 60%, each lasting approximately 30 minutes. For statistical comparison, the Makima interpolation technique (a one-dimensional interpolation algorithm) was applied, considering a stable 5-minute window of data at each set point.

The statistical results from the second and third tests are shown in Tables 4.5 and 4.6. This high-precision climatic chamber experiment with calibrated reference sensors allowed for the evaluation of radioprobe sensor performance. In most cases, the behavior of the radioprobe sensors fell within the manufacturer's specifications (temperature accuracy ± 1 ^oC and relative humidity ±3% RH). Minor deviations in relative humidity measurements might be attributed to uncertainties associated with the reference sensor itself (accuracy ±3% RH).

4.3.2 Fixed-point measurements: balloon-radioprobe configuration testing

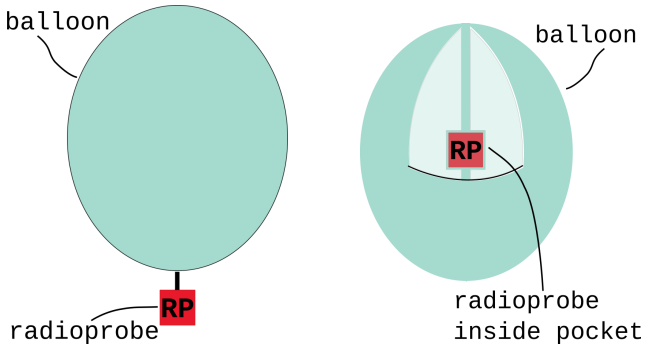

Figure 4.9: The radioprobe electronic board was tested in two different radiosonde configurations. (a) Configuration A: the radioprobe board is **outside** the balloon. (b) Configuration B: the radioprobe board is in a pocket **inside** the balloon.

Initial field tests aimed to evaluate different radiosonde (balloon-radioprobe) configurations and validate sensor measurements against a fixed-point ground station. Two configurations (shown in panels a and b of Figure 4.9) were assembled and tested near the Vaisala WXT510 station at the INRIM campus in Turin, Italy, on July 20th, 2021. Sensor readings from both configurations were analyzed to determine the optimal setup. Figure 4.10 compares pressure, humidity, and temperature data for both configurations. Measurements were taken before (panels a, c, and e) and after (panels b, d, and f) attaching the radioprobe electronic board to a balloon. The data is also compared with readings from the WXT510 station, known for its highly accurate and frequent (1-minute interval) pre-calibrated sensor outputs.

During the initial phase (11:10 to 11:20), the radiosonde sensors, particularly those measuring humidity and temperature, exhibited a typical MEMS sensor behavior: a short warm-up period due to a ”cold start,” requiring time to reach equilibrium with the WXT510 readings. This cold start issue is not explicitly addressed in the sensor datasheet, and it is assumed to be caused by two main factors: the sensor’s slow response time and its housing design. Slow adaptation to environmental conditions, coupled with sensor drift, may be exacerbated by insufficient airflow through the sensor’s vent hole, which is extremely small (mm size). To improve future designs, the sensor housing should be optimized to allow better airflow, and alternative sensing approaches should be considered, such as using a small wire dongle connected to the board that is freely exposed to ambient conditions without interference from surrounding electronics, allowing for more accurate humidity and temperature measurements.

Further validation confirmed that the BME280 MEMS sensor from BOSCH suffers from a slow response time. According to its datasheet (BME280 datasheet, page 9 [151]),

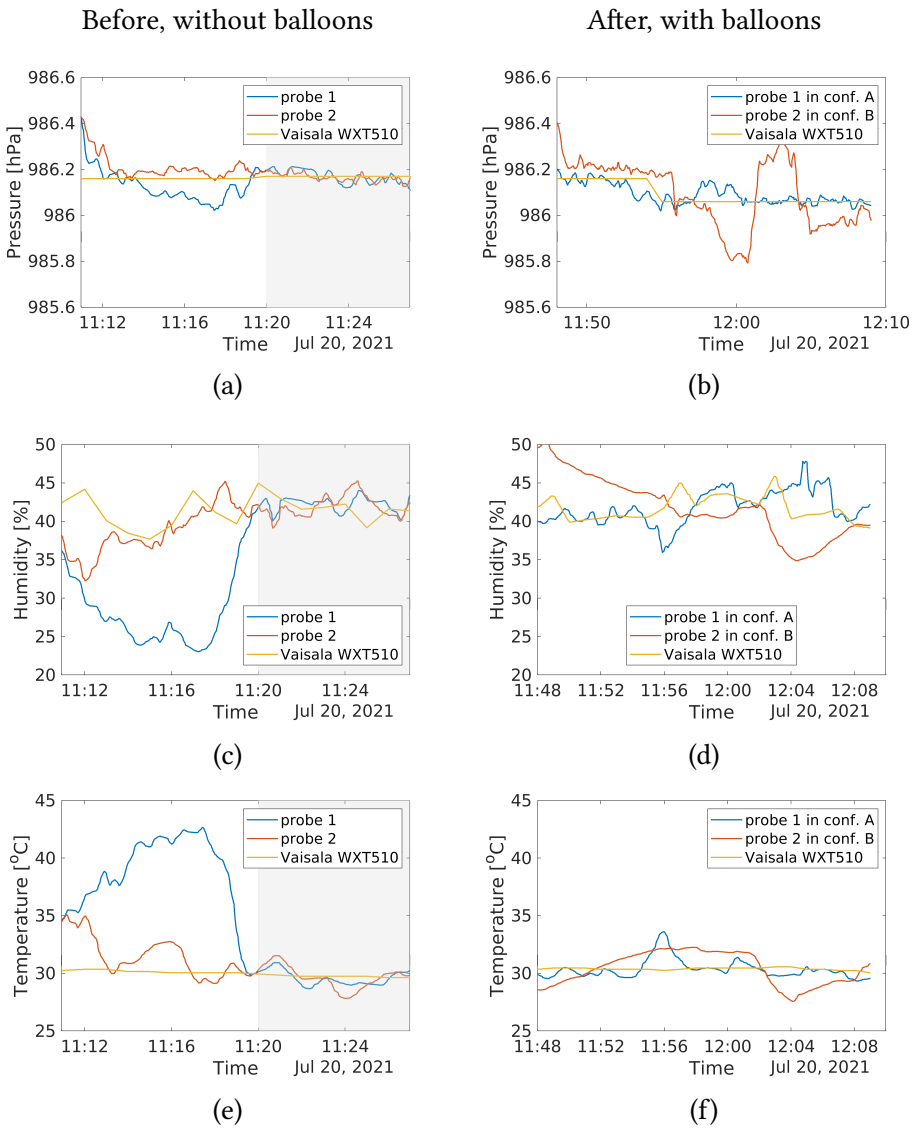

Figure 4.10: Comparison of radiosonde sensor readings (**configurations A & B**, refer to Figure 4.9 for details on configurations). **First Column** (a, c, e): Sensor readings on the ground (not attached to the balloon). The gray shaded regions highlight readings after the warm-up period for the radiosonde sensors. Note that the continuously operating WXT510 station (reference) does not exhibit a warm-up transient. **Second Column (b, d, f)**: Comparison of sensor readings after attaching the radiosonde to the balloon.

the sensor requires over one second to reach 63% of a step change, which is inadequate for effectively tracking rapid ambient fluctuations in real operational conditions. The accuracy of the humidity sensor readings will be further explored in the subsequent subsection on vertical profiling dual-launch experiments.

After attaching the electronic boards to the balloons, configuration B showed significant discrepancies from the reference station measurements (rightmost panels of Figure 4.10), whereas configuration A demonstrated better alignment, particularly in pressure and temperature readings. Minor fluctuations in temperature and humidity for configuration A could be attributed to the movement of the probes near the station. It is important to note that the gray-shaded areas in the left panels of Figure 4.10 represent the primary focus, as they exclude the sensor warm-up period. This initial phase is highlighted only to showcase the warm-up behavior, and in all subsequent experiments, the sensors were warmed up before the actual experiment or radiosonde launch to ensure accurate readings during free flight.

Although configuration B offered advantages in terms of floating dynamics and improved protection of the electronics (e.g., water resistance), its insulating effect resulted in significant biases in temperature and humidity readings. The delayed sensor response time ultimately led to the selection of configuration A for all subsequent field experiments.

4.3.3 Dual-sounding experiments

The first two dual-sounding experiments were conducted in collaboration with ARPA-Piemonte on October 28th, 2020 and June 9th, 2021, at Levaldigi Airport, Cuneo, Italy. The experiment site is equipped with an automatic sounding system that launches radiosondes twice daily for atmospheric profiling. The last dual-sounding experiment was conducted on July 6th, 2023, at Chilbolton Observatory, UK, within the Wessex Convection Campaign.

During the first experiment, interference issues were observed with the GNSS sensor when the radioprobe board was directly attached to the Vaisala RS41-SG probe. To address this, the radioprobe was attached with an 80 cm offset during the second launch.

This section primarily focuses on the results from the second experiment with ARPA-Piemonte. In the following figures, our radiosonde is referred to as ”COMPLETE” (H2020 project) for comparison with reference data.

Data transmission

The first experiment (October 28th, 2020) established the maximum transmission range of the radioprobe system in an open environment through radio propagation measurements. While the reference atmospheric sounding system is designed for vertical atmospheric profiling (troposphere and low stratosphere) rather than warm-cloud environments (1-2 km altitude), it provided a valuable reference for testing our system in a dynamic atmosphere free of obstacles. A summary of the results is presented in Table 4.7.

During the second experiment (June 9th, 2021), data transmission continued for

Table 4.7: Point-to-point packet transmission statistic from experiment at Levaldigi Airport, Cuneo, Italy on Oct 28, 2020. Distance is estimated from radio signal strength of the LoRa module.

Distance [m]	**SNR Mean [dB]**	**RSSI Mean [dBm]**	**Total Transmitted Packets**	**Number of Received Packets**	**Received Packets** [%]
Up to 1000	5	−95	40	37	92.5
Up to 2000	4	−99	103	98	95.2
Up to 3000	2	−102	156	146	93.6
Up to 4000	2	−103	210	196	93.3
Up to 5000	1	−104	243	226	93.0
Up to 6000	1	−104	276	240	87.0
Up to 7000	0	−105	297	259	87.2
Up to 8000	0	−105	322	283	87.9
Up to 9000	−1	−106	348	294	84.5
Up to 10,000	−1	−106	376	296	78.7
Up to 11,000	−1	−106	449	297	66.2
Up to 14,000	−1	−106	462	298	64.5

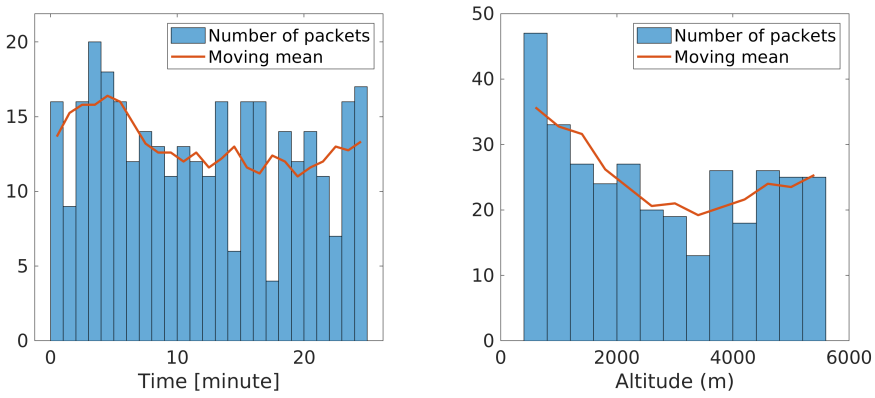

(a) (b)

Figure 4.11: **Radiosonde data transmission performance** from the radiosonde during a dual-sounding experiment conducted at Levaldigi Airport in collaboration with ARPA-Piemonte on June 9, 2021 [7, 40]. The packet size was approximately 100 bytes, and the experiment achieved a maximum transmission range of 12-13 km. **(a):** Average number of packets received per minute during the first 25 minutes of the launch.**(b):** Average number of packets received at different altitude levels (bin size = 400 meters). Red lines: Average transmission trends over time (a) and altitude (b).

approximately 1 hour as the radioprobe reached an altitude of nearly 9 km and a distance of 13 km. Figure 4.11 (panel a) shows the average number of received packets

per minute for the first 25 minutes of the launch. Panel b depicts the average number of packets received at different altitudes (between 400 m and 6000 m). The radioprobe transmitted packets at a rate of one per 3-4 seconds during the flight.

These results are promising and meet our target altitude range (1-3 km). While a transmission rate of 1 Hz was initially envisioned, achieving this is currently challenging due to computational limitations of the radioprobe and data packet size. Additionally, congestion in the receiver can introduce delays and packet losses.

The current prototype receiver station, based on the Adafruit Feather 32u4, is designed for direct P2P LoRa communication. A more powerful, multi-channel receiver station is being developed to address congestion and reduce receiver delays. This new design could receive data packets from 10-20 radiosondes simultaneously without packet collisions.

Post-processing techniques, such as re-sampling and filtering, can further reduce the impact of packet losses. The specific approach should consider the application context. In atmospheric measurements, factors like the atmospheric lapse rate, temperature gradient, and complementary sensor data (pressure and GNSS altitude; acceleration and GNSS velocity) can be combined to enhance the accuracy and completeness of the results.

Position and velocity measurements

Figure 4.12 compares GNSS sensor measurements from the radiosonde with those from the reference Vaisala RS41-SG radiosonde. Panel a and b show good agreement between the raw longitude, latitude, and altitude readings from both instruments.

- The inset plots in panel a provide magnified views of longitude and latitude for a smaller range.
- The inset plot in panel b highlights the altitude difference between the radiosondes ($\Delta Z = Z_{complete} - Z_{RS41}$).

The comparison yielded the following Root Mean Square Error (RMSE) and Mean Bias Error (MBE) values:

- Longitude : RMSE = 2.97e-4 and MBE = 2.95e-5 degrees.
- Latitude: RMSE = 3.7e-4 and MBE = -2.41e-4 degrees.
- Altitude: RMSE = 22.3 m and MBE = 11.05 m.

The longitude and latitude readings provided by ARPA-Piemonte exhibited lower resolution compared to our radiosonde data, affecting the calculation of RMSE and MBE. This is evident in the stair-like pattern observed in the reference readings of panel a (Figure 4.12). ARPA's data provided these coordinates accurate only to the 3rd decimal place, whereas our probe measured up to the 6th decimal place.

A UBX-PVT packet from the GNSS sensor provides north, east, and down velocity readings (Figure 4.13a). The horizontal wind speed was calculated from the north and east velocity components and compared with the RS41 probe's readings (Figure 4.13b).

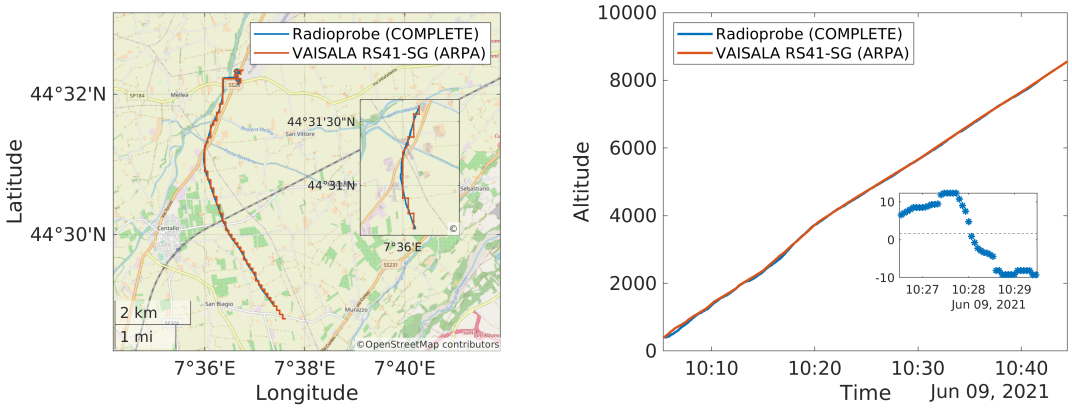

(a) (b)

Figure 4.12: Comparison GNSS positioning measurements from the COMPLETE radioprobe with the reference Vaisala RS41-SG probe during the dual-sounding experiment on June 9, 2021, at Levaldigi Airport, Cuneo, Italy. (a) Trajectories of the radiosondes on a map. Longitude: RMSE = 2.97e-4 and MBE = 2.95e-5 degrees, latitude: RMSE = 3.7e-4 and MBE = -2.41e-4 degrees. (b) Altitude readings from radiosondes over the time axis. In this case, RMSE = 22.3 m and MBE = 11.05 m. The inset plot highlights the altitude difference, $\Delta Z = Z_{complete} - Z_{RS41}$, between the COMPLETE and reference RS41-SG probes.

The wind speed data was further analyzed using FFT to obtain preliminary power spectra of the fluctuations. A 30-minute wind speed dataset with a 4-second time step was used for this analysis (Figure 4.13c). This resulted in a frequency range of 5 x 10^{-4} Hz to 0.25 Hz and a Nyquist frequency of 0.12 Hz (π/4 rad/s).

Similar FFT analysis can be performed on vertical velocity and temperature datasets. Analyzing the power spectra of vertical velocity can help identify the Brunt-Vaisala frequency cutoff point. Additionally, the vertical temperature profile (Figure 4.14c) can be used to derive a complete altitude profile of the Brunt-Vaisala frequency [167, 168].

Pressure, humidity and temperature measurements

Sensor data comparisons between the COMPLETE radiosonde and the reference RS41-SG probe are shown in Figure 4.14.

- **Pressure**: Good agreement was observed between the pressure readings from both instruments.
- **Temperature**: The COMPLETE probe readings aligned well with the reference data below 4000 meters of altitude. Above this point, a near-linear deviation trend emerged.
- **Humidity**: The BME280 MEMS sensor on the COMPLETE probe underestimated

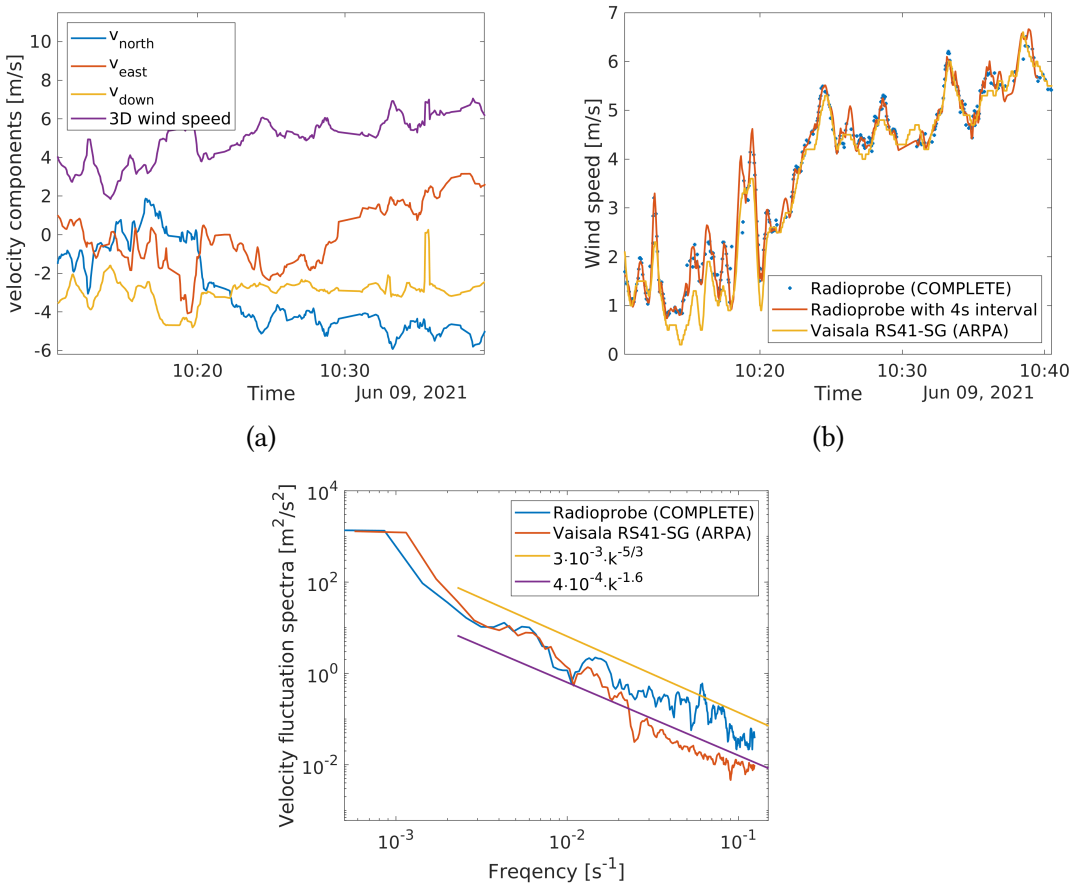

Figure 4.13: Velocity measurements of the radioprobe during the dual-sounding experiment on June 9, 2021, at Levaldigi Airport, Cuneo, Italy. (a) 3D wind speed components and magnitude derived from GNSS. (b) Comparison of horizontal wind speed with RS41-SG probe (raw and resampled data for COMPLETE radioprobe shown). (c) Power spectrum comparison of wind speed fluctuations (Nyquist frequency reference lines included), denoted as $f_s/2 = 0.125s^{-1}$. Alongside the raw spectrum dataset, two trend lines (in yellow and violet) are presented for reference.

readings in high relative humidity ranges (65-85%) and overestimated them in lower ranges (20-40%). However, it effectively captured the variation trend and tracked humidity fluctuations (Figure 4.14d). As expected, the magnitude of the COMPLETE probe's humidity fluctuation spectra was lower than the reference data (Figure 4.14d).

Our radiosonde network primarily targets an operational altitude range of surface to 2500 meters, with occasional extensions up to 3000-4000 meters. Temperature data from dual-launch experiments was compared with reference radiosondes across an altitude range of 400 to 3600 meters. The analysis divided the altitude into 400-meter intervals

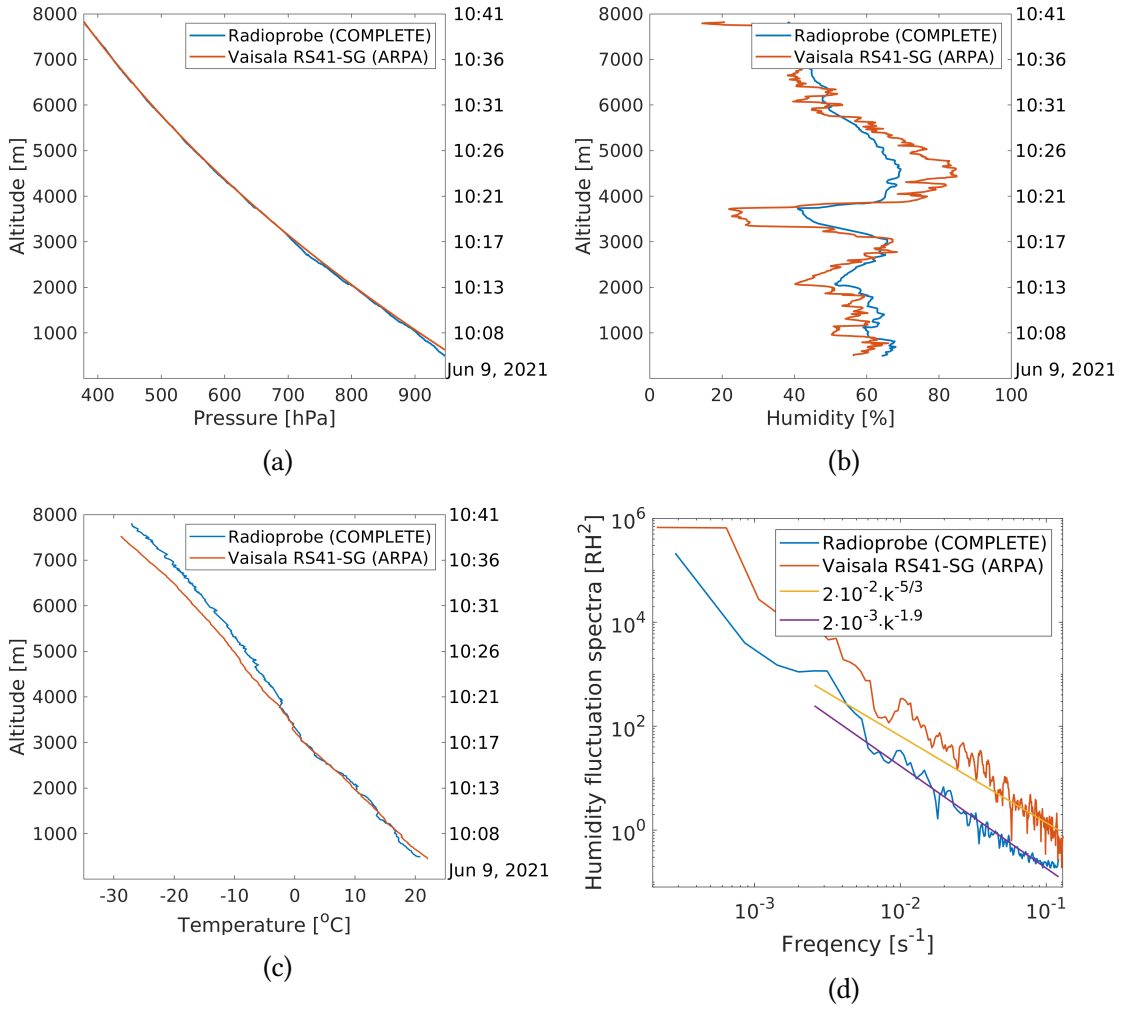

Figure 4.14: Pressure, humidity, and temperature readings from radiosondes during the dual-sounding experiment on June 9, 2021, at Levaldigi Airport, Cuneo, Italy. (a), (b), (c): Pressure, humidity, and temperature comparisons. (d) Humidity fluctuation spectra comparison. Two trend lines (yellow and violet) are provided for comparison purposes.

and calculated the mean and normalized mean temperature differences relative to the reference data for each segment. Table 4.8 summarizes the comparative analysis for three dual-sounding experiments.

As previously noted, temperature readings exhibited linear drift at higher altitudes, above the ABL. This trend was analyzed using data from all three dual-sounding tests. In the absence of an inversion cap (ARPA-2021), the linear deviation began above 4000 meters. When an inversion cap was present (ARPA-2020 and MET-OFFICE-2023), the deviation started at lower altitudes, around 3000 meters.

Figure 4.15 presents the raw and compensated data using the ground fixed-point

Table 4.8: Comparative analysis of temperature measurements across the altitude ranges with respect to the reference radiosonde data in dual-launch experiments conducted from October 2020 to July 2023. The table includes mean differences (<T-T_{ref} >), normalized mean differences relative to the reference sensor readings (<T-T_{ref}/T_{ref} >) and the temperature measurement range (T_{ref}) for each experiment site.

Altitude interval	**Experiment sites**								
	ARPA-2020, Levaldigi, Italy(Ref: Vaisala RS41-SG; Oct 28, at 12:05, local CET time; mild wind, clear-sunny day), COMPLETE probe fastened to the Vaisala sonde case			ARPA-2021, Levaldigi, Italy (Ref: Vaisala RS41-SG; June 9, at 12:05, local CET time; mild wind, clear-sunny day), COMPLETE probe hanged with a 0.8m long wire to the Vaisala sonde case			MET-OFFICE-2023, Chilbolton, UK(Ref: Vaisala RS41-SGP; July 6, at 09:04, local UK time; strong wind, partially cloudy, partially rainy), COMPLETE probe fastened to the RS41-SGP sonde case		
	Temp. Range (T_{ref})	<T-T_{ref} >	<T-T_{ref}/T_{ref} >	Temp. Range (T_{ref})	<T-T_{ref} >	<T-T_{ref}/T_{ref} >	Temp. Range (T_{ref})	<T-T_{ref} >	<T-T_{ref}/T_{ref} >
400 – 800 m	282.4 ÷ 284.0 K	0.14 K	0.05 %	291.9 ÷ 295.0 K	-1.26 K	-0.4 %	283.1 ÷ 285.3 K	-0.25 K	-0.08 %
800 – 1200 m	280.5 ÷ 282.2 K	-0.16 K	-0.06 %	288.7 ÷ 291.9 K	-0.57 K	-0.19 %	279.5 ÷ 283.1 K	0.20 K	0.07 %
1200 –1600 m	279.9 ÷ 282.4 K	-0.24 K	-0.08 %	286.1 ÷ 288.7 K	-0.36 K	-0.13 %	275.8 ÷ 279.5 K	0.20 K	0.07 %
1600 – 2000 m	280.9 ÷ 283.2 K	-0.62 K	-0.21 %	282.9 ÷ 286.1 K	0.27 K	0.09 %	272.5 ÷ 275.8 K	0.58 K	0.21 %
2000 – 2400 m	277.6 ÷ 280.7 K	0.78 K	0.28 %	279.5 ÷ 282.9 K	+0.49 K	0.17 %	272.5 ÷ 276.9 K	0.69 K	0.25 %
2400 – 2800 m	275.0 ÷ 277.4 K	1.40 K	0.51 %	276.1 ÷ 279.5 K	-0.37 K	-0.13 %	274.6 ÷ 276.9 K	1.53 K	0.56 %
2800 – 3200 m	273.6 ÷ 275.0 K	1.11 K	0.41 %	273.5 ÷ 276.1 K	0.03 K	0.01 %	271.5 ÷ 274.6 K	2.81 K	1.03 %
3200 – 3600 m	270.3 ÷ 273.5 K	1.29 K	0.47 %	271.9 ÷ 273.5 K	-0.06 K	-0.02 %	269.3 ÷ 271.5 K	3.31 K	1.22 %

bias obtained from Vaisala weather stations at each launch location. The legends in the rightmost panels illustrate the linear scaling of the temperature measurement drift at altitudes beyond empirically observed thresholds, which are still above the intended operational range of the mini radiosonde cluster.

The observed temperature drift above the ABL is likely, at least partially, caused by solar irradiance. The reference RS-41SG radiosondes include compensation for this effect, as reported by Vaisala [50]. Currently, the mini-radiosondes do not implement any correction for radiation on the sensing element. Future studies within an upper-air simulator (UAS) can determine the link between the observed deviation trends and solar irradiance, allowing for proper corrections (as done by Lee et al. [169]). Analysis of a radiation effect during a pre-launch test with a radiosonde cluster at OAVdA, Saint-Barthelemy, Italy (February 10, 2022) is presented in Chapter 5.

Accuracy of humidity measurements

Figure 4.14 highlights biases in the radiosonde's humidity readings compared to the reference Vaisala RS-41 probe during launch. These biases, particularly evident on sunny days, are likely caused by heating and radiation effects.
The sensor datasheet emphasizes proper airflow design to ensure adequate air exchange

Chilbolton, UK. July 6th, 2023. COMPLETE probe was directly attached to Vaisala RS-41 SGP probe, **possible heating**

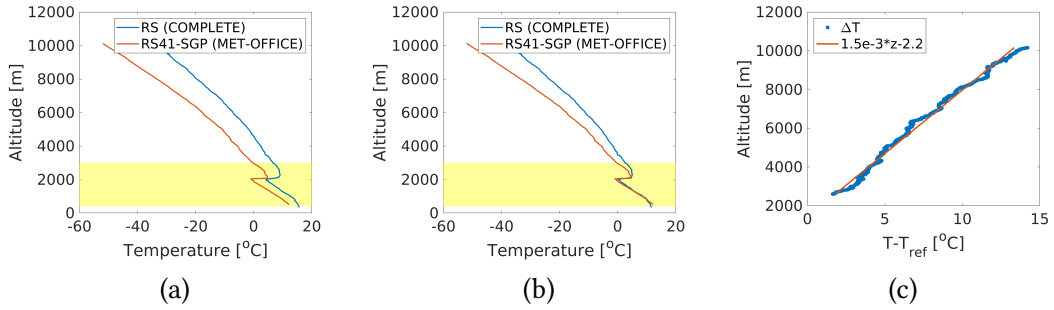

Levaldigi Airport, Cuneo, Italy. June 9th, 2021. COMPLETE probe detached from Vaisala RS41-SG probe with a 80-cm long thread. **No heating**.

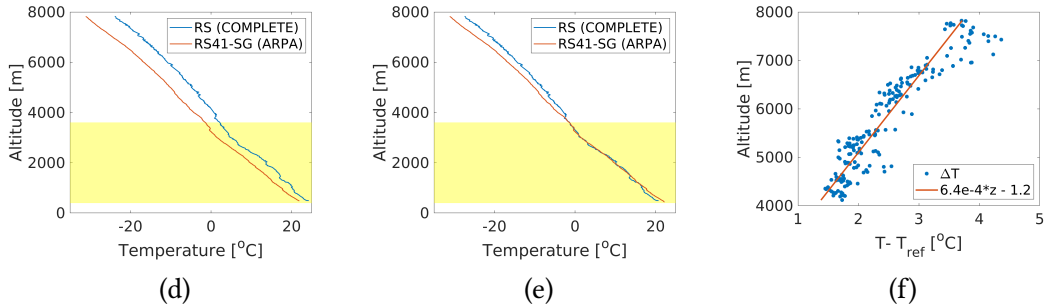

Levaldigi Airport, Cuneo, Italy. October 28th, 2020. COMPLETE probe was directly attached to Vaisala RS-41 SG probe, **possible heating**.

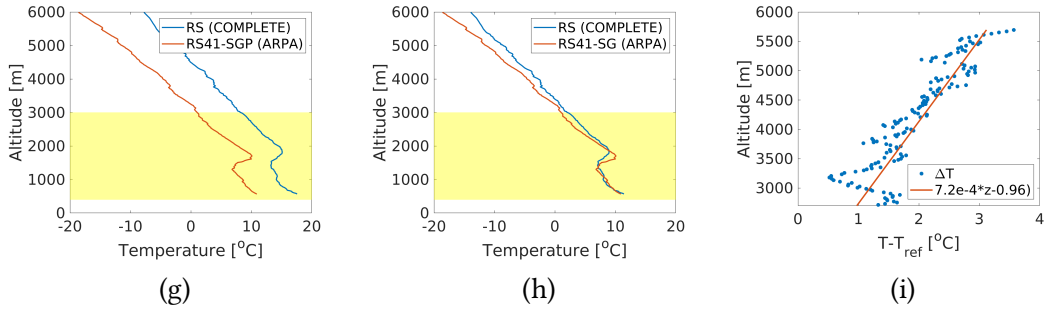

Figure 4.15: Comparison of temperature measurements from COMPLETE radiosonde with reference Vaisala RS41-SG/SGP radiosonde during dual-soundings experiments. (a,d,g) Raw temperature readings along the altitude. (b,e,h) Temperature readings along the altitude after removing an initial bias. (c,f,i) Linear trends of the measurement drift above 3600 m due to radiation issues (the empirically observed altitude threshold).

around the sensor. Our design addressed this aspect in chamber tests and field experiments [40]. However, further PCB board improvements are expected to enhance humidity measurements.

The sensor's slow response time necessitates using low data rates for atmospheric observations. An air velocity of about 1 m/s is needed for the sensor to reach 63% of a humidity step change within 1 second [151]. This response time was validated within a climatic chamber, and the results aligned with manufacturer specifications (refer to Section 4.3.1 for details).

The PHT sensor was chosen due to its compact size, low power consumption, and affordability, which are common characteristics for sensors used in Internet-of-Things (IoT) systems [170]. Our observations confirm underestimation of high humidity values by low-cost RH sensors, as reported by Wilson et al. [171]. To address this issue, we are exploring two solutions: (i) Developing a compensation technique: Similar to the approach used for Vaisala RS-41SG probes [50]; (ii) Adopting an alternative sensor: Sensors specifically designed for atmospheric monitoring applications, such as the KFS140-FA [172] or the P14 4051 Rapid Thermo [173].

4.4 Setup of the multiple tethered radiosondes

Following validation tests with single and dual radiosonde setups, we evaluated the feasibility of a radiosonde cluster network using multiple *tethered radiosondes*. As mentioned in the previous sections, the cluster network employs a star architecture, where each radiosonde communicates *directly* (point-to-point) with a central receiver station. Additional receiver stations are used to mitigate packet loss due to congestion in the receiving module. If the primary receiver misses a packet, a secondary receiver might capture it. Before conducting free-flight experiments, tethered radiosonde launches were conducted under controlled conditions. Two such tests were carried out:

- September 29, 2021, at INRIM campus (Italy)
- February 10, 2022, at OAVdA, St. Barthelemy (Italy)

These tests assessed the overall performance of a five-radiosonde cluster transmitting to two ground stations as receivers. Figure 4.16 shows the configuration used in the INRIM test during the tethered flight. For position validation, a Sony HDV camera captured the footage of radiosondes (one marked in red, one in black). However, a single camera proved insufficient for precise reconstruction due to the limitations of monocular vision. To address this limitation, a two-camera setup was implemented for subsequent tests (February 10 and Nov 3, 2022, Aosta) to enable reliable stereo vision analysis.

Figure 4.17 presents pressure, humidity, and temperature measurements from the tethered cluster launch, including pre-launch checks. These readings were validated against data from the Vaisala WXT510 weather station at the INRIM campus, which records data at one-minute intervals and is positioned two meters above the ground. As in the previous tests, sensor readings were affected by cold-start effects; however this initial warm-up phase has been omitted from the plots on the left-hand side. The

Figure 4.16: Experiment with five tethered radiosondes at INRIM on September 29, 2021. Two radiosondes tracked using video camera were marked in red and black.

WXT510 station, equipped with a helical solar shield and fully exposed to ambient airflow, is not subject to direct or indirect solar radiation from electronic boards. The comparison shows minutely averaged sensor readings from all five radiosondes against the WXT510 station data, which is also reported on a one-minute basis. Pressure readings were well-aligned, though humidity and temperature readings still exhibited some bias and radiation effects.

Pre-launch check results revealed the following:

- Accurate pressure readings, consistent with previous dual-sounding observations.
- Humidity and temperature sensors performed well without solar irradiance compensation, with an average Root Mean Square Deviation (RMSD) of 3.57% and 1.21°C, respectively, aligning with manufacturer specifications, reported in Table 4.9. These values are acceptable for tracking relative changes but may be insufficient for precise ambient monitoring.
- Sensor uncertainties could be further reduced through extensive comparative tests across various atmospheric conditions.

The right-hand panels show sensor readings during the tethered flight setup as depicted in Figure 4.16. During this phase, the radiosondes experienced varying airflow and radiation due to their movement in the experimental area. Altitude data indicates that probe 3 was at a lower altitude than the others, and in general, all probes exhibited fluctuations while tethered. This experiment once again highlighted that temperature and humidity readings require careful post-processing to address biases, radiation effects, and potential correction mechanisms. Future electronic board designs should also consider alternative sensor options and improved housing to mitigate these issues.

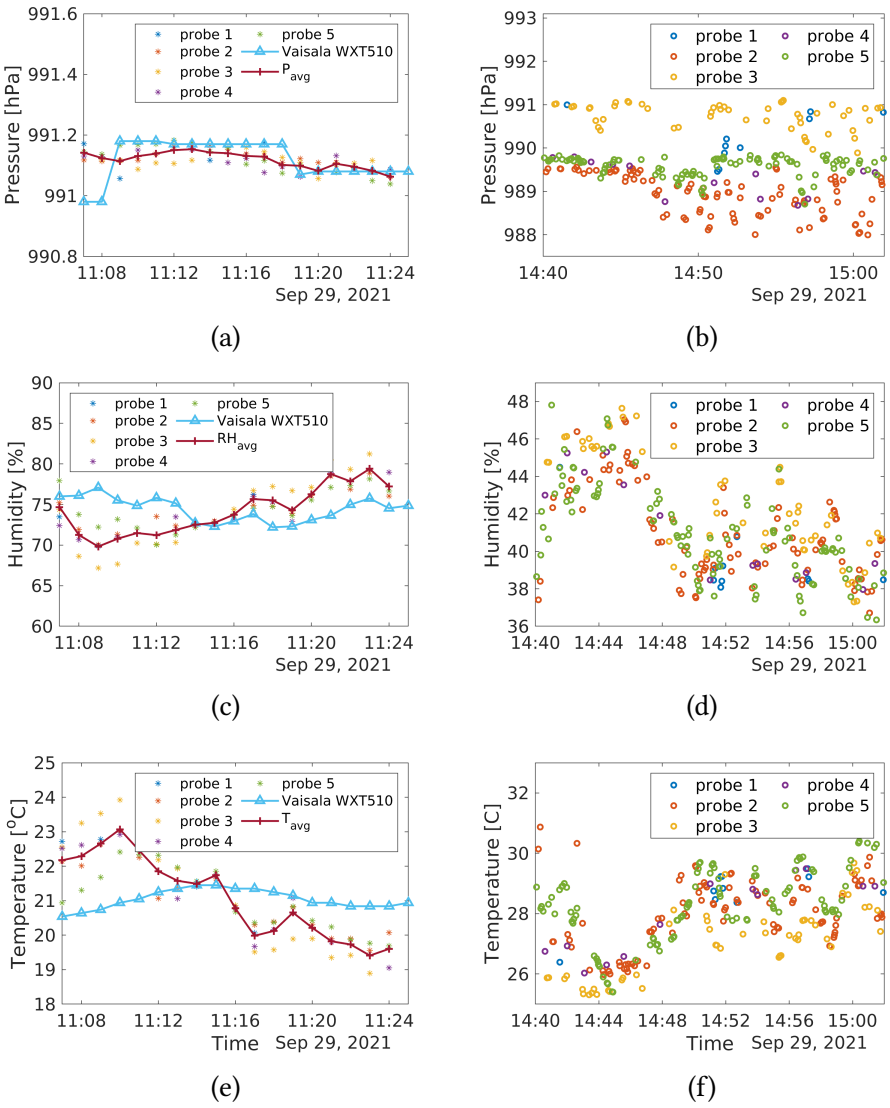

Figure 4.17: **INRIM tethered radiosonde sensor measurements (September 29, 2021)**: pressure, humidity and temperature readings. **Left Column (a, c, e)**: Pre-launch sensor readings averaged over one minute. Solid red line: Average values per minute for the five COMPLETE probes (not shielded from solar radiation). Comparison with Vaisala **WXT510** station data (shielded by a solar helical protection). **Right Column (b, d, f)**: Tethered radiosonde measurements from 14:40 to 15:02. During this phase, radiosondes were launched in tethered mode as shown in Figure 4.16.

4.4.1 Position Validation with Stereo Vision Analysis

Accurate position and trajectory information for each radiosonde is essential for acquiring Lagrangian statistics on various atmospheric flow quantities.

Table 4.9: Comparison of pressure, humidity, and temperature readings from five tethered radiosondes with measurements from the Vaisala WXT510 station at the INRIM campus (September 29th, 2021). RMSD values are presented for each sensor type. The last two rows show the average RMSD for all radiosondes compared to the manufacturer's specifications [151].

Quantity/ probe	Pressure [hPa]	Humidity [% RH]	Temperature [^{o}C]
probe 1	0.08	3.45	1.15
probe 2	0.06	3.06	1.11
probe 3	0.06	5.24	1.69
probe 4	0.06	3.38	1.29
probe 5	0.06	2.70	0.82
Average	0.065	3.57	1.21
Datasheet	1.0	3.0	0.5 - 1.5

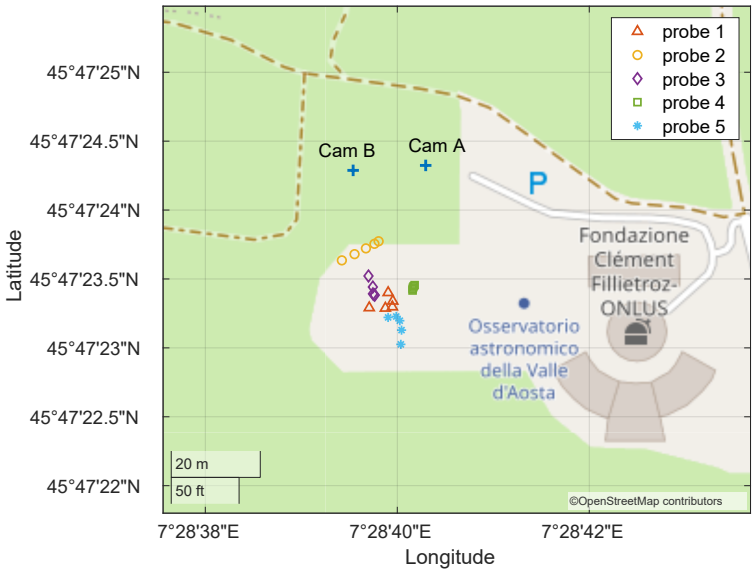

Figure 4.18: Stereo vision experiment setup in Saint-Barthelemy, Italy, on February 10, 2022, with tethered radiosondes. Multiple positions were recorded between 16:15 and 16:17 using two Sony HDV cameras, 16 meters apart from each other(Cam A and Cam B).

Several tests were conducted during radiosonde development to validate the performance of positioning sensors (GNSS and IMU). Earlier work [40] compared 2D radiosonde position data with a phone's positioning data (considered a good reference due

to A-GNSS). Additionally, 3D position data and other sensor measurements were assessed through dual launches with Vaisala RS41-SG probes (described in Section 4.3.3).

An in-field experiment at OAVdA, St. Barthelemy (February 10, 2022) evaluated relative distance tracking using a multi-radiosonde setup. This experiment aimed to validate GNSS-based relative position changes against distances tracked by a stereo vision camera system. Experimental setup is described in Figure 4.18, where positions of two cameras and few instances of radiosonde positions are shown on the map around OAVdA observatory.

The relative movement between two red and black marked radiosondes was chosen for validation (Figure 4.19). Relative distances were obtained from two datasets: (i) GNSS (longitude, latitude, altitude) coordinates; (ii) Video frames recorded by the Sony HDV cameras.

A pinhole camera model with basic calibration [174] was used for distance computation using stereo vision. The CSRT tracker [175] from OpenCV [176] was employed to track the marked radiosondes in subsequent video frames due to its superior performance (approximately 90% accuracy and 85% success rate), see also Appendix B.2 for details fo the workflow of the distance tracking algorithm. The camera coordinate frame for stereo vision offered the following estimated accuracy:

- Horizontal direction: ± 0.5 m within 20 m (2.5%)
- Vertical direction: ± 0.8 m within 20 m (4%)
- Horizontal depth direction: ± 4 meters within 100 m (4%).

The relative distances obtained from GNSS and stereo vision showed good agreement for most of the time window. The mean absolute difference for the first 60 seconds was 2.6 meters, increasing to 5.2 meters for the entire window. This discrepancy is attributed to the rapid change in radiosonde trajectories due to strong winds near the end of the experiment, when both balloons were close to the ground with limited visibility in the camera frames.

A comparison of 2D and 3D distances from the GNSS dataset confirmed this observation. While stereo vision data served as a reference here, based on visual analysis, the GNSS sensor is believed to have performed better. Additionally, the GNSS distance differences fall within the manufacturer's specified accuracy range (± 4-8 meters).

This investigation primarily focused on GNSS data to evaluate the system's positioning and trajectory tracking capabilities. Sensor fusion algorithms like Madgwick [161] or Kalman filters [162] could be used to combine GNSS data with IMU data for enhanced positioning. However, detailed analysis and discussion of position tracking using sensor fusion are deferred for future studies.

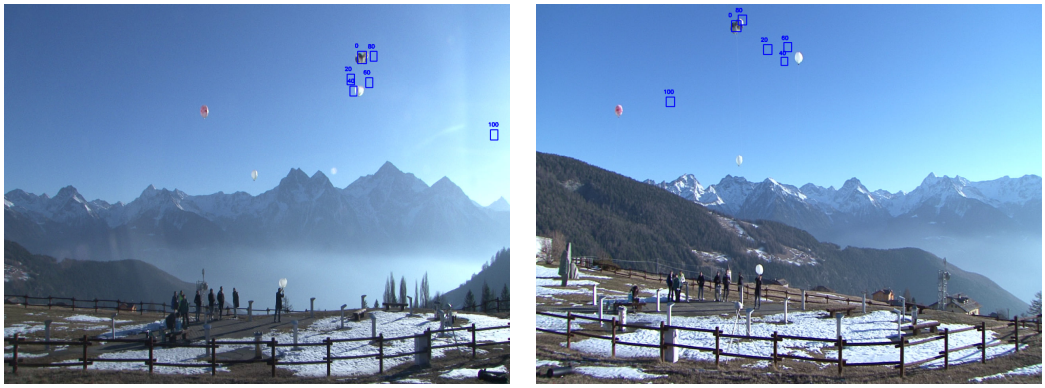

(a) (b)

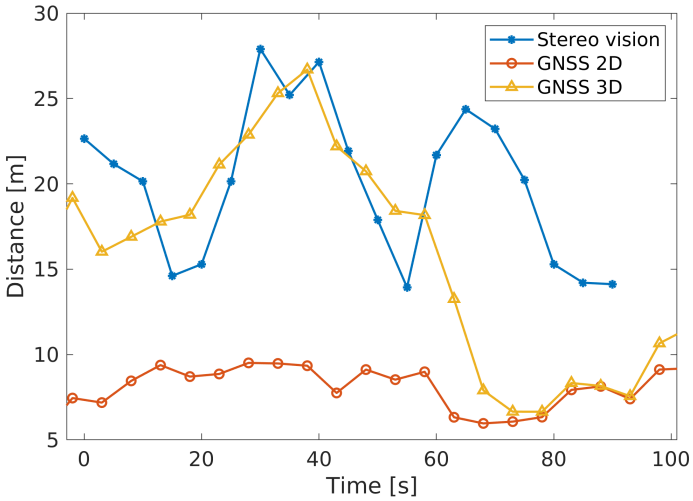

(c)

Figure 4.19: The relative distances between radiosondes, determined by stereo vision and GNSS coordinates during the OAVdA experiment (Figure 4.18). (a) Initial frame from camera A. (b) Initial frame from camera B. The blue rectangles in these frames indicate the subsequent positions of the radiosonde with a black balloon, with the corresponding time (in seconds relative to the initial frame) displayed in the upper left corner of each blue rectangle. (c) Relative distance over time with reference to the initial frame at 16:25:37.

Chapter 5

In-field measurements with a cluster of radiosondes

A radiosonde cluster experiment enables detailed observation of atmospheric flow by simultaneously gathering data from multiple regions within the flow domain. By combining the trajectory data of each radiosonde with the corresponding physical measurements recorded along their paths, we can generate a multi-Lagrangian dataset. This dataset is highly valuable for analyzing turbulent fluctuations and Lagrangian dispersion within the atmospheric boundary layer and warm clouds. Additionally, using clusters to track multiple physical quantities significantly increases the potential for Lagrangian cross-correlation analyses across various parameters.

In the previous chapter, the focus was primarily on measurements obtained from single, dual, or tethered radiosonde setups. In this chapter, we present preliminary results from simultaneous measurements collected by a cluster of radiosondes. At the time of writing this thesis, six in-field experiments involving free cluster launches had been conducted: the first launch at the OAVdA Observatory, Aosta, Italy in November 2022, two launches in July 2023 during the Wessex Convection (WESCON) Campaign, a launch during the CISM summer school in Udine, and two recent experiments at Chilbolton. Table 5.1 provides summary of the conducted experiments in chronological order.

5.1 Setup and pre-launch tests

Each cluster launch experiment requires meticulous planning and thorough pre-launch checks, ranging from selecting the launch site and assessing weather conditions to preparing the balloons, helium, radiosondes, and receiver stations. Additionally, radiosonde sensor readings are tested beforehand to ensure proper data acquisition, identify and compensate for biases, and confirm calibration accuracy. Final checks include verifying transmission and geolocation data acquisition. However, these steps can vary

Table 5.1: In-field experiments conducted with a *cluster of free-floating radiosondes*, listed in chronological order.

Date	Description	Place	Coverage
Nov 3, 2022	The first experiment with the free flying cluster of **10 radiosondes**	OAVdA, St. Barthelemy, Aosta, Italy	long-range, freely floating setup, distance up to 9 km, floating within altitude of 1700-3500 m in alpine environment
July 5, 2023	1st cluster launch during the WESCON 2023 campagin, **10 radiosondes**	Chilbolton Observatory, Chilbolton, UK	long-range, horizontal distance up to 45 km and free floating within altitude range of 500-2500 m
July 6, 2023	2nd cluster launch during the WESCON 2023 campagin, **12 radiosondes**	Chilbolton Observatory, Chilbolton, UK	long-range, horizontal distance up to 50 km and free floating within altitude range of 500-2000 m
June 19, 2024	A cluster launch during the summer school at International Centre for Mechanical Sciences (CISM), **10 radiosondes**	Udine, Italy	long-range, horizontal distance up to 30 km and free floating within altitude range of 1000-2000 m
Sep 24, 2024	1st cluster launch during the AMOF linked experiment, **8 radiosondes**	Chilbolton Observatory, Chilbolton, UK	long-range, horizontal distance up to 30 km and free floating within altitude range of 200-2300 m
Sep 26, 2024	2nd cluster launch during the WESCON 2023 campagin, **9 radiosondes**	Chilbolton Observatory, Chilbolton, UK	long-range, horizontal distance up to 40 km and free floating within altitude range of 300-2300 m

depending on the specific conditions encountered during each experiment.

5.1.1 Aosta experiment setup: the first cluster launch

Building on preliminary tests and in-field experiments, we successfully conducted a cluster of freely floating radiosondes at the OAVdA Observatory in St. Barthelemy, Aosta, Italy, on November 3, 2022. To the best of our knowledge, this represents one of the first observation experiments utilizing a cluster of radiosondes to track fluctuations in physical quantities within clouds and the atmospheric flow field.

(a) Pre-launch check

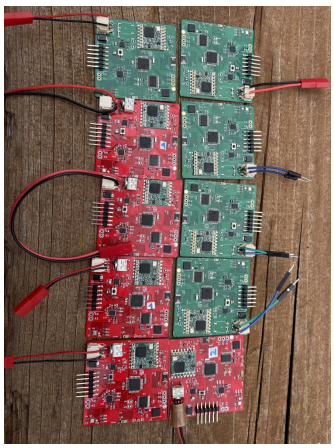

(b) radioprobe boards

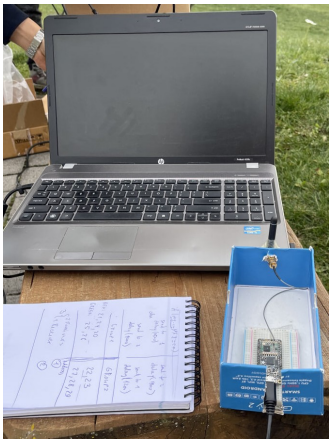

(c) receiver station

(d) balloon inflation

Figure 5.1: Experiment setup at OAVdA, St. Barthelemy, Aosta, Italy, on November 3, 2022. (a) The radiosondes during pre-launch calibration with INRIM reference instrumentation. (b) Prepared radioprobe electronic boards. (c) A ground station connected to the laptop PC. (d) Balloon preparation for radiosonde assembly.

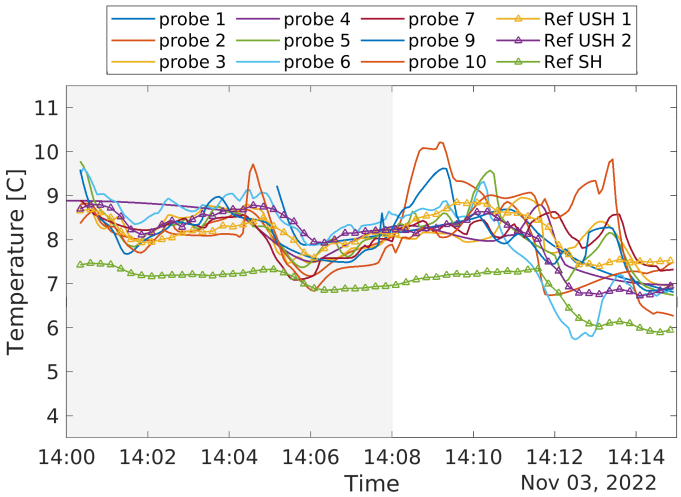

Figure 5.2: *Pre-launch* calibration during the OAVdA experiment at Saint-Barthelemy, Aosta, Italy, on November 3, 2022. Temperature measurements were compared with INRIM reference instrumentation using readings from a Fluke DAQ 1586A multimeter. All the radiosondes were fixed to the fence during the first phase (highlighted in light gray) as in Figure 5.1a, while the radiosondes were picked up for the free launching in the second phase. See Table 5.2 for the standard deviations and mean differences in the temperature measurements.

The preparation and instrumentation of the experimental setup are detailed in Figure 5.1. Prior to launching, all radiosondes were secured to wooden fences for pre-launch checks and calibration as shown in Figure 5.1a. The pre-launch checks were divided into two phases: (i) from 13:58 to 14:08, the radiosondes remained attached to the fences; (ii) from 14:08 to 14:15, they were individually picked up and grouped together for free-launching. These two intervals were considered for temperature calibration against the INRIM reference instrumentation, specifically the Fluke DAQ 1586A multimeter (see Figure 5.1a). Three PT100 platinum resistance thermometers were connected to multi-meter: sensors 1 and 2, without a solar shield, while sensor 3, equipped with a helical passive solar shield, was placed between the two unshielded sensors.

Figure 5.2 displays the measurements conducted during the pre-launch checks. Probe readings were compared with the reference sensor readings with (Ref SH) and without solar shields (Ref USH1 or USH2). The two phases of the pre-launch checks are indicated by light gray and white backgrounds in the figure. During the first phase, the probe and reference sensor readings (Ref USH1 and USH2) showed good agreement. In the second phase, after 14:08, some spikes were observed, likely caused by the manual handling of the radiosondes during their final preparation for the free-flight launch.

Table 5.2 presents the RMSD of the temperature measurements from the radiosondes, in comparison to INRIM reference sensors. Depending on the sensor compensation

Table 5.2: RMSD values for temperature measurements from each radiosonde, calculated relative to three reference temperature sensors (denoted as σ_{USH1}, σ_{USH2}, σ_{SH}), shown in the first three columns. The last column provides the temperature bias offsets (μ_{USH}), representing the average difference between the radiosonde temperature readings (without solar shields) and the unshielded reference sensors. These offsets were compensated in the radiosonde readings before calculating the RMSD values. The radiation offset was also determined as the difference between σ_{SH} and σ_{USH1} (and σ_{USH2}), found to remain within the 1.15–1.40 ˚C range, with an average value of 1.28 ˚C. Note: Data for Probe 8 is unavailable due to reasons discussed elsewhere in the text.

Probes	σ_{USH1}	σ_{USH2}	σ_{SH}	μ_{USH}
Probe 1	0.10	0.09	1.33	0.36
Probe 2	0.30	0.40	1.73	0.37
Probe 3	0.20	0.33	1.48	0.63
Probe 4	0.21	0.17	1.40	0.21
Probe 5	0.14	0.21	1.48	0.31
Probe 6	0.51	0.18	1.71	1.55
Probe 7	0.17	0.43	1.51	1.41
Probe 8	-	-	-	-
Probe 9	0.21	0.33	1.56	1.77
Probe 10	0.53	0.86	1.90	2.64
Average	0.26	0.33	1.57	1.03

method and environmental conditions, sensors may introduce an internal bias offset. During the pre-launch calibration, these offsets were determined as the mean difference between the probe's measurements and the reference sensor's readings (as shown in column 5 of Table 5.2). This calibration was carried out using unshielded reference sensors, allowing us to distinguish between the *radiation offset* and the *bias offset*.

If T_i^k is temperature measurements from probe k at time instance i, then the RMSD of the readings with respect ot the reference sensor readings T_i^{ref} is

$$\sigma_{\text{ref}} = \sqrt{\frac{1}{n}\sum_{i=1}^{n}(T_i^k - T_i^{\text{ref}})^2} \tag{5.1}$$

RMSD deviations of the sensor readings were computed after compensating for the bias offsets as displayed in columns 2-4 of Table 5.2. The RMSD values and their averages, in comparison to each reference sensor, aligned well with the values declared by the manufacturer, falling within the range of 0.5–1.5 ˚C [151]. The deviation values were higher than the first reference sensor (with a solar shield) due to the radiation effect naturally experienced by radiosondes.

Figure 5.2 also illustrates the radiation effect, showing a consistent offset between

shielded (Ref SH) and unshielded (Ref USH) reference sensors. This radiation offset, calculated as the difference between σ_{SH} and σ_{USH1} (and σ_{USH2}), typically ranged from 1.15 to 1.40 °C, with an average value of 1.28 °C. This finding suggests that future radiosonde designs should incorporate radiation shielding to minimize this effect, as also noted in the previous experiments discussed in Chapter 4.

Additionally, each probe may experience different bias offsets, so individual bias compensation mechanisms should be optimized. Nevertheless, our current focus is on the relative changes (fluctuations) in measurements over time and space. I believe the current sensor readings offer sufficient accuracy for analyzing these relative measurements.

5.1.2 MET OFFICE - Wessex Convection 2023 experiment setup

The Wessex Convection Campaign (WESCON) 2023, organized by the UK Meteorological Office during the summer convective period in the southwest UK, provided a valuable environment to test and validate the radiosondes cluster network in an operational setting. Two cluster launches were conducted throughout the campaign (July 3-7, 2023) to investigate Lagrangian fluctuations within the Atmospheric Boundary Layer. This participation not only facilitated the international validation of our innovative measurement system but also yielded a rich dataset from various instrumentation sources (radar, lidar, ground, and airplane sensors) for verification and comparison purposes. Additionally, a dual-sonde launch experiment was performed to measure atmospheric fluctuations along a vertical profile extending up to 12 km. The context of the experiment and some measurement platforms employed during the campaign are detailed in Figure 5.3.

Unlike the Aosta experiment, similar calibration tests were not conducted during WESCON. However, validation of the results is possible using the extensive measurement data collected on a specific IOP (Intensive Observation Period) day, which can be retrieved from the JASMIN database. Figure 5.4 depicts the flight instances of the two cluster launches alongside the receiver stations. These stations comprised a combination of fixed and mobile units, contrasting with the solely fixed receiver station used in the Aosta experiment. Furthermore, two distinct balloon configurations were employed: a combination of biodegradable and Mylar balloons, and two Mylar balloons alone. The two-balloon setup ensured that the radiosondes reached the target altitude of 1500-2000 meters. The use of Mylar balloons solely in this campaign stemmed from delays encountered in preparing the biodegradable balloons.

The pre-launch procedures ensure the functionality and accuracy of the radiosondes before deployment. These procedures involve several key steps:

1. **Radioprobe Board Preparation**: This step involves preparing the radiosonde board, including its enclosure.
2. **Balloon Preparation:** Balloons are filled with the appropriate gas for buoyancy.

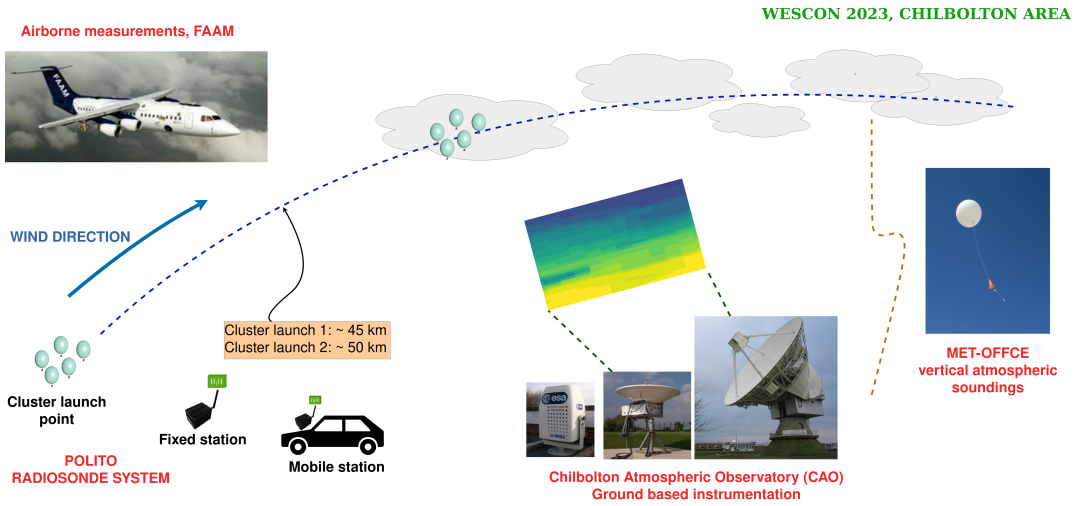

Figure 5.3: The experimental context for WESCON 2023 involved cluster launches of the POLITO radiosonde system conducted on the intensive observation period (IOP) days, which took place on July 5-6, 2023. Throughout these IOP days, a comprehensive observational dataset was also obtained through the instrumentation of both the UK MET-OFFICE and the Chilbolton Observatory Facility (NCAS).

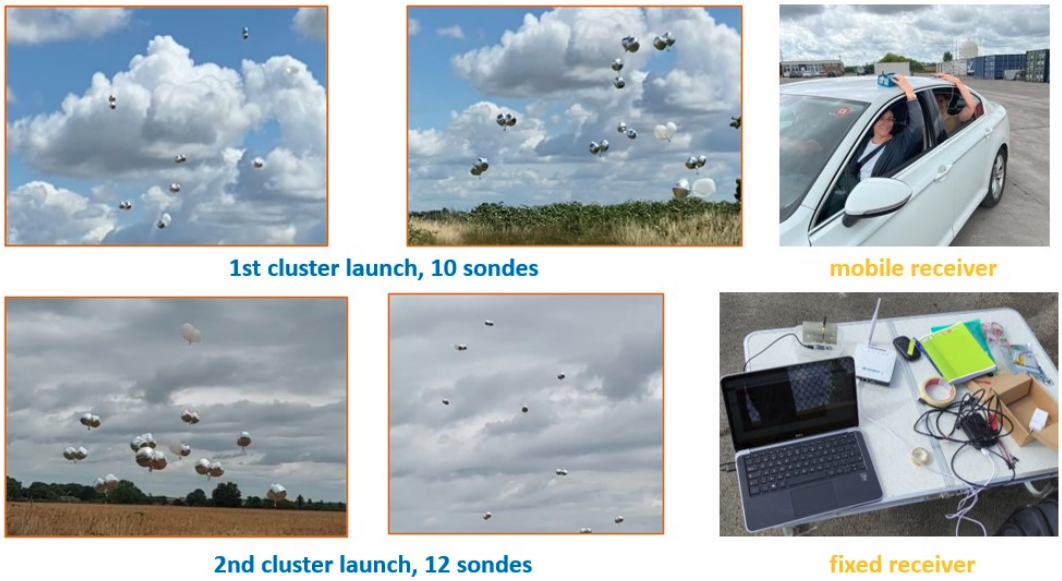

Figure 5.4: Two cluster launches and used receiver stations (fixed and mobile) during WESCON experiments. Experiments were conducted on July 5 and 6, 2023. Mobile receiver stations was used to increase transmission range of the LoRa signals.

3. **Radiosonde Assembly:** The radiosonde is assembled by integrating the radioprobe board, sensors, and other necessary components.

4. **Transmission and Sensor Checks**: Pre-launch checks are performed to verify proper data transmission and sensor readings. These checks typically include: (a) Transmission checks: Confirming data packet reception from all radiosondes with the expected sample rate (1 packet in each 4-5 seconds); (b) Sensor reading checks: Verifying the accuracy of sensor readings (e.g., temperature, humidity, and position) compared to known reference values.

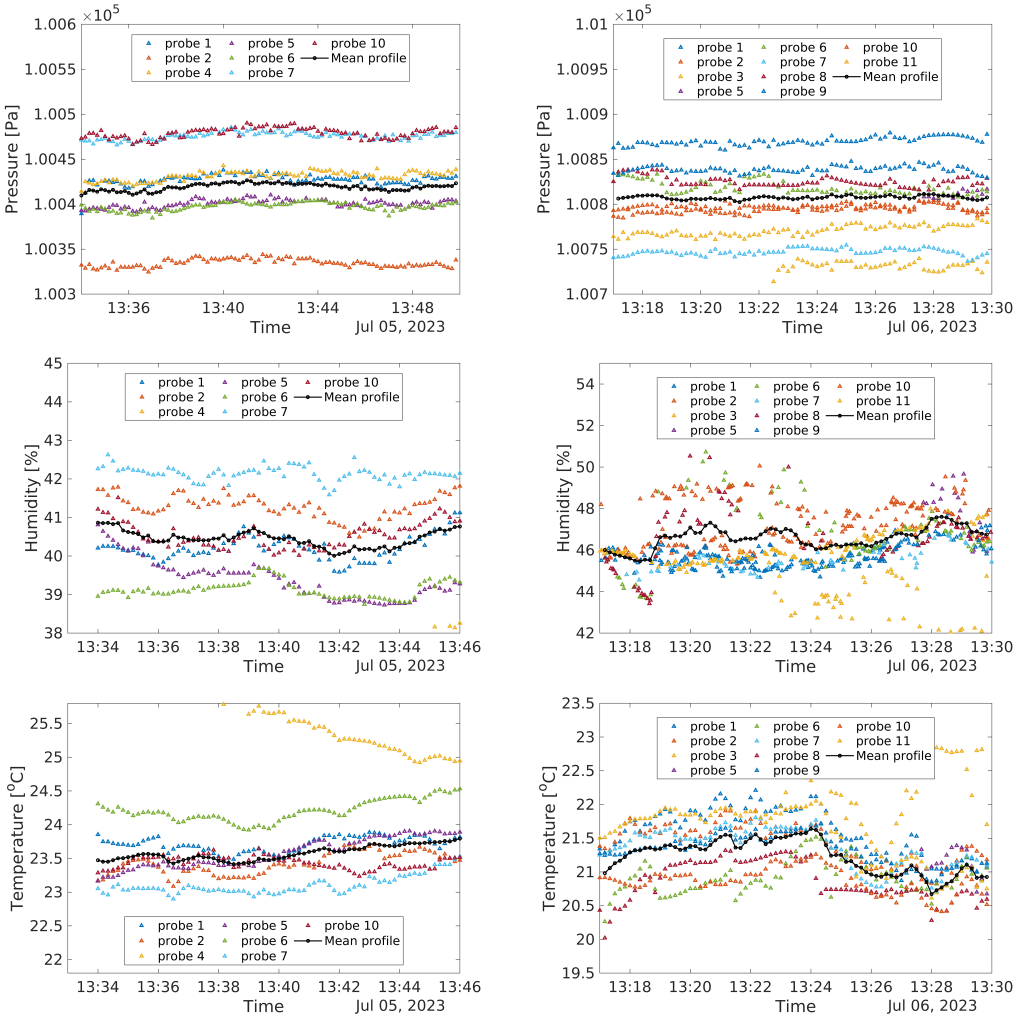

Figure 5.5: Pressure, humidity and temperature readings prior to the launch.

Figure 5.5 presents sample sensor readings obtained during pre-launch transmission and sensor measurement tests. These intermittent measurements serve to verify the functionality of batteries, boards, and sensors. Such checks are essential to ensure data integrity and reliable radiosonde operation during flight. Pre-launch measurements typically require approximately 1.5-2 hours, with probes remaining within a protected

preparation area due to potential strong ground-level winds (approximately 20-25 m/s on the days of the experiments). The figure depicts sensor measurement profiles of pressure (P), humidity (H), and temperature (T) for a brief pre-launch period on both experiment days. The measurements from all operational probes during each flight (7 probes for the first flight and 10 probes for the second) are synchronized for comparison purposes, with interval of 10 seconds inside a common time range. The black dotted line in each panel represents the average measurement profile calculated across all probes available for that specific flight.

The left-hand panels of Figure 5.5 highlight readings acquired during the preparation period for the first experiment (July 5, 2023), specifically from 13:34 to 13:45 (10 minutes before launch). The right-hand panels depict readings from the second experiment's preparation period (July 6, 2023), collected between 13:17 and 13:30 (10 minutes before launch). It's important to note that the measurement profiles are only presented for probes that participated in the corresponding flight.

To assess potential variations among individual probes, the relative offset was calculated with respect to the mean profile of each reading, derived from all probes involved in the flight. To compute the Root Mean Square Deviation (RMSD) values, Equation 5.1 was modified to utilize the average measurement profiles instead of reference sensors. Considering T_i^k as probe k's reading at time instance i and T_i^{avg} as the average measurement profile computed from m probe readings (represented by the black dotted lines in Figure 5.5):

$$T_i^{\text{avg}} = \sum_{k=1}^{m} T_i^k \tag{5.2}$$

$$\text{RMSD} = \sqrt{\frac{1}{n}\sum_{i=1}^{n}(T_i^k - T_i^{\text{avg}})^2} \tag{5.3}$$

Tables 5.3 and 5.3 present statistical evaluations of the relative measurements among all probes. This analysis aims to understand potential discrepancies between individual probe readings. It's noteworthy that, in the preceding Aosta experiment, probe measurements were compared with high-quality, standardized INRIM sensors whenever possible, enabling the determination of *"absolute bias"* within the operational environment. Here, the focus lies on comprehending possible *"relative offsets"*. As previously mentioned, the mean profile was calculated using data solely from probes that participated in the flight. However, both tables incorporate pre-launch statistics for all probes that were prepared for the flights. The average statistical values in the tables indicate that the relative RMS deviations and offset values for PHT readings remain within the specifications reported in the sensor datasheet (±1 hPa, ±3%, ±1 ^{o}C [151]).
Table 5.3 highlights *Probes 3, 8*, and *9* (underlined) that were not operational during the first flight. Strong winds caused two probes to be dropped during launch, and one became entangled in a tree roughly 200-300 meters from the launch site. Excluding

Table 5.3: **WESCON, cluster launch 1, July 5, 2023.** RMSD (σ_P, σ_{RH}, σ_T) and mean offset (μ_P, μ_{RH}, μ_T) of the PHT readings from a cluster of the radiosondes relative to the mean measurement profile. Mean offset values were compensated from the PHT readings prior to computing RMSD. Bottom row shows the average statistical quantities, while computing them absolute values of negative numbers are considered. Underlined probes are presented only during preparation tests, not present during flight.

Probes	σ_P [hPa]	σ_{RH} [%]	σ_T [^{o}C]	μ_P [hPa]	μ_{RH} [%]	μ_T [^{o}C]
Probe 1	0.10	0.21	0.07	0.08	-0.30	0.15
Probe 2	0.83	0.18	0.09	-0.84	0.82	-0.14
Probe 3	0.24	0.43	0.20	0.24	-3.75	1.39
Probe 4	0.11	1.36	0.81	0.11	-4.80	2.35
Probe 5	0.19	0.37	0.13	-0.19	-1.00	-0.01
Probe 6	0.22	0.21	0.08	-0.22	-1.32	0.62
Probe 7	0.56	0.22	0.05	0.56	1.73	-0.49
Probe 8	0.20	2.49	1.27	-0.19	4.22	-1.02
Probe 9	0.62	2.55	0.92	-1.63	-6.86	3.85
Probe 10	0.60	0.27	0.16	0.60	0.07	-0.13
Average	0.47	0.83	0.38	0.47	2.49	1.01

these three probes from the statistical calculations can further improve the RMSD and offset values, as illustrated in Figure 5.5:

- RMSD: 0.47 hPa, 0.83 %, 0.38 ^{o}C (all 10 probes) vs. 0.41 hPa, 0.25 %, 0.26 ^{o}C (7 probes).
- Mean offset: 0.47 hPa, 2.49 %, 1.01 ^{o}C (all 10 probes) vs. 0.42 hPa, 0.87 %, 0.26 ^{o}C (7 probes).

However, this improvement is primarily noticeable for the mean offset values of humidity and temperature readings relative to the average measurement profile.

Similarly, during the second launch, one probe was dropped, and another became stuck in a tree within close proximity (400-500 meters). These probes are identified as *Probe 4* and Probe *12* in Table 5.4. Once again, statistical metrics can be enhanced by excluding these two probes from the calculations:

- RMSD: 0.29 hPa, 1.04 %, 0.23 ^{o}C (all 12 probes) vs 0.31 hPa, 0.78 %, 0.16 ^{o}C (10 probes).
- Mean offset: 0.31 hPa, 1.34 %, 0.42 ^{o}C (all 12 probes) vs 0.30 hPa, 0.73 %, 0.27 ^{o}C (10 probes).

During both launches, the radiosondes experienced bias offsets, which were identified and compensated appropriately. However, the radiation effect was not calculated in this case. It's important to note that since the radiosondes operated under similar environmental conditions, the readings were likely affected equally by radiation. This

Table 5.4: **WESCON, cluster launch 2, July 6, 2023.** RMSD (σ_P, σ_{RH}, σ_T) and mean offset (μ_P, μ_{RH}, μ_T) of the PHT readings from a cluster of the radiosondes relative to the mean measurement profile. Mean offset values were compensated from the PHT readings prior to computing RMSD. Bottom row shows the average statistical quantities, while computing them absolute values of negative numbers are considered. Underlined probes are presented only during preparation tests, not present during flight.

Probes	σ_P [hPa]	σ_{RH} [%]	σ_T [^{o}C]	μ_P [hPa]	μ_{RH} [%]	μ_T [^{o}C]
Probe 1	0.62	0.73	0.14	0.63	-0.76	0.37
Probe 2	0.14	0.55	0.12	-0.14	0.01	0.19
Probe 3	0.75	1.33	0.49	-0.76	-2.83	0.82
Probe 4	0.14	0.88	0.24	-0.13	-1.42	0.70
Probe 5	0.05	1.45	0.28	0.03	2.16	-0.14
Probe 6	0.13	1.42	0.29	0.10	0.68	-0.32
Probe 7	0.60	0.46	0.11	-0.60	-1.04	0.13
Probe 8	0.18	1.26	0.17	0.18	0.40	-0.37
Probe 9	0.31	0.45	0.08	0.31	-0.72	0.09
Probe 10	0.11	0.59	0.14	-0.11	1.83	-0.38
Probe 11	0.37	0.75	0.21	0.37	-0.39	0.28
Probe 12	0.07	2.66	0.41	0.28	3.86	-1.19
Average	0.29	1.04	0.23	0.31	1.34	0.42

observation underscores the need for future designs to incorporate radiation shields, even though the current setup ensured consistent relative measurements across the probes.

5.2 Raw measurements from floating cluster

Following successful completion of pre-launch checks and calibration, the radiosondes were launched simultaneously from the same initial position, enabling them to freely drift together. Figures 5.4 and 5.6 depict the initial flight paths for the WESCON and Aosta experiments, respectively.

This section presents raw measurements collected during the Aosta and WESCON experiments to investigate the contrasting environmental contexts. The Aosta experiment was conducted in an alpine, mountainous region, while the WESCON experiment took place in a flat, near-coastal region near Chilbolton. The data will be presented as time series and vertical profiles (across altitude) to facilitate comparison. We will analyze raw measurements including probe trajectories on a map, as well as pressure, humidity, and temperature readings at various altitudes.

Figure 5.6: Release of a cluster of 10 radiosondes into alpine atmosphere for free floating during **OAVdA experiment, November 3, 2022.**

5.2.1 Aosta: Alpine environment, 1700-4000 m

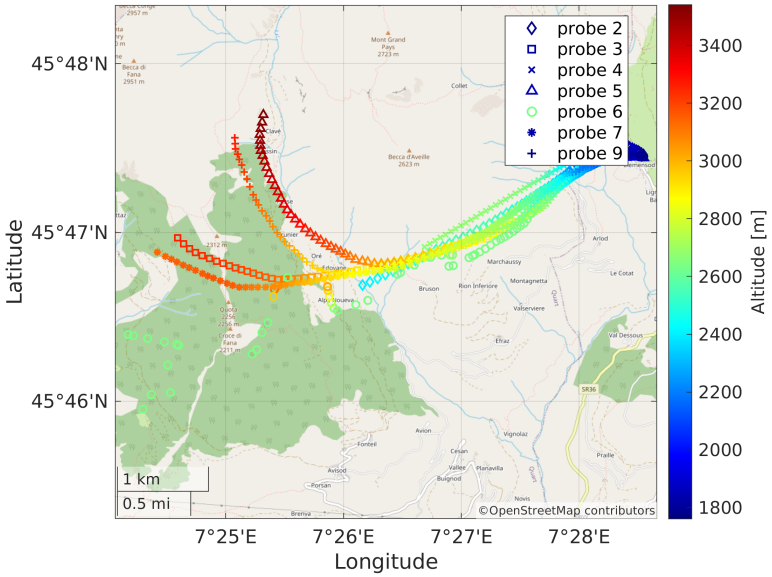

Figure 5.7: **Free-launch of radiosondes during OAVdA experiment.** The trajectories of radiosondes during the first 25 minutes of the free-launch period (14:15 to 14:40) following their release on November 3, 2022, as part of the OAVdA experiment in St. Barthelemy, Aosta, Italy. The color gradient along the trajectories indicates the altitude reached by each radiosonde, starting from an initial altitude of 1700 meters.

Figure 5.7 depicts the trajectories of the radiosondes during the initial 25 minutes of the free-launch period. The radiosondes ascended from an initial altitude of 1700 meters to a maximum altitude of 3950 meters, covering a horizontal distance of up to 8300 meters. It's important to note that data from some radiosondes are excluded from Figures 5.2 and 5.7. This exclusion can be attributed to two main reasons. In some

cases, the amount of data collected during the flight was insufficient for analysis. Other radiosondes experienced technical malfunctions during or after launch. For instance, Probe 1 only transmitted readings during pre-launch checks and briefly after launch. Probe 10 transmitted measurements but couldn't acquire a GNSS fix (proper position signal from satellite). Finally, Probe 8 didn't transmit any readings after launch despite passing pre-launch checks (between 8:47 and 9:17). We hypothesize that the disconnection experienced by Probe 8, potentially caused by mechanical stress and launch oscillations, could be mitigated by implementing a lightweight yet robust enclosure for the electronic components.

Figure 5.8 presents temperature and humidity measurements collected over a 35-minute period, from 14:15 to 14:50. The radiosondes ascended from an initial altitude of 1700 meters, with some reaching as high as 3800 meters. However, not all radiosondes exhibited continuous ascent. Instead, they tended to **reach an equilibrium altitude** and then float horizontally within an isopycnic layer (a layer of equal air density). This behavior is evident for Probes 2 (orange), 6 (light blue), and 4 (violet) in panels (c) and (d) of Figure 5.8.

Probe 2 initially ascended to 2600 meters due to an updraft along the mountain slope. After surpassing the mountain peak, the probe descended slightly and then maintained a horizontal trajectory at its equilibrium altitude. Probes 4 and 6 reached an altitude of approximately 2700 meters before maintaining that level until communication was lost. Notably, they were able to sustain their equilibrium altitude for a period of time (10-15 minutes for Probe 6 and 3-4 minutes for Probe 4). Panels (e) and (f) of Figure 5.8 further illustrate this horizontal floating behavior for Probe 6, by plotting the probe's altitude readings alongside the corresponding humidity and temperature measurements. It's important to note that the height of the surrounding hills was significantly lower than the equilibrium altitude, typically ranging from 1700 to 2000 meters.

5.2.2 Chilbolton: near-coastal region, 100 - 2500 m

The WESCON experiments involved launching radiosonde clusters from Chilbolton Observatory, situated approximately 40 kilometers inland from the nearest coastline. Figure 5.9 depicts the trajectories of these radiosonde clusters during both experiment days. Data transmission was maintained throughout the flights for about 1.5 hours, with the radiosondes reaching horizontal distances of nearly 50 kilometers. Notably, the dispersed radiosonde clusters remained within the boundary layer (500-2000 meters) throughout their flights.

Data packets from the radiosondes were received at an average interval of 4-5 seconds by a network of two receiver stations: a fixed station and a mobile station installed on top of a vehicle. The mobile station significantly extended the operational range for data reception, as evidenced by its successful capture of the final transmissions from Probes 1, 2, and 5 (see Figure 5.10).

While the mobile station's trajectory was not recorded during this experiment, it

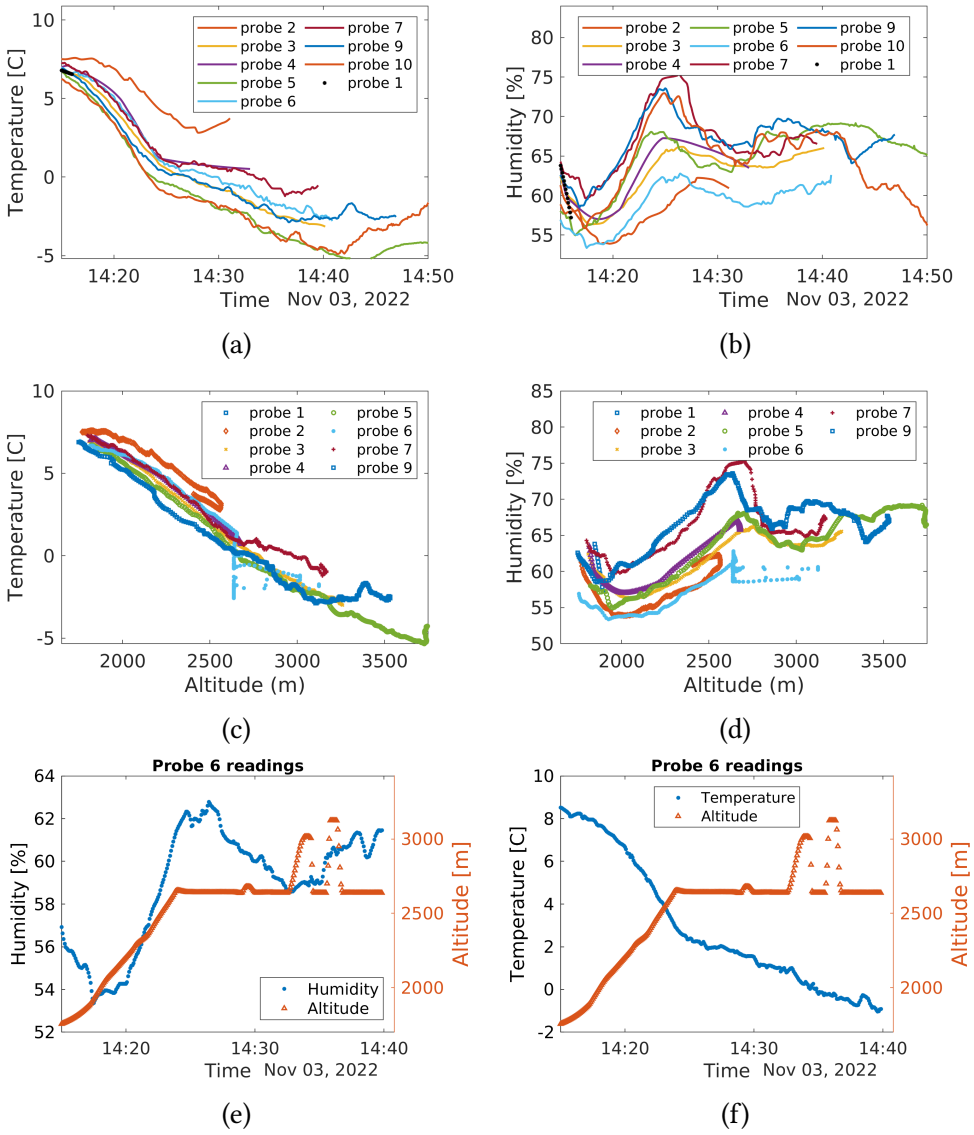

Figure 5.8: Temperature and humidity measurements during the **OAVdA experiment in St. Barthelemy on November 3, 2022**. Panels a and b show temperature and humidity measurements during the launch from 14:15 to 14:50. Panels c and d display measurements along the altitude range of 1740 to 3800 meters. Panels e and f present temperature and humidity readings of Probe 6 with corresponding altitudes.

would be beneficial for future deployments to capture this data. The initial plan involved utilizing two fixed stations positioned approximately 10-20 kilometers apart. However, the success of the mobile station in this experiment highlights its potential to expand data coverage and merits its inclusion in future tracking efforts.

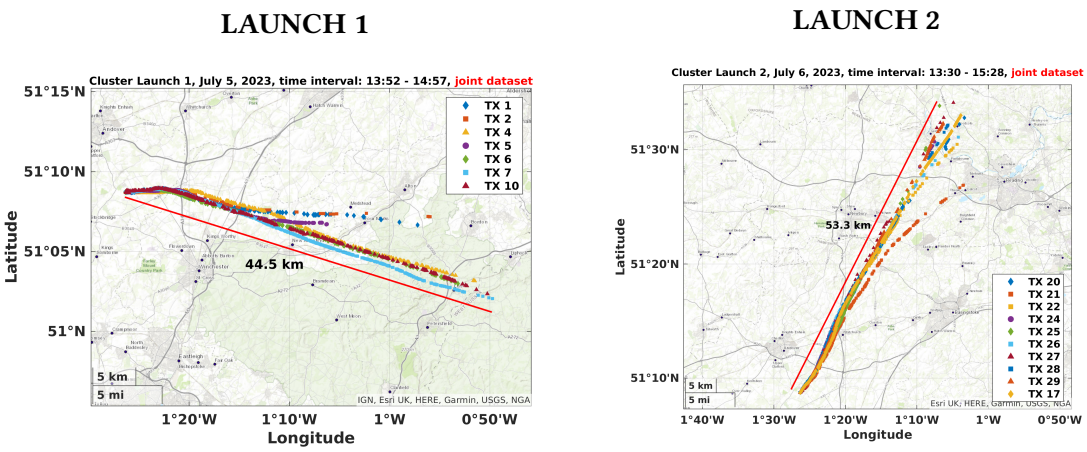

Figure 5.9: **Trajectories of radiosondes during two flights within WESCON experiments, Chilbolton, UK, July 5-6, 2023**. Data transmission continued during the experiments for about 1.5 hour until the radioprobe reached almost ∼ 50 km in horizontal distance. The radiosonde clusters dispersed during the flights but remained within the boundary layer (typically ranging from 500 to 2000 meters altitude). Data packets were received from the radiosondes at an average interval of 4-5 seconds.

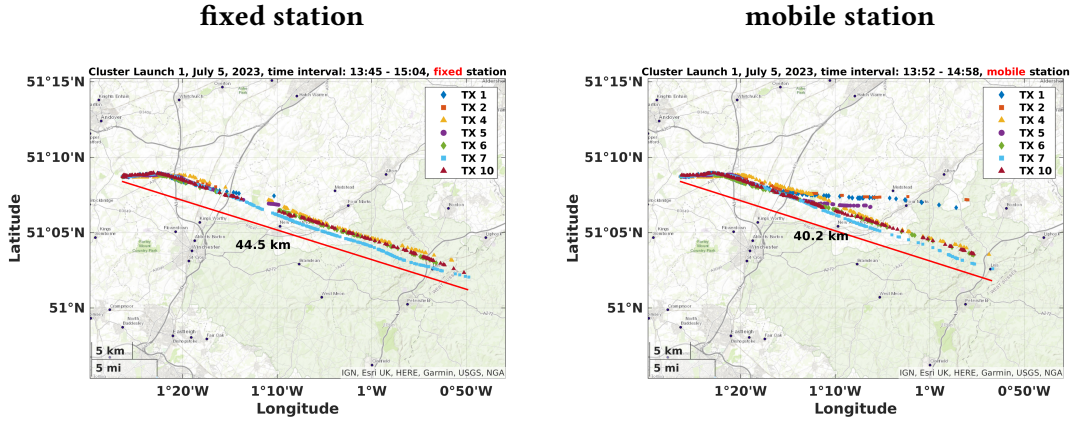

Figure 5.10: **Radiosonde trajectories from the first flight (Chilbolton, UK, July 5, 2023)**. Data reception was facilitated by a network of **fixed** and **mobile** receiver stations. Data transmission continued throughout the flight for approximately 1.5 hours, with the radiosondes reaching a horizontal distance of nearly 45 kilometers.

Figure 5.11 presents radiosonde trajectories visualized as scatter plots within a two-dimensional (2D) East (E), North (N), and Up (U) reference frame. This reference frame was established by converting the GNSS Latitude, Longitude, and Altitude (LLA) data using the World Geodetic System 1984 (WGS84) spheroid model and the launch position as a reference point (Latitude = 51.1454°, Longitude = -1.4390°, Altitude = 85 m). Each color in the scatter plots represents a distinct time instance. The positions of all

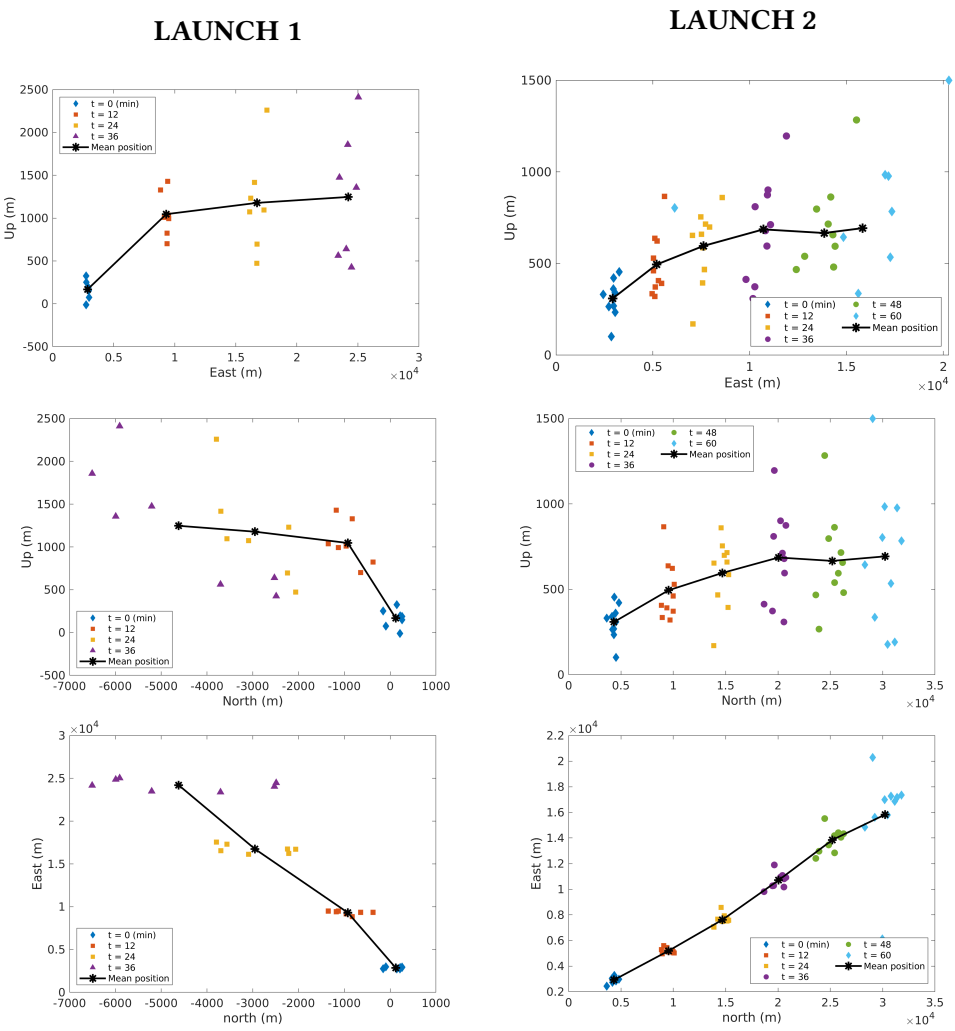

Figure 5.11: 2D scatter plots visualizing the positions of radiosondes during two separate flights conducted as part of the WESCON experiments at Chilbolton, UK, on July 5th and 6th, 2023. The positions are projected onto three planes within an ENU reference frame. The left-hand panels correspond to the first launch, while the right-hand panels depict data from the second launch.

radiosondes at a specific time point are plotted using the same color, allowing for a clear visualization of the cluster's spatial distribution within each 2D plane. This data can be further analyzed to infer wind direction. For example, the bottom two panels of Figure 5.11 suggest the presence of strong south-easterly winds (negative north) on the first day, while winds on the second day appear to have a north-easterly direction.

An analysis of wind speed data reveals a stronger eastward component on the first day, reaching nearly 25 kilometers eastward compared to approximately 7 kilometers

southward. Conversely, the second day exhibited a more balanced displacement pattern, with the radiosondes traveling roughly 20 kilometers eastward and 30 kilometers northward.

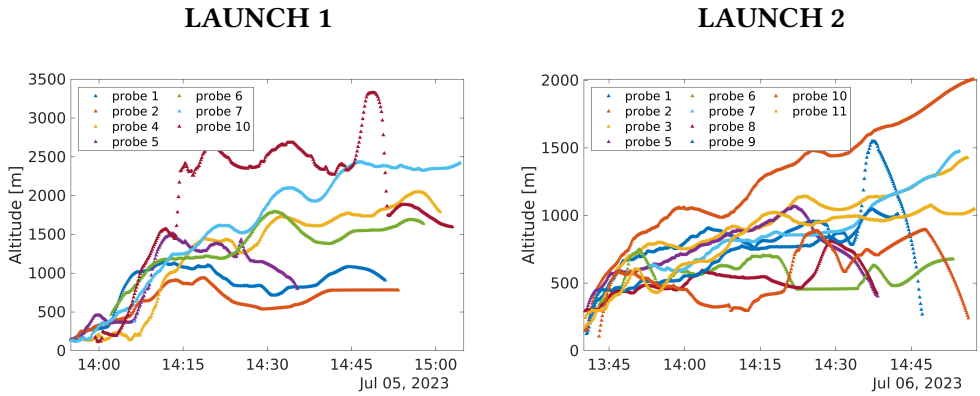

Figure 5.12: The altitude profiles of the radiosondes during the two WESCON experiment flights conducted at Chilbolton, UK, on July 5th and 6th, 2023. Datasets were resampled with equal 10 second intervals, after removing outliers. To fill the missing values, shape preserving cubic spline interpolation has been adopted.

Furthermore, the black lines in Figure 5.11 represent the mean displacement profile within each plane (East-Up, North-Up). It is noteworthy that the mean profiles in both the East-Up and North-Up panels appear to plateau after approximately 12 minutes on the first day and 24 minutes on the second day. This suggests that the radiosonde cluster requires some time to ascend before transitioning to predominantly horizontal movement within the boundary layer. Examining the altitude profiles of the radiosondes in Figure 5.12 can provide further insights into this aspect.

Figure 5.13 presents time series plots of pressure, humidity, and temperature (PHT) measurements collected during two separate radiosonde cluster launch experiments conducted at Chilbolton, UK, on July 5th and 6th, 2023. The left-hand side of the figure (panels (a), (c), and (e)) displays data from the first launch (occurring within a 70-minute interval from 13:55 to 15:05), while the right-hand side (panels (b), (d), and (f)) shows data from the second launch (occurring within an 80-minute interval from 13:40 to 15:00).

The pressure readings in all panels exhibit a similar profile for the initial 10-15 minutes of the first launch. This initial convergence aligns with the observations from Figures 5.11 and 5.12, where the radiosondes remained in a collective ascent phase for approximately the first 12 minutes. However, the pressure profiles diverge after this initial period, indicating increasing variation in the individual flight paths of the radiosondes. The ascent phase for the second launch is less evident in the pressure profiles, and it appears to have lasted slightly longer than in the first experiment.

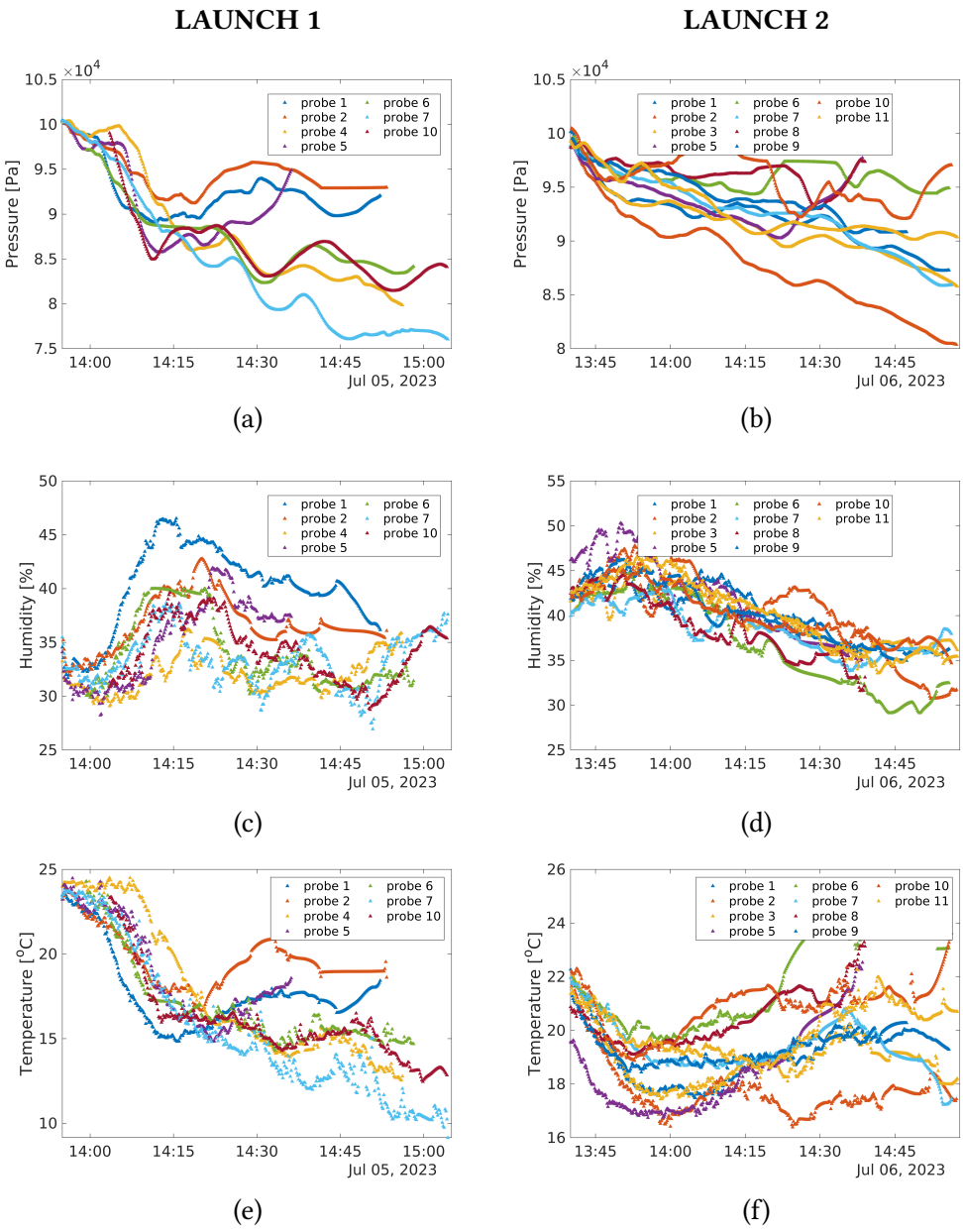

Figure 5.13: Cluster launch experiments at Chilbolton, UK, July 5-6, 2023. **Pressure, humidity and temperature readings** (a, c, e) during the first flight (July 5) and (b, d, f) the second flight (July 6). The data has been resampled at 10-second intervals for improved visualization.

The temperature and humidity profiles exhibit similar trends for a slightly longer duration compared to the pressure profiles. During the first flight, this period of convergence lasts for roughly 15-20 minutes, while in the second flight, it persists for approximately 20-25 minutes. Following this period, the plots reveal increasing divergence

between the readings from different probes, suggesting greater variation in the environmental conditions experienced by the individual radiosondes.

5.2.3 Integration cluster dataset with other instrument data: CLOUDNET

The present radiosonde cluster offers a unique capability for multi-point, high-resolution observations within the atmospheric boundary layer and any embedded cloud formations. This capability allows for a more comprehensive understanding of atmospheric processes compared to single-point measurements. Additionally, the observed quantities from the radiosonde cluster can be integrated with data from other instrumentation, facilitating further validation and enhancing our interpretation of the observed phenomena.

Figure 5.14 exemplifies this approach. The figure illustrates the radiosonde cluster approaching cloud formations. Cloud data for this analysis were obtained from the CLOUDNET Chilbolton dataset (O'Connor [177]). A specific portion of the cloud dataset relevant to the experiment time window and altitude range was extracted. The altitude readings of the radiosondes during this time window are overlaid on top of the extracted cloud fraction data. This example plot is from the second day of the experiments (July 6th, 2023). We plan to perform a more in-deep similar validation analysis for our research group's ongoing work on Lagrangian dispersion within clouds.

While CLOUDNET is a valuable resource for accessing atmospheric data, the WESCON 2023 dataset is also available through the JASMIN data repository. JASMIN offers a broader range of data types collected during the campaign, including Radars (weather, cloud), Lidars, vertical profiling radiosondes and airborne measurements. This variety of data provides a richer picture of the atmospheric conditions during WESCON 2023. Compared to the post-processed averaged profiles offered by CLOUDNET, the raw datasets available from JASMIN might be more suitable for direct comparison with the raw data collected by the radiosonde cluster.

5.3 Tracking fluctuations: temperature, humidity, wind speed and magnetic field

As discussed earlier, a crucial objective of the present measurement system is to examine fluctuations of physical quantities along Lagrangian trajectories and to perform relative measurements within a radiosonde cluster. This approach offers valuable insights into turbulent intermittency, dispersion, and diffusion processes within atmospheric isopycnic layers. Kaimal, Finnigan, and Kaimal [178] highlight the importance of record length (flight duration) and sampling rate for spectral analysis. Ensemble averaging, where data from multiple radiosondes within the cluster is combined, can also be beneficial for time-averaged data analysis and to improve spectral profiles.

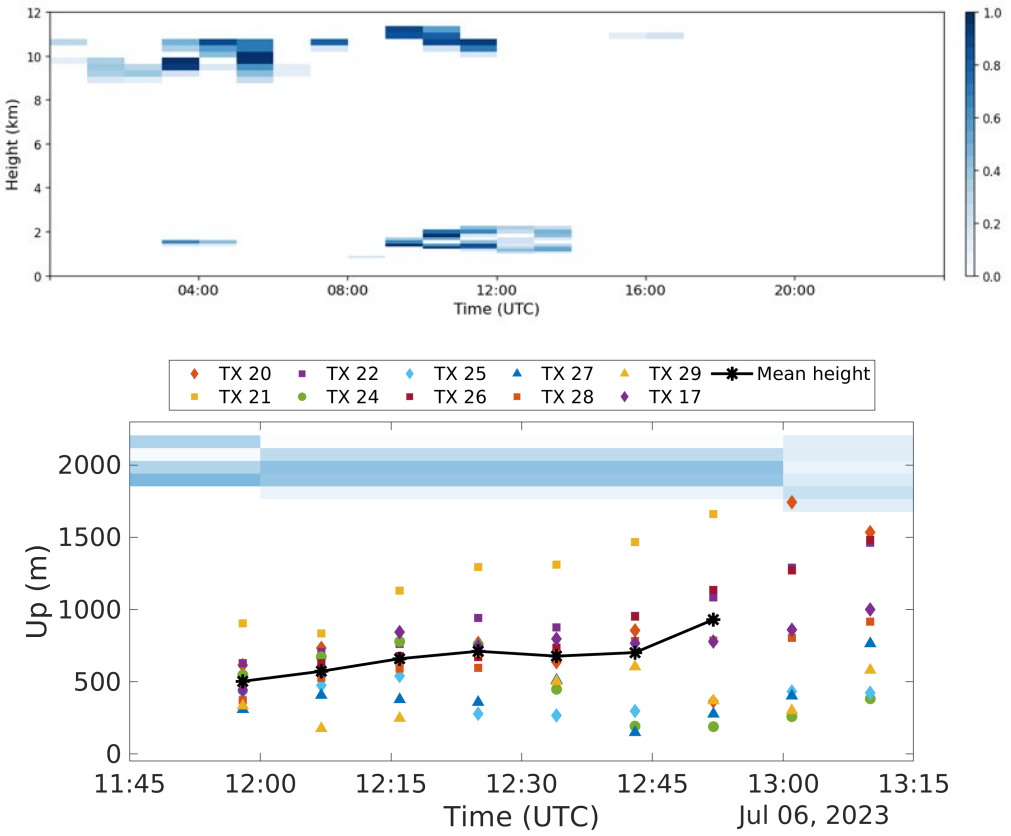

Figure 5.14: A floating cluster of radiosondes are approaching to the boundary layer clouds. Cloud fraction is generated using ECMWF (European Centre for Medium-Range Weather Forecasts) IFS forecast model using Chilbolton CL51 ceilometer and Chilbolton Copernicus cloud radar dataset.

Figure 5.15 presents humidity and temperature readings alongside the achieved altitudes for a selected subset of radiosondes (probes 5, 7, and 9) during the cluster launch experiment in Aosta Valley, Italy on November 3, 2022. The data encompasses a 30-minute period, ranging from 14:15 to 14:45, with a sampling rate of 5 seconds. As described for wind speed analysis in Section 4.3.3, a FFT transform was employed to convert the data from the time domain to the frequency domain for spectral analysis (presented in Figure 5.17).

Continuing with the same experiment, Figure 5.16 displays the raw measurements of north, east, and up wind velocity components (retrieved from the GNSS sensor's PVT data packet). The data is presented along both time (left panels) and altitude (right panels) axes. During the initial phase (approximately 10 minutes) of the flight, the east component exhibited a relatively constant value around -2 m/s. The up component displayed an increase in the first 5-6 minutes, potentially indicating an **updraft**. The north component initially decreased to -2 m/s, suggesting a south-west wind direction.

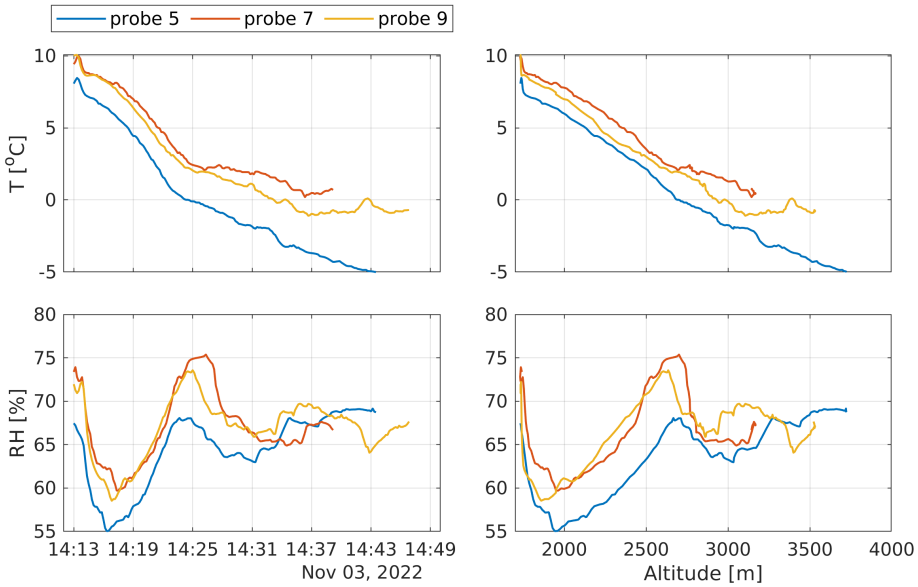

Figure 5.15: Humidity and temperature measurements from the OAVdA experiment on November 3, 2022, from a subset of probes. Panels a and c depicts readings along the time duration, while b and d shows their profile along the altitude levels.

However, it later increased towards positive values, indicating a shift towards a south-east direction during the ascent. More prominent fluctuations started beyond 2500-2600 meters of altitude. This may suggest the diminishing influence of the valley updraft as the radiosondes ascended above the surrounding hills (approximately 2200 meters).

Spectral analysis of velocity, temperature, and humidity data can provide valuable insights into the intensity and frequency of environmental changes during the flight. However, as shown in Figures 5.17 the environmental sensor readings exhibit relatively low fluctuations across most of the frequency range (excluding the initial peak). This is particularly evident for the temperature data (panel d), which is consistent with the findings of Kaimal, Finnigan, and Kaimal [178] that temperature fluctuations are generally higher near the surface and decrease with altitude. Temperature fluctuations are generally higher near the surface and decrease with altitude. Additionally, longer record length and higher sampling rate can further improve the temperature spectrum profile. While temperature fluctuations are informative for studying dissipation, mixing, and dispersion processes along with velocity data, they are typically measured with specialized Ultra-Fast Thermometer (UFT) sensors (Siebert et al. [179] and Kumala et al. [180]).

The power spectral densities (PSDs) calculated from the velocity components (left

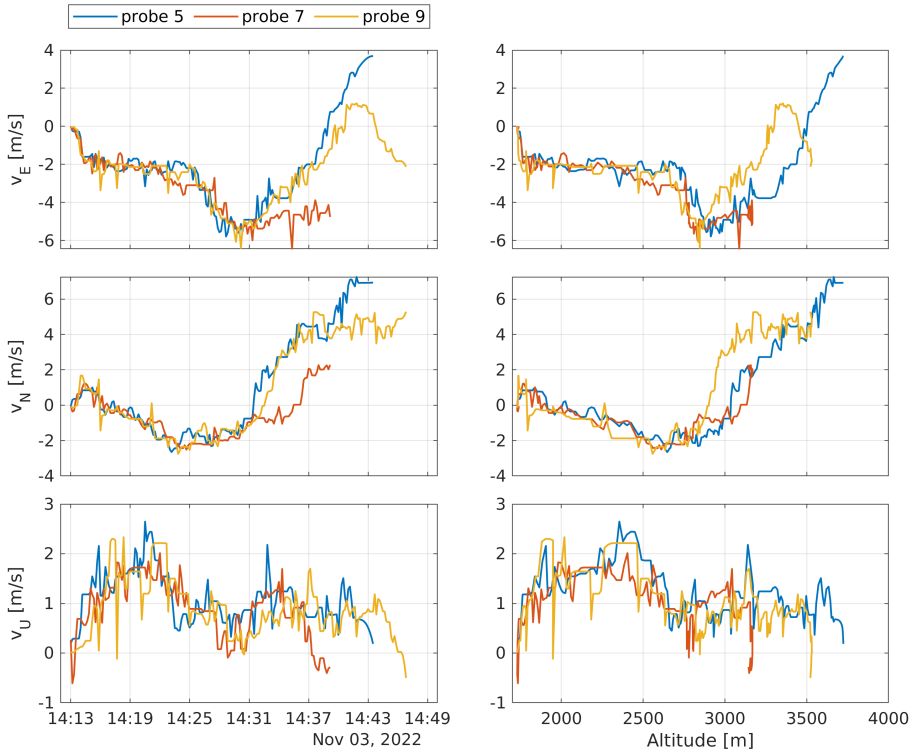

Figure 5.16: Measurements of East (E), North (N) and Up (U) velocity components from a subset of radiosondes during the OAVdA experiment, Aosta Valley on November 3, 2022.

panels) and horizontal wind speed (top right) are presented in Figure 5.17. As anticipated from Figure 5.16, the magnitudes of fluctuations are similar for all three components. Notably, the spectral slopes for the velocity components exhibit a better agreement with the theoretical -5/3 slope compared to the temperature and humidity spectra. The steeper slopes observed in the temperature and humidity spectra deviate from the theoretical -5/3 Kolmogorov spectrum, which is typically observed for well-resolved velocity spectra in the inertial subrange (smaller scales).

The following Figures 5.18 and Figure 5.19 highlight spectral analysis of temperature, humidity and 3D velocity components for a subset of probes during the flight during both WESCON epxeriments, CHilbolton, UK, July 5-6, 2023. Results are obtained from raw resampled readings of humidity temperature and velocity measurements (Figures 5.13). Measurements were resampled with 10 s equal intervals.

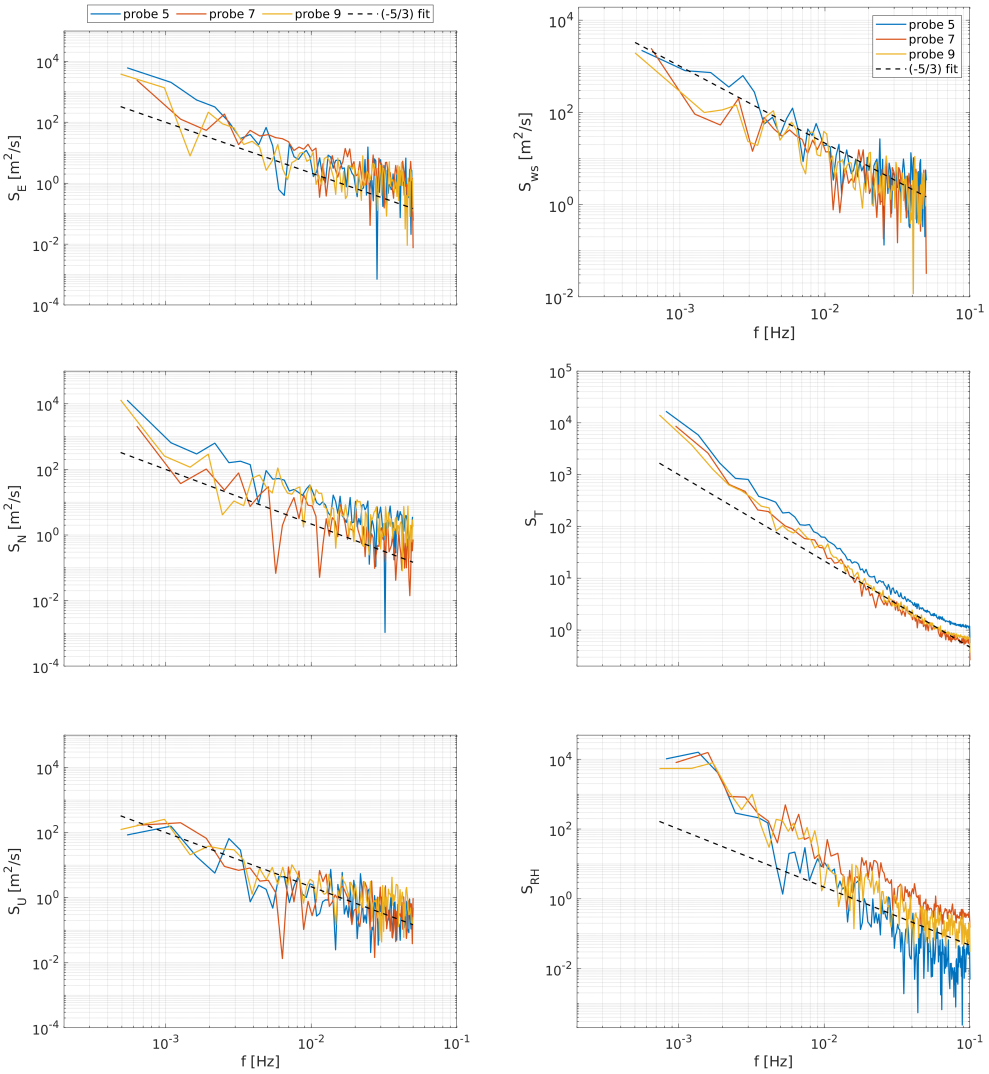

Figure 5.17: **Alpine boundary layer experiment. OAVdA, Valle d'Aosta, Nov 3, 2022**. Spectral analysis of velocity, wind speed, temperature and humidity fluctuations during the free flight of the radiosondes. Trend line (dashed black) is included for reference.

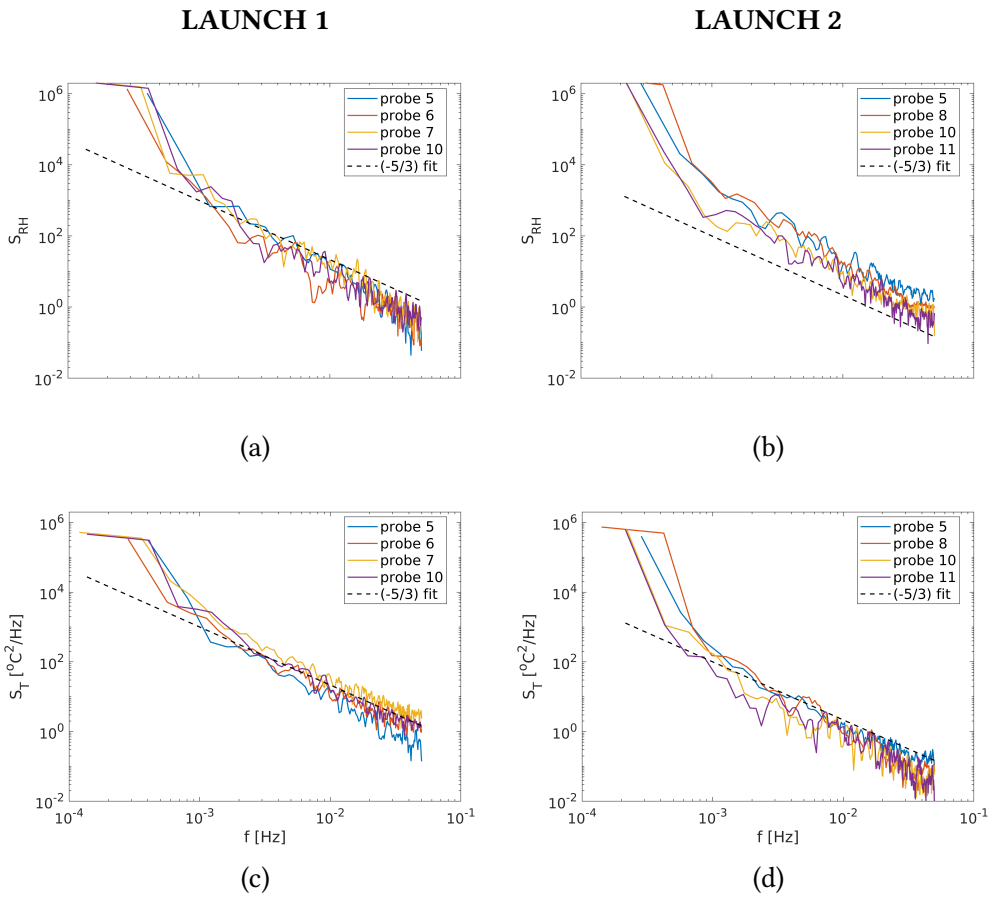

Figure 5.18: Cluster launch experiments at Chilbolton, UK, July 5-6, 2023. (a, c, e) **Pressure, humidity and temperature (PHT) readings** during the flight for a subset of probes. (b, d, f) Power spectral densities computed from PHT fluctuations. Panels are shown for the first launch (July 5, 2023).

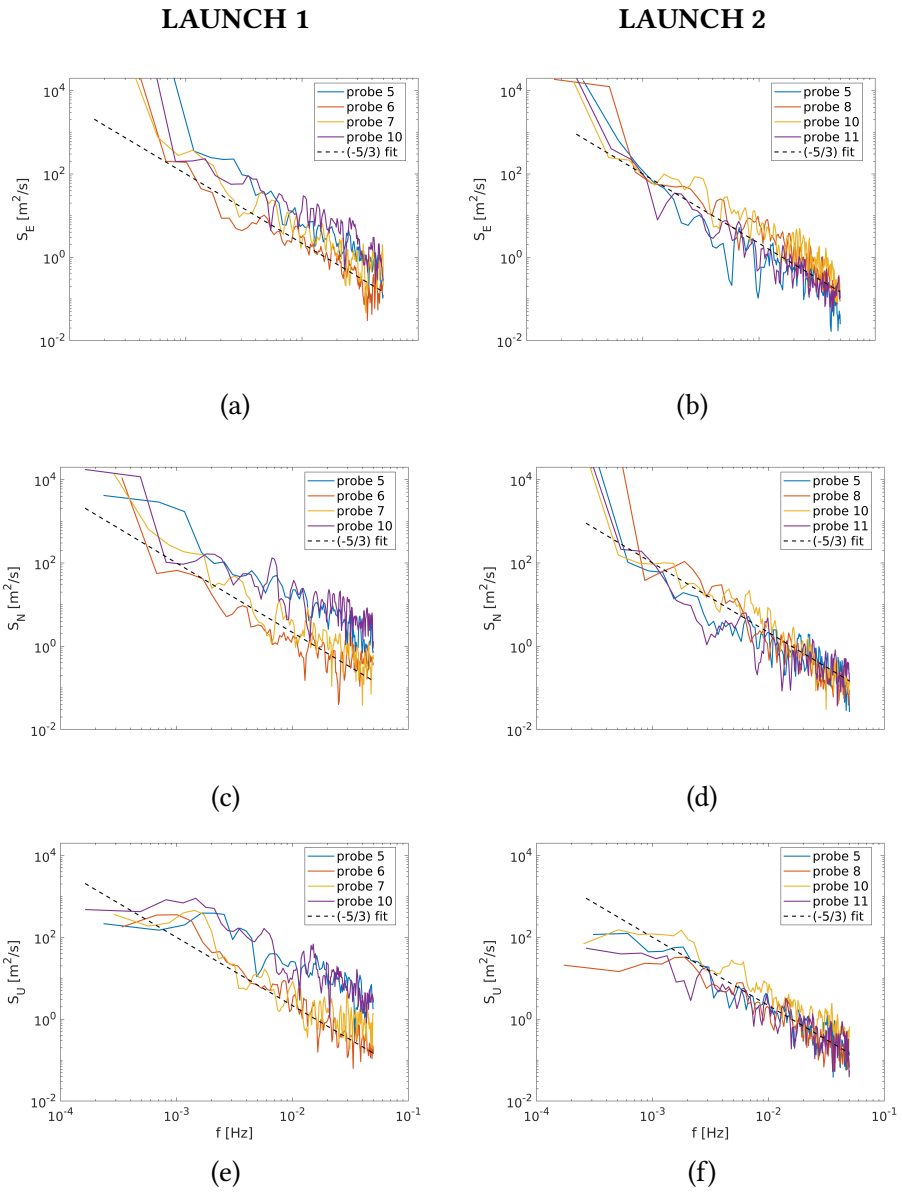

Figure 5.19: Power spectral densities of fluctuations of **3D velocity components** for a subset of probes during WESCON experiments, July 5-6, 2023, Chilbolton, UK.

5.3.1 Estimation of turbulent characteristics from cluster dataset

Established methods for estimating the dissipation rate of turbulent kinetic energy (TKE) rely on high-frequency measurements of turbulent velocities. These methods typically involve transforming the velocity spectra into the frequency domain. Large eddies, with characteristic length scales exceeding 100 meters, dominate the production of TKE. Through a process known as the inertial subrange, these large eddies transfer their energy to progressively smaller eddies. Eventually, as the eddy sizes decrease further, the energy dissipates into heat through molecular diffusion within the viscous subrange, where characteristic scales are on the order of centimeters or less [181].

As discussed in Chapter 2, most existing instrumentation for studying atmospheric turbulence characteristics relies on the Eulerian reference frame. Despite their bulkier nature, these Eulerian instruments offer advantages. They can provide highly accurate, state-of-the-art turbulence property estimations, including dissipation rate, turbulence intensity, TKE, velocity fluctuations, and resolution across the entire inertial range of the TKE spectrum. This capability is significantly aided by their high data rate sampling capabilities.

For example, the ACTOS tethered balloon system by Siebert, Lehmann, and Wendisch [8] offers high-resolution measurements of velocity components and temperature readings, with data rates of up to 100 Hz and potential length scale resolution down to 10 cm. These systems are well-suited for studying turbulence within the atmospheric boundary layer under various environmental conditions (Akansu et al. [31] and Muñoz-Esparza, Sharman, and Lundquist [182]).

For isotropic turbulence within the inertial subrange (in both wavenumber and frequency domains) as described by Batchelor [183], the following relationships hold:

$$F(k) = \alpha \varepsilon^{2/3} k^{-5/3}, \tag{5.4}$$

$$S(f) = \alpha \varepsilon^{2/3} \left(\frac{U}{2\pi} \right) f^{-5/3} \tag{5.5}$$

where $F(k)$ represents the wavenumber spectrum, k is the wavenumber, ε is the mean energy dissipation rate, $S(f)$ is the power spectral density in the frequency domain, f is the frequency, U is the mean wind speed, and α is the one-dimensional Kolmogorov constant (approximately 0.5 for the streamwise velocity component u). Equation (5.5) relates the power spectral density $S(f)$ to $F(k)$ using the Taylor hypothesis ($k = 2\pi f/U$).

With measurements of S(f) within the inertial subrange, the mean dissipation rate $\overline{\varepsilon}$ can be estimated using the following equation:

$$\overline{\varepsilon} = \frac{2\pi}{\overline{U}} \left(\frac{f^{5/3} S(f)}{\alpha} \right)^{3/2} \tag{5.6}$$

Alpine boundary layer experiment. Valle d'Aosta, Nov 3, 2022.

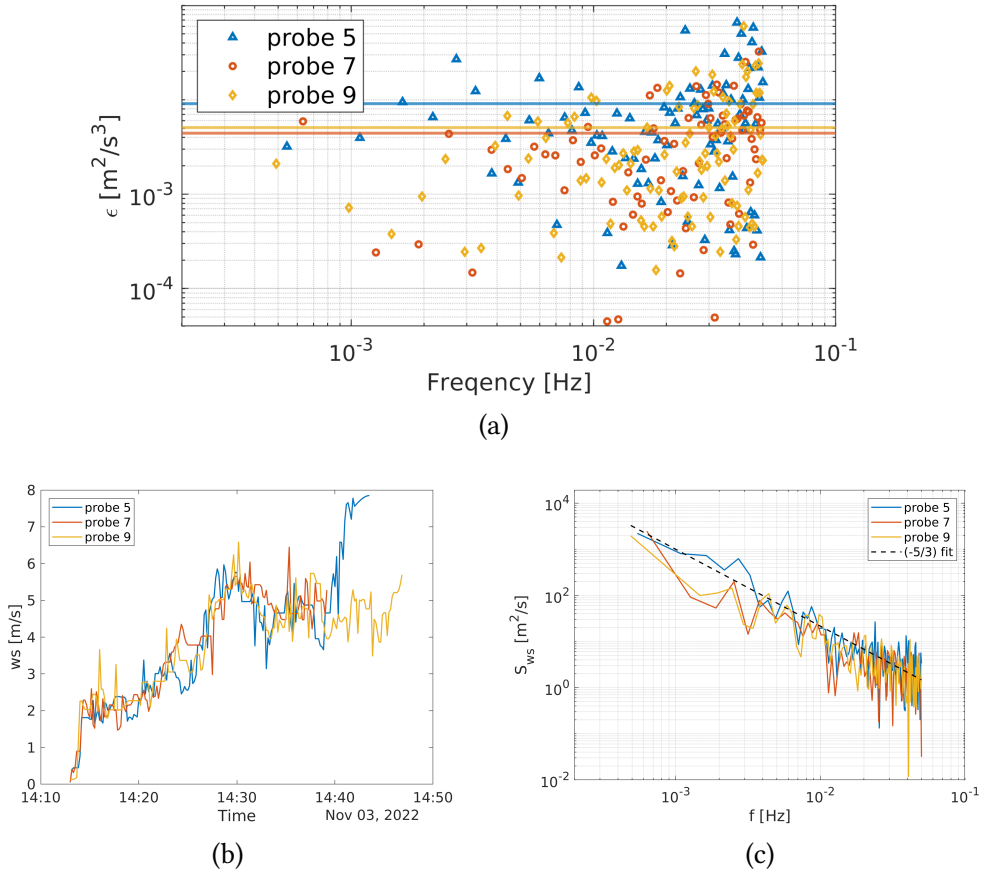

Figure 5.20: Mean energy dissipation rates estimated from horizontal wind speed measurements. (a) Estimations are presented for a subset of radiosondes using Eq. 5.6. Mean values are highlighted with solid lines (m^2/s^3): Probe 5 = 9.2 x 10^{-3}, Probe 7 = 4.4 x 10^{-3}, Probe 9 = 5.1 x 10^{-3}. Panels (b, c) shows time series and power spectral density of horizontal wind speed.

It is important to acknowledge two key limitations in applying these relationships to our data. First, verifying isotropic turbulence conditions is essential, and this may require additional instrumentation for independent verification. Second, resolving the full inertial subrange remains challenging with our current data acquisition rate.

Despite these limitations, the presented relationships provide a valuable framework for estimating flow turbulence properties based on experimental data, as demonstrated in existing literature. Therefore, as a preliminary analysis of the cluster data, we propose tentatively adopting these relations. However, for future detailed studies, it will be necessary to incorporate both anisotropy considerations and the broader wavenumber

range resolvable by our radiosonde cluster. It is also worth to mention that horizontal wind speed measurements were adopted for computation of dissipation rates. This is because stream of radiosondes mainly move along horizontal path by following wind in that direction.

The mean dissipation rate of turbulent kinetic energy (TKE) was estimated across the entire frequency range using horizontal wind speed data from the Aosta Valley experiment. The horizontal wind speed was calculated from the east and north velocity components presented in Figure 5.16. Equation 5.6 was employed for this dissipation rate estimation. Figure 5.20(a) presents the calculated mean dissipation rates for a subset of radiosondes (probes 5, 7, and 9). The dashed lines represent the mean dissipation values integrated across the entire frequency range, while the individual data points depict the dissipation rate at each specific frequency. The mean values of the estimated dissipation rates range from 4.4 x 10^{-3} to 9.2 x 10^{-3} m^2/s^3.

These estimated values fall within the range reported by O'Connor et al. [181] for TKE dissipation rate in the atmospheric boundary layer using lidar and in-situ tethered balloon measurements (100-600 m). As noted in their study, the dissipation rate typically falls between 10^{-6} and 10^{-2} m^2/s^3 within the boundary layer.

Similar analysis was performed for the WESCON experiment dataset for both cluster launches (Chilbolton, UK, July 5-6, 2023). Figures 5.21(a) and 5.22(a) show the estimated mean dissipation values during the launch. Horizontal wind speed measurements and power spectral densities are presented in panels (b) and (c) in both figures. During the first day, mean values of the estimated dissipation rates lay between 8.3 x 10^{-5} and 2.1 x 10^{-3} m^2/s^3. While, in the second day observed values were generally lower, which fall between 1.0 x 10^{-4} to 5.8 x 10^{-4} m^2/s^3 range. The main reason is that values of power spectra is lower during the second day. This generally holds for all component of velocity as shown in Figure 5.19. However mean values show more similar, since they lay within the same decade.

The WESCON 2023 campaign yielded a rich dataset that opens doors to exciting possibilities for expanding our analysis of turbulent characteristics beyond the radiosonde cluster data. The WESCON 2023 data provides a valuable opportunity to validate the frequency domain dataset obtained from the radiosonde cluster. Instruments like the Chilbolton Weather Radar serve as ideal tools for this purpose. The Chilbolton radar boasts a significantly larger range (up to 250 km) and continuous operation capabilities (potentially over 24 hours). This enables data collection over a much broader spatial and temporal domain compared to the radiosonde cluster (limited to about 50 km and 1.5-2 hours). By combining these datasets, we can gain insights into large-scale turbulent structures and their evolution across extended timeframes.

The WESCON 2023 data can also be employed to investigate anisotropy and mixing within the atmospheric boundary layer (ABL) and warm clouds using various methodologies:

- *Local isotropy assumption:* One approach assumes local isotropy within the inertial

Chilbolton boundary layer experiment. Chilbolton, UK, July 5, 2023.

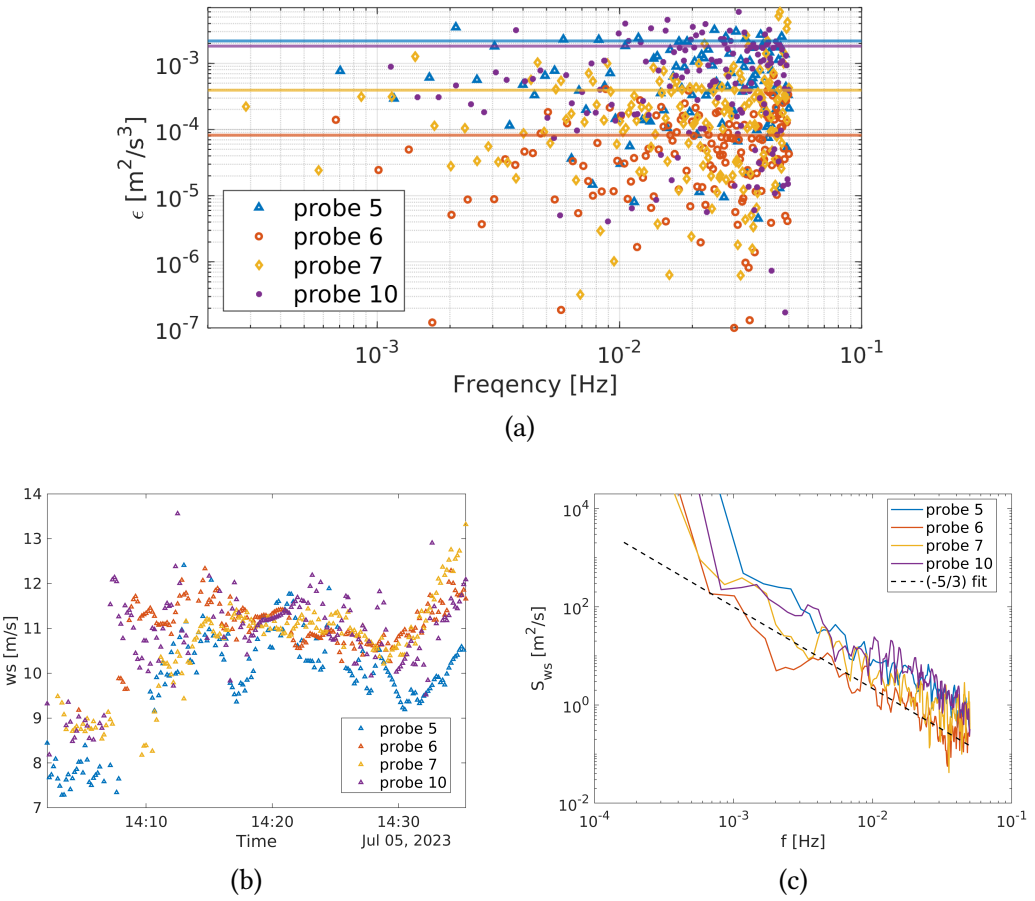

Figure 5.21: Mean energy dissipation rates computed from horizontal wind speed spectra for of subset of radiosondes (see Eq. 1). Dashed lines highlight the mean estimated values over all frequency range (m2/s3): Probe 5 = 2.1 x 10^{-3}, Probe 6 = 8.3 x 10^{-5}, Probe 7 = 3.9 x 10^{-4}, Probe 10 = 1.8 x 10^{-3}.

subrange of the turbulence spectrum. This method relies on the expected 4/3 ratio between the spectral densities ($S(f)$) of lateral and longitudinal wind velocity components (Siebert, Lehmann, and Wendisch [8]).

- *Event-based framework*: An alternative method utilizes the event-based framework, where "burst-like" activities identified during radiosonde flights, can help detect anisotropic regions within the ABL (Chowdhuri and Banerjee [184]).

By strategically combining data from the radiosonde cluster with information from other instruments deployed during WESCON 2023 and employing these advanced techniques, it is possible to achieve a significantly more comprehensive understanding of

Chilbolton boundary layer experiment. Chilbolton, UK, July 6, 2023.

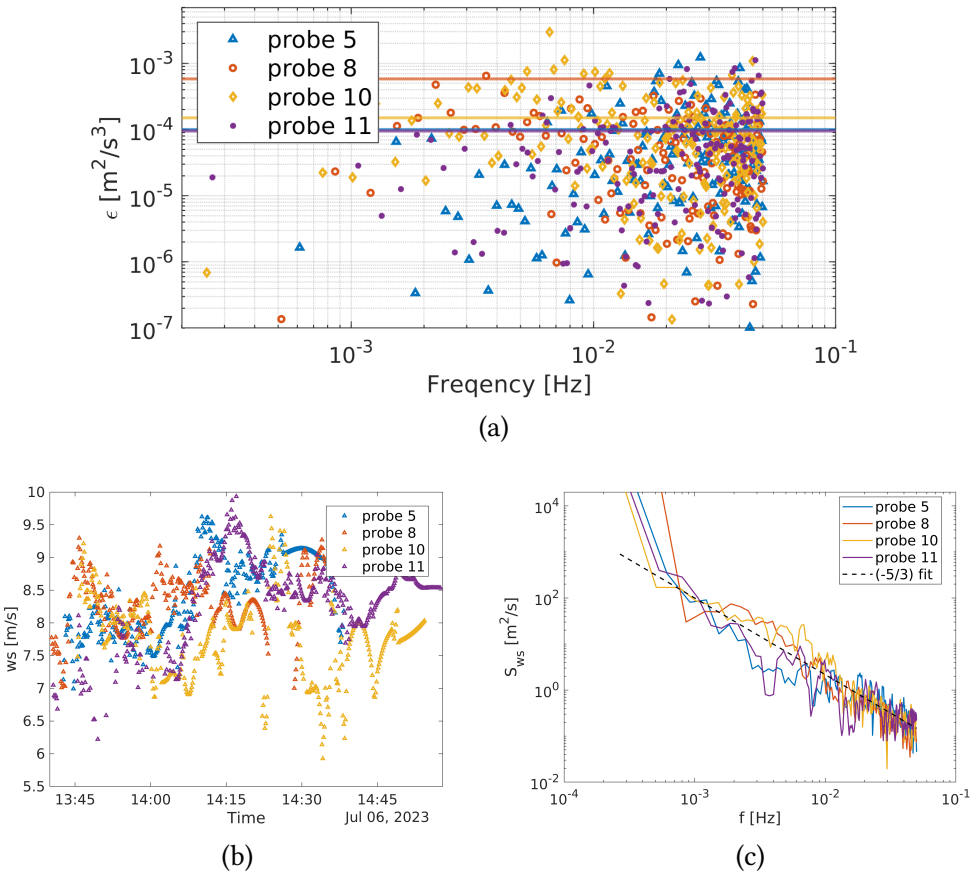

Figure 5.22: Mean energy dissipation rates computed from horizontal wind speed spectra for of subset of radiosondes (see Eq. 1). Dashed lines highlight the mean estimated values over all frequency range (m2/s3): Probe 5 = 1.0 x 10^{-4}, Probe 8 = 5.8 x 10^{-4}, Probe 10 = 1.5 x 10^{-4}, Probe 11 = 1.0 x 10^{-4}.

the dynamics and structures of turbulence within the ABL and warm clouds.

5.3.2 Capturing stability conditions inside ABL with cluster dataset

The Brunt-Väisälä ($\mathcal{N}^2$) frequency is a fundamental parameter in atmospheric dynamics and geophysics. It quantifies the stability or instability of a stratified air layer at a particular altitude. A positive $\mathcal{N}^2$ indicates a stable layer where vertical displacements of air parcels are opposed by buoyancy forces, while a negative $\mathcal{N}^2$ signifies an unstable layer where vertical displacements are enhanced. Stratification can vary considerably at different altitudes, leading to alternating stable and unstable regions within the lower

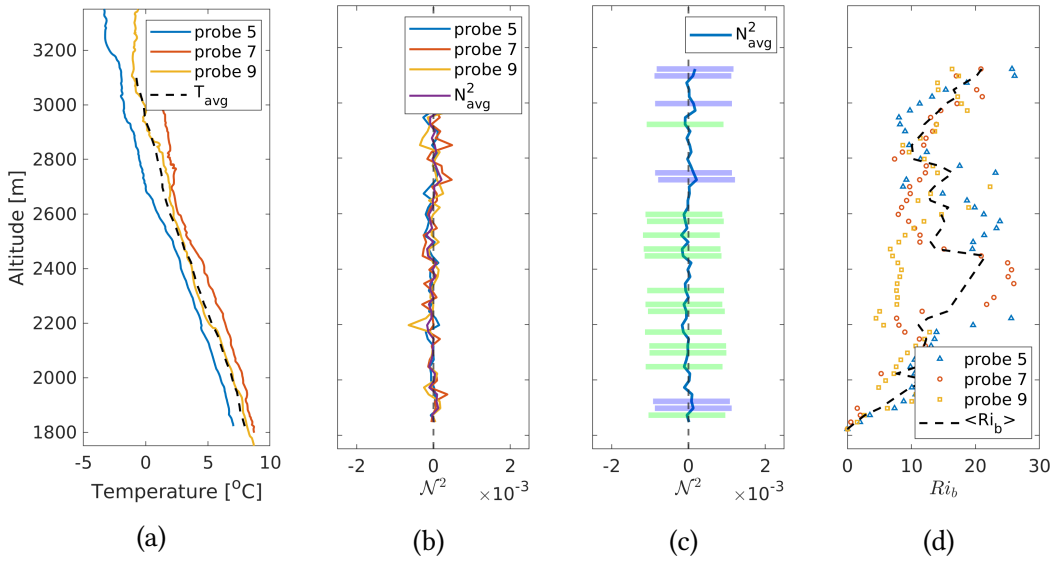

Figure 5.23: **Temperature profile and Brunt-Väisälä frequency (OAVdA Experiment, November 3rd, 2022).** (a) The vertical profile of temperature measurements throughout the altitude range. (b) The calculated Brunt-Väisälä frequency ($\mathcal{N}^2 = g\frac{\delta T}{T_0}\frac{1}{\Delta z}$) as a function of altitude, where T_0 = 281 K and g = 9.81 m/s^2. (c) The average Brunt-Väisälä profile calculated from the profiles of probes 5, 7, and 9. The shaded regions highlight the altitude ranges where all three probes exhibited a consistent temperature gradient: violet indicates a positive (stable) gradient, and green indicates a negative (unstable) gradient. (d) Estimated bulk Richardson number, Ri_b, see Eq. 5.8.

atmosphere.

Figure 5.23 presents the vertical profiles of temperature and the calculated BV frequency for the Aosta radiosonde dataset. The $\mathcal{N}^2$ values were computed using the established formula [171]:

$$\mathcal{N}^2 = g\frac{\delta T}{T_0}\frac{1}{\Delta z} \tag{5.7}$$

where g represents the acceleration due to gravity (9.81 m/s^2), δT is the change in temperature, T_0 is a reference temperature (281 K in this case), and δz is the vertical displacement. To calculate the BV profiles shown in panel (b), temperature readings were averaged within each 25-meter altitude interval. The positive $\mathcal{N}^2$ values in this panel correspond to a local stable stratification, with frequencies ranging from 0.002 to 0.007 Hz. A higher measurement rate is believed to enhance the spectrum profile and Brunt-Väisälä frequency representation, while constant bias and radiation offsets can be effectively removed during spectral analysis.

Panel (c) illustrates the statistically averaged $\mathcal{N}^2$ profile calculated within specific altitude intervals using data from probes 5, 7, and 9. The shaded regions highlight

altitude ranges where all three probes consistently experienced similar stability conditions: violet indicates stable (positive $\mathcal{N}^2$), and green indicates unstable (negative $\mathcal{N}^2$) conditions. The unshaded regions represent altitudes where probes exhibited varying stability conditions.

Another important non-dimensional measure of stability in the atmospheric boundary layer is the Richardson number. While the gradient Richardson number (Ri) is commonly used, its calculation can be sensitive to observational uncertainties. For observational datasets, the bulk Richardson number (Ri_b) is a more practical tool for estimating the relationship between thermodynamic stability and turbulence-related horizontal wind ([185, 186]). It is calculated using the following equation:

$$Ri_b(z) = \frac{g \cdot z \cdot \Delta\theta}{< \theta(z) > \cdot U_{ws}(z)^2}, \tag{5.8}$$

where θ_0 is the potential temperature of dry air at the surface and $\Delta\theta = \theta(z) - \theta_0$ is the temperature difference between the surface and altitude z. $< \theta >$ indicates mean θ between surface level (z_0) and z.

Panel (d) of Figure 5.23 presents the estimated values for Ri_b for three probes along with the mean profile computed from all probe values. Values are scattered between 0 to 30 and the mean profile lays between 10 and 20. The Ri_b is particularly useful for detecting the ABL height, which corresponds to the first elevation z with Ri_b exceeding a critical threshold. This threshold can be 0.22 for unstable (daytime) conditions or 0.33 for stable (nighttime) conditions [186, 185].

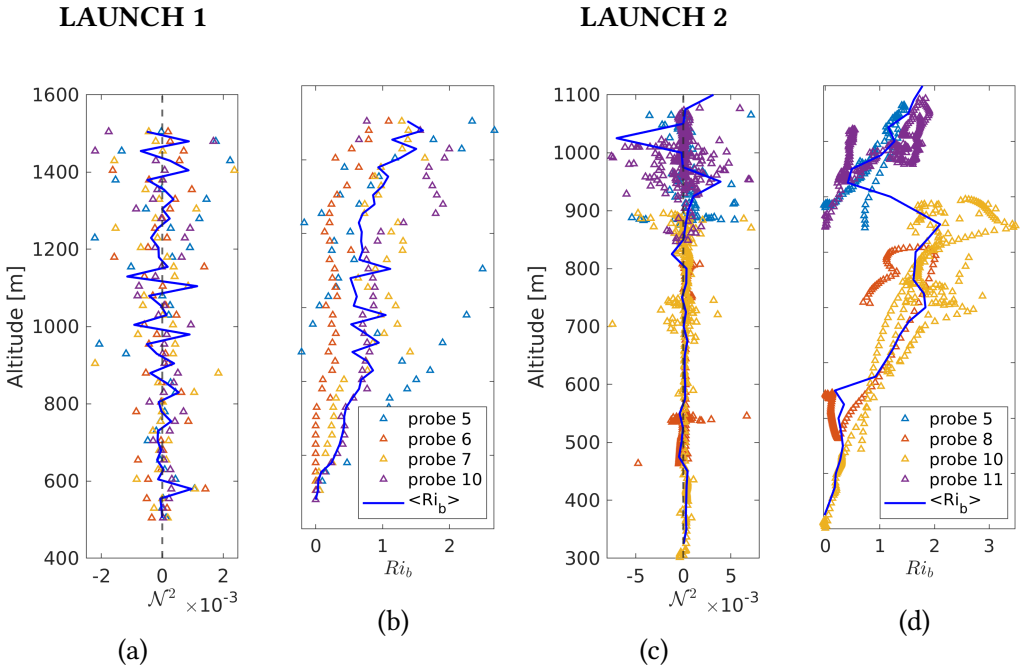

Figure 5.24: Vertical profiles of Brunt-Väisälä frequency ($\mathcal{N}^2$) and bulk Richardson number (Ri_b) during two WESCON launches (July 5-6, 2023, Chilbolton, UK). Panels a, b presents profiles for the first day of the experiment and c, d for the second day. (a, c) The calculated Brunt-Väisälä frequency, $\mathcal{N}^2$, as a function of altitude, where T_0 = 281 K and g = 9.81 m/s^2. (b, d) Estimated bulk Richardson number, Ri_b, see equation 5.8. It should be noted that the altitude for each probe is a function of the time and the position along their trajectories.

5.4 Relative dispersion analysis using radiosonde clusters

Following Richardson's (1926) [41] framework for turbulent dispersion, we analyze the relative motion of a cluster of radiosondes using the probability distribution function of their separation distances. Radiosondes, acting as "marked particles," are ideal for this analysis if they rise to a designated altitude and passively drift within the airflow. While recent studies have focused on the PDF of pair separation distances, we revisit Richardson's original PDF definition through the DNG function (Q) introduced in Equation 2.2.

The DNG, denoted by Q, describes the average number of neighboring radiosondes within specific distance intervals. Each element $Q_{n,n+1}$ represents the average number of radiosondes found within the distance range between n*h and (n+1)*h, where h is the constant size of the distance interval (neighborhood). Equation 5.9 details the calculation of Q. Here, N represents the total number of radiosondes, and $P^k_{n,n+1}$ signifies the number of neighbors for the k-th radiosonde (probe) within the distance bin (n,n+1):

$$Q_{n,n+1} = \frac{1}{N}(P^1_{n,n+1} + P^2_{n,n+1} + P^3_{n,n+1} + ... + P^N_{n,n+1}). \tag{5.9}$$

To obtain P^k for each radiosonde, we calculate its separation distance from all other radiosondes (N-1) and construct a histogram of these distances across all neighborhood intervals. For example, if h = 10 meters, $P^1_{0,1}$ represents the number of radiosondes neighboring radiosonde 1 within the 0-10 meter range. $P^1_{1,2}$ denotes the number of neighbors found between 10 and 20 meters for radiosonde 1, and so on.
Finally, $Q_{0,1}$ is calculated as the average of the $P^k_{0,1}$ values for all radiosondes, providing the average number of neighbors within the 0-10 meter range.

The DNG (Q) is a *space-time varying PDF*, computed from radiosonde position data for each time instance and distance interval. Initially, we applied the DNG concept to analyze water droplet dispersion within a simulated turbulent domain (see Appendix A.3). The algorithm was then adapted for experimental data.

We begin by analyzing datasets from the WESCON experiments conducted in Chilbolton, UK (July 5-6, 2023). Figure 5.25 highlights the space-time variations of Q values. The left and right panels represent the first and second launches, respectively. The colorbar indicates the average number of neighbors per unit area, characterized by both time (seconds) and distance interval (with a width of 500 meters). These color plots suggest potential linear diffusion patterns.

Figure 5.26 presents the extracted Q values for specific time instances across different distance intervals (line plots with points). The top panels depict variations of Q over distance intervals, while the bottom panels show the maximum Q value variations over time. The bottom panels include three DNG realizations for each launch, obtained by changing the neighborhood size (h) between 500 meters, 100 meters, and

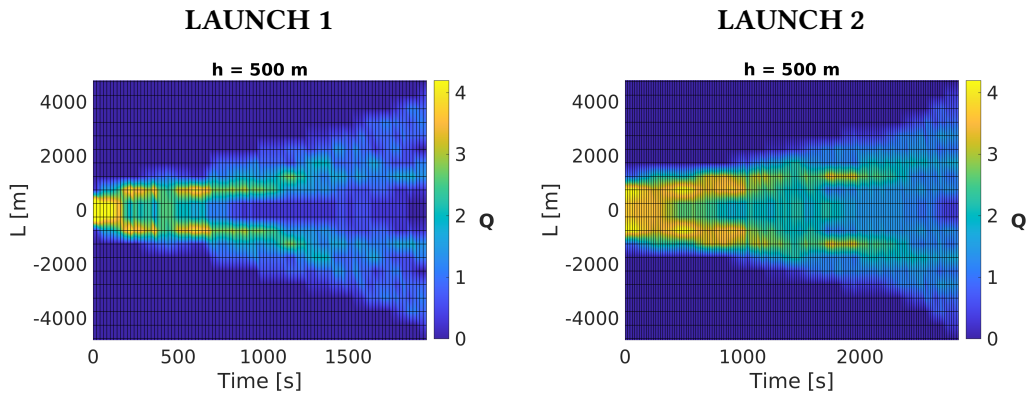

Figure 5.25: Cluster launch experiments during WESCON 2023 campagin, July 5-6, Chilbolton, UK. A number of neighbors plotted over time and neighborhood bins.

200 meters. As expected, smaller neighborhoods result in lower Q values due to the reduced search range for neighboring radiosondes. The bottom panel line plots (c) and (d) suggest an exponential scaling of Q values over time for different realizations. Table 5.6 summarizes the observed exponential scaling.

Table 5.5: Exponential scaling of number of neighbors inside neighborhood for different size of the neighborhood.

	Launch 1	Launch 2
h = 100 m	1.9 * exp(-0.0006 * t)	1.4 * exp(-0.0002 * t)
h = 200 m	3 * exp(-0.0007 * t)	2.1 * exp(-0.0002 * t)
h = 500 m	4.5 * exp(-0.0006 * t)	4.4 * exp(-0.0003 * t)

While Richardson's (1926) analysis using DNGs provided valuable insights, it did not account for temporal variations in the diffusion process [1]. To address this limitation in our study of both numerical simulations and radiosonde cluster experiments, we propose employing a time-dependent diffusion function:

$$F(l, t, \varepsilon) \sim \varepsilon^{\alpha}\, t^{\beta}\, l^{\gamma}$$

where $F(l, t, \varepsilon)$ represents the diffusion function as a function of separation distance (l), time (t), and the TKE (turbulent kinetic energy) dissipation rate (ε). α, β, and γ are constants to be determined.

For now, we will focus on analyzing the DNG (Q) itself, including its scaling behavior and its relationship to other dispersion metrics like mean separation distance and volumetric scaling. In a later stage, we will revisit the diffusion function analysis by incorporating or combining data from both numerical simulations (millimeter-scale water

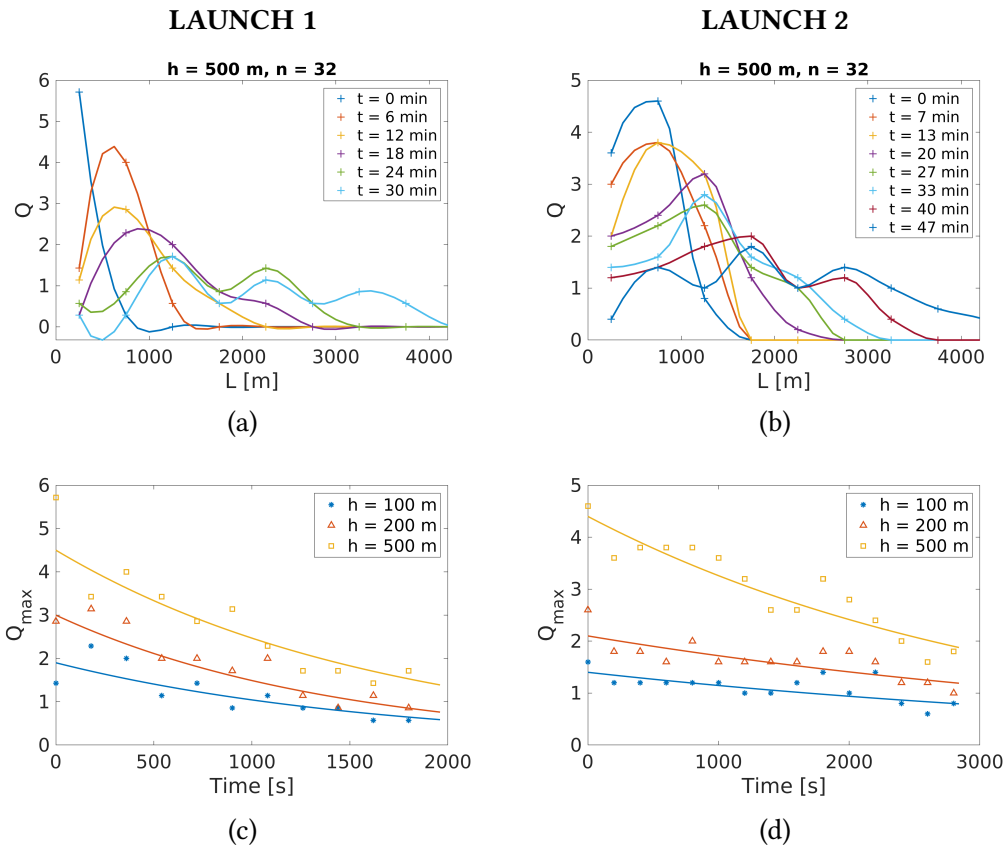

Figure 5.26: The distance-neighbor graph PDF computed from radiosonde position dataset. The left panels highlight the first launch, while the right panel shows the second launch. See below Table 1 for the scaling of exponential interpolations.

droplet diffusion) and experimental radiosonde cluster data (10s of km dispersion). This combined approach aims to provide a more complete picture of the diffusion function across various scales.

5.4.1 L_{Qmax} and mean separation

Mean square separation analysis is a widely used technique for studying dispersion, particularly in the context of homogeneous and isotropic turbulent flows [56, 58, 64, 67] The well-known Richardson-Obukhov (R-O) scaling relates the mean square separation distance (l^2) to time (t) with a cubic dependence (t^3):

$$l^2 = {l_0}^2 + g_l \varepsilon t^3$$

as shown in Eq. 2.7 (recalled from Chapter 2). Here, l_0 represents the initial separation distance, g_l is a constant related to the scaling behavior, and ε is the TKE dissipation

rate. It's important to note that while g_l is often assumed to be a universal constant, its precise value remains debated [67].

Before delving into DNG results, we performed a basic mean square separation analysis on the data from the WESCON experiments conducted in Chilbolton, UK (July 5-6, 2023). Figure 5.27 depicts the mean separation distance over time, with power-law scaling applied to highlight potential trends. Interestingly, the data for the second day appears to exhibit faster time scaling. This fact should be further investigated considering atmospheric flow conditions in the experiment day (obtained from radars, weather stations, numerical predictions, etc.).

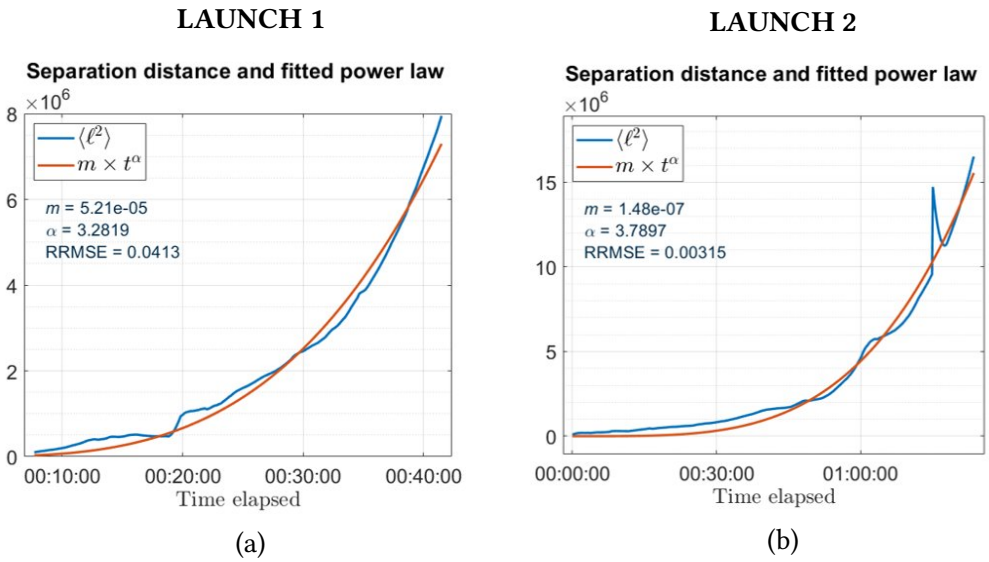

Figure 5.27: Mean relative distances and power law scaling. The left panels highlight the first launch, while the right panels show the second launch.

We further analyzed the DNG data by examining the scaling behavior of L_{Qmax}, which represents the separation distance corresponding to the peak value (Q_{max}) of the DNG function (Q). In simpler terms, L_{Qmax} indicates the distance range where the highest number of neighboring radiosondes are likely to be found. While not identical to the mean separation distance, these values are often quite close in practice.

Table 5.6 and Figure 5.28 summarize the scaling properties of L_{Qmax}. Three different neighborhood sizes (h) of 100 meters, 200 meters, and 500 meters were used to generate multiple realizations of the analysis.

Our findings share similarities with the work by Lacorata et al. [53], who revisited the EOLE experiment data [52]. Initially, they explored power-law scaling but later observed an exponential scaling behavior. They concluded that the prediffusive regime (initial dispersion phase) exhibited exponential scaling, while the power-law behavior might characterize a later stage with a time-dependent exponent between 1 and 3 [53,

55]. For a more comprehensive analysis, it would be beneficial to identify and differentiate between the prediffusive and diffusive phases within our radiosonde position data.

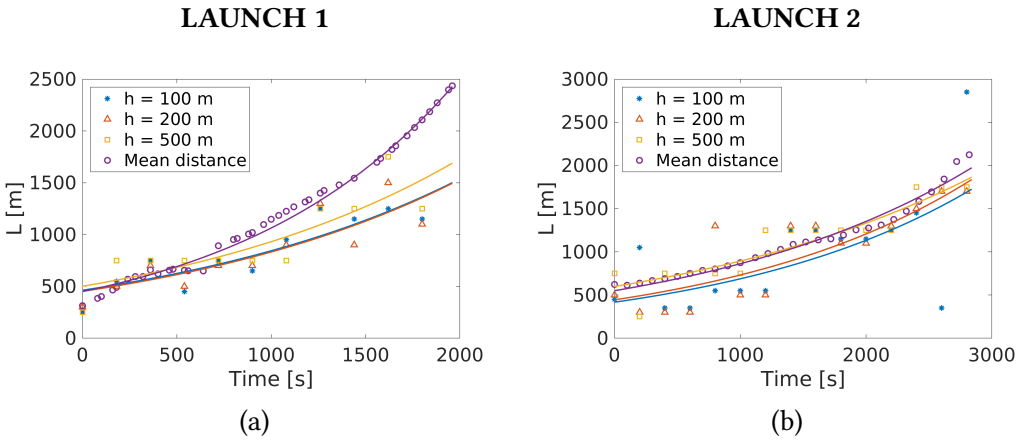

Figure 5.28: Relative distance estimation comparison. The left panel highlights the first launch, while the right panel shows the second launch. See below Table 2 for the scaling of exponential interpolations.

Table 5.6: Exponential scaling of relative distance (L_{max} or mean distance) within radiosonde cluster. L_{max} was computed for different values of neighborhood size, H.

	Launch 1	Launch 2
h = 100 m	463 * exp(0.0006 * t)	417 * exp(0.0005 * t)
h = 200 m	452 * exp(0.0006 * t)	444 * exp(0.0005 * t)
h = 500 m	501 * exp(0.0006 * t)	599 * exp(0.0004 * t)
Mean distance	450 * exp(0.0009 * t)	550 * exp(0.00045 * t)

5.4.2 Generalization of Q graph for relative measurements

Figure 5.29 demonstrates the application of the DNG function (Q) to analyze the relative dispersion of radiosonde measurements. We extracted a 20-minute temperature and humidity dataset (starting at 14:18) and a 12-minute position and velocity dataset from the OAVdA experiment (Aosta, Italy, Nov 3, 2023).

Panel (a) shows the DNG (Q_L) computed for the relative distances between radiosondes. Here, h represents the distance interval size (set to 100 meters in 3D) and Q was calculated every 10 seconds and then averaged over each minute. The graph displays Q values for the 1st, 4th, 7th, and 10th minutes across the distance range of -400 to

400 meters. We can observe the DNG widening over time. Initially, there are roughly 2.5 neighboring radiosondes within the first distance interval (100 meters). As time progresses, this number decreases for the central interval but increases for intervals further away, indicating dispersion.

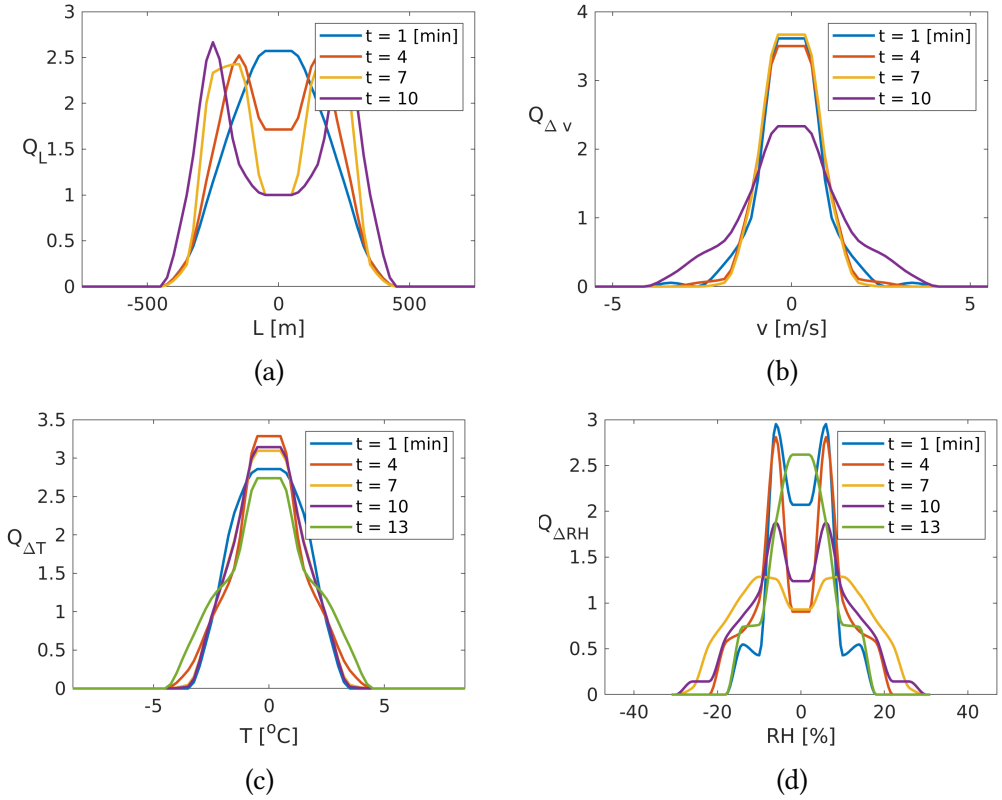

Figure 5.29: Relative measurements of the temperature, humidity, distance, and wind speed during the free-floating experiment in OAVdA, November 3, 2022. Distributions of the these quantities were computed using the distance-neighbor graph function (eq. 5.9) between the radiosondes inside a cluster: (a) relative distance, (b) relative wind speed, (c) relative temperature, and (d) relative humidity. The analysis was initiated at 14:18.

By extending the "distance interval" concept to other "relative measurements," we can compute Q for temperature ($Q_{\Delta T}$), humidity ($Q_{\Delta RH}$) and wind speed ($Q_{\Delta v}$) differences. Instead of distance, we use the absolute value of the difference in readings (ΔT, ΔRH, Δv) between radiosonde pairs. The chosen absolute difference range sizes (h) are 1°C, 2%, and 0.75 m/s for temperature, humidity, and wind speed, respectively.

A key advantage of DNGs is their ability to directly quantify the turbulent dispersion of these physical quantities, as shown in Figure 5.29. Additionally, since all panels share the same structure as Equation 5.9, it facilitates the identification of potential high correlations between different measured fields.

5.4.3 Volumetric scaling analysis using convex hulls

This section explores a non-trivial dispersion analysis technique using three-dimensional convex hulls. A convex hull represents the minimal volume convex object encompassing all the 3D positions of the radiosondes. Analyzing convex hulls provides insights into the volumetric scaling of cluster dispersion(l^3 scaling). This complements the l^2 scaling observed in the mean square separation analysis (Figure 5.27) and the l_{max} scaling identified using DNG analysis (Figure 5.28).

LAUNCH 1

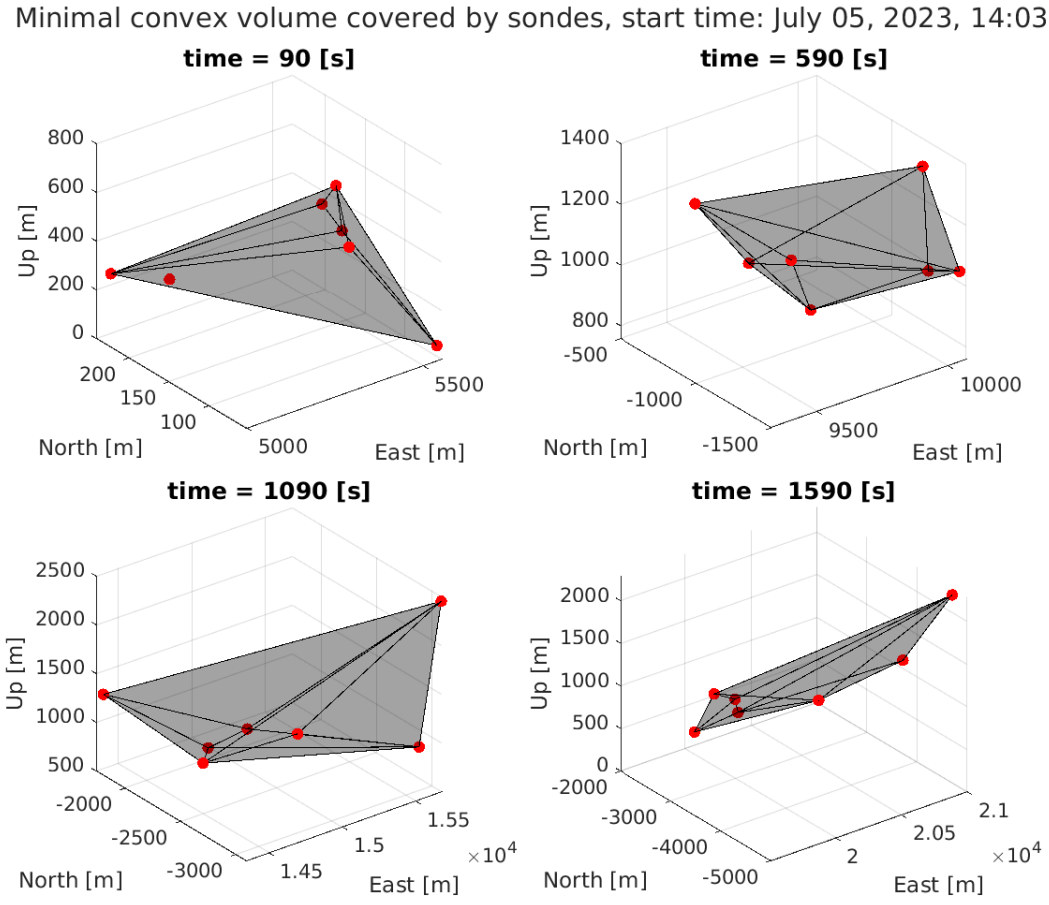

Figure 5.30: Minimal convex shapes covered by all sondes during the first cluster launch, **July 5, 2023**, Chilbolton, UK. Panels highlight four time instances, starting from **14:03**. Red dots highlight actual positions of sondes in ENU (East, North, Up) frame.

Figures 5.30 and 5.31 visualize the convex hulls for different time instances during the two WESCON experiments (July 5-6, Chilbolton, UK). The analysis considers the

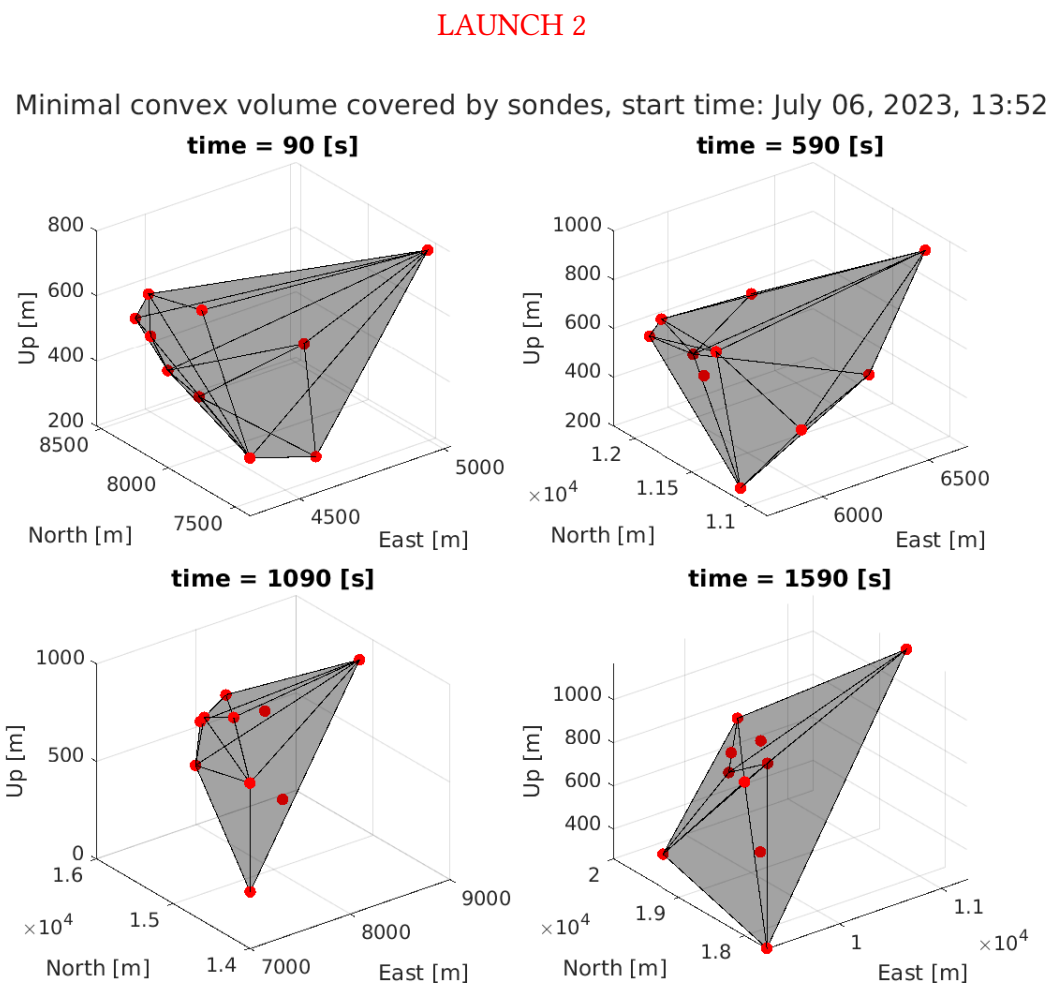

Figure 5.31: Minimal convex shapes covered by all sondes during the first cluster launch, **July 6, 2023**, Chilbolton, UK. Panels highlight four time instances, starting from **13:52**. Red dots highlight actual positions of sondes in ENU (East, North, Up) frame.

common range encompassed by the radiosonde ENU (East-North-Up) data readings.

Figure 5.33 combines the results from the three dispersion analysis methods. Panels (a) and (b) compare the dispersion (separation) of radiosondes obtained using the different methods for the two WESCON launches. The figures also include the $l\ t^{3/2}$ Richardson-Obukhov scaling (dashed gray line) for reference. Panels (c) and (d) plot half of the DNG data (Q-graph). The red and black lines represent the cubic root of the convex volume and the mean separation distance, respectively.

For comparison purposes, the cubic root of the convex volumes ($V_{\text{conv}}^{1/3}$) was calculated. Three different realizations of L_{Qmax} are provided here: l_{100}, l_{200} and l_{500} ,

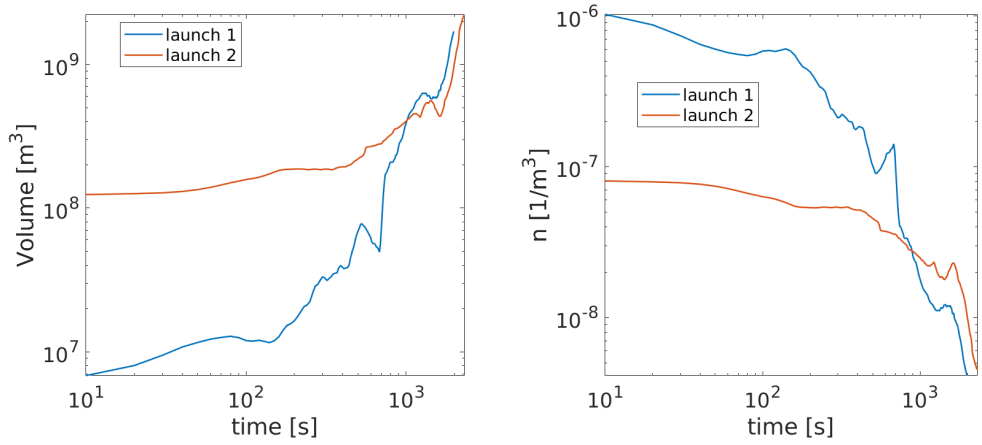

Figure 5.32: Minimal convex volume covered by all sondes and computed numerical concentration per volume during the WESCON cluster launches, July 5-6, 2023, Chilbolton, UK. (a, b) minimal convex volume, covered by all radiosondes. (c, d) Numerical concentration of radiosondes within the convex volume.

corresponding to different neighborhood sizes (h) used in the DNG analysis.

We observe similar trends between the mean separation distance and the cubic root of the convex volume, particularly for the second day of the experiment. The raw L_{Qmax} values (shown here) differ from the exponentially fitted lines presented in Figure 5.28. While it's challenging to discern a clear trend from the raw L_{Qmax} values, panels (c) and (d) incorporate volume and mean separation scaling lines on top of the space-time color plot of the Q-graph for better comparison.

In general, all three methods exhibit good agreement. The color plots in panels (c) and (d) suggest the potential formation of two sub-clusters towards the end of the observation window. This is further supported by the scattered ENU data plots in Figure 5.11 (panels a, c, and e), which reveal a division into two smaller sub-clusters (three and four radiosondes each).

However, mean separation and convex hull volume are more aggregated (averaged) measures and cannot capture this sub-clustering as effectively. The only possible indication in the mean separation values is a change in slope, suggesting an acceleration in separation. The discretized step-like behavior of the L_{Qmax} values can be attributed to the smaller number of radiosondes used in the analysis. When this analysis was applied to a numerical simulation dataset with ~500 water droplets (results included in Appendix A.3), the results were smoother. Due to brevity, only the experimental data results are presented here. Simulations should be extended for longer durations to draw more definitive conclusions (refer to Figure A.8 panel (f)).

Another observation is that the $V_{\text{conv}}^{1/3}$ values are generally lower than the l_{sep} values.

However, normalizing both values with their initial counterparts (initial volume $V_0^{1/3}$ and initial separation distance l_0) yields comparable values. This further validates the consistency between these two approaches.

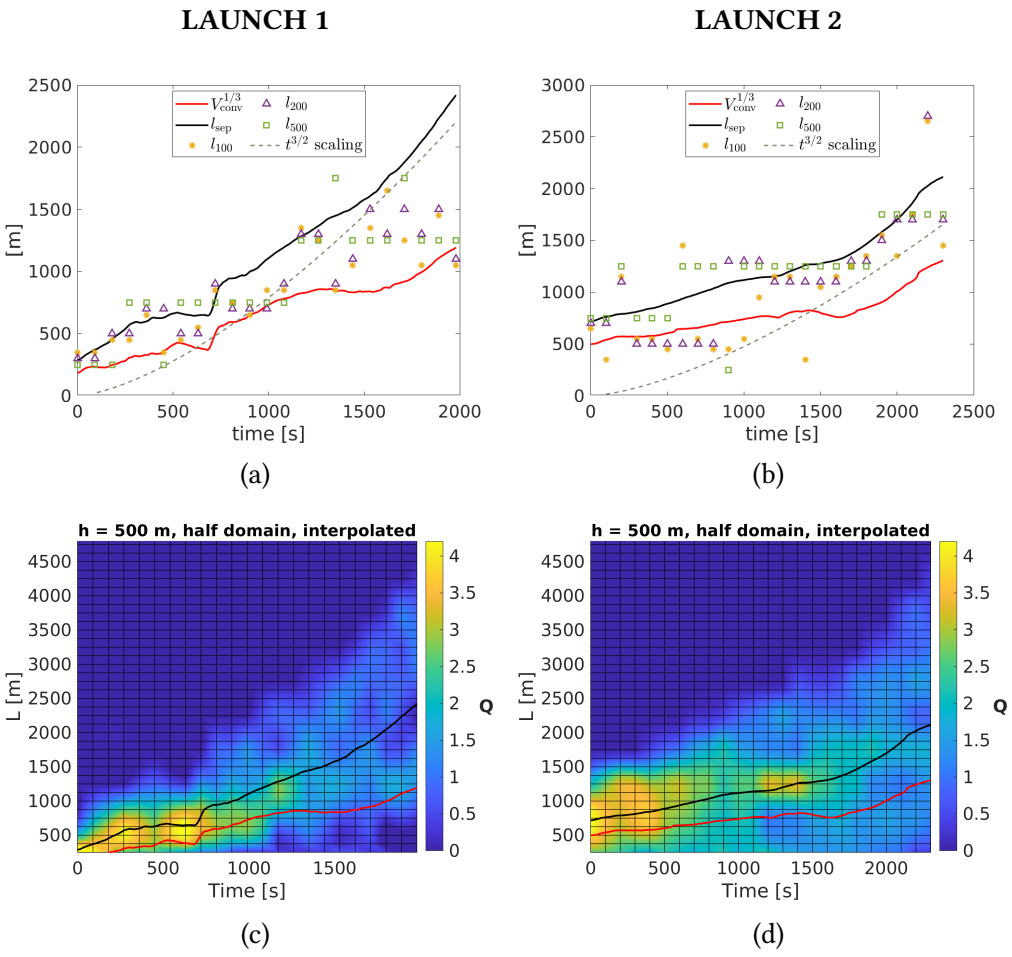

Figure 5.33: Comparison among different types of analysis to compute dispersion (separation) of radiosondes during two WESCON launches (July 5-6, 2023, Chilbolton, UK). (a, b) Convex volume, mean separation and L_{Qmax} values as indicator of dispersion. $l \sim t^{3/2}$ scaling is provided for comparison. (c, d) Half domain of Q graph is plotted. On top of the Q graph, cubic root of convex volume and mean separation distance lines plotted.

5.5 Towards space-time Lagrangian correlation analysis

Space-time correlations have played a crucial role in turbulence research for decades. They provide a vital statistical tool for analyzing turbulent flows by capturing the rich information present within a turbulent field at different spatial and temporal separations (Wallace [187]). These correlations are calculated in both Eulerian (fixed point in space) and Lagrangian (following a fluid particle) reference frames, offering valuable insights into the dynamic coupling between various scales of motion within turbulent flows (He, Jin, and Yang [188]).

Space-time correlations quantify how fluctuations at one location and time co-vary with fluctuations at another location and time. By analyzing these correlations, scientists gain a deeper understanding of how turbulent fluctuations interact and evolve across both space and time [188].

In the context of the radiosonde cluster system, the autocorrelation function serves as a valuable tool for analyzing the temporal variability of measured quantities. It measures the correlation between the fluctuations of a time series data set $X'(t)$ and $X'(t+\tau)$, where τ is the time lag. In the context of the radiosonde cluster system, a time series $X(t)$ data can be constructed from any Lagrangian dataset obtained along the trajectory. For instance, consider the separation distance, $\mathrm{d}_{i,j}(t)$, between radiosonde i and radiosonde j (Figure 5.34(b)). This separation distance is computed based on the 3D positions, $\mathrm{r}_i(t)$, of the probes along their trajectories, as shown in Figure 5.34(a). The mean separation distance can be found in Figures 5.27 and 5.33.

The mathematical definition of the autocorrelation function, denoted as $R_X(\tau)$, for a time series with mean μ_X and variance σ_X^2 is given by [44]:

$$R_X(\tau) = \frac{\overline{(X(t) - \mu_X)(X(t+\tau) - \mu_X)}}{\sigma_X^2} \tag{5.10}$$

where, overbar indicates al over time range.

By analyzing the autocorrelation function for different time lags, we can gain insights into the *characteristic turbulent timescales* of the fluctuations within the measured quantities. For example, a rapidly decaying autocorrelation function suggests that the fluctuations are short-lived and uncorrelated over longer timescales. Conversely, a slowly decaying autocorrelation function indicates that the fluctuations are persistent and have a longer memory. The autocorrelation of $\mathrm{r}(t)$ provides insights into when the trajectory deviates from local flow dynamics and becomes increasingly deviated from initial conditions.

This approach can be applied to various Lagrangian datasets obtained from the radiosonde cluster system. Analyzing the autocorrelation of separation distances between radiosondes, for instance, can provide information about the characteristic timescales

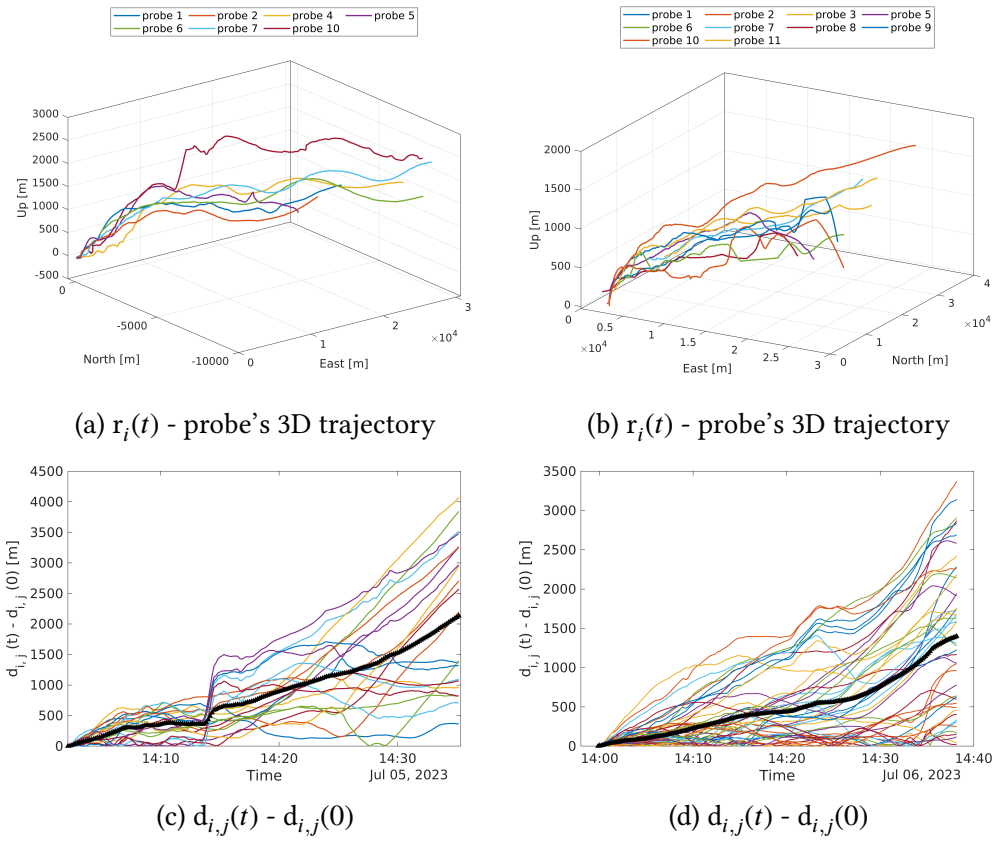

(a) $r_i(t)$ - probe's 3D trajectory

(b) $r_i(t)$ - probe's 3D trajectory

(c) $d_{i,j}(t)$ - $d_{i,j}(0)$

(d) $d_{i,j}(t)$ - $d_{i,j}(0)$

Figure 5.34: Separation distances over time between pair of radiosondes. it should be in the form of $(r(t)-r_0)^2$

of dispersion within the cluster. Similarly, the autocorrelation of other measured quantities, such as velocity or temperature fluctuations, can offer insights into the temporal variability of these parameters.

Figures 5.35 and 5.36 present the computed autocorrelation functions for various quantities measured by the radiosonde cluster system. These functions reveal the characteristic timescales over which fluctuations in the measured quantities persist.

Panel (a) shows the autocorrelation functions for the east, north, and up components of the radiosonde trajectories. Since only mean values are reported here, a detailed analysis is not possible. However, it's noteworthy that high correlation values along the north and east directions agree with the observations in Figure 5.11, which indicated a strong southeast wind. The faster decay of the vertical component's correlation is expected as the trajectory doesn't exhibit a monotonic trend in altitude.

Panels (c) and (d) depict the mean autocorrelation profiles for horizontal wind speed and temperature fluctuations, respectively. The black lines with triangular markers represent the mean profiles. Both quantities exhibit a similar trend, with correlation

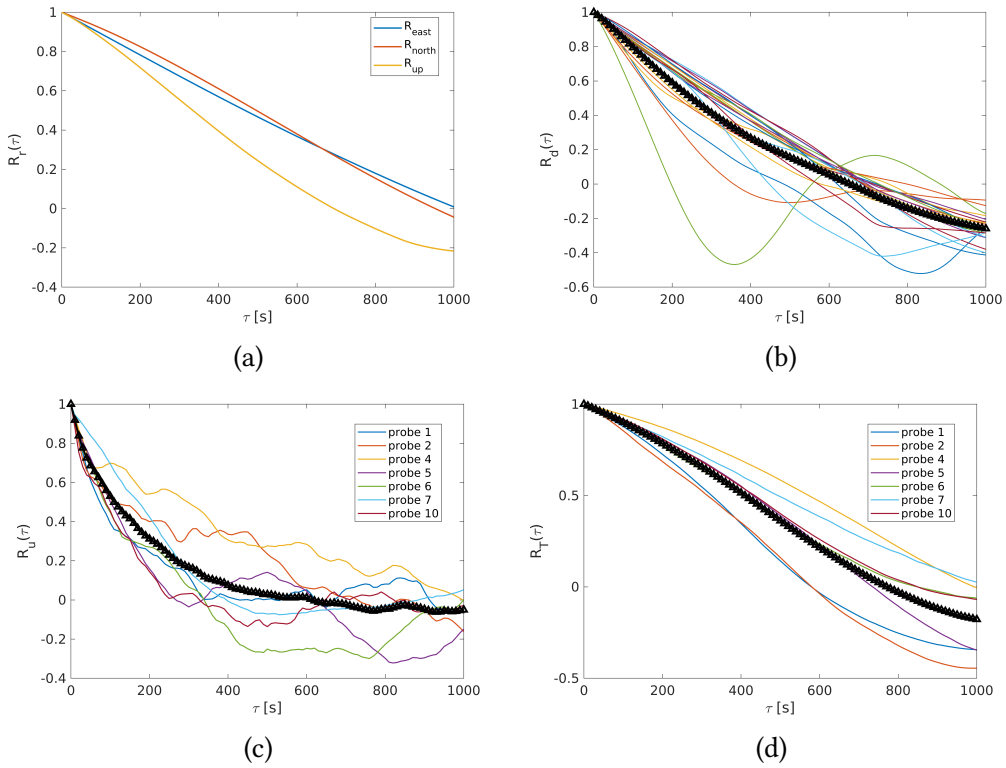

Figure 5.35: Sample autocorrelations of 3 components of trajectory data, separation distance between pair of radiosondes, horizontal wind speed and temperature fluctuations during the first day of the WESCON 2023 experiments, July 5, 2023, Chilbolton, UK.

values decaying over time. However, the decay is faster for horizontal wind speed, dropping below 0.5 after approximately 100 and 180 seconds for the first and second days, respectively. Temperature fluctuations show a slower decay, staying above 0.5 for a longer duration (around 450 and 350 seconds for days 1 and 2, respectively).

The autocorrelation function for separation distances between radiosondes (panel (b)) displays a similar timescale to temperature (around 300 seconds for both days). However, unlike the other quantities, the separation distance autocorrelation exhibits negative correlation values at some lags.

In ideal homogeneous and stationary scenarios, the autocorrelation function should approach zero (or at least saturate) as the time lag increases. This behavior is observed for the wind speed autocorrelation in both days, suggesting a well-defined timescale for wind speed fluctuations. The separation distance autocorrelation shows a similar, but less pronounced, tendency towards saturation.

The temperature autocorrelation, on the other hand, deviates from this ideal behavior, not exhibiting a clear saturation trend. This may indicate non-stationarity or inhomogeneity in the temperature field. The trajectory components (panel (a)) also

show a non-zero value at the maximum lag, suggesting potential non-stationarity in the overall trajectory patterns. However, the slight saturation trend towards the end for the up-component autocorrelation might indicate a characteristic timescale for vertical fluctuations. These observations highlight the importance of considering potential non-stationarity or inhomogeneity when interpreting the autocorrelation functions. Further analysis may be required to fully understand the dynamics of the measured quantities, particularly for temperature and trajectory components.

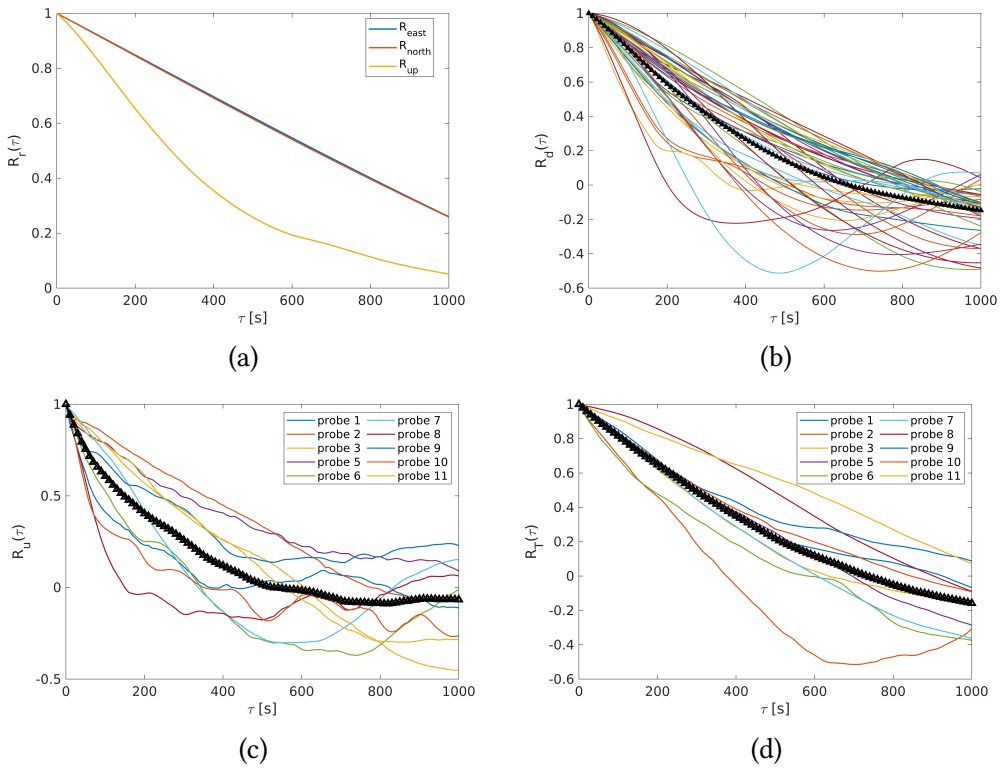

Figure 5.36: Sample autocorrelations of 3 components of trajectory data, separation distance between pair of radiosondes, horizontal wind speed and temperature fluctuations during the second day of the WESCON 2023 experiments, July 6, 2023, Chilbolton, UK.

Time-dependent correlations

Estimating autocorrelation values and integral timescales from finite time series data can be statistically challenging. This is particularly true for non-stationary data, which commonly occurs in various turbulent flows, such as decaying isotropic turbulence, homogeneous shear flow, or unsteady mixing scenarios [44].

A common approach to address non-stationarity effects is to introduce time windows for correlation computations. This essentially allows the autocorrelation function

(ACF) to vary over time. Equation (5.10) is modified by incorporating a time window index, k, as shown in Equation (5.11). This new equation, denoted as $R_X(t^k, \tau)$, represents the autocorrelation function calculated for a specific time window, t^k:

$$R_X(t^k, \tau) = \frac{\overline{(X(t^k) - \mu_{X(t^k)})(X(t^k + \tau) - \mu_{X(t^k)})}}{\sigma^2_{X(t^k)}} \tag{5.11}$$

Here, $\mu_{X(t^k)}$ and $\sigma^2_{X(t^k)}$ represent the mean and variance of the time series $X(t)$ within the specific time window t^k. By calculating the ACF for multiple time windows, we can observe how the correlation structure of the data evolves over time.

Figure 5.37 explores how the autocorrelation function (ACF) of wind speed and temperature data evolves over time. This analysis considers a subset of probes and presents the ACF for five different time intervals (panels (a) and (b)). Dashed lines represent the ACF profile for each time window, with different colors corresponding to different probes. The solid line depicts the mean ACF profile for each probe within all time windows. Panels (c) and (d) show the average correlation values ($\overline{R_X(t^k, \tau)}$') for all probes within each time window.

To account for potential non-stationarity, the entire time series was segmented into overlapping 15-minute time windows with a 450-second moving step size (chosen based on the longest characteristic timescale observed previously). This allows for the ACF to potentially vary within the overall measurement period. The shorter time window allows for a more localized analysis, revealing changes in the correlation structure within smaller spatial domains.

The ACF profiles for wind speed (panel (c)) exhibit a clear time dependence. The correlation values at the end of the time lag range (τ) show different trends compared to the results in Figure 5.35 (which used the entire time series). Notably, the last time window displays a non-monotonic decay in correlation, suggesting a more complex behavior in the wind speed fluctuations over shorter timescales. The temperature ACF profiles (panel (d)) show less variation across different time windows. The profiles for each window tend to collapse onto the overall mean profile, indicating a weaker time dependence for temperature fluctuations compared to wind speed.

The discussion so far has focused on autocorrelations. Future work can be extended to:

- *Cross-correlations:* Analyze the correlations between data from different probes or between different measured quantities (e.g., wind speed and temperature).
- *Cross-instrument correlations:* Utilize data from other instruments deployed in campaigns like WESCON 2023. The diverse datasets available during such campaigns offer opportunities for cross-instrument validation and advanced spatiotemporal analysis.

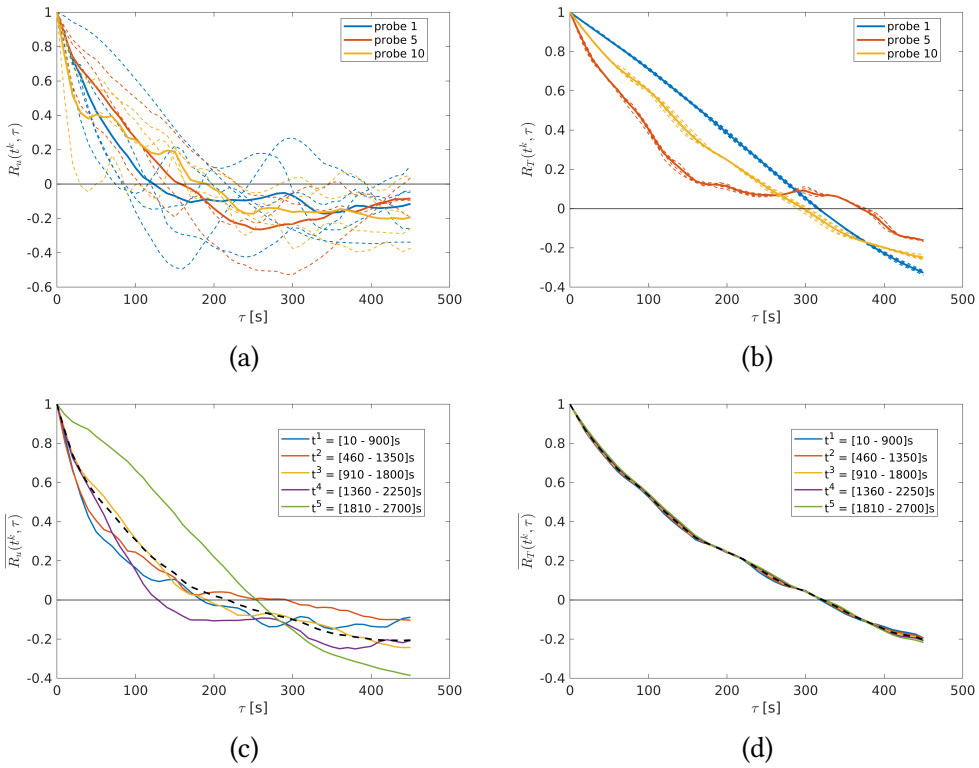

Figure 5.37: Time-dependant autocorrelations of horizontal wind speed and temperature fluctuations computed using Equation 5.11 for the first day of the WESCON 2023 experiments, July 5, 2023, Chilbolton, UK. (a,b) Autocorrelation values for subset of probes. Each color represent different probe: dashed lines for various time windows and solid line average among all time windows. (c,d) Average autocorrelation values averaged among all probes for various time windows. Time window size is 10 minutes and it is moving window with step size of 7.5 minutes (450 seconds). Black dashed line presents the average profile.

For instance, the Chilbolton Advanced Meteorological Radar (CAMRa) with its long-range ($\sim$ 250 km) and high-resolution (75 m spatially) capabilities could be used for cross-correlation analysis. Comparing these radar observations with the radiosonde cluster data (covering a smaller spatial and temporal domain) could offer valuable insights into wind dynamics across different measurement scales. Similarly, correlations between radiosonde humidity and radar reflectivity can provide a more comprehensive picture of atmospheric moisture distribution.

Space-time correlations

While autocorrelations provide valuable insights into the temporal variability of a single location, true space-time correlations offer a more comprehensive picture of how turbulent fluctuations are interconnected across both space and time within a flow. However, calculating these correlations, particularly in the Lagrangian reference frame (following fluid particles), presents significant challenges.

The primary difficulty lies in tracking a large number of particles' trajectories that originate from a specific region or closely spaced points within the flow. Ideally, we would then analyze the covariance between the initial positions of these particles and their positions at different points along the flow trajectory after a time lag (τ). One approach to address this challenge involves Lagrangian correlations. As presented by Wang, Squires, and Wu [189], Wallace [187] and He, Jin, and Yang [188], the Lagrangian correlation coefficient, denoted as $R_U^L(x_0, \tau)$, for a measured quantity U can be expressed as shown in the following Equation:

$$R_U^L(x_0,\tau) = \frac{\overline{[U_i(x_0) - \overline{U_i(x_0)}][U_j(x_0 + r(t_0+\tau)) - \overline{U_j(x_0 + r(t_0+\tau))}]}}{\sqrt{\overline{[U_i(x_0) - \overline{U_i(x_0)}]^2}}\sqrt{\overline{[U_j(x_0 + r(t_0+\tau)) - \overline{U_j(x_0 + r(t_0+\tau))}]^2}}} \tag{5.12}$$

Here, $x_0 = x(t_0)$ represents the initial position, $r(t_0 + \tau)$ denotes the displacement of a particle at time $t_0+\tau$ relative to its initial position, and i and j represent different probes or particles. The overline signifies the mean value. It's important to note that unlike the time lag (τ) in autocorrelations, the displacement (r) in Lagrangian correlations is not an independent variable. They are inherently linked, as highlighted by [187].

The main distinction between this expression and the previous autocorrelations (Equations 5.10 and 5.11) lies in the calculation of correlations. Here, the correlation is computed between the readings of all probes at two specific times (t_0 and $t_0 + \tau$). Additionally, the average values are calculated across all probe readings at these times. In contrast, autocorrelations analyze the correlation of a single probe's readings across different time lags within a single time window or the entire time series.

Figure 5.38 presents the space-time correlations computed using Equation (5.12) for horizontal wind speed and temperature fluctuations for both experiment days. As expected, the correlation profiles are less smooth compared to the autocorrelations observed in Figures 5.35 and 5.36. This is likely due to the inherent variability in particle trajectories and the limited number of probes used in the experiments. Two potential strategies can be explored to improve the analysis of space-time correlations:

- *Increased Number of Probes:* Employing a larger number of probes during future experiments would likely lead to smoother correlation profiles by capturing a more comprehensive picture of the flow dynamics.

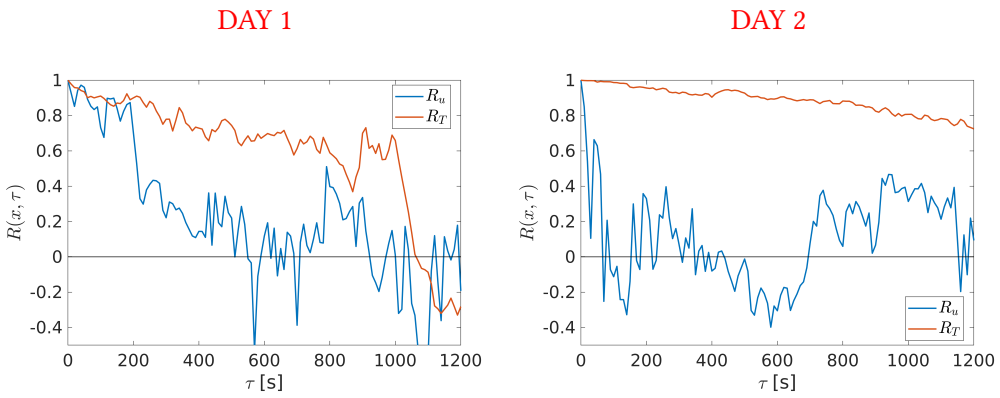

Figure 5.38: Space-time Lagrangian correlations of horizontal wind speed and temperature fluctuations computed using Equation 5.12 for both experiment days, July 5-6, 2023, Chilbolton, UK. Starting instance for the first day at 14:03, July 5 and for the second day at 13:53, July 6.

- *Correlation Based on Separation Distance:* Alternatively, Lagrangian correlations can be calculated by considering pairs of probes and relating them to the separation distance ($d_{i,j}$) between the probes. This approach would involve analyzing the correlation between the initial separation distance of a pair and their separation distance after a time lag (τ), rather than focusing on individual displacement and differences in readings. This would utilize 21 and 45 pairs for the first and second day of experiments, respectively.

The exploration of Lagrangian correlations based on probe pairs (considering separation distances) is a promising avenue for future research. This approach holds potential for providing a more detailed understanding of the relationships between spatial separation and temporal variations in measured quantities within the flow.

Chapter 6

Conclusions

This work presents a novel approach for studying cloud dynamics by combining in-field observations using a radiosonde cluster network with numerical simulations of cloud-turbulence interactions. Both approaches provide valuable insights into the internal fluctuations and forces that govern cloud formation, growth, and dissipation.

6.1 In-field observations

A new balloon-borne radiosonde network system is introduced for cluster measurements of atmospheric properties. Field tests and experiments have validated the system's functionality and potential for real-world applications. The system successfully tracks Lagrangian fluctuations (temporal and spatial variations) of various physical quantities, including position, velocity, pressure, humidity, temperature, acceleration, and magnetic field.

Post-processing analysis using distance-neighbor graphs (DNGs) enables the quantification of turbulent dispersion from spatial and temporal measurements. Generalizing the DNG approach to other relative measurements offers the possibility of performing space-time correlations between different quantities or between the same quantities measured by different radiosondes within the cluster.

The system utilizes low-cost and lightweight MEMS sensors, enabling cost-effective atmospheric measurements. The radiosonde electronic board weighs only 7 grams (measuring around 5 cm x 5 cm), with the entire system (including battery, balloon, and support connections) weighing approximately 18-20 grams. A new prototype is under development with further weight and size reductions (3 grams and 4 cm x 3.5 cm), minimizing the overall system weight and helium gas consumption.

The radiosonde cluster system offers a wide range of potential applications beyond the scope of this work: (i) Observing the structure of atmospheric and marine boundary layers (not possible with single radiosondes); (ii) Studying lightning by analyzing space-time variations in magnetic field strength; (iii) Environmental monitoring in urban and

industrial areas; (iv) Cost-effective radiosonde measurements for diverse atmospheric experiments, including vertical profiling.

Future works on in-field observations

Ongoing optimization efforts aim to improve data transmission and acquisition rates. A new ground station with higher reception capabilities and multi-channel support is under development, along with custom LoRa peer-to-peer gateways. Sensor protection using lightweight shields will mitigate radiation and precipitation effects on radiosonde boards.

The post-processing module will be further extended to explore advanced techniques like space-time Lagrangian correlations. A new module for lightning detection applications via magnetic field fluctuation sensing is under consideration. Future experiments in diverse environments will further enhance system robustness and enable testing of components under development.

Future analysis will extend beyond autocorrelations, venturing into: (i) Cross - correlations: Analyze the correlations between data from different probes or measured quantities (e.g., wind speed and temperature). (ii) Cross-instrument correlations: Utilize data from diverse instruments deployed during campaigns like WESCON 2023. This allows for cross-instrument validation and advanced spatio-temporal analysis. For example, the Chilbolton Advanced Meteorological Radar offers promising opportunities for cross-correlation analysis due to its long range and high resolution. Comparing these radar observations with the radiosonde data can provide insights into wind dynamics across different scales. Similarly, correlations between radiosonde humidity and radar reflectivity can improve our understanding of atmospheric moisture distribution.

The WESCON 2023 data, along with the new datasets from recent cluster experiments at Udine and Chilbolton, will be further analyzed to investigate anisotropy and mixing within the atmospheric boundary layer and warm clouds using two approaches: (i) Local isotropy assumption: This approach assumes local isotropy within the inertial subrange of the turbulence spectrum and relies on the expected ratio between spectral densities of lateral and longitudinal wind velocity components. (ii) Event-based framework: This novel method utilizes ”burst-like” activities identified during radiosonde flights to detect anisotropic regions within the ABL.

We envision combining results from numerical simulations with in-field measurements for a more comprehensive analysis of warm clouds and the atmospheric boundary layer, considering cloud microphysics, turbulent fluctuations, and related diffusion processes. This could involve analyzing the coupling between NWP simulations and experimental data from the radiosonde cluster (as suggested by Schnierstein et al. [190], for the Arctic Boundary Layer), potentially refining current Large Eddy Simulation (LES) models and developing data assimilation techniques between numerical simulations and experiments.

Minimizing the environmental impact of atmospheric instrumentation remains a

priority. Despite ongoing efforts to reduce impacts, effects on wildlife persist. Recommendations for mitigation include adopting biodegradable materials in the system's design and implementing improved retrieval protocols (as discussed by Goldberg et al. [191]).

6.2 Numerical studies

Numerical studies investigated the dynamics of droplet populations within a shearless, transient cloud-air interface, mimicking a stage in the lifecycle of natural clouds. Two types of initial droplet populations were considered: monodisperse (uniform initial size) and polydisperse (various initial sizes). Both type of simulations included realistic numbers of droplets (∼10 million) to match the liquid water content of warm clouds (0.8 g/m^3).
Key findings and observations include:

- **Enhanced droplet dynamics**: The unsteady turbulence mixing within the interface significantly enhances droplet dynamics, including evaporation and collisional activity. This acceleration is observed despite the overall decay of turbulence throughout the system.
- **Rapid size differentiation**: The size distribution of droplets evolves rapidly within the interface compared to the cloud region. For the monodisperse case, the standard deviation of the size distribution grows faster in the interface (∼15 times), while the peak radius increases slightly. Conversely, for the polydisperse case, the distribution width shrinks faster in the interface (∼4 times), while the peak radius remains almost constant.
- **Potential link to rainfall formation**: The observed rapid droplet size differentiation within the interface might partially explain the rapid increase in droplet size observed in some cumulus clouds, especially maritime ones, which can lead to localized rainfall [192], [193].
- **Role of small-scale anisotropy**: It is hypothesized that the observed acceleration in the interface is linked to the small-scale anisotropy and intermittency of the flow. This small-scale structure is likely to enhance the rate of droplet collisions and evaporation.
- **Limitations of collision kernel concept**: The traditional collision kernel concept, developed for stationary and isotropic turbulence, may not be suitable for transient and inhomogeneous systems like cloud interfaces. This is evidenced by the observed dependence of the collision kernel on both time and location within the interface, suggesting the need for an extended theoretical approach.
- **Comparison with Saffman-Turner model**: The collision kernel values observed in present simulations are generally lower than those predicted by the Saffman-Turner model for stationary and isotropic turbulence. Additionally, the morphology of the collision kernel differs, especially within the mixing region.

- **Clustering of microphysical time scales**: Inside the cloud top, where turbulent transport towards the subsaturated environment occurs, the evaporation, reaction, and phase relaxation time scales converge to a value around 20-30 seconds, just before the location of maximum supersaturation flux variation. This convergence includes the condensation time scale for polydisperse populations.

Future steps on numerical studies

The future of this computational simulation can leverage modern hybrid architectures. While this will necessitate changes to the code structure and computational aspects, the overall outcome and resolved fields will remain consistent with the non-hybrid approach when using the same simulation parameters. However, the advantage of hybrid systems lies in their expanded capabilities. They can handle larger domains (either spatially or temporally, with finer time steps) and potentially resolve a wider range of variables, including pressure fluctuations.

Our research team is currently conducting DNS simulations with water droplets as part of the "**L**agrangian **T**urbulent dispersion in ABL and **I**ntermittency **A**cceleration of water droplet populations at **C**loud **E**dges (LATIACE) 2024" project, funded by the ISCRA initiative and running on CINECA machines. The newly available datasets will enable us to delve deeper into several key areas: (i) We can gain a more comprehensive understanding of how the water droplet population accelerates within the turbulent flow; (ii) The data will allow for a more detailed examination of the turbulent dispersion processes affecting the droplets. (iii) We will be able to investigate Lagrangian correlations within the decaying turbulent flow over a longer temporal domain ($t/\tau_0 \simeq$ 50-60) .

Another promising direction involves utilizing high-resolution DNS datasets for training machine learning (ML) and artificial intelligence (AI) models. Initially, post-processing of these datasets could provide valuable insights into droplet dynamics concepts like clustering, correlations, filament stretching/enhancement, and dispersion. Subsequently, these models could potentially be used to generate artificial flow fields. However, it's crucial to maintain a level of transparency within the model, avoiding a completely "black-box" approach. Explainable AI (XAI) techniques can offer a viable solution in this regard.

Appendix A

Numerical simulations

Numerical simulations readily create shearless velocity fluctuation mixing layers in 2D and 3D by utilizing periodic boundary conditions. These layers arise from the interaction of two initially HIT flows with differing levels of:

- Turbulent kinetic energy [81, 82, 83, 113, 84],
- Temperature [194, 96],
- Water vapor and supersaturation levels [87],
- A population of inertial point particles [195].

This setup has been explored not only in simulations but also in laboratory experiments, starting with Gilbert [79] and Veeravalli and Warhaft [80] for single-phase fluid turbulence and progressing to configurations with inertial particles [196, 197].

A.1 Governing equations

The governing equations encompass the turbulent velocity field (u_i), temperature field (T), pressure field (p), and vapor mixing ratio (q_v). These equations employ the Boussinesq Navier-Stokes framework for incompressible flow, which is integrated with passive and active scalar transport equations (as seen in previous works [36, 86, 198, 96,

87, 134, 98]). The Einstein convention applies to indices within following equations:

$$\frac{\partial u_i}{\partial x_i} = 0 \tag{A.1}$$

$$\frac{\partial u_i}{\partial t} + u_j \frac{\partial u_i}{\partial x_j} = -\frac{1}{\rho_0}\frac{\partial p}{\partial x_i} + \nu \frac{\partial^2 u_i}{\partial x_j^2} - \mathscr{B}\,\delta_{zi}, \tag{A.2}$$

$$\frac{\partial T}{\partial t} + u_j \frac{\partial T}{\partial x_j} = \kappa \frac{\partial^2 T}{\partial x_j^2} + \frac{\mathscr{L}}{c_p} C_d \tag{A.3}$$

$$\frac{\partial q_v}{\partial t} + u_j \frac{\partial q_v}{\partial x_j} = \kappa_v \frac{\partial^2 q_v}{\partial x_j \partial x_j} - C_d \tag{A.4}$$

The simulation relies on the following key quantities and parameters (details in Table A.1):

- ν: the kinematic viscosity of air,
- g: the gravitational acceleration,
- ρ_0: is the reference value for the density of dry air,
- c_p: the specific heat at constant pressure,
- $\mathscr{L}$: the latent heat,
- k: the temperature diffusivity,
- D: the diffusivity of the vapor mixing ratio,
- C_d: the condensation rate field,
- $\mathscr{B}$: the buoyancy field.

We denote an average over a slice of the domain perpendicular to the vertical direction (x_3) and with a thickness equal to one grid step as <>. In this context, temperature fluctuations are defined as:

$$T'(x_j, t) = T(x_j, t) - < T(x_3, t) > \tag{A.5}$$

Here, the volume-averaged temperature ($< T(x_3) >= T_0 + Gx_3$) is constant over time and consists of two parts:

- T_0: Average temperature across the entire domain.
- Gx_3: A linear background negative variation, creating an unstable stratification (details in Table A.1).

The initial temperature field term T' depends only on the x_3 coordinate and has an hyperbolic tangent representation (explained in Section A.1.1).

Similar to temperature fluctuations, vapor mixing ratio fluctuations are defined as:

$$q_v'(x_j, t) = q_v(x_j, t) - < q_v(t) > . \tag{A.6}$$

Here, the average is taken over the entire domain and is time-dependent, unlike the average for temperature fluctuations.

The buoyancy field, represented by $\mathscr{B}$ in the momentum equation (Eq. A.2) incorporates both temperature and vapor mixing ratio fluctuations. It is defined as:

$$\mathscr{B} = g[T'/ < T > +\alpha q_v'] \tag{A.7}$$

where $\alpha = M_a/M_v - 1 = 0.608$ and M_a and M_v are the dry air and vapor molar masses, respectively [101]. This equation essentially combines the effects of temperature and vapor content on the buoyancy force acting on the fluid.

The condensation term $C_d = C_d(x_i, t)$ in the energy and vapor density equation expresses the water vapor mass absorption (depletion) rate at the surface of all the spherical droplets contained in the cubic computational cell of volume $(\Delta)^3$. To incorporate condensation effects in our simulations, we need to express the condensation rate field in the Eulerian frame of reference (compatible with equations A.3 and A.4). This rate is calculated for each grid cell using the following equation [95]:

$$C_d(x_i, t) = \frac{1}{m_a}\frac{dm_l(x_i, t)}{dt} = \frac{4\pi\rho_l K_s}{\rho_0 \Delta^3}\sum_{j=1}^{N_\Delta} \mathrm{R}_j(t) S(X_j(t), t) \tag{A.8}$$

Here, m_a and m_l are the air mass and liquid (water) mass per grid cell, ρ_l is density of water, ρ_0 is reference density of dry air, $\mathrm{R}_j(t)$ and $X_j(t)$ are the radius and vector space coordinate of the $j-th$ droplet within the grid cell, respectively. N_Δ represents the number of droplets inside the grid with volume Δ^3. Supersaturation is denoted by S, and K_s is a temperature and pressure dependent diffusion coefficient that includes the self-limiting effects of latent heat release (see also Eq. A.10).

The equation essentially sums the contribution of each droplet within the cell to the overall condensation rate, considering their size, number, and the level of supersaturation. It should be noted that the second-order Lagrange polynomials were adopted for interpolating grid values onto droplet positions and vice versa when calculating the condensation rate (Eq. 3.4).

The supersaturation S which is defined in terms of the vapor mixing ratio and the saturation vapor mixing ratio as

$$S\left(X_i, t\right) = \frac{q_v(X_i, t)}{q_{vs}(T)} - 1 = RH - 1. \tag{A.9}$$

The relative humidity $RH = q_v/q_{vs}(T)$ and supersaturation (or saturation deficit) are functions of the saturated vapor density, $q_{vs}(T)$, whose value at the droplet position is obtained from the Tetens formula [199]:

$$q_{vs}(X_i, t) = \frac{e_s(T)}{R_v \rho_0 T} = \epsilon_0 \frac{610.78}{\rho_0 T} exp[17.63\frac{T - 272.16}{T - 35.86}] \tag{A.10}$$

Table A.1: The list of thermodynamic constants and flow field parameters used in DNS simulations

Quantity	Symbol	Value	Unit
Latent heat of evaporation	$\mathscr{L}$	$2.48 \cdot 10^6$	$\mathrm{J\,kg^{-1}}$
Heat capacity of the air at constant pressure	c_p	1005	$\mathrm{J\,kg^{-1}\,K^{-1}}$
Gravitational acceleration	g	9.81	$\mathrm{m/s^2}$
Gas constant for water vapour	R_v	461.5	$\mathrm{J\,kg^{-1}\,K}$
Gas constant for air	R_a	286.7	$\mathrm{J\,kg^{-1}\,K}$
Diffusivity of water vapour	κ_v	$2.52 \cdot 10^{-5}$	$\mathrm{m^2\,s^{-1}}$
Thermal conductivity of dry air	κ	$2.5 \cdot 10^{-2}$	$\mathrm{J\,K^{-1}\,m^{-1}\,s^{-1}}$
Density of liquid water	ρ_l	1000	$\mathrm{kg\,m^3}$
Dry air density, altitude 1000 m	ρ_0	1.11	$\mathrm{kg\,m^{-3}}$
Reference kinematic viscosity	ν	$1.399 \cdot 10^{-5}$	$\mathrm{m^2\,s^{-1}}$
Entire domain average temperature	T_0	281.16	K
Temperature in cloud region	T_1	282.16	K
Temperature in clear air region	T_2	280.16	K
Background temperature gradient	G	-2	K/m
Diffusion coefficient in eq.s 8 and 14	K_s	$8.6 \cdot 10^{-11}$	$\mathrm{m^2\,s^{-1}}$
Accumulation diameter	r_d	$0.01 \cdot 10^{-6}$	m
Kelvin droplet curvature constant	A	$1.15 \cdot 10^{-7}$	cm
Raoult solubility parameter for inorganic hygroscopic substances (e.g., ammonium sulfate, lithium chloride)	B	$0.7 \cdot 10^{-18}$	$\mathrm{cm^3}$
Initial relative humidity inside cloud	S (cloud)	1.02	-
Initial relative humidity inside clear air	S (clear air)	0.7	-
Saturation vapor mixing ratio at T_1	q_{vs}(cloud)	$0.79 \cdot 10^{-2}$	$\mathrm{kg\,m^{-3}}$
Saturation vapor mixing ratio at T_2	q_{vs}(clear air)	$0.69 \cdot 10^{-2}$	$\mathrm{kg\,m^{-3}}$
Water saturation pressure at $T_0 = 281$	e_s	1.061	kPa
Molar mass of air	m_{air}	28.96	$\mathrm{kg\,mol^{-1}}$
Molar mass of water	m_v	18	$\mathrm{kg\,mol^{-1}}$
Initial liquid water content	LWC	$7.9 \cdot 10^{-4}$	$\mathrm{kg/m^3}$

where e_s is the saturation pressure, and $\epsilon_0 = R_a/R_v \sim 0.62$ is the ratio between the gas constants for dry air and water vapor, R_a and R_v, respectively. For temperature above 273.16 K, see also [200].

A.1.1 Initial and boundary conditions

This research investigates the simplest form of anisotropic turbulent flow, arising from the interaction of two homogeneous, isotropic, and decaying turbulence fields. These fields differ only in their kinetic energy levels. The simplicity of this flow stems from the

absence of an average velocity gradient. This means there's no production of turbulent kinetic energy and no mean convective transport. All interactions occur due to the fluctuating pressure and velocity fields.

Without external forcing, the system aims to realistically represent a small cloud perturbation near the boundary. The inherent turbulence energy gradient, combined with the anisotropic and intermittent nature of velocity fluctuations and their derivatives (see Figure 3.16 in the results section 3.2), is sufficient to drive the system away from a Gaussian distribution.

The simulated cloud-clear-air boundary layer experiences an unstable stratification, as indicated by the Brunt-Väisälä fluctuation growth factor (N^2) of -0.0687. This triggers a characteristic pattern in the background flow, which is the same for both droplet populations: an initial amplification of velocity followed by a gradual decay, observable in panel (a) of Figure A.1.

Although the two interacting flows are identical except for their kinetic energy content, this difference creates a ratio (and therefore, a gradient) of kinetic energy across the layer. Notably, the integral length scale of a turbulence field can be independent of its kinetic energy. This allows us to numerically obtain an inhomogeneity in the kinetic energy of two HIT fields while maintaining homogeneity in their integral length scales [183, 83, 34, 35, 36].

The initial conditions are generated by building a homogeneous isotropic velocity field within a volume $2\pi \cdot 2\pi \cdot 2\pi$ Mansour and Wray [201]. Then, two such velocity fields are matched and merged using a hyperbolic tangent function. Resulting paralllepiped domain with size $4\pi \cdot 2\pi \cdot 2\pi$ domain, has initial mixing layer of 1/40 of the 4π domain.

The resulting matched field along non-homogeneous direction x_3 can be expressed mathematically as:

$$u(x) = u_1(x)p(x_3) + u_2(x)\sqrt{1 - p^2(x_3)} \tag{A.11}$$

$$p(x_3) = \frac{1}{2}\left[1 + \tanh\left(a\frac{x_3}{L}\right)\tanh\left(a\frac{x_3 - L/2}{L}\right)\tanh\left(a\frac{x_3 - L}{L}\right)\right] \tag{A.12}$$

In these equations, the subscripts 1 and 2 represent the high and low energy sides of the cloud interface model, respectively and L is the width of the computational domain in the x_3 direction.

The constant a in the equation for $p(x_3)$ determines the initial thickness of the mixing layer (Δ), conventionally defined as the distance between points with normalized energy values of 0.25 and 0.75. By carefully choosing the value of a, we ensure that the initial thickness is large enough to be accurately resolved in the simulations while remaining small enough to maintain large regions of homogeneous turbulence. With $a = 12\pi$ the initial ratio Δ/L is about 0.026.

Similar to the velocity field, the temperature and water mixing ratio fields are also

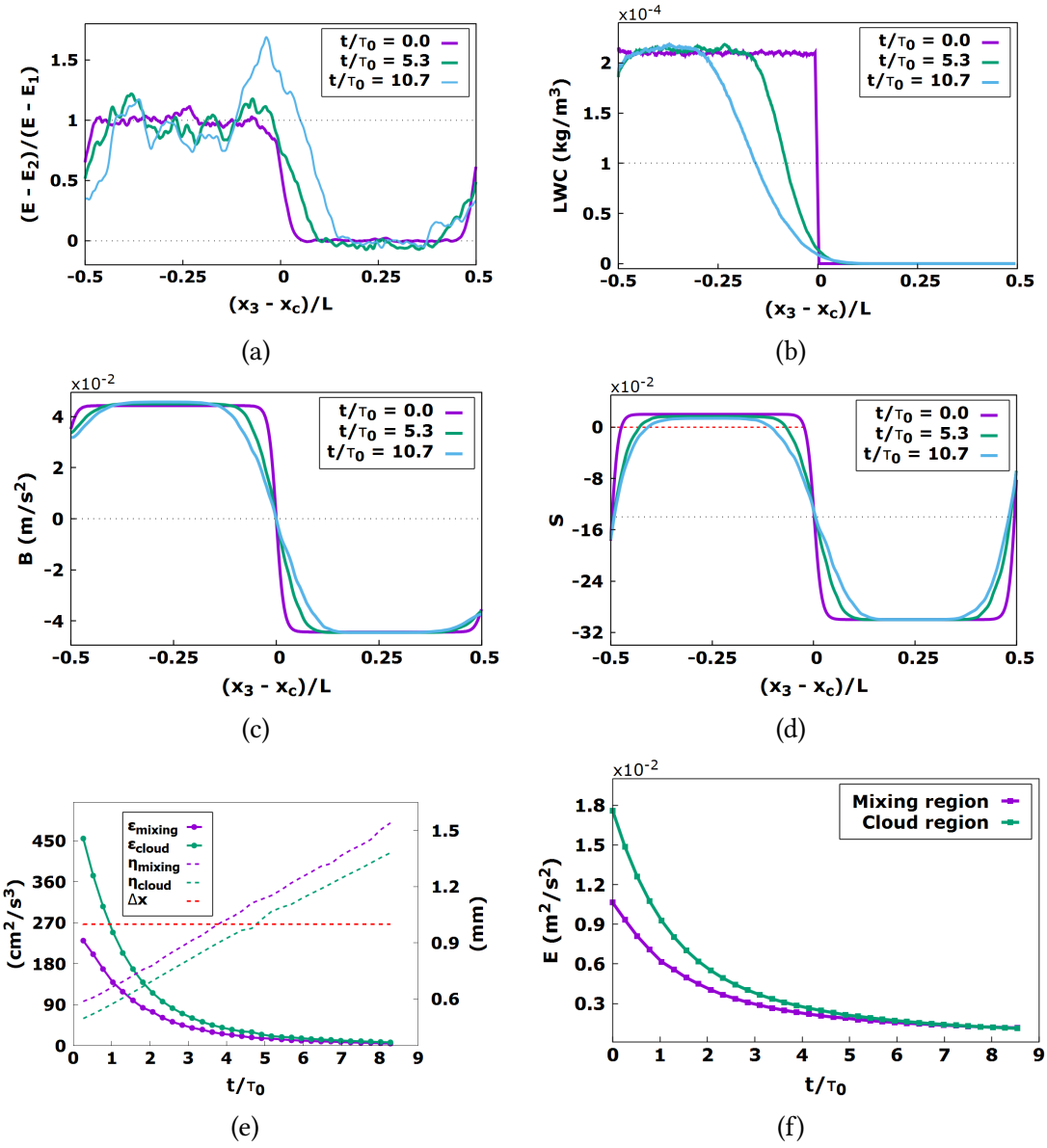

Figure A.1: Kinetic energy, Liquid Water Content (LWC) for the polydisperse droplet population, buoyancy and supersaturation mean values along the in-homogeneous direction at three stages along the temporal evolution. In physical non normalized terms, the evolution lasts a few seconds ($\tau_0 = 0.42$ s, see Table 2). The top left panel shows the turbulent energy excess with respect to the clear-air part, normalized with the difference difference between the two regions ($E_1 = 6.7xE_2$) at $t = 0$.

generated using a periodic function:

$$T'(x_3,0) = \Delta T \cdot \left[tanh\left(55\left(\frac{x_3}{L} - \frac{1}{2}\right)\right) - \frac{2x_3}{L} + 1 \right], \tag{A.13}$$

$$q_v \text{~~162~~} q_1 p(x_3) + q_2\sqrt{1 - p^2(x_3)} \tag{A.14}$$

This ensures a smooth transition between the cloud and clear air regions. See Figure 3.2 (right panel) for a visual representation. While Figure A.1 highlights initial conditions and the temporal evolution of the both scalar fields, together with the kinetic energy, LWC, $\mathscr{B}$, S and along the inhomogeneous direction x_3.

Tables A.1 and A.2 provide detailed information about the parameters used in our simulations. This includes: (i) physical and thermodynamic constants (Table A.1); (ii) domain specifications, grid structure, turbulence scales, field control parameters, and water droplet information (Table A.2).

To obtain statistically reliable results, we perform multiple simulations with slightly different initial conditions. This is achieved by rotating the initial velocity field within the cloud region while keeping its overall properties unchanged. For example, one simulation might use the original field, another might use it rotated by 90 degrees around a specific axis, and so on.

Table A.2: List of parameters for the DNS simulations of unstable cloud-clear interface hosting the monodisperse and polidisperse distribution of water droplets.

Quantity	**Symbol**	**Value**	**Unit**
Simulation domain size	$L_{x_1} \cdot L_{x_2} \cdot L_{x_3}$	$0.512 \cdot 0.512 \cdot 1.024$	m^3
Simulation domain discretization	$N_1 \cdot N_2 \cdot N_3$	$512 \cdot 512 \cdot 1024$	-
Simulation grid step	Δx	0.001	m
Initial Kolmogorov time (cloud)	τ_η	$2.65 \cdot 10^{-2}$	s
Initial Kolmogorov scale (cloud)	η	0.6	mm
Initial rms velocity (cloud)	u_{rms}	0.11	m/s
Particle response time at $R_0 = 15\mu$m	τ_p	$3.6 \cdot 10^{-3}$	s
Initial eddy turn over time	τ_0	0.38	s
Initial droplet radius (monodisperse)	R_{mono}	15	m
Initial droplet radius (polydisperse)	R_{poly}	0.6 - 30	m
Initial number of droplets (monodisperse)	N_{mono}	$8 \cdot 10^6$	-
Initial number of droplets (polydisperse)	N_{poly}	10^7	-
Simulation time step	Δt	$4.6 \cdot 10^{-4}$	s
Initial energy ratio	$E_{cloud}/E_{clear-air}$	6.7	-
Initial integral scale	l	0.027	m
Initial Taylor microscale Reynolds number	Re_λ	52	-
Reynolds number based on domain dimension	Re_L	5000	-
Brunt-Väisälä amplification factor	$\mathscr{N}^2$	–0.068	s^{-2}

A.2 Numerical experiment setup and computational aspects of DNS

This study utilizes a computational domain measuring 0.512m x 0.512m x 1.024m, discretized by a grid of 512 x 512 x 1024 points (Figure 3.2). Two separate air fluctuation fields fill the domain, representing the cloud and clear air regions.

The cloud region initially holds significantly higher turbulent kinetic energy (E) and dissipation rate (ϵ) compared to the clear air region, mimicking real-world cumulus clouds. The cloud region boasts a root-mean-square velocity of u_{rms} ≈0.11 m/s, representing the large-scale energy within the cumulus cloud's spectral range of wavelengths (0.002 to 0.25 m). Since our system decays over time, the initial dissipation rate was intentionally set high to reflect typical values observed in the transient phase of cumulus clouds. Notably, this initial rate ($\epsilon_{cloud} \approx 500$ cm^2/s^3) aligns with measurements from MacPherson and Isaac [202] near the top of real clouds, despite their higher air fluctuation kinetic energy (∼2 m/s). Lower dissipation rates (10-20 cm^2/s^3) have been reported during transient decay phases, as shown in Figure A.1, panel e.

The Kolmogorov scale within the simulation is around $\eta_0 \cong 0.5$mm, with the highest resolved wavenumber is $k_{max} = \pi/\Delta x = \pi \cdot 10^3 \mathrm{m}^{-1}$ [203]. Following previous studies [204, 195], the ratio of k_{max} the Kolmogorov scale η_1 is approximately 1.6, indicating sufficient resolution for our analysis.

The study employs the dealiased pseudospectral Navier-Stokes solver developed by Iovieno, Cavazzoni, and Tordella [43]. This software has been extensively applied to study various turbulence aspects, including scenarios with passive and active scalars, as well as water droplet populations [83, 113, 84, 194, 34, 35, 36]. The solver uses Fourier-Galerkin spectral discretization for advection in momentum, vapor, and energy transport equations. Linear terms are solved in the spectral domain, while non-linear terms are computed in the physical domain.

Time integration utilizes a second-order explicit Runge-Kutta method Ireland and Collins [195] and Brucker et al. [205], where diffusive terms are handled through exponential integration. Droplet velocities and accelerations are integrated using second-order explicit and implicit methods, respectively.

A.2.1 DNS software

The DNS code stores velocity, temperature, and vapor fields in 3D arrays distributed across one direction in both physical and Fourier spaces. Fast Fourier Transform (FFT) libraries handle the 3D discrete Fourier transforms. The software primarily uses slab parallelization with Message Passing Interface (MPI) libraries [43, 34, 35].

Several DNS software versions available as listed in the Philofluid Research Group's website[206]. Here are three relevant versions used in the recent numerical experiments:

- **Version 1.4scal (slab parallelization) :** Extends the original pseudospectral Navier-Stokes code [43] to simulate transport equations for passive scalars (up to six quantities with varying Schmidt numbers or initial conditions). It was later extended to solve *stratified flows* within the Boussinesq approximation.
- **Version 1.4p (slab parallelization):** Adds a particle/droplet module to *1.4scal*, enabling tracking of small inertial particles/droplets in the fluid. This version was used most for present simulations.
- **Version 1.7 (two-direction stencil parallelization):** A new hybrid (shared/distributed) version using Fortran 2018 for improved readability and efficiency of shared routines. However, it currently lacks water droplet capabilities. It employs stencil parallelization across two directions to distribute the domain across processes (up to $N_{cores}^2/2$ - theoretical value). See Gallana et al. [36] and Gallana [207] for simulation results and parallelization details.

A.2.2 Version 1.4p: parallelization in presence of water droplets

Most analyses in this chapter rely on data generated with version 1.4p, primarily utilizing CINECA SuperComputing center and HPC@POLITO for simulations and post-processing (Table A.3 summarizes the software, parallelization, and optimal configuration).

Table A.3: Summary of the developed and tested DNS software version 1.4p during ISCRA C project. The final code was mainly tested in the following architecture and setup conditions.

Architecture	Distributed, MPI
Language	Fortran
Libraries	OpenMPI, FFTW
Machine	Marconi-A2 (KNL), CINECA HACTAR, HPC@POLITO
Processes	256
Configuration (Optimal)	8 nodes x 32 processes
Problem size	5 x 1 GB (3 velocity components, 2 scalars) $\sim$ 460 MB (107 droplets x 12 x 4)

Introducing water droplets significantly increases communication between processes due to their turbulent clustering. This unpredictable clustering leads to uneven workload distribution across cores, hindering performance and limiting parallelization effectiveness. Additionally, clustering intensifies over time, impacting droplet collision rates and growth patterns.

In this version, parallelization is handled in two different directions from computational perspective (see also Figure A.2):

1. **Slab parallelization**: Each process handles fluid flow calculations (velocity and scalars) for two adjacent planes in the domain.
2. **Balanced droplet distribution**:. Droplets are evenly distributed among processes (around 40k per process), with each process computing 12 parameters for each droplet. Periodic redistribution balances the workload after a fixed number of iterations (100-200).

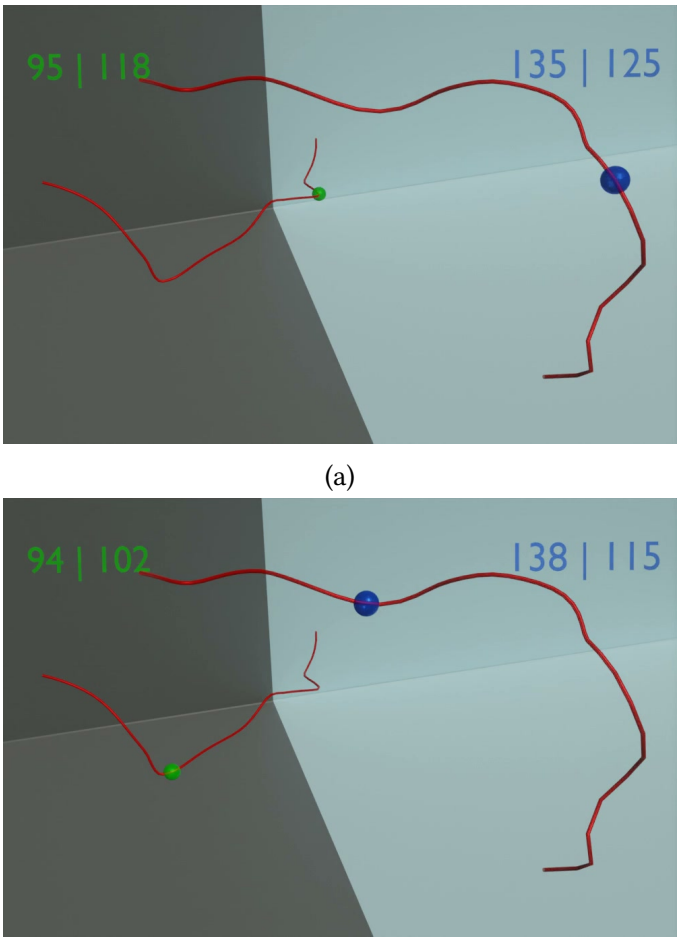

(a)

(b)

Figure A.2: This illustration highlights the parallel computations in **Version 1.4p** for both flow and droplet motion equations. It is showcased the trajectories of two droplets at two specific times, highlighting two assigned process IDs. Process ID (i) handles Lagrangian equations, while process ID (ii) manages Eulerian equations at the interpolated droplet location.

A.2.3 Code scalability

This section delves into the code's scalability and the parallelization strategies employed. Scientific parallel computing can utilize various memory handling approaches:

- **Distributed-memory:** The domain is divided among processes, each with its own memory. Communication between processes (cores) occurs via data passing protocols like MPI.
- **Shared-memory:** Tasks are divided among threads, with communication happening through shared memory (e.g., OpenMP).
- **Hybrid:** A combination of both approaches. Version 1.7 of the DNS code uses this approach, with MPI for distributed parallelization (1st level) and OpenMP for shared parallelization (2nd level). Note that this is different from parallelization on modern CPU/GPU architectures.

MPI-only implementations (*Versions 1.4p, 1.4scal*) distribute the domain among processes (cores) on a single direction (aligned with homogeneous flow direction). The most expensive part (70-85% of time) is the pseudospectral computation of non-linear terms, requiring data transformation between physical and wavenumber spaces. The code uses 1D real-to-real FFT subroutines and data transposition integrated with dealiasing [43].

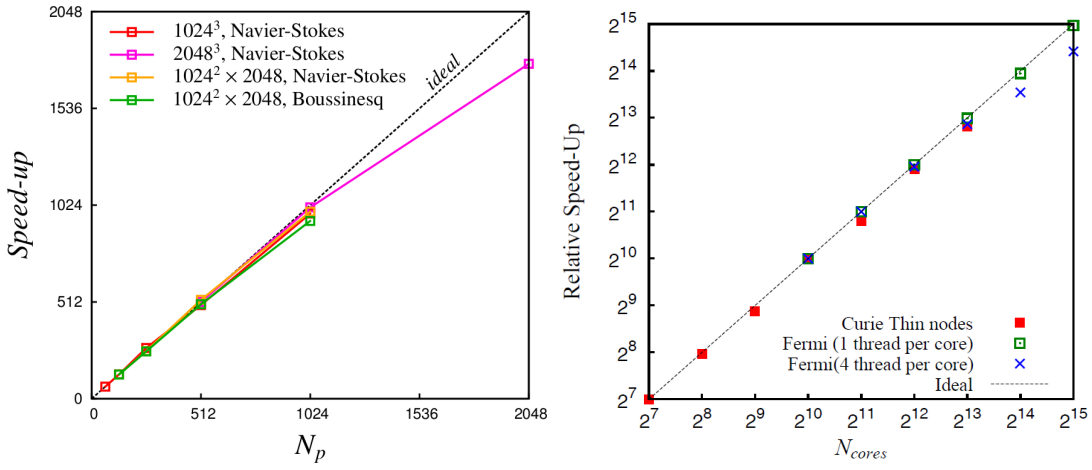

Figure A.3: Computational scaling of the two different versions of the DNS code. (a) Version 1.4 (1D slab parallelization). Scaling was assessed using IBM Power 6 (SP6 at CINECA, 2011) for different meshes of computational domain. See also Table A.4. (b) Version 1.7 (2D pencil parallelization). Scaling was measured for the different machines: the Curie Thin nodes (at GENCI-CEA) and IBM BlueGene/Q (Fermi at CINECA) with two different configurations.

The DNS software undergoes continuous development and testing. After each major upgrade (e.g., new modules), its scaling capabilities are analyzed and benchmarked. Results for versions 1.4 and 1.7 are available on the research group's website [208] and also presented in Figure A.3. For version 1.4p with Lagrangian particles, benchmarking was done by Ruggiero, V and Codoni, D and Tordella, D [209].

Table A.4: Computational scaling of the DNS code, tested with different mesh sizes. Version 1.4 scaling was assessed using IBM Power 6 (SP6 at CINECA, 2011). The last part of the table shows the code with Boussinesq equations for a stratified flow.

N_{cores}	**Run time (s)**	**Relative Scaling**
Cube with mesh: 1024^3		
64	264.8	64 (assumed)
128	131.6	128.7
256	63.1	268.7
512	34.2	495.5
1024	17.3	979.6
Cube with mesh: 2048^3		
512	716.1	512(assumed)
1024	362.2	1012.2
2048	207.1	1771.1
Parallelliped with mesh: 1024^2 x 2048		
128	280.7	128 (assumed)
256	142.2	252.5
512	68.7	522.9
1024	36.3	989.7
Parallelliped with mesh: 1024^2 x 2048 (Boussinesq)		
128	370.5	128 (assumed)
256	189.5	250.3
512	94.9	499.8
1024	50.4	940.4

The analysis of the hybrid version (Ver. 1.7) assumes a cubic domain with with N^3 in wavenumber space, and $M^3 = 27/8N^3$ points in physical space. Without expansion/contraction, the number of single FFTs would be $27/4N^2$, but the code achieves a 30% saving by using a global communication subroutine for transformations and I/O via MPI 3.0. OpenMP handles the shared parallelization. This version (shown in Figure A.3(b)) is 5 times faster and achieves near-linear speedup, utilizing massively parallel supercomputers effectively. Simulations were performed on the TGCC Curie supercomputer (PRACE project no. RA07732011) for a total of 3 million CPU hours.

However, this version struggles with including droplet motion and collision modules. Figure A.4 shows the difference in speedup between the two versions. Pencil

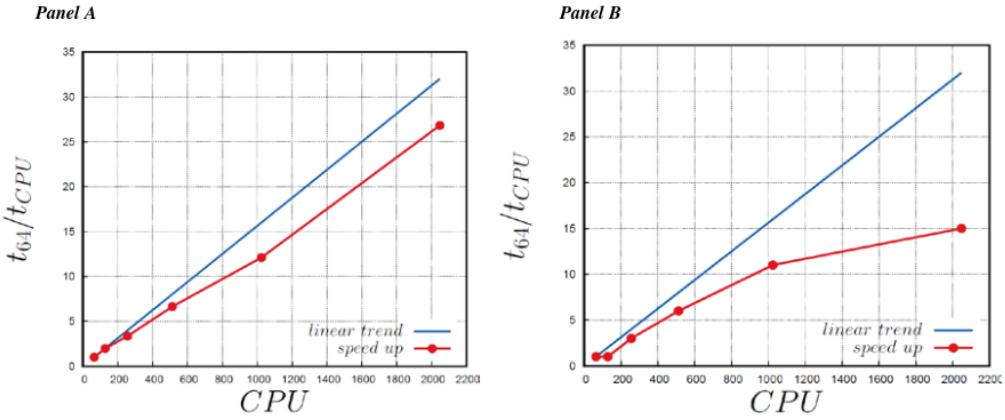

Figure A.4: Panel A: speedup curve for the code version without water droplets. Panel B: speed up curve for the version with water droplets. (t_{64} execution time for 64 cores on CINECA Marconi KNL, t_{CPU} execution time for the cluster with the number of nodes specified in the ordinate (computational grid `4096 x 2048`^{2}).

parallelization increases communication time by ∼3x on average. The bottleneck is increased MPI communication (`MPI_Send_receive_replace()`), associated with both the presence of droplets and the number of processes [209].

This is further complicated by the unpredictable nature of turbulence, which can lead to long-distance droplet displacements requiring communication between non-adjacent cores within short timesteps.

A.2.4 Exploring hybrid architectures for DNS simulations

Beyond CPUs (Central Processing Unit), modern computers often have massively parallel GPUs (Graphical Processing Unit) originally designed for graphics processing. However, they have evolved into general-purpose processors suitable for various computations.

Our research team is investigating the potential of running DNS code on modern CPU/GPU hybrid architectures. This approach leverages the capabilities of these powerful machines to accelerate simulations. We chose Version 1.4p for this analysis due to its existing MPI integration in Fortran 90, which can resolve both flow and droplet motion equations.

Modern GPU vendors like NVIDIA offer libraries such as CUDA (Compute Unified Device Architecture) to optimize code for their hardware. Combining MPI and CUDA within languages like Fortran or C/C++ enables the creation of hybrid code that can run on these architectures.

While hybrid code and hybrid memory management are distinct concepts, they can share some structural similarities. Our previous version 1.7 code relies on CPU-only architectures for hybrid simulations. However, the new version under development

(version 1.4p_hybrid) aims to utilize both CPUs and GPUs concurrently. It's important to note that GPU threads are physical rather than logical like in OpenMP, and GPUs employ a shared-memory paradigm among these threads in similar way.

Initial testing on a Dell Precision Tower 3620 with an NVIDIA Quadro K620 GPU (384 CUDA cores, 2 GB shared memory) highlighted the crucial role of adequate GPU memory. Shared variables between MPI processes and GPU threads require sufficient memory space. For instance, storing a single velocity component for a 512x512x1024 domain demands 1 GB, exceeding the K620's capacity.

This underscores the need for high-performance computing resources like CINECA's LEONARDO system. It offers powerful and memory-rich GPUs, with each node housing 4 units of NVIDIA A100 SXM6 cards, boasting 64 GB of memory each.

A.2.5 Hybrid code example

Several versions of DNS software are available for the pseudospectral Navier-Stokes solver, as listed on the Philofluid Research Group's website[206]. For the development of our hybrid code, we specifically adopted `Version 1.4p` of their DNS code with Lagrangian tracking of water droplets.

Figure A.5 compares code snippets from both the MPI and hybrid (MPI+CUDA) versions of the DNS software. While achieving the same functionality, the hybrid version (right) includes additional lines commented out in Fortran 90 (green). These comments are actually CUDA directives, only interpreted by the compiler when targeting Graphics Processing Units (GPUs). For Central Processing Units (CPUs), these directives are treated as standard Fortran comments, allowing compilation and execution on CPU-only architectures. This approach facilitates a smooth transition from the original MPI implementation to the hybrid one while maintaining compatibility with CPU-only systems (which only require the MPI library).

A.3 Distance neighbor-graph PDF computation

Building upon the theoretical framework presented in Sections 2.4 and 5.4 (Equations 2.2 and 5.9), the following pseudocode (Alg. 1) outlines the implementation of the Distance neighbor-graph (DNG) algorithm. This algorithm was initially developed for numerical simulation data (DNS with water droplets as Lagrangian particles) and later adapted for experimental data from radiosonde clusters (details in Section 5.4).

Figures A.6 and A.7 illustrate the dispersion of Lagrangian water droplets within the turbulent simulation domain.

Cloudy Region (Figure A.6): This figure depicts water droplets extracted from the cloudy half of the simulation, representing time-decaying homogeneous isotropic turbulence (as described in Figure 3.2). Around 500 droplets are scattered across the xz plane (z-axis representing buoyancy and the direction affected by gravity). The initial

Algorithm 1: Distance-neighbor graph PDF computation within time range [1; *max_time*] and length interval of [1; *max_length*] and neighborhood size *h*.

Data: *positions* array, *h* neighborhood size
Result: *Q* graph
for *i = 1 to max_time* **do**
  $N = \text{length}(positions(i))$;
  $X = positions(i).X$; /* coordinates of all droplets */
  $Y = positions(i).Y$;
  $Z = positions(i).Z$;
  $L = \sqrt{(X - X')^2 + (Y - Y')^2 + (Z - Z')^2}$; /* X' is a transpose of X */
  for *n = 1 to max_length* **do**
    $check = L < n \text{ x } h \;\&\; L > (n-1) \text{ x } h$; /* *check* is a boolean array */
    $count = sum(check)$;
    $Q(max\_length + n, i) = sum(count)/N$;
    $Q(max\_length - n + 1, i) = sum(count)/N$;
  end
end

```
do j=0,kmax
    kappa12(j)=dfloat(j) !normalized wavenumbers
    kappa3(j)=dfloat(j) !normalized wavenumbers
    kappae12(j)=dfloat(j) !normalized wavenumbers
    kappae3(j)=dfloat(j) !normalized wavenumbers
end do

do j=1,kmax-1
    kappae12(2*kmax-j)=dfloat(j) !normalized wavenumbers - 2nd
    derivative
    kappae3(2*kmax-j)=dfloat(j) !normalized wavenumbers - 2nd
    derivative
end do


!GENERATING THE MODEL ENERGY SPECTRUM
allocate(spectrum(0:2*n12-1),xmod(0:2*n12-1))
!2*n12 is the length of the cube's diagonal,
!maximum length of the wavenumber vector
spectrum=0.0d0

do j=0,kappa_peak
    spectrum(j)=float(j)**kappa_slope
end do

do j=kappa_peak+1,2*n12-1
    spectrum(j)=spectrum(kappa_peak)*(dfloat(j)/kappa_peak)**(-5/3)
    spectrum(j)=spectrum(j)*dexp(-0.8*dfloat(j-kmax))/(1+dexp(-0.
    8*dfloat(j-kmax)))
end do
```

```
!Call kernel loop directive for kappa computation
!arrays must be device/managed type
!$cuf kernel do <<<*,*>>>
do j=0,kmax
    kappa12(j)=dfloat(j) !normalized wavenumbers
    kappa3(j)=dfloat(j) !normalized wavenumbers
    kappae12(j)=dfloat(j) !normalized wavenumbers
    kappae3(j)=dfloat(j) !normalized wavenumbers
end do
!$cuf kernel do <<<*,*>>>
do j=1,kmax-1
    kappae12(2*kmax-j)=dfloat(j) !normalized wavenumbers - 2nd
    derivative
    kappae3(2*kmax-j)=dfloat(j) !normalized wavenumbers - 2nd
    derivative
end do
! syncronize threads
istat = cudaDeviceSynchronize()

!GENERATING THE MODEL ENERGY SPECTRUM
allocate(spectrum(0:2*n12-1),xmod(0:2*n12-1))
!2*n12 is the length of the cube's diagonal,
!maximum length of the wavenumber vector
spectrum=0.0d0
!$cuf kernel do <<<*,*>>>
do j=0,kappa_peak
    spectrum(j)=float(j)**kappa_slope
end do
!$cuf kernel do <<<*,*>>>
do j=kappa_peak+1,2*n12-1
    spectrum(j)=spectrum(kappa_peak)*(dfloat(j)/kappa_peak)**(-5/3)
    spectrum(j)=spectrum(j)*dexp(-0.8*dfloat(j-kmax))/(1+dexp(-0.
    8*dfloat(j-kmax)))
end do

! syncronize threads
istat = cudaDeviceSynchronize()
!print *, istat, nid
```

Figure A.5: Comparison of the MPI (left) and MPI+CUDA (right, hybrid) based code snippets from DNS software. The green highlights in the right-hand code snippet indicate CUDA directives, which are comments interpreted by the compiler only when targeting GPUs.

panel (t/τ_0 = 0.454) shows the droplets concentrated within a small neighborhood (2cm x 2cm x 2cm cubic domain) located at (24.4, 24.4, 24.4) cm relative to the simulation domain's origin (bottom edge of the parallelepiped in Figure 3.2).

Mixing Region (Figure A.7): This figure follows a similar approach for the mixing region of the simulation domain, which represents a time-evolving anisotropic turbulent region. Here, 428 droplets were extracted at the initial position (24.4, 24.4, 48.9).

Figure A.8 presents the DNG plots for both the cloud and mixing regions. It also highlights the evolution of the DNG's maximum value (Q_{max}) over time and separation distance (panels c and d). Panel (e) shows the length interval corresponding to the peak value of Q (L_{Qmax}), while panel (f) depicts the mean squared separation distance among all droplets (L^2). Additionally, panel (f) includes power-law interpolations for both regions, emphasizing that the simulation observation window might be insufficient to capture the expected Richardson-Obukhov scaling ($\sim t^3$).

Overall, this section effectively describes the DNG computation method and presents initial findings on Lagrangian water droplet dispersion in different turbulence regimes. The analysis highlights the potential limitations of the current observation window for capturing the full dispersion behavior.

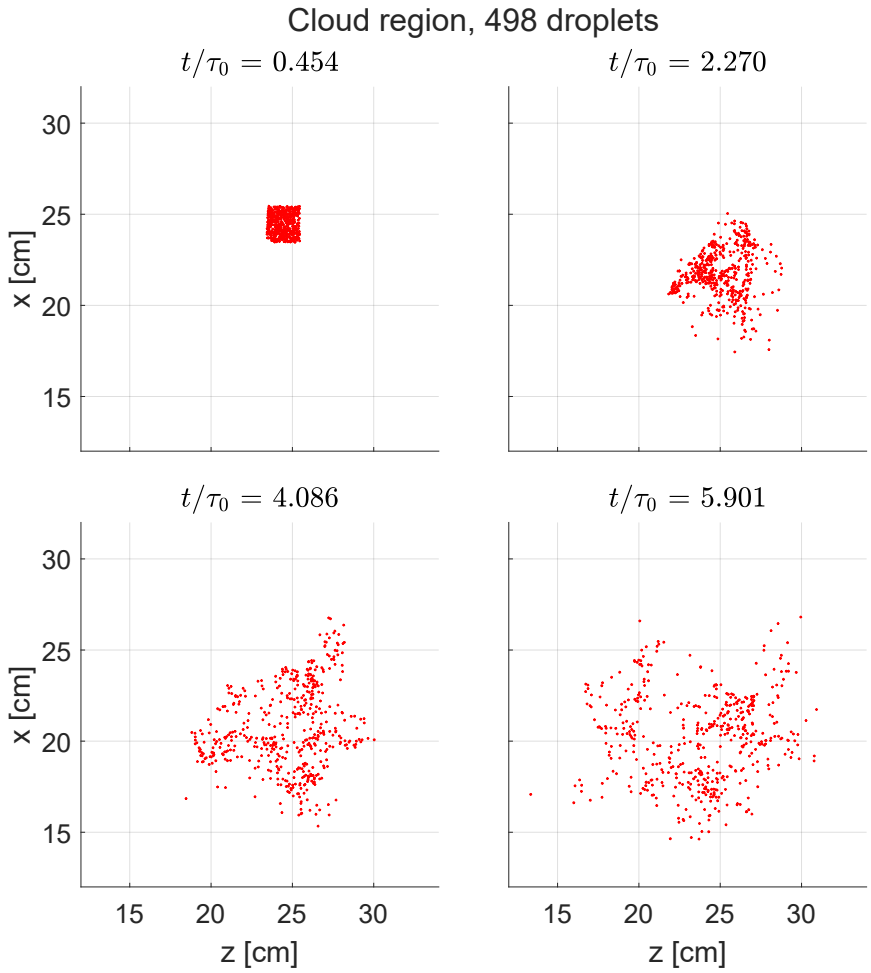

Figure A.6: Droplet positions in simulation domain represented in xz plane at four time instances for **cloud region**. **498** droplets are selected within the same cell (neighborhood) initially and they are located in 2cm x 2cm x 2cm cubic domain, which has a center in (24.4,24.4,24.4) cm. Reference system is parallelliped described in Figure 3.2 with origin at the bottom edge.

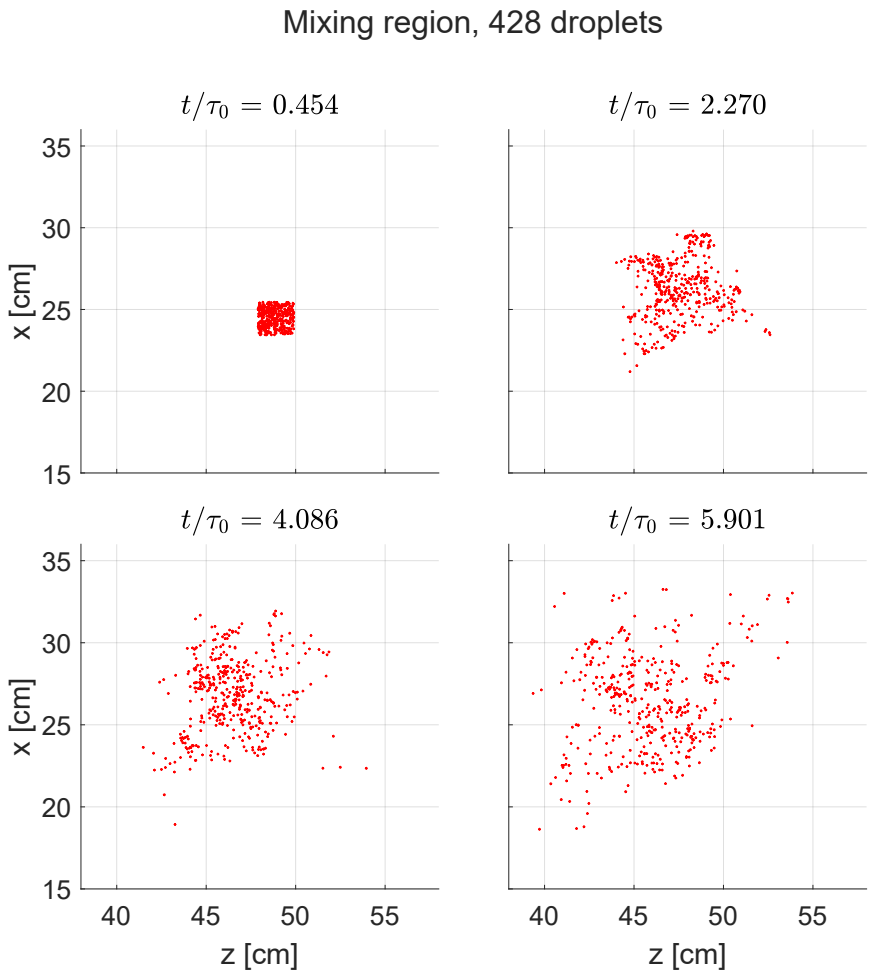

Figure A.7: Droplet positions in simulation domain represented in xz plane. Figures are generated for 4 different time instances. **428** droplets are selected within the same cell (neighborhood) initially and they are located in 2cm x 2cm x 2cm domain around position (24.4,24.4,48.9). Reference system is parallelliped described in Figure 3.2 with origin at the bottom edge.

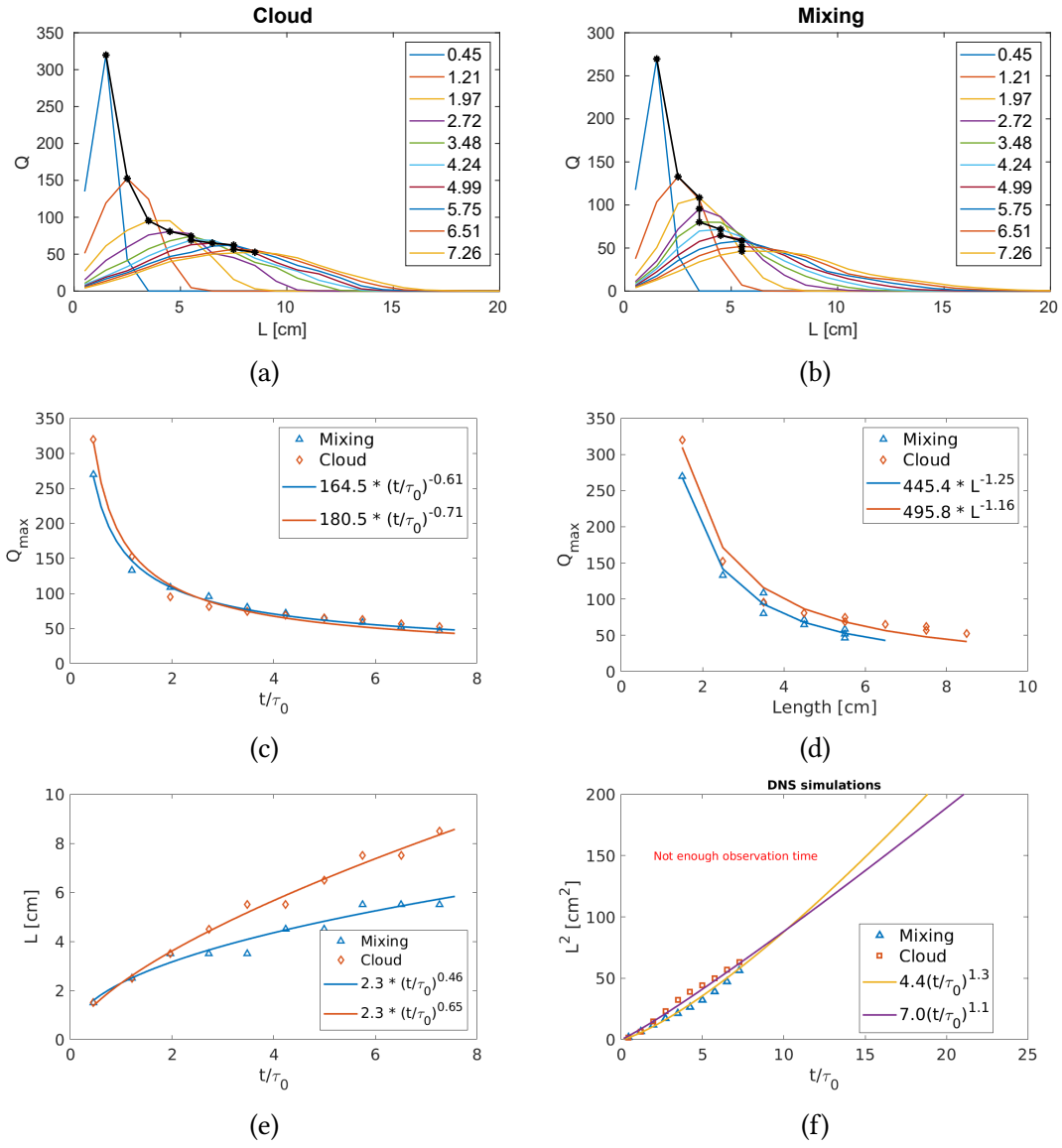

Figure A.8: Q graph at several temporal instances. Time instances are given in legend in terms of t/τ_0. Q_{max} is highlighted for each temporal instance and its trend was shown with solid black lines (Panels a,b).Panels c and d represent the evolution of Q_{max} over time and dispersion length. Cloud: 498 drops, at (x,y,z) = (24.4, 24.4, 24.4)[cm]; mixing: 428 drops, at (x,y,z) = (24.4, 24.4, 48.9) [cm].

Appendix B

Radiosonde and field experiment related

B.1 Dataset description

Current version of the radioprobe comprises a set of components, such as:

- Radio transmission module;
- GNSS (Global Navigation Satellite System) sensor;
- IMU (Inertial Measurement Unit) sensor;
- PHT (Pressure, Humidity, Temperature) sensor.

Each radioprobe transmits a data packet to the receiver station with proprietary LoRa based transmission protocol. The data packet is uniquely identified with the pair of radioprobe id and data packet counter values. In the following Table B.1 we can see the detailed description of the raw data packet.

B.2 Workflow of the relative distance detection via stereo vision

In the current scenario, the stereo vision workflow comprises the following steps:

(i) Simple camera calibration and the extracting of the camera settings, such as effective focal distances over the horizontal (u) and vertical (v) directions. The image resolution is 1440 x 1080 pixels, and the center of the image is considered the origin of the image coordinate frame.

(ii) Dataset extraction from video recordings with the OpenCV CSRT tracker. The tracker provides the u and v coordinates of the radiosonde balloon in the image coordinate frame, in terms of pixels.

Table B.1: Description of the raw obtained dataset from COMPLETE/POLITO radiosondes.

#	**Quantity**	**Format and range**	**Comments**
1	Timestamp of the receiver station	Date:hour:minute:second	Recorded when data packet is received
2			
3	Timestamp of the radiosonde	Seconds	Number of seconds passed since the launch of the radiosonde
4	Data packet counter		
5	GNSS sensor timestamp	Hour:minute:second	GNSS time is given as hour, minute and seconds in GMT0 time zone
6	GNSS sensor data fix		GNSS sensor data quality
7	Longitude	Decimal degrees	-
8	Latitude		-
9	Altitude	meters	-
10	North, east and down direction velocity	[0, 500] m/s	Velocity measurements from GNSS sensor
11	3D acceleration measurements	[-16, +16] g	IMU sensor
12	Orientation of radiosondes	Unit quaternions	4D quaternion vector from IMU sensor data. It is used for post-processing to obtain acceleration readings in NED (north, east, down) reference frame
13	Pressure	[300, 1100] mbar	PHT sensor
14	Humidity	[0, 100] %	PHT sensor
15	Temperature	[-40, +85] °C	PHT sensor

(iii) Computing the 3D x, y, and z coordinates in the camera reference frame with calibrated stereo vision. The coordinate frame of the camera on the left (camera A) was used as a reference.

(iv) Computation of the relative distance between the red and black balloons with the above computed x, y, and z coordinates.

References

[1] Howard B Bluestein, Frederick H Carr, and Steven J Goodman. "Atmospheric observations of weather and climate." In: *Atmosphere-Ocean* 60.3-4 (2022), pp. 149–187. DOI: 10.1080/07055900.2022.2082369. eprint: https://doi.org/10.1080/07055900.2022.2082369. URL: https://doi.org/10.1080/07055900.2022.2082369.

[2] WMO. *Observation components of the Global Observing System*. 2023. URL: https://community.wmo.int/en/observation-components-global-observing-system (visited on 12/05/2023).

[3] J. Heintzenberg and Robert J. Charlson, eds. *Clouds in the perturbed climate system: their relationship to energy balance, atmospheric dynamics, and precipitation*. Strüngmann Forum reports. Cambridge, Mass: MIT Press, 2009. 597 pp. ISBN: 978-0-262-01287-4. URL: https://doi.org/10.7551/mitpress/9780262012874.001.0001.

[4] S. A. Ackerman, S. Platnick, P. K. Bhartia, B. Duncan, T. L'Ecuyer, A. Heidinger, G. Skofronick-Jackson, N. Loeb, T. Schmit, and N. Smith. "Satellites See the World's Atmosphere." In: *Meteorological Monographs* 59 (2019), pp. 4.1–4.53. DOI: https://doi.org/10.1175/AMSMONOGRAPHS-D-18-0009.1. URL: https://journals.ametsoc.org/view/journals/amsm/59/1/amsmonographs-d-18-0009.1.xml.

[5] ISCCP. *Cloud Climatology. International Satellite Cloud Climatology Program, NASA. Cloud Climatology: net effect on energy and water balances*. [Online; accessed 18-March-2022]. 2022. URL: https://isccp.giss.nasa.gov/role.html#:~:text=A%20cloudless%20Earth%20would%20absorb,summer%27s%20day%20at%20the%20beach..

[6] E. Bodenschatz, S. P. Malinowski, R. A. Shaw, and F. Stratmann. "Can We Understand Clouds Without Turbulence?" In: *Science* 327.5968 (2010), pp. 970–971. DOI: 10.1126/science.1185138. eprint: https://www.science.org/doi/pdf/10.1126/science.1185138. URL: https://www.science.org/doi/abs/10.1126/science.1185138.

[7] Shahbozbek Abdunabiev, Chiara Musacchio, Andrea Merlone, Miryam Paredes, Eros Pasero, and Daniela Tordella. "Validation and traceability of miniaturized multi-parameter cluster radiosondes used for atmospheric observations." In: *Measurement* 224 (Jan. 2024), p. 113879. ISSN: 0263-2241. DOI: 10.1016/j.measurement.2023.113879. URL: https://www.sciencedirect.com/science/article/pii/S0263224123014434 (visited on 11/22/2023).

[8] Holger Siebert, Katrin Lehmann, and Manfred Wendisch. "Observations of Small-Scale Turbulence and Energy Dissipation Rates in the Cloudy Boundary Layer." In: *Journal of the Atmospheric Sciences* 63.5 (2006), pp. 1451–1466. DOI: https://doi.org/10.1175/JAS3687.1. URL: https://journals.ametsoc.org/view/journals/atsc/63/5/jas3687.1.xml.

[9] Raymond A. Shaw. "Particle-Turbulence Interactions in Atmospheric Clouds." In: *Annual Review of Fluid Mechanics* 35.1 (2003). _eprint: https://doi.org/10.1146/annurev.fluid.35.101101.161125, pp. 183–227. DOI: 10.1146/annurev.fluid.35.101101.161125. URL: https://doi.org/10.1146/annurev.fluid.35.101101.161125 (visited on 12/11/2023).

[10] CORDIS EU research results. *Cloud-MicroPhysics-Turbulence-Telemetry: An inter-multidisciplinary training network for enhancing the understanding and modeling of atmospheric clouds.* [Online; accessed 25-Jan-2023]. DOI: 10.3030/675675. URL: https://cordis.europa.eu/project/id/675675 (visited on).

[11] JEAN-LOUIS Brenguier and ROBERT Wood. "Observational strategies from the micro to meso scale." In: *Clouds in the Perturbed Climate System: Their Relationship to Energy Balance, Atmospheric Dynamics, and Precipitation* 487 (2009), p. 510.

[12] Paul A. Vaillancourt and M. K. Yau. "Review of Particle-Turbulence Interactions and Consequences for Cloud Physics." In: *Bulletin of the American Meteorological Society* 81.2 (2000), pp. 285–298. DOI: https://doi.org/10.1175/1520-0477(2000)081<0285:ROPIAC>2.3.CO;2. URL: https://journals.ametsoc.org/view/journals/bams/81/2/1520-0477_2000_081_0285_ropiac_2_3_co_2.xml.

[13] COMPLETE ITN - ETN NETWORK. *COMPLETE ITN - ETN NETWORK | EU Horizon 2020.* 2023. URL: https://www.complete-h2020network.eu/ (visited on 12/05/2023).

[14] AJ Illingworth, RJ Hogan, EJ O'connor, Dominique Bouniol, ME Brooks, Julien Delanoë, DP Donovan, JD Eastment, N Gaussiat, JWF Goddard, et al. "Cloudnet: Continuous evaluation of cloud profiles in seven operational models using ground-based observations." In: *Bulletin of the American Meteorological Society* 88.6 (2007), pp. 883–898.

[15] Chenbin Xue, Zhiying Ding, Xinyong Shen, and Xian Chen. "Three-Dimensional Wind Field Retrieved from Dual-Doppler Radar Based on a Variational Method: Refinement of Vertical Velocity Estimates." In: *Advances in Atmospheric Sciences* 39 (2022), pp. 145–160. DOI: https://doi.org/10.1007/s00376-021-1035-9.

[16] Steven V. Vasiloff. "Improving Tornado Warnings with the Federal Aviation Administration's Terminal Doppler Weather Radar." en. In: *Bulletin of the American Meteorological Society* 82.5 (May 2001), pp. 861–874. ISSN: 0003-0007, 1520-0477. DOI: 10.1175/1520-0477(2001)082<0861:ITWWTF>2.3.CO;2. URL: http://journals.ametsoc.org/doi/10.1175/1520-0477(2001)082%3C0861:ITWWTF%3E2.3.CO;2 (visited on 01/06/2024).

[17] NASA. *Tiros 1 Meteorological Satellite System Final Report*. Tech. rep. NASA-TR-R-131. NASA, Jan. 1962. URL: https://ntrs.nasa.gov/citations/19640007992 (visited on 01/07/2024).

[18] Bruce A. Wielicki, Bruce R. Barkstrom, Edwin F. Harrison, Robert B. Lee, G. Louis Smith, and John E. Cooper. "Clouds and the Earth's Radiant Energy System (CERES): An Earth Observing System Experiment." In: *Bulletin of the American Meteorological Society* 77.5 (May 1996), pp. 853–868. ISSN: 0003-0007, 1520-0477. DOI: 10.1175/1520-0477(1996)077<0853:CATERE>2.0.CO;2. URL: https://journals.ametsoc.org/view/journals/bams/77/5/1520-0477_1996_077_0853_catere_2_0_co_2.xml (visited on 12/06/2023).

[19] Graeme L. Stephens, Deborah G. Vane, Simone Tanelli, Eastwood Im, Stephen Durden, Mark Rokey, Don Reinke, Philip Partain, Gerald G. Mace, Richard Austin, Tristan L'Ecuyer, John Haynes, Matthew Lebsock, Kentaroh Suzuki, Duane Waliser, Dong Wu, Jen Kay, Andrew Gettelman, Zhien Wang, and Rojer Marchand. "CloudSat mission: Performance and early science after the first year of operation." In: *Journal of Geophysical Research: Atmospheres* 113.D8 (2008). _eprint: https://onlinelibrary.wiley.com/doi/pdf/10.1029/2008JD009982. ISSN: 2156-2202. DOI: 10.1029/2008JD009982. URL: https://onlinelibrary.wiley.com/doi/abs/10.1029/2008JD009982 (visited on 01/07/2024).

[20] D. M. Winker, J. Pelon, J. A. Coakley, S. A. Ackerman, R. J. Charlson, P. R. Colarco, P. Flamant, Q. Fu, R. M. Hoff, C. Kittaka, T. L. Kubar, H. Le Treut, M. P. Mccormick, G. Mégie, L. Poole, K. Powell, C. Trepte, M. A. Vaughan, and B. A. Wielicki. "The CALIPSO Mission: A Global 3D View of Aerosols and Clouds." In: *Bulletin of the American Meteorological Society* 91.9 (Sept. 2010), pp. 1211–1230. ISSN: 0003-0007, 1520-0477. DOI: 10.1175/2010BAMS3009.1. URL: https://journals.ametsoc.org/view/journals/bams/91/9/2010bams3009_1.xml (visited on 01/07/2024).

[21] Andrew K. Heidinger, Michael J. Foster, Andi Walther, and Xuepeng (Tom) Zhao. "The Pathfinder Atmospheres–Extended AVHRR Climate Dataset." In: *Bulletin of the American Meteorological Society* 95.6 (June 2014), pp. 909–922. ISSN: 0003-0007, 1520-0477. DOI: 10.1175/BAMS-D-12-00246.1. URL: https://journals.ametsoc.org/view/journals/bams/95/6/bams-d-12-00246.1.xml (visited on 01/07/2024).

[22] WMO. *The AMDAR Observing System Description | World Meteorological Organization*. 2024. URL: https://community.wmo.int/en/activity-areas/aircraft-based-observations/amdar/amdar-description#sys_comp (visited on 01/07/2024).

[23] FAAM MET-OFFICE. *Science instruments on the FAAM aircraft*. 2024. URL: https://www.faam.ac.uk/the-facility/instrumentation/ (visited on 01/07/2024).

[24] Doug W. Johnson, Simon Osborne, Robert Wood, Karsten Suhre, Randy Johnson, Steven Businger, Patricia K. Quinn, Alfred Wiedensohler, Philip A. Durkee, Lynn M. Russell, Meinrat O. Andreae, Colin O'Dowd, Kevin J. Noone, Brian Bandy, J. Rudolph, and Spyros Rapsomanikis. "An overview of the Lagrangian experiments undertaken during the North Atlantic regional Aerosol Characterisation Experiment (ACE-2)." In: *Tellus B: Chemical and Physical Meteorology* 52.2 (Jan. 2000), pp. 290–320. ISSN: null. DOI: 10.3402/tellusb.v52i2.16110. URL: https://doi.org/10.3402/tellusb.v52i2.16110 (visited on 12/21/2023).

[25] S. R. Osborne, J. M. Haywood, and N. Bellouin. "In situ and remote-sensing measurements of the mean microphysical and optical properties of industrial pollution aerosol during ADRIEX." In: *Quarterly Journal of the Royal Meteorological Society* 133.S1 (2007). _eprint: https://onlinelibrary.wiley.com/doi/pdf/10.1002/qj.92, pp. 17–32. ISSN: 1477-870X. DOI: 10.1002/qj.92. URL: https://onlinelibrary.wiley.com/doi/abs/10.1002/qj.92 (visited on 01/07/2024).

[26] Tami C. Bond, Theodore L. Anderson, and Dave Campbell. "Calibration and Intercomparison of Filter-Based Measurements of Visible Light Absorption by Aerosols." In: *Aerosol Science and Technology* 30.6 (June 1999), pp. 582–600. ISSN: 0278-6826, 1521-7388. DOI: 10.1080/027868299304435. URL: http://www.tandfonline.com/doi/abs/10.1080/027868299304435 (visited on 01/07/2024).

[27] Nobuyuki Yajima, Naoki Izutsu, Takeshi Imamura, and Toyoo Abe. *Scientific Ballooning*. en. New York, NY: Springer, 2009. ISBN: 978-0-387-09725-1 978-0-387-09727-5. DOI: 10.1007/978-0-387-09727-5. URL: http://link.springer.com/10.1007/978-0-387-09727-5 (visited on 01/08/2024).

[28] Wikimedia Commons. *File:Early flight 02562u (2).jpg — Wikimedia Commons, the free media repository*. [Online; accessed 17-October-2023]. 2022. URL: https://commons.wikimedia.org/w/index.php?title=File:Early_flight_02562u_(2).jpg&oldid=667803559.

[29] World Meteorological Organization (WMO). *Guide to Instruments and Methods of Observation | Volume III – Observing Systems*. en. Tech. rep. WMO-No. 8. Geneva: WMO, 2021, p. 428. URL: https://library.wmo.int/idurl/4/68661 (visited on 01/11/2024).

[30] GRUAN. *GCOS Reference Upper-Air Network | The climate reference network*. website. 2024. URL: https://www.gruan.org/ (visited on 01/11/2024).

[31] Elisa F. Akansu, Holger Siebert, Sandro Dahlke, Jürgen Graeser, Ralf Jaiser, and Anja Sommerfeld. "Tethered Balloon-Borne Turbulence Measurements in Winter and Spring during the MOSAiC Expedition." en. In: *Scientific Data* 10.1 (Oct. 2023), p. 723. ISSN: 2052-4463. DOI: 10.1038/s41597-023-02582-5. URL: https://www.nature.com/articles/s41597-023-02582-5 (visited on 01/12/2024).

[32] Holger Siebert, Manfred Wendisch, Thomas Conrath, Ulrich Teichmann, and Jost Heintzenberg. "A New Tethered Balloon-Borne Payload for Fine-Scale Observations in the Cloudy Boundary Layer." en. In: *Boundary-Layer Meteorology* 106.3 (Mar. 2003), pp. 461–482. ISSN: 1573-1472. DOI: 10.1023/A:1021242305810. URL: https://doi.org/10.1023/A:1021242305810 (visited on 01/12/2024).

[33] Jakub L. Nowak, Holger Siebert, Kai-Erik Szodry, and Szymon P. Malinowski. "Coupled and decoupled stratocumulus-topped boundary layers: turbulence properties." English. In: *Atmospheric Chemistry and Physics* 21.14 (July 2021). Publisher: Copernicus GmbH, pp. 10965–10991. ISSN: 1680-7316. DOI: 10.5194/acp-21-10965-2021. URL: https://acp.copernicus.org/articles/21/10965/2021/ (visited on 12/21/2023).

[34] Mina Golshan, Shahbozbek Abdunabiev, Mattia Tomatis, Federico Fraternale, Marco Vanni, and Daniela Tordella. "Intermittency acceleration of water droplet population dynamics inside the interfacial layer between cloudy and clear air environments." In: *International Journal of Multiphase Flow* 140 (2021), p. 103669. ISSN: 0301–9322. DOI: https://doi.org/10.1016/j.ijmultiphaseflow.2021.103669. URL: https://www.sciencedirect.com/science/article/pii/S0301932221001178.

[35] Ludovico Fossà, Shahbozbek Abdunabiev, Mina Golshan, and Daniela Tordella. "Microphysical timescales and local supersaturation balance at a warm cloud top boundary." In: *Physics of Fluids* 34.6 (2022). _eprint: https://doi.org/10.1063/5.0090664, p. 067103. DOI: 10.1063/5.0090664. URL: https://doi.org/10.1063/5.0090664.

[36] L. Gallana, S. Abdunabiev, M. Golshan, and D. Tordella. "Diffusion of turbulence following both stable and unstable step stratification perturbations." In: *Physics of Fluids* 34.6 (2022), p. 065122. DOI: 10.1063/5.0090042. eprint: https://doi.org/10.1063/5.0090042. URL: https://doi.org/10.1063/5.0090042.

[37] Laureline Hentgen, Nikolina Ban, Nico Kröner, David Leutwyler, and Christoph Schär. "Clouds in Convection-Resolving Climate Simulations Over Europe." In: *Journal of Geophysical Research: Atmospheres* 124.7 (2019), pp. 3849–3870. DOI: https://doi.org/10.1029/2018JD030150. URL: https://agupubs.onlinelibrary.wiley.com/doi/abs/10.1029/2018JD030150.

[38] PRACE. *Climate simulations reach the next level of precision. Project Access Success Stories.* [Online; accessed 6-Dec-2022]. 2020. URL: https://prace-ri.eu/climate-simulations-reach-the-next-level-of-precision/ (visited on).

[39] Zhanjie Zhang and Guang J. Zhang. "Dependence of Convective Cloud Properties and Their Transport on Cloud Fraction and GCM Resolution Diagnosed from a Cloud-Resolving Model Simulation." In: *Journal of Marine Science and Engineering* 10.9 (2022). ISSN: 2077-1312. DOI: 10.3390/jmse10091318. URL: https://www.mdpi.com/2077-1312/10/9/1318.

[40] Miryam E. Paredes Quintanilla, Shahbozbek Abdunabiev, Marco Allegretti, Andrea Merlone, Chiara Musacchio, Eros G. A. Pasero, Daniela Tordella, and Flavio Canavero. "Innovative Mini Ultralight Radioprobes to Track Lagrangian Turbulence Fluctuations within Warm Clouds: Electronic Design." In: *Sensors* 21.4 (2021). ISSN: 1424-8220. DOI: 10.3390/s21041351.

[41] Lewis Fry Richardson. "Atmospheric diffusion shown on a distance-neighbour graph." In: *Proceedings of the Royal Society A* 110.756 (1926). Publisher: Royal Society, pp. 709–737. DOI: 10.1098/rspa.1926.0043. URL: https://royalsocietypublishing.org/doi/10.1098/rspa.1926.0043 (visited on 04/30/2024).

[42] Tessa C. Basso, Giovanni Perotto, Chiara Musacchio, Andrea Merlone, Athanassia Athanassiou, and Daniela Tordella. "Evaluation of Mater Bi and Polylactic Acid as materials for biodegradable innovative mini-radiosondes to track small scale fluctuations within clouds." In: *Materials Chemistry and Physics* 253 (2020), p. 123411. ISSN: 0254-0584. DOI: 10.1016/j.matchemphys.2020.123411.

[43] Michele Iovieno, Carlo Cavazzoni, and Daniela Tordella. "A new technique for a parallel dealiased pseudospectral Navier–Stokes code." In: *Computer Physics Communications* 141.3 (2001), pp. 365–374. ISSN: 0010-4655. DOI: https://doi.org/10.1016/S0010-4655(01)00433-7. URL: https://www.sciencedirect.com/science/article/pii/S0010465501004337.

[44] P. K. Yeung. "Lagrangian Investigations of Turbulence." In: *Annual Review of Fluid Mechanics* 34.1 (2002). _eprint: https://doi.org/10.1146/annurev.fluid.34.082101.170725, pp. 115–142. DOI: 10.1146/annurev.fluid.34.082101.170725. URL: https://doi.org/10.1146/annurev.fluid.34.082101.170725 (visited on 11/14/2023).

[45] Steven Businger, Steven R Chiswell, Warren C Ulmer, and Randy Johnson. "Balloons as a Lagrangian measurement platform for atmospheric research." In: *Journal of Geophysical Research: Atmospheres* 101.D2 (1996), pp. 4363–4376.

[46] S. Businger, R. Johnson, and R. Talbot. "Scientific Insights from Four Generations of Lagrangian Smart Balloons in Atmospheric Research." en. In: *Bulletin of the American Meteorological Society* 87.11 (Nov. 2006), pp. 1539–1554. ISSN: 0003-0007, 1520-0477. DOI: 10.1175/BAMS-87-11-1539. URL: https://journals.ametsoc.org/view/journals/bams/87/11/bams-87-11-1539.xml (visited on 12/18/2023).

[47] Paul M. Markowski, Yvette P. Richardson, Scott J. Richardson, and Anders Petersson. "Aboveground Thermodynamic Observations in Convective Storms from Balloonborne Probes Acting as Pseudo-Lagrangian Drifters." In: *Bulletin of the American Meteorological Society* 99.4 (2018), pp. 711–724. DOI: 10.1175/BAMS-D-17-0204.1. URL: https://journals.ametsoc.org/view/journals/bams/99/4/bams-d-17-0204.1.xml.

[48] S. R. Hanna, G. A. Briggs, and Jr Hosker. *Handbook on atmospheric diffusion.* DOE/TIC-11223. National Oceanic and Atmospheric Administration, Oak Ridge, TN (USA), Jan. 1, 1982. DOI: 10.2172/5591108. URL: https://www.osti.gov/biblio/5591108 (visited on 04/30/2024).

[49] JHt LaCasce. "Statistics from Lagrangian observations." In: *Progress in Oceanography* 77.1 (2008), pp. 1–29.

[50] VAISALA. *Vaisala Radiosonde RS41 Measurement Performance.* [Online; accessed 25-Jan-2023]. 2013. URL: https://www.vaisala.com/sites/default/files/documents/White%20paper%20RS41%20Performance%20B211356EN-A.pdf (visited on).

[51] Pierre Morel and William Bandeen. "the Eole experiment: early results and current objectives." en. In: *Bulletin of the American Meteorological Society* 54.4 (Apr. 1973), pp. 298–306. ISSN: 0003-0007, 1520-0477. DOI: 10.1175/1520-0477-54.4.298. URL: https://journals.ametsoc.org/view/journals/bams/54/4/1520-0477-54_4_298.xml (visited on 12/20/2023).

[52] Pierre Morel and Michèle Larceveque. "Relative dispersion of constant–level balloons in the 200–mb general circulation." In: *Journal of Atmospheric Sciences* 31.8 (1974), pp. 2189–2196.

[53] Guglielmo Lacorata, Erik Aurell, Bernard Legras, and Angelo Vulpiani. "Evidence for a $k^{-5/3}$ Spectrum from the EOLE Lagrangian Balloons in the Low Stratosphere." EN. In: *Journal of the Atmospheric Sciences* 61.23 (Dec. 2004), pp. 2936–2942. ISSN: 0022-4928, 1520-0469. DOI: 10.1175/JAS-3292.1. URL: https://journals.ametsoc.org/view/journals/atsc/61/23/jas-3292.1.xml (visited on 12/20/2023).

[54] The TWERLE Team. "The TWERL Experiment." en. In: *Bulletin of the American Meteorological Society* 58.9 (Sept. 1977), pp. 936–949. ISSN: 0003-0007, 1520-0477. DOI: 10.1175/1520-0477-58.9.936. URL: https://journals.ametsoc.org/view/journals/bams/58/9/1520-0477-58_9_936.xml (visited on 12/20/2023).

[55] Joseph Er-El and Richard L Peskin. "Relative diffusion of constant-level balloons in the Southern Hemisphere." In: *Journal of Atmospheric Sciences* 38.10 (1981), pp. 2264–2274.

[56] A Obukhov. "On the distribution of energy in the spectrum of turbulent flow." In: *Dokl. Akad. Nauk SSSR*. Vol. 32. 1941, p. 22.

[57] Bruce A. Albrecht, Christopher S. Bretherton, Doug Johnson, Wayne H. Scubert, and A. Shelby Frisch. "The Atlantic Stratocumulus Transition Experiment—ASTEX." en. In: *Bulletin of the American Meteorological Society* 76.6 (June 1995), pp. 889–904. ISSN: 0003-0007, 1520-0477. DOI: 10.1175/1520-0477(1995)076<0889:TASTE>2.0.CO;2. URL: https://journals.ametsoc.org/view/journals/bams/76/6/1520-0477_1995_076_0889_taste_2_0_co_2.xml (visited on 12/18/2023).

[58] Juan PLC Salazar and Lance R Collins. "Two-particle dispersion in isotropic turbulent flows." In: *Annual review of fluid mechanics* 41 (2009), pp. 405–432.

[59] Federico Toschi and Eberhard Bodenschatz. "Lagrangian Properties of Particles in Turbulence." In: *Annual Review of Fluid Mechanics* 41.1 (2009). _eprint: https://doi.org/10.1146/annurev.fluid.010908.165210, pp. 375–404. DOI: 10.1146/annurev.fluid.010908.165210. URL: https://doi.org/10.1146/annurev.fluid.010908.165210 (visited on 11/27/2023).

[60] N. A. Malik, Th. Dracos, and D. A. Papantoniou. "Particle tracking velocimetry in three-dimensional flows." en. In: *Experiments in Fluids* 15.4 (Sept. 1993), pp. 279–294. ISSN: 1432-1114. DOI: 10.1007/BF00223406. URL: https://doi.org/10.1007/BF00223406 (visited on 03/27/2024).

[61] Marko Virant and Themistocles Dracos. "3D PTV and its application on Lagrangian motion." en. In: *Measurement Science and Technology* 8.12 (Dec. 1997), p. 1539. ISSN: 0957-0233. DOI: 10.1088/0957-0233/8/12/017. URL: https://dx.doi.org/10.1088/0957-0233/8/12/017 (visited on 04/05/2024).

[62] A. La Porta, Greg A. Voth, Alice M. Crawford, Jim Alexander, and Eberhard Bodenschatz. "Fluid particle accelerations in fully developed turbulence." en. In: *Nature* 409.6823 (Feb. 2001). Publisher: Nature Publishing Group, pp. 1017–1019. ISSN: 1476-4687. DOI: 10.1038/35059027. URL: https://www.nature.com/articles/35059027 (visited on 04/05/2024).

[63] D. J. Thomson and B. J. Devenish. "Particle pair separation in kinematic simulations." en. In: *Journal of Fluid Mechanics* 526 (Mar. 2005). Publisher: Cambridge University Press, pp. 277–302. ISSN: 1469-7645, 0022-1120. DOI: 10.1017/S0022112004002915. URL: https://www.cambridge.org/core/journals/journal-of-fluid-mechanics/article/particle-pair-separation-in-kinematic-simulations/6880E3B39858879A12C3D3C081CBC4CD (visited on 01/22/2024).

[64] Brian Sawford. "Turbulent Relative Dispersion." In: *Annual Review of Fluid Mechanics* 33.1 (2001). _eprint: https://doi.org/10.1146/annurev.fluid.33.1.289, pp. 289–317. DOI: 10.1146/annurev.fluid.33.1.289. URL: https://doi.org/10.1146/annurev.fluid.33.1.289 (visited on 11/14/2023).

[65] Michael S. Borgas and P. K. Yeung. "Relative dispersion in isotropic turbulence. Part 2. A new stochastic model with Reynolds-number dependence." en. In: *Journal of Fluid Mechanics* 503 (Mar. 2004), pp. 125–160. ISSN: 1469-7645, 0022-1120. DOI: 10.1017/S0022112003007596. URL: https://www.cambridge.org/core/journals/journal-of-fluid-mechanics/article/relative-dispersion-in-isotropic-turbulence-part-2-a-new-stochastic-model-with-reynoldsnumber-dependence/660014764DF603B2C0B4AA7 (visited on 03/27/2024).

[66] G. Boffetta and I. M. Sokolov. "Relative Dispersion in Fully Developed Turbulence: The Richardson's Law and Intermittency Corrections." In: *Physical Review Letters* 88.9 (Feb. 2002). Publisher: American Physical Society, p. 094501. DOI: 10.1103/PhysRevLett.88.094501. URL: https://link.aps.org/doi/10.1103/PhysRevLett.88.094501 (visited on 03/27/2024).

[67] Nadeem A Malik and Fazle Hussain. "New scaling laws predicting turbulent particle pair diffusion, overcoming the limitations of the prevalent Richardson–Obukhov theory." In: *Physics of Fluids* 33.3 (2021), p. 035135.

[68] Said Elghobashi. "Direct Numerical Simulation of Turbulent Flows Laden with Droplets or Bubbles." en. In: *Annual Review of Fluid Mechanics* 51.Volume 51, 2019 (Jan. 2019). Publisher: Annual Reviews, pp. 217–244. ISSN: 0066-4189, 1545-4479. DOI: 10.1146/annurev-fluid-010518-040401. URL: https://www.annualreviews.org/content/journals/10.1146/annurev-fluid-010518-040401 (visited on 04/05/2024).

[69] B. J. Devenish and D. J. Thomson. "A Lagrangian stochastic model for tetrad dispersion." In: *Journal of Turbulence* 14.3 (Mar. 2013). Publisher: Taylor & Francis _eprint: https://doi.org/10.1080/14685248.2013.780658, pp. 107–120. ISSN: null. DOI: 10.1080/14685248.2013.780658. URL: https://doi.org/10.1080/14685248.2013.780658 (visited on 01/22/2024).

[70] Jörg Schumacher. "Lagrangian studies in convective turbulence." In: *Physical Review E* 79.5 (May 2009). Publisher: American Physical Society, p. 056301. DOI: 10.1103/PhysRevE.79.056301. URL: https://link.aps.org/doi/10.1103/PhysRevE.79.056301 (visited on 12/01/2023).

[71] M. Sommerfeld and S. Stübing. "A novel Lagrangian agglomerate structure model." In: *Powder Technology* 319 (Sept. 2017), pp. 34–52. ISSN: 0032-5910. DOI: 10.1016/j.powtec.2017.06.016. URL: https://www.sciencedirect.com/science/article/pii/S0032591017304758 (visited on 04/05/2024).

[72] J. Pratt, A. Busse, W.-C. Müller, N. W. Watkins, and S. C. Chapman. "Extreme-value statistics from Lagrangian convex hull analysis for homogeneous turbulent Boussinesq convection and MHD convection." en. In: *New Journal of Physics* 19.6 (June 2017). Publisher: IOP Publishing, p. 065006. ISSN: 1367-2630. DOI: 10.1088/1367-2630/aa6fe8. URL: https://dx.doi.org/10.1088/1367-2630/aa6fe8 (visited on 04/05/2024).

[73] G. K. Batchelor. "Diffusion in a field of homogeneous turbulence: II. The relative motion of particles." In: *Mathematical Proceedings of the Cambridge Philosophical Society* 48.2 (1952), pp. 345–362. DOI: 10.1017/S0305004100027687.

[74] Z. Warhaft. "Laboratory studies of droplets in turbulence: towards understanding the formation of clouds." en. In: *Fluid Dynamics Research* 41.1 (Dec. 2008), p. 011201. ISSN: 1873-7005. DOI: 10.1088/0169-5983/41/1/011201. URL: https://dx.doi.org/10.1088/0169-5983/41/1/011201 (visited on 12/12/2023).

[75] B.W. Atkinson and J.W. Zhang. "Mesoscale shallow convection in the atmosphere." In: *Review of Geophysics* 34 (1996), pp. 403–431. DOI: 10.1029/96RG02623.

[76] J Warner. "The microstructure of cumulus cloud. Part I. General features of the droplet spectrum." In: *Journal of Atmospheric Sciences* 26.5 (1969), pp. 1049–1059.

[77] J. Latham and R. L. Reed. "Laboratory studies of the effects of mixing on the evolution of cloud droplet spectra." In: *Quarterly Journal of the Royal Meteorological Society* 103.436 (1977), pp. 297–306. DOI: https://doi.org/10.1002/qj.49710343607.

[78] M. B. Baker, R. G. Corbin, and J. Latham. "The influence of entrainment on the evolution of cloud droplet spectra: I. A model of inhomogeneous mixing." In: *Quarterly Journal of the Royal Meteorological Society* 106.449 (1980), pp. 581–598. DOI: https://doi.org/10.1002/qj.49710644914.

[79] B Gilbert. "Diffusion Mixing In Grid Turbulence without Mean Shear." In: *Journal of Fluid Mechanics* 100 (1980), pp. 349–365. DOI: 10.1017/S002211208000119X.

[80] S. Veeravalli and Z. Warhaft. "The shearless turbulence mixing layer." In: *Journal of Fluid Mechanics* 207 (1989), pp. 191–229. DOI: 10.1017/S0022112089002557.

[81] B. Knaepen, O. Debly Quy, and D. Carati. "Direct numerical simulation and large-eddy simulation of a shear-free mixing layer." In: *Journal Of Fluid Mechanics* 514 (2004), pp. 153–172. DOI: 10.1017/S0022112004000035.

[82] D. A. Briggs, J. H. Ferziger, J. R. Koseff, and S. G. Monismith. "Entrainment in a shear-free turbulent mixing layer." In: *Journal of Fluid Mechanics* 310 (1996), pp. 215–241. DOI: 10.1017/S0022112096001784.

[83] D. Tordella and M. Iovieno. "Numerical experiments on the intermediate asymptotics of shear-free turbulent transport and diffusion." In: *Journal of Fluid Mechanics* 549.-1 (Feb. 8, 2006), p. 429. ISSN: 0022-1120, 1469-7645. DOI: 10.1017/S0022112005007688. URL: http://www.journals.cambridge.org/abstract_S0022112005007688 (visited on 01/26/2024).

[84] D. Tordella and M. Iovieno. "Small scale anisotropy in turbulent shearless mixing." In: *Physical Review Letters* 19.8 (2011), pp. 555–574.

[85] C. N. Franklin. "Collision rates of cloud droplets in turbulent flow." In: *Journal Of The Atmospheric Sciences* 62.7 (2005), pp. 2451–2466. DOI: 10.1175/JAS3493.1.

[86] P. A. Vaillancourt, M. K. Yau, and W. W. Grabowski. "Microscopic Approach to Cloud Droplet Growth by Condensation. Part I: Model Description and Results without Turbulence." In: *Journal of the Atmospheric Sciences* 58.14 (2001), pp. 1945–1964. DOI: 10.1175/1520-0469(2001)058<1945:MATCDG>2.0.CO;2.

[87] Paul Gotzfried, Bipin Kumar, Raymond A. Shaw, and Jörg Schumacher. "Droplet dynamics and fine-scale structure in a shearless turbulent mixing layer with phase changes." In: *Journal of Fluid Mechanics* 814 (2017), pp. 452–483. DOI: 10.1017/jfm.2017.23.

[88] B.J. Devenish, P. Bartello, J. L. Brenguier, L. R. Collins, W. W. Grabowski, R. H. A. Ijzermans, S. P. Malinowski, M. W. Reeks, J. C. Vassilicos, L. P. Wang, and Z. Warhaft. "Droplet growth in warm turbulent clouds." In: *Quarterly Journal of the Royal Meteorological Society* 138.667 (2012), pp. 1401–1429. DOI: 10.1002/qj.1897.

[89] V. Armenio and V. Fiorotto. "The importance of the forces acting on particles in turbulent flows." In: *Physics of Fluids* 13 (2001), pp. 2437–2440. DOI: 10.1063/1.1385390.

[90] L. Bergougnoux, G. Bouchet, D. Lopez, and E. Guazzelli. "The motion of solid spherical particles falling in a cellular flow field at low Stokes number." In: *Physics of Fluids* 26 (2014). DOI: 10.1063/1.4895736.

[91] Hilding Köhler. "The nucleus in and the growth of hygroscopic droplets." In: *Transactions of the Faraday Society* 32.0 (Jan. 1, 1936). Publisher: The Royal Society of Chemistry, pp. 1152–1161. ISSN: 0014-7672. DOI: 10.1039/TF9363201152. URL: https://pubs.rsc.org/en/content/articlelanding/1936/tf/tf9363201152 (visited on 11/23/2023).

[92] W.E. Howell. "The Growth Of Cloud Drops In Uniformly Cooled Air." In: *Journal of meteorology* (June 1949).

[93] H. R. Pruppacher and J. D. Klett. *Micro physics of Clouds and Precipitation.* Atmospheric and Oceanographic Sciences Library, 1997.

[94] Jeffrey I. Steinfeld. "Atmospheric Chemistry and Physics: From Air Pollution to Climate Change." In: *Environment: Science and Policy for Sustainable Development* (Sept. 1, 1998). Publisher: Taylor & Francis Group. ISSN: 0013-9157. URL: https://www.tandfonline.com/doi/abs/10.1080/00139157.1999.10544295 (visited on 04/30/2024).

[95] P. A. Vaillancourt, M. K. Yau, and W. W. Grabowski. "Microscopic Approach to Cloud Droplet Growth by Condensation. Part I: Model Description and Results without Turbulence." In: *Journal of the Atmospheric Sciences* 58.14 (2001), pp. 1945–1964. DOI: 10.1175/1520-0469(2001)058<1945:MATCDG>2.0.CO;2.

[96] B. Kumar, J. Schumacher, and R. A. Shaw. "Lagrangian Mixing Dynamics at the Cloudy–Clear Air Interface." In: *Journal of the Atmospheric Sciences* 71.7 (2014), pp. 2564–2580. DOI: 10.1175/JAS-D-13-0294.1.

[97] Toshiyuki Gotoh, Tamotsu Suehiro, and Izumi Saito. "Continuous growth of cloud droplets in cumulus cloud." In: *New Journal of Physics* 18.4 (2016), p. 043042. DOI: http://stacks.iop.org/1367-2630/18/i=4/a=043042.

[98] Zheng Gao, Yangang Liu, Xiaolin Li, and Chunsong Lu. "Investigation of Turbulent Entrainment-Mixing Processes With a New Particle-Resolved Direct Numerical Simulation Model." In: *Journal of Geophysical Research: Atmospheres* 123.4 (2018), pp. 2194–2214.

[99] James G. Hudson and Xiaoyu Da. "Volatility and size of cloud condensation nuclei." In: *Journal Of Geophysics Research-Atmospheres* 101 (1996), pp. 4435–4442. DOI: 10.1029/95JD00192.

[100] Steven J. Ghan, Hayder Abdul-Razzak, Athanasios Nenes, Yi Ming, Xiaohong Liu, Mikhail Ovchinnikov, Ben Shipway, Nicholas Meskhidze, Jun Xu, and Xiangjun Shi. "Droplet nucleation: Physically-based parameterizations and comparative evaluation." In: *Journal of Advances in Modeling Earth Systems* 3.4 (2011). ISSN: 1942-2466. DOI: 10.1029/2011MS000074. URL: https://onlinelibrary.wiley.com/doi/abs/10.1029/2011MS000074 (visited on 04/30/2024).

[101] I. Saito and T. Gotoh. "Turbulence and cloud droplets in cumulus clouds." In: *New Journal Of Physics* 20.023001 (2018). DOI: 10.1088/1367-2630/aaa229.

[102] M. K. Yau and R. R. Rogers. *A Short Course in Cloud Physics*. en. Google-Books-ID: ClKbCgAAQBAJ. Elsevier, May 1996. ISBN: 978-0-08-057094-5.

[103] R.R. Rogers. "Raindrop Collision Rate." In: *Journal of the Atmospheric Sciences* 46 (15 1989), pp. 2469–72.

[104] K.K. Chandrakar, I. Saito, F. Yang, W. Cantrell, T. Gotoh, and R. A. Shaw. "Droplet size distributions in turbulent clouds: experimental evaluation of theoretical distributions." In: *Quarterly Journal of the Royal Meteorological Society* 146 (2020), pp. 483–504. DOI: 10.1002/qj.3692.

[105] Y. G. Liu and J. Hallett. "On size distributions of cloud droplets growing by condensation: A new conceptual model." In: *Journal of Atmospheric Science* 55 (1998), pp. 527–536. DOI: 10.1175/1520-0469(1998)055<0527:OSDOCD>2.0.CO;2.

[106] W. Wu and G. M. McFarquhar. "Statistical Theory on the Functional Form of Cloud Particle Size Distributions." In: *Journal of Atmospheric Science* 75 (2018), pp. 2801–2814. DOI: 10.1175/JAS-D-17-0164.1.

[107] R. McGraw and Y. G. Liu. "Brownian drift-diffusion model for evolution of droplet size distributions in turbulent clouds." In: *Geophysical Research Letters* 33 (2006), p. L03802. DOI: 10.1029/2005GL023545.

[108] Chandrakar, Kamal Kant, Cantrell, Will, Kelken Chang, David Ciochetto, Dennis Niedermeier, Mikhail Ovchinnikov, Raymond Shaw, and Fan Yang. "Aerosol indirect effect from turbulence-induced broadening of cloud-droplet size distributions." In: *Proceedings of the National Academy of Sciences* 113.50 (2016), pp. 14243–14248. DOI: 10.1073/pnas.1612686113.

[109] C. Siewert, J. Bec, and G. Krstulovic. "Statistical steady state in turbulent droplet condensation." In: *Journal Of Fluid Mechanics* 810 (2017), pp. 254–280. DOI: 10.1017/jfm.2016.712.

[110] I. Saito, T. Gotoh, and T. Watanabe. "Broadening of Cloud Droplet Size Distributions by Condensation in Turbulence." In: *Journal Of The Meteorological Society Of Japan* 19 (2019), pp. 867–891. DOI: 10.2151/jmsj.2019-049.

[111] P. G. Saffman and J. S. Turner. "On the collision of drops in turbulent clouds." In: *Journal of Fluid Mechanics* 1 (1955), pp. 16–30. DOI: https://doi.org/10.1017/S0022112056000020.

[112] Lian-Ping Wang, Anthony S. Wexler, and Yong Zhou. "Statistical mechanical description and modelling of turbulent collision of inertial particles." In: *Journal of Fluid Mechanics* 415 (July 2000), pp. 117–153. ISSN: 0022-1120, 1469-7645. DOI: 10.1017/S0022112000008661. URL: https://www.cambridge.org/core/product/identifier/S0022112000008661/type/journal_article (visited on 02/12/2024).

[113] D. Tordella, M. Iovieno, and P. R. Bailey. "Sufficient condition for Gaussian departure in turbulence." In: *Physical Review E* 77.1 (2008), pp. 016–309. DOI: 10.1103/PhysRevE.77.016309.

[114] D. Tordella and M. Iovieno. "Decaying turbulence: What happens when the correlation length varies spatially in two adjacent zones." In: *Physica D Nonlinear Phenomena* 241 (2012), pp. 175–185. DOI: 10.1016/j.physd.2011.09.001.

[115] T. W. R. East and J. S. Marshall. "Turbulence in clouds as a factor in precipitation." In: *Royal Meteorological Society* (1954). DOI: https://doi.org/10.1002/qj.49708034305.

[116] M. Kostoglou and A. J. Karabelas. "Evaluation of Zero Order Methods for Simulating Particle Coagulation." In: *Journal of Collide and Interface Science* 163 (1994), pp. 420–431. DOI: 10.1006/jcis.1994.1121.

[117] M. Vanni. "Approximate population balance equations for aggregation-breakage processes." In: *Journal of Collide and Interface Science* 22.2 (1999), pp. 143–160. DOI: 10.1006/jcis.1999.6571.

[118] A. Aiyer, D. Yang, M. Chamecki, and C. Meneveau. "A population balance model for large eddy simulation of polydisperse droplet evolution." In: *Journal of Fluid Mechanics* 878 (2019), pp. 700–739. DOI: 10.1017/jfm.2019.649.

[119] Lian-Ping Wang, Bogdan Rosa, Hui Gao, Guowei He, and Guodong Jin. "Turbulent collision of inertial particles: Point-particle based, hybrid simulations and beyond." In: *International Journal of Multiphase Flow*. Special Issue: Point-Particle Model for Disperse Turbulent Flows 35.9 (Sept. 1, 2009), pp. 854–867. ISSN: 0301-9322. DOI: 10.1016/j.ijmultiphaseflow.2009.02.012. URL: https://www.sciencedirect.com/science/article/pii/S030193220900024X (visited on 04/30/2024).

[120] W.W. Grabowski and L.P. Wang. "Growth of Cloud Droplets in a Turbulent Environment." In: *ANNUAL REVIEW OF FLUID MECHANICS* 45 (2013), pp. 293–324. DOI: 10.1146/annurev-fluid-011212-140750.

[121] J. K. Eaton and J. R. Fessler. "Preferential concentration of particles by turbulence." In: *International Journal Of Multiphase Flow* 20 (1994), pp. 169–209. DOI: 10.1016/0301-9322(94)90072-8.

[122] J. D. Woods and Mason B. J. "The wake capture of water drops in air." In: *Quarterly Journal of the Royal Meteorological Society* 91 (1965), pp. 35–43. DOI: https://doi.org/10.1002/qj.49709138706.

[123] K. V. Beard, R. I. Durkee, and H. T. Ochs. "Coalescence Efficiency Measurements for Minimally Charged Cloud Drops." In: *Journal of the Atmospheric Sciences* 59 (2002), pp. 233–243. DOI: 10.1175/1520-0469(2002)059<0233:CEMFMC>2.0.CO;2.

[124] Bipin Kumar, J. Schumacher, and R. A. Shaw. "Cloud microphysical effects of turbulent mixing and entrainment." In: *Theoretical and Computational Fluid Dynamics* 27.3–4 (2013), pp. 361–376. DOI: 10.1007/s00162-012-0272-z.

[125] Chunsong Lu, Yangang Liu, Bin Zhu, Seong Soo Yum, Steven K. Krueger, Yujun Qiu, Shengjie Niu, and Shi Luo. "On Which Microphysical Time Scales to Use in Studies of Entrainment-Mixing Mechanisms in Clouds." In: *Journal of Geophysical Research: Atmospheres* 123.7 (2018), pp. 3740–3756. DOI: 10.1002/2017JD027985.

[126] P. Squires. "The Growth of Cloud Drops by Condensation. I. General Characteristics." In: *Australian Journal of Chemistry* 5.1 (1952), pp. 59–86.

[127] S. Twomey. "The nuclei of natural cloud formation part II: The supersaturation in natural clouds and the variation of cloud droplet concentration." In: *Geofisica pura e applicata* 43.1 (May 1959), pp. 243–249. ISSN: 1420-9136. DOI: 10.1007/BF01993560.

[128] William A. Cooper. "Effects of Variable Droplet Growth Histories on Droplet Size Distributions. Part I: Theory." In: *Journal of Atmospheric Sciences* 46.10 (1989), pp. 1301–1311. DOI: 10.1175/1520-0469(1989)046<1301:EOVDGH>2.0.CO;2.

[129] Holger Siebert and Raymond A. Shaw. "Supersaturation Fluctuations during the Early Stage of Cumulus Formation." In: *Journal of the Atmospheric Sciences* 74.4 (2017), pp. 975–988. DOI: 10.1175/JAS-D-16-0115.1.

[130] Gaetano Sardina, Francesco Picano, Luca Brandt, and Rodrigo Caballero. "Continuous Growth of Droplet Size Variance due to Condensation in Turbulent Clouds." In: *Physical Review Letters* 115.18 (Oct. 29, 2015). Publisher: American Physical Society, p. 184501. DOI: 10.1103/PhysRevLett.115.184501. URL: https://link.aps.org/doi/10.1103/PhysRevLett.115.184501 (visited on 04/30/2024).

[131] V.I. Khvorostyanov and J.A. Curry. *Thermodynamics, Kinetics, and Microphysics of Clouds*. Cambridge University Press, 2014. ISBN: 9781316060711.

[132] Katrin Lehmann, Holger Siebert, and Raymond A. Shaw. "Homogeneous and Inhomogeneous Mixing in Cumulus Clouds: Dependence on Local Turbulence Structure." In: *Journal of the Atmospheric Sciences* 66.12 (2009), pp. 3641–3659. DOI: 10.1175/2009JAS3012.1.

[133] Kamal Kant Chandrakar, Will Cantrell, Kelken Chang, David Ciochetto, Dennis Niedermeier, Mikhail Ovchinnikov, Raymond A. Shaw, and Fan Yang. "Aerosol indirect effect from turbulence-induced broadening of cloud-droplet size distributions." In: *Proceedings of the National Academy of Sciences* 113.50 (2016), pp. 14243–14248. ISSN: 0027-8424. DOI: 10.1073/pnas.1612686113.

[134] Bipin Kumar, Paul Götzfried, Neethi Suresh, Jörg Schumacher, and Raymond A. Shaw. "Scale Dependence of Cloud Microphysical Response to Turbulent Entrainment and Mixing." In: *Journal of Advances in Modeling Earth Systems* 10.11 (2018), pp. 2777–2785. DOI: 10.1029/2018MS001487.

[135] Miroslaw Andrejczuk, Wojciech W. Grabowski, Szymon P. Malinowski, and Piotr K. Smolarkiewicz. "Numerical Simulation of Cloud–Clear Air Interfacial Mixing: Homogeneous versus Inhomogeneous Mixing." In: *Journal of the Atmospheric Sciences* 66.8 (2009), pp. 2493–2500. DOI: 10.1175/2009JAS2956.1.

[136] A Hertzog, C Basdevant, F Vial, and CR Mechoso. "The accuracy of stratospheric analyses in the northern hemisphere inferred from long-duration balloon flights." In: *Quarterly Journal of the Royal Meteorological Society: A journal of the atmospheric sciences, applied meteorology and physical oceanography* 130.597 (2004), pp. 607–626.

[137] Sara Swenson, Brian Argrow, Eric Frew, Steve Borenstein, and Jason Keeler. "Development and Deployment of Air-Launched Drifters from Small UAS." In: *Sensors* 19.9 (2019), p. 2149.

[138] Guillaume Novelli, Cédric M Guigand, Charles Cousin, Edward H Ryan, Nathan JM Laxague, Hanjing Dai, Brian K Haus, and Tamay M Özgökmen. "A biodegradable surface drifter for ocean sampling on a massive scale." In: *Journal of Atmospheric and Oceanic Technology* 34.11 (2017), pp. 2509–2532.

[139] Shahbozbek Abdunabiev, C. Basso Tessa, Daniela Tordella, Miryam Paredes, Eros Pasero, and Flavio Canavero. "Innovative, mini, biodegradable radiosondes to track small-scale fluctuations in warm cloud and clear air environments." In: *BULLETIN OF THE AMERICAN PHYSICAL SOCIETY*. Vol. Volume 64, Number 13. APS, 2019. URL: http://meetings.aps.org/Meeting/DFD19/Session/B18.6.

[140] Miryam Paredes, Shahbozbek Abdunabiev, Marco Allegretti, Giovanni Perona, Daniela Tordella, Eros Pasero, Flavio Canavero, Andrea Merlone, and Chiara Musacchio. "Progress on the development of innovative, floating, biodegradable radio-probes for atmospheric monitoring inside warm clouds." In: *NP6.1*

Lagrangian methods for atmosphere and ocean science. Vienna: EGU General Assembly 2020, 2020. DOI: 10.5194/egusphere-egu2020-22374. URL: https://doi.org/10.5194/egusphere-egu2020-22374.

[141] Shahbozbek Abdunabiev, Mina Golshan, Antonella Abba, and Daniela Tordella. "Free flying cluster of miniaturized radiosondes for multi-parameter atmospheric fluctuation observations." In: *European Turbulence Conference*. Vol. 18. EUROMECH - European Mechanics Society, 2023, pp. 1–1. URL: https://etc18.webs.upv.es/wp-content/uploads/2023/08/Program_final_impresion.pdf.

[142] Shahbozbek Abdunabiev, Andrea Caporali, Miryam Paredes, EROS GIAN ALESSANDRO Pasero, Andrea Merlone, Chiara Musacchio, and Daniela Tordella. "Validation and traceability of multi-parameter miniaturized radiosondes for environmental observations." In: *WMO TECO-2022*. Vol. 2022. World Meteorological Organization, 2022.

[143] Miryam Paredes, Silvano Bertoldo, Lorenzo Carosso, Claudio Lucianaz, Emanuele Marchetta, Marco Allegretti, and Patrizia Savi. "Propagation measurements for a LoRa network in an urban environment." In: *Journal of Electromagnetic Waves and Applications* 33.15 (2019), pp. 2022–2036. DOI: 10.1080/09205071.2019.1661287.

[144] Shahbozbek Abdunabiev, EROS GIAN ALESSANDRO Pasero, and Daniela Tordella. "LoRa based remote expendable radiosonde network for environmental observations." In: *IEEE MetroInd2023 Proceedings*. IEEE Xplore, 2023, pp. 78–83. DOI: 10.1109/MetroInd4.0IoT57462.2023.10180026. URL: https://ieeexplore.ieee.org/document/10180026.

[145] Silvano Bertoldo, Lorenzo Carosso, Emanuele Marchetta, Miryam Paredes, and Marco Allegretti. "Feasibility analysis of a LoRa-based WSN using public transport." In: *Applied System Innovation* 1.4 (2018), p. 49.

[146] Silvano Bertoldo, Claudio Lucianaz, Miryam Paredes, Marco Allegretti, Lorenzo Carosso, and Patrizia Savi. "Feasibility Study of LoRa Ad-Hoc Network in an Urban Noisy Environment." In: *2018 18th Mediterranean Microwave Symposium (MMS)*. 2018, pp. 357–360. DOI: 10.1109/MMS.2018.8612027.

[147] HOPERF. *RFM95W LoRa Module*. [Online; accessed 7-Jan-2023]. 2019. URL: https://www.hoperf.com/modules/lora/RFM95.html (visited on).

[148] ETSI. *Short Range Devices (SRD) operating in the frequency range 25 MHz to 1 000 MHz; Part 2: Harmonised Standard for access to radio spectrum for non specific radio equipment SRDs (25 MHz to 1 GHz)-Part 2*. [Online; accessed 7-Jan-2023]. 2022. URL: https://www.etsi.org/deliver/etsi_en/300200_300299/30022002/03.02.01_60/en_30022002v030201p.pdf (visited on).

[149] Atmel. *ATMEGA328P*. en-US. 2024. URL: https://www.microchip.com/en-us/product/atmega328p (visited on 03/06/2024).

[150] Miryam ELIZABETH Paredes QUINTANILLA. "Electronic design of innovative mini ultralight radioprobes aimed at tracking lagrangian turbulence fluctuations within warm clouds." In: *Doctoral thesis, Dipartimento di Elettronica e Telecomunicazioni (DET), Politecnico di Torino* (2021). URL: https://hdl.handle.net/11583/2950496.

[151] BOSCH. *BME280 - Combined humidity and pressure sensor*. https://www.bosch-sensortec.com/media/boschsensortec/downloads/datasheets/bst-bme280-ds002.pdf. Rev. 1.23, [Online; accessed 16-Jan-2023]. 2022.

[152] U-Blox. *ZOE-M8B - Ultra-small, super low-power u-blox M8 GNSS SiP module Data sheet*. https://www.u-blox.com/sites/default/files/ZOE-M8B_DataSheet_UBX-17035164.pdf. [Online; accessed 4-October-2023]. 2021.

[153] STMicroelectronics. *LSM9DS1 – 9 axis inertial module: 3-axis magnetometer, 3-axis acelerometer and 3-axis gyroscope*. https://www.st.com/resource/en/datasheet/lsm9ds1.pdf. Rev. 3, [Online; accessed 09-Oct-2023]. 2015.

[154] U-Blox. *u-blox 8/u-blox M8 Receiver description*. https://www.u-blox.com/en/docs/UBX-13003221. [Online; accessed 17-March-2022]. 2021.

[155] Wikipedia contributors. *NMEA 0183 — Wikipedia, The Free Encyclopedia*. [Online; accessed 8-Jan-2023]. 2022. URL: https://en.wikipedia.org/w/index.php?title=NMEA_0183&oldid=1116811683 (visited on).

[156] Federico Flores, Roberto Rondanelli, Marcos Díaz, Richard Querel, Karel Mundnich, Luis Alberto Herrera, Daniel Pola, and Tomás Carricajo. "The Life Cycle of a Radiosonde." In: *Bulletin of the American Meteorological Society* 94.2 (2013), pp. 187–198. DOI: https://doi.org/10.1175/BAMS-D-11-00163.1. URL: https://journals.ametsoc.org/view/journals/bams/94/2/bams-d-11-00163.1.xml.

[157] Thomas Lafon, Jennifer Fowler, John Fredy Jiménez, and Gabriel Jaime Tamayo Cordoba. "A Viable Alternative for Conducting Cost-Effective Daily Atmospheric Soundings in Developing Countries." In: *Bulletin of the American Meteorological Society* 95.6 (2014), pp. 837–842. DOI: https://doi.org/10.1175/BAMS-D-13-00125.1. URL: https://journals.ametsoc.org/view/journals/bams/95/6/bams-d-13-00125.1.xml.

[158] International organization for standardization. "ISO 2533:1975, Standard Atmosphere." In: *ISO* 2533 (1975), p. 1975.

[159] Adafruit. *Adafruit Feather 32u4 with LoRa Radio Module*. en-US. 2024. URL: https://learn.adafruit.com/adafruit-feather-32u4-radio-with-lora-radio-module/overview (visited on 03/06/2024).

[160] Dragino. *LG01v2 – LoRa Gateway User Manual - DRAGINO*. 2024. URL: http://wiki.dragino.com/xwiki/bin/view/Main/User%20Manual%20for%20All%20Gateway%20models/LG01v2/#H1.2Specifications (visited on 03/06/2024).

[161] Sebastian O. Madgwick, Andrew J. Harrison, and Ravi Vaidyanathan. "Estimation of IMU and MARG orientation using a gradient descent algorithm." In: *2011 IEEE International Conference on Rehabilitation Robotics* (2011), pp. 1–7. DOI: 10.1109/ICORR.2011.5975346.

[162] Rudolf E. Kalman. "A New Approach to Linear Filtering and Prediction Problems." In: *Journal of Basic Engineering* 82.1 (Mar. 1960), pp. 35–45. ISSN: 0021-9223. DOI: 10.1115/1.3662552.

[163] A. Merlone, G. Lopardo, F. Sanna, S. Bell, R. Benyon, R. A. Bergerud, F. Bertiglia, J. Bojkovski, N. Böse, M. Brunet, A. Cappella, G. Coppa, D. del Campo, M. Dobre, J. Drnovsek, V. Ebert, R. Emardson, V. Fernicola, K. Flakiewicz, T. Gardiner, C. Garcia-Izquierdo, E. Georgin, A. Gilabert, A. Grykałowska, E. Grudniewicz, M. Heinonen, M. Holmsten, D. Hudoklin, J. Johansson, H. Kajastie, H. Kaykısızlı, P. Klason, L. Kňazovická, A. Lakka, A. Kowal, H. Müller, C. Musacchio, J. Nwaboh, P. Pavlasek, A. Piccato, L. Pitre, M. de Podesta, M. K. Rasmussen, H. Sairanen, D. Smorgon, F. Sparasci, R. Strnad, A. Szmyrka- Grzebyk, and R. Underwood. "The MeteoMet project – metrology for meteorology: challenges and results." In: *Meteorological Applications* 22.S1 (2015), pp. 820–829. DOI: https://doi.org/10.1002/met.1528. eprint: https://rmets.onlinelibrary.wiley.com/doi/pdf/10.1002/met.1528. URL: https://rmets.onlinelibrary.wiley.com/doi/abs/10.1002/met.1528.

[164] A Merlone, F Sanna, G Beges, S Bell, G Beltramino, J Bojkovski, M Brunet, D del Campo, A Castrillo, N Chiodo, M Colli, G Coppa, R Cuccaro, M Dobre, J Drnovsek, V Ebert, V Fernicola, A Garcia-Benadí, C Garcia-Izquierdo, T Gardiner, E Georgin, A Gonzalez, D Groselj, M Heinonen, S Hernandez, R Högström, D Hudoklin, M Kalemci, A Kowal, L Lanza, P Miao, C Musacchio, J Nielsen, M Nogueras-Cervera, S Oguz Aytekin, P Pavlasek, M de Podesta, M K Rasmussen, J del-Río-Fernández, L Rosso, H Sairanen, J Salminen, D Sestan, L Šindelářová, D Smorgon, F Sparasci, R Strnad, R Underwood, A Uytun, and M Voldan. "The MeteoMet2 project—highlights and results." In: *Measurement Science and Technology* 29.2 (Jan. 2018), p. 025802. DOI: 10.1088/1361-6501/aa99fc. URL: https://dx.doi.org/10.1088/1361-6501/aa99fc.

[165] Marco Rosoldi, Graziano Coppa, Andrea Merlone, Chiara Musacchio, and Fabio Madonna. "Intercomparison of Vaisala RS92 and RS41 Radiosonde Temperature Sensors under Controlled Laboratory Conditions." In: *Atmosphere* 13.5 (2022). ISSN: 2073-4433. DOI: 10.3390/atmos13050773. URL: https://www.mdpi.com/2073-4433/13/5/773.

[166] Chiara Musacchio, Simone Bellagarda, Marion Maturilli, Jürgen Graeser, Vito Vitale, and Andrea Merlone. "Arctic metrology: calibration of radiosondes ground check sensors in Ny-Ålesund." In: *Meteorological Applications* 22.S1 (2015), pp. 854–860. DOI: https://doi.org/10.1002/met.1506. eprint: https://rmets.onlinelibrary.wiley.com/doi/pdf/10.1002/met.1506. URL: https://rmets.onlinelibrary.wiley.com/doi/abs/10.1002/met.1506.

[167] Debashis Nath, M. Venkat Ratnam, A. K. Patra, B. V. Krishna Murthy, and S. Vijaya Bhaskar Rao. "Turbulence characteristics over tropical station Gadanki (13.5°N, 79.2°E) estimated using high-resolution GPS radiosonde data." In: *Journal of Geophysical Research: Atmospheres* 115.D7 (2010). DOI: https://doi.org/10.1029/2009JD012347. eprint: https://agupubs.onlinelibrary.wiley.com/doi/pdf/10.1029/2009JD012347. URL: https://agupubs.onlinelibrary.wiley.com/doi/abs/10.1029/2009JD012347.

[168] Aditya Jaiswal, D. V. Phanikumar, S. Bhattacharjee, and Manish Naja. "Estimation of Turbulence Parameters Using ARIES ST Radar and GPS Radiosonde Measurements: First Results From the Central Himalayan Region." In: *Radio Science* 55.8 (2020), e2019RS006979. DOI: https://doi.org/10.1029/2019RS006979. eprint: https://agupubs.onlinelibrary.wiley.com/doi/pdf/10.1029/2019RS006979. URL: https://agupubs.onlinelibrary.wiley.com/doi/abs/10.1029/2019RS006979.

[169] S.-W. Lee, S. Kim, Y.-S. Lee, B. I. Choi, W. Kang, Y. K. Oh, S. Park, J.-K. Yoo, J. Lee, S. Lee, S. Kwon, and Y.-G. Kim. "Radiation correction and uncertainty evaluation of RS41 temperature sensors by using an upper-air simulator." In: *Atmospheric Measurement Techniques* 15.5 (2022), pp. 1107–1121. DOI: 10.5194/amt-15-1107-2022. URL: https://amt.copernicus.org/articles/15/1107/2022/.

[170] Matías Tagle, Francisca Rojas, Felipe Reyes, Yeanice Vásquez, Fredrik Hallgren, Jenny Lindén, Dimitar Kolev, Ågot K Watne, and Pedro Oyola. "Field performance of a low-cost sensor in the monitoring of particulate matter in Santiago, Chile." In: *Environmental monitoring and assessment* 192.3 (2020), p. 171.

[171] Richard Wilson, Hubert Luce, Hiroyuki Hashiguchi, Masato Shiotani, and Francis Dalaudier. "On the effect of moisture on the detection of tropospheric turbulence from in situ measurements." In: *Atmospheric Measurement Techniques* 6.3 (2013), pp. 697–702.

[172] B+B Thermo-Technik. *Capacitive humidity sensor KFS140-FA*. https://shop.bb-sensors.com/out/media/Datasheet_humidity_sensor_KFS140-FA.pdf. [Online; accessed 01-Oct-2023]. 2021.

[173] Innovative Sensor Technology. *P14 4051 Rapid Thermo humidity sensor*. https://www.ist-ag.com/sites/default/files/downloads/DHP14-Rapid_E.pdf. [Online; accessed 01-Oct-2023]. 2019.

[174] Shree K. Nayar. *First Principles of Computer Vision: Reconstruction II*. [Online; accessed 14-March-2023]. 2023. URL: https://fpcv.cs.columbia.edu/ (visited on 03/14/2023).

[175] Alan Lukezic, Tomas Vojir, Luka Cehovin Zajc, Jiri Matas, and Matej Kristan. "Discriminative Correlation Filter With Channel and Spatial Reliability." In: *Proceedings of the IEEE Conference on Computer Vision and Pattern Recognition (CVPR)* (July 2017).

[176] OpenCV - Open Source Computer Vision. *Tracking API*. [Online; accessed 14-March-2023]. 2023. URL: https://docs.opencv.org/3.4/d9/df8/group__tracking.html (visited on).

[177] Ewan O'Connor. *Model data from Chilbolton on 5 July 2023*. 2023. URL: https://hdl.handle.net/21.12132/1.bb07bdeb9739418f.

[178] Jagadish C. Kaimal, John J. Finnigan, and J. C. Kaimal. *Atmospheric boundary layer flows: their structure and measurement*. eng. New York: Oxford University Press, 1994. ISBN: 978-0-19-506239-7.

[179] Holger Siebert, Kai-Erik Szodry, Ulrike Egerer, Birgit Wehner, Silvia Henning, Karine Chevalier, Janine Lückerath, Oliver Welz, Kay Weinhold, Felix Lauermann, Matthias Gottschalk, André Ehrlich, Manfred Wendisch, Paulo Fialho, Greg Roberts, Nithin Allwayin, Simeon Schum, Raymond A. Shaw, Claudio Mazzoleni, Lynn Mazzoleni, Jakub L. Nowak, Szymon P. Malinowski, Katarzyna Karpinska, Wojciech Kumala, Dominika Czyzewska, Edward P. Luke, Pavlos Kollias, Robert Wood, and Juan Pedro Mellado. "Observations of Aerosol, Cloud, Turbulence, and Radiation Properties at the Top of the Marine Boundary Layer over the Eastern North Atlantic Ocean: The ACORES Campaign." EN. In: *Bulletin of the American Meteorological Society* 102.1 (Jan. 2021), E123–E147. ISSN: 0003-0007, 1520-0477. DOI: 10.1175/BAMS-D-19-0191.1. URL: https://journals.ametsoc.org/view/journals/bams/102/1/BAMS-D-19-0191.1.xml (visited on 12/18/2023).

[180] W. Kumala, K. E. Haman, M. K. Kopec, D. Khelif, and S. P. Malinowski. "Modified ultrafast thermometer UFT-M and temperature measurements during Physics of Stratocumulus Top (POST)." English. In: *Atmospheric Measurement Techniques* 6.8 (Aug. 2013). Publisher: Copernicus GmbH, pp. 2043–2054. ISSN: 1867-1381. DOI: 10.5194/amt-6-2043-2013. URL: https://amt.copernicus.org/articles/6/2043/2013/ (visited on 03/27/2024).

[181] Ewan J. O'Connor, Anthony J. Illingworth, Ian M. Brooks, Christopher D. Westbrook, Robin J. Hogan, Fay Davies, and Barbara J. Brooks. "A Method for Estimating the Turbulent Kinetic Energy Dissipation Rate from a Vertically Pointing Doppler Lidar, and Independent Evaluation from Balloon-Borne In Situ Measurements." EN. In: *Journal of Atmospheric and Oceanic Technology* 27.10 (Oct. 2010), pp. 1652–1664. ISSN: 0739-0572, 1520-0426. DOI: 10.1175/2010JTECHA1455.1. URL: https://journals.ametsoc.org/view/journals/atot/27/10/2010jtecha1455_1.xml (visited on 11/14/2023).

[182] Domingo Muñoz-Esparza, Robert D. Sharman, and Julie K. Lundquist. "Turbulence Dissipation Rate in the Atmospheric Boundary Layer: Observations and WRF Mesoscale Modeling during the XPIA Field Campaign." EN. In: *Monthly Weather Review* 146.1 (Jan. 2018). Publisher: American Meteorological Society Section: Monthly Weather Review, pp. 351–371. ISSN: 1520-0493, 0027-0644. DOI: 10.1175/MWR-D-17-0186.1. URL: https://journals.ametsoc.org/view/journals/mwre/146/1/mwr-d-17-0186.1.xml (visited on 11/14/2023).

[183] G. K. Batchelor. "The Theory of Homogeneous Turbulence." In: *Cambridge University Press* 38 (1953), pp. 64–65. DOI: 10.2151/jmsj.2019-049.

[184] Subharthi Chowdhuri and Tirtha Banerjee. "Revisiting "bursts" in wall-bounded turbulent flows." In: *Physical Review Fluids* 8.4 (Apr. 2023). Publisher: American Physical Society, p. 044606. DOI: 10.1103/PhysRevFluids.8.044606. URL: https://link.aps.org/doi/10.1103/PhysRevFluids.8.044606 (visited on 04/09/2024).

[185] Elisa F. Akansu, Sandro Dahlke, Holger Siebert, and Manfred Wendisch. "Evaluation of methods to determine the surface mixing layer height of the atmospheric boundary layer in the central Arctic during polar night and transition to polar day in cloudless and cloudy conditions." English. In: *Atmospheric Chemistry and Physics* 23.24 (Dec. 2023). Publisher: Copernicus GmbH, pp. 15473–15489. ISSN: 1680-7316. DOI: 10.5194/acp-23-15473-2023. URL: https://acp.copernicus.org/articles/23/15473/2023/ (visited on 01/12/2024).

[186] M. Collaud Coen, C. Praz, A. Haefele, D. Ruffieux, P. Kaufmann, and B. Calpini. "Determination and climatology of the planetary boundary layer height above the Swiss plateau by in situ and remote sensing measurements as well as by the COSMO-2 model." English. In: *Atmospheric Chemistry and Physics* 14.23 (Dec. 2014). Publisher: Copernicus GmbH, pp. 13205–13221. ISSN: 1680-7316. DOI: 10.5194/acp-14-13205-2014. URL: https://acp.copernicus.org/articles/14/13205/2014/ (visited on 01/12/2024).

[187] James M. Wallace. "Space-time correlations in turbulent flow: A review." In: *Theoretical and Applied Mechanics Letters* 4.2 (Jan. 2014), p. 022003. ISSN: 2095-0349. DOI: 10.1063/2.1402203. URL: https://www.sciencedirect.com/science/article/pii/S2095034915303081 (visited on 12/01/2023).

[188] Guowei He, Guodong Jin, and Yue Yang. "Space-Time Correlations and Dynamic Coupling in Turbulent Flows." en. In: *Annual Review of Fluid Mechanics* 49.Volume 49, 2017 (Jan. 2017). Publisher: Annual Reviews, pp. 51–70. ISSN: 0066-4189, 1545-4479. DOI: 10.1146/annurev-fluid-010816-060309. URL: https://www.annualreviews.org/content/journals/10.1146/annurev-fluid-010816-060309 (visited on 04/23/2024).

[189] Qunzhen Wang, Kyle D. Squires, and Xiaohua Wu. "Lagrangian statistics in turbulent channel flow." In: *Atmospheric Environment* 29.18 (Sept. 1995), pp. 2417–2427. ISSN: 1352-2310. DOI: 10.1016/1352-2310(95)00190-A. URL: https://www.sciencedirect.com/science/article/pii/135223109500190A (visited on 04/24/2024).

[190] Niklas Schnierstein, Jan Chylik, Matthew D. Shupe, and Roel Neggers. "Standardized daily high-resolution large-eddy simulations of the Arctic boundary layer and clouds during the complete MOSAiC drift." In: *Authorea Preprints* (2024). Publisher: Authorea. URL: https://essopenarchive.org/doi/pdf/10.22541/essoar.171033230.00246941 (visited on 03/20/2024).

[191] D. W. Goldberg, C. Sardinha, D. E. Oliveira, P. V. Castilho, J. V. Vieira, J. Ikeda, C. A. Marques, T. S. Neves, and G. Canani. "Fatal interactions of albatrosses with weather radiosondes/balloons on the Southern and Southeastern coasts of Brazil." In: *Marine Pollution Bulletin* 201 (Apr. 2024), p. 116267. ISSN: 0025-326X. DOI: 10.1016/j.marpolbul.2024.116267. URL: https://www.sciencedirect.com/science/article/pii/S0025326X24002443 (visited on 03/27/2024).

[192] B. J. Mason and C. W. Chien. "Cloud-droplet growth by condensation in cumulus." en. In: *Quarterly Journal of the Royal Meteorological Society* 88.376 (1962). _eprint: https://onlinelibrary.wiley.com/doi/pdf/10.1002/qj.49708837603, pp. 136–142. ISSN: 1477-870X. DOI: 10.1002/qj.49708837603. URL: https://onlinelibrary.wiley.com/doi/abs/10.1002/qj.49708837603 (visited on 03/03/2024).

[193] Xiang-Gui Li, Yongyong Cai, and Pengde Wang. "Operator-compensation methods with mass and energy conservation for solving the Gross-Pitaevskii equation." In: *Applied Numerical Mathematics* 151 (May 2020), pp. 337–353. ISSN: 0168-9274. DOI: 10.1016/j.apnum.2020.01.004. URL: https://www.sciencedirect.com/science/article/pii/S0168927420300052 (visited on 03/03/2024).

[194] Michele Iovieno, Silvio DI SAVINO, Luca Gallana, and Daniela Tordella. "Mixing of a passive scalar across a thin shearless layer: Concentration of intermittency on the sides of the turbulent interface." In: *JOURNAL OF TURBULENCE* 15.5 (2014). Publisher: Taylor & Francis, pp. 311–334. DOI: 10.1080/14685248.2014.905393. URL: http://www.tandfonline.com/doi/abs/10.1080/14685248.2014.905393#.U2j9WFeylCM.

[195] P. J. Ireland and L. R. Collins. "Direct numerical simulation of inertial particle entrainment in a shearless mixing layer." In: *Journal of fluid mechanics* 704 (2012), p. 301.

[196] G. Good, S. Gerashchenko, and Z. Warhaft. "Intermittency and inertial particle entrainment at a turbulent interface: the effect of the large-scale eddies." In: *Journal of fluid mechanics* 694 (2012), p. 371.

[197] S. Gerashchenko, G. Good, and Z. Warhaft. "Entrainment and mixing of water droplets across a shearless turbulent interface with and without gravitational effects." In: *Journal of fluid mechanics* 668 (2011), p. 293.

[198] Miroslaw Andrejczuk, Wojciech W. Olshanrabowski, Szymon P. Malinowski, and Piotr K. Smolarkiewicz. "Numerical Simulation of Cloud–Clear Air Interfacial Mixing." In: *Journal of the Atmospheric Sciences* 61.14 (2004), pp. 1726–1739. DOI: 10.1175/1520-0469(2004)061<1726:NSOCAI>2.0.CO;2.

[199] Otto Tetens. "Uber einige meteorologische Begriffe." In: *Z Geophys* 6 (1930), pp. 297–309.

[200] John Monteith and Mike Unsworth. "Principles of Environmental Physics, 3rd Edition." In: *Academic Press* (2008), p. 440.

[201] N. N. Mansour and A. A. Wray. "Decay of isotropic turbulence at low Reynolds number." en. In: *Physics of Fluids* 6.2 (1994), pp. 808–814. ISSN: 1070-6631, 1089-7666. DOI: 10.1063/1.868319. URL: https://pubs.aip.org/pof/article/6/2/808/420919/Decay-of-isotropic-turbulence-at-low-Reynolds (visited on 02/13/2024).

[202] J. I. MacPherson and G. A. Isaac. "Turbulent Characteristics of Some Canadian Cumulus Clouds." In: *Journal of Applied Meteorology* 16.1 (1977), pp. 81–90. DOI: 10.1175/1520-0450(1977)016<0081:TCOSCC>2.0.CO;.

[203] Stephen B. Pope. *Turbulent Flows*. 1st ed. Cambridge University Press, Aug. 10, 2000. ISBN: 978-0-521-59125-6 978-0-521-59886-6 978-0-511-84053-1. DOI: 10.1017/CBO9780511840531. URL: https://www.cambridge.org/core/product/identifier/9780511840531/type/book (visited on 04/30/2024).

[204] Takashi Ishihara, Toshiyuki Gotoh, and Yukio Kaneda. "Study of High–Reynolds Number Isotropic Turbulence by Direct Numerical Simulation." In: *Annual Review of Fluid Mechanics* 41.1 (2009), pp. 165–180. DOI: 10.1146/annurev.fluid.010908.165203.

[205] Kyle A. Brucker, Juan C. Isaza, T. Vaithianathan, and Lance R. Collins. "Efficient algorithm for simulating homogeneous turbulent shear flow without remeshing." In: *Journal of Computational Physics* 225.1 (2007), pp. 20–32. ISSN: 0021-9991. DOI: https://doi.org/10.1016/j.jcp.2006.10.018.

[206] Philofluid Research Group. *DNS pseudospectral codes*. 2024. URL: https://areeweb.polito.it/ricerca/philofluid/software/95-turbulent-flows.html (visited on 02/14/2024).

[207] Luca Gallana. "Statistical analysis of inhomogeneous fluctuation fields. Scalar transport in shearless turbulent mixing, effects of stratification, solar wind and solar wind-interstellar medium interaction." Publisher: Politecnico di Torino. PhD thesis. Politecnico di Torino, 2016. URL: https://iris.polito.it/handle/11583/2653026 (visited on 02/01/2024).

[208] Philofluid Research Group. *Code scaling*. 2024. URL: https://areeweb.polito.it/ricerca/philofluid/software/255-code-scaling (visited on 02/14/2024).

[209] Ruggiero, V and Codoni, D and Tordella, D. "A Numerical Code for The Study of Water Droplets' Growth, Collision, Coalescence and Clustering Inside Turbulent Warm Cloud-Clear Air Interfaces." In: *Partnership for Advanced Computing in Europe (PRACE)* (May 24, 2018). URL: https://prace-ri.eu/wp-content/uploads/WP266.pdf (visited on 02/14/2024).

This Ph.D. thesis has been typeset by means of the TEX-system facilities. The typesetting engine was LuaLATEX. The document class was `toptesi`, by Claudio Beccari, with option `tipotesi=scudo`. This class is available in every up-to-date and complete TEX-system installation.